

REPORT DOCUMENTATION PAGE

AFRL-SR-BL-TR-01-

Public reporting burden for this collection of information is estimated to average 1 hour per response, including the gathering and maintaining the data needed, and completing and reviewing the collection of information. Send comment collection of information, including suggestions for reducing this burden, to Washington Headquarters Services, Directorate for Information Operations and Reports, 1215 Jefferson Davis Highway, Suite 1204, Arlington, VA 22202-4302, and to the Office of Management and Budget, Paperwork Reduction Project (0330-0187).

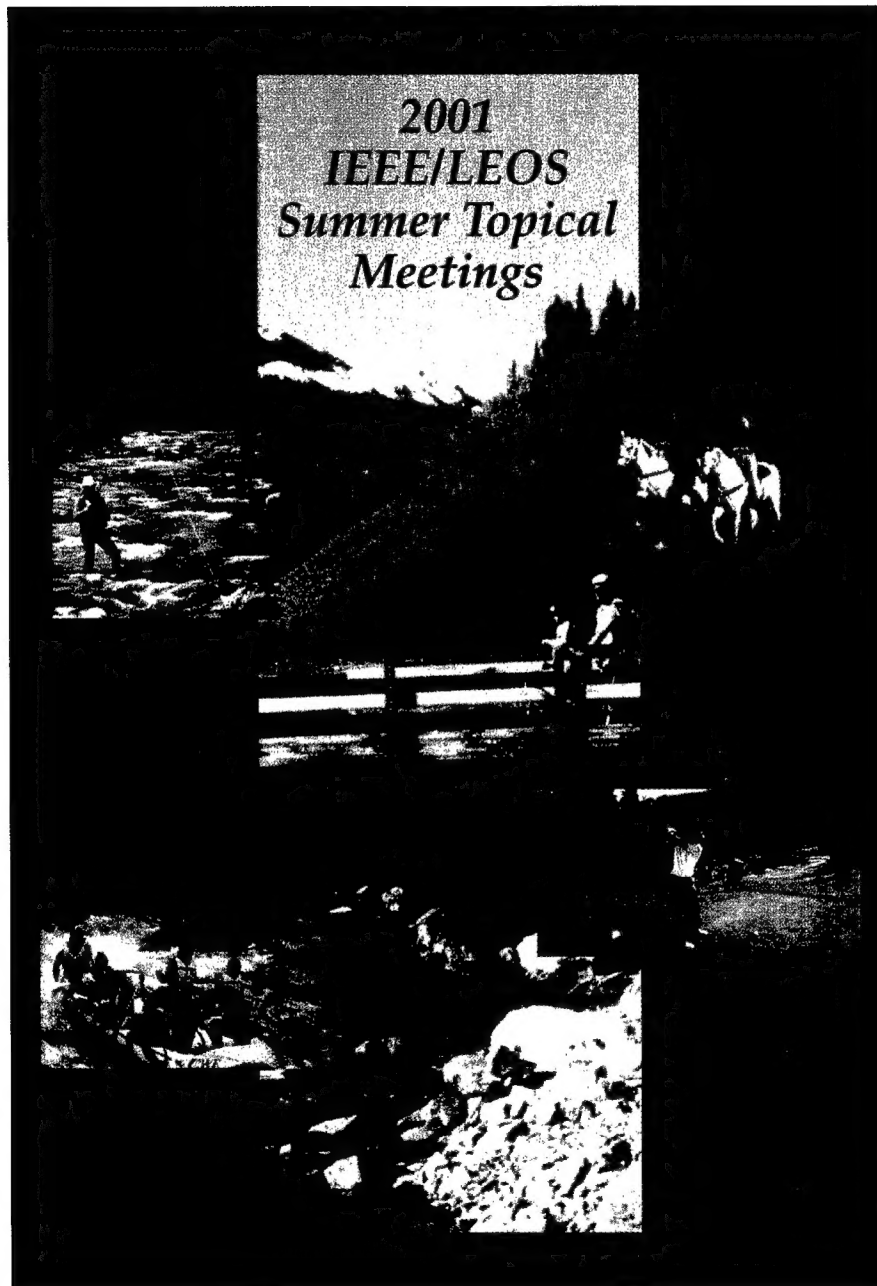
0357

1. AGENCY USE ONLY (Leave Blank)		2. REPORT DATE July 2001		3. REPORT TYPE AND DATES COVERED Final Technical	
4. TITLE AND SUBTITLE Technical Digest of the 2001 Summer Topical Meeting on Ultraviolet and Blue Lasers and their Applications				5. FUNDING NUMBERS G F49620-01-1-0404	
6. AUTHORS Multiple					
7. PERFORMING ORGANIZATION NAME(S) AND ADDRESS(ES) Institute of Electrical and Electronics Engineers, Inc. 445 Hoes Lane, P.O. Box 1331 Piscataway, NJ 08855-1331				8. PERFORMING ORGANIZATION REPORT NUMBER	
9. SPONSORING / MONITORING AGENCY NAME(S) AND ADDRESS(ES) AFOSR/NE 801 N. Randolph St Room 732 Arlington, VA 22203-1977				10. SPONSORING / MONITORING AGENCY REPORT NUMBER	
11. SUPPLEMENTARY NOTES					
12a. DISTRIBUTION / AVAILABILITY STATEMENT APPROVED FOR PUBLIC RELEASE				<p>AIR FORCE OFFICE OF SCIENTIFIC RESEARCH (AFOSR) NOTICE OF TRANSMITTAL DTIC. THIS TECHNICAL REPORT HAS BEEN REVIEWED AND IS APPROVED FOR PUBLIC RELEASE LAW AFR 190-12. DISTRIBUTION IS UNLIMITED.</p>	
13. ABSTRACT (Maximum 200 words)					
<p>2001 Digest of the LEOS Summer Topical Meetings, Advanced Semiconductor Lasers and Applications, Ultraviolet and Blue Lasers and their Applications, Ultralong Haul DWDM Transmission and Networking and WDM Components.</p>					
14. SUBJECT TERMS blue and ultraviolet solid state, fiber, diode and gas lasers, primary solid state crystalline and glass sources, fiber systems, GaN diodes, frequency converted lamp and diode pumped blue and uv lasers, nonlinear conversion materials for blue/uv generation from the infrared, optical parametric oscillators, upconversion techniques, high order harmonic generation, system applications,				15. NUMBER OF PAGES 186	
				16. PRICE CODE	
17. SECURITY CLASSIFICATION OF REPORT Unclassified	18. SECURITY CLASSIFICATION OF THIS PAGE Unclassified	19. SECURITY CLASSIFICATION OF ABSTRACT Unclassified	20. LIMITATION OF ABSTRACT UL		

20011126 091

2001 Digest of the LEOS Summer Topical Meetings

*Advanced Semiconductor Lasers and Applications
Ultraviolet and Blue Lasers and their Applications
Ultralong Haul DWDM Transmission and Networking
WDM Components*

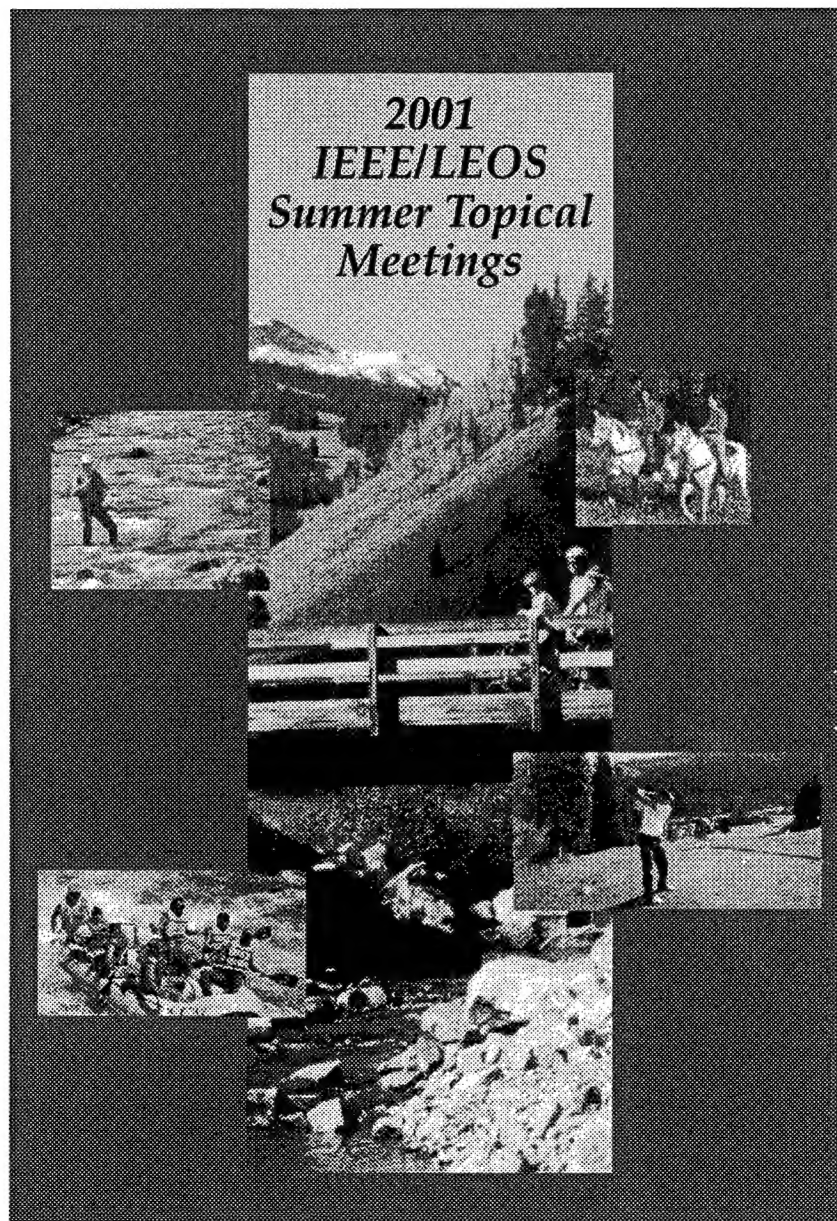


*30 July - 1 August 2001
Copper Mountain Resort,
Copper Mountain, Colorado*

IEEE Catalog # 01TH8572 ISBN #0-7803-7100-3

2001 Digest of the LEOS Summer Topical Meetings

*Advanced Semiconductor Lasers and Applications
Ultraviolet and Blue Lasers and their Applications
Ultralong Haul DWDM Transmission and Networking
WDM Components*



*30 July - 1 August 2001
Copper Mountain Resort,
Copper Mountain, Colorado*

IEEE Catalog # 01TH8572 ISBN #0-7803-7100-3

**2001 IEEE/LEOS
Summer Topical Meeting**

30 July – 1 August 2001

**Advanced Semiconductor
Lasers and Applications**

**Copper Mountain Resort
Copper Mountain, CO**

IEEE Catalog Number: 01TH8572

ISBN: 0-7803-7100-3

ISSN: 1099-4742

The papers in this book comprise the digest of the meeting mentioned on the cover and title page. They reflect the authors' opinions and are published as presented and without change in the interest of timely dissemination. Their inclusion in this publication does not necessarily constitute endorsement by the editors, the Institute of Electrical and Electronics Engineers, Inc.

© 2001 by the Institute of Electrical and Electronics Engineers, Inc. All rights reserved.

Copyright and Reprint Permissions: Abstracting is permitted with credit to the source. Libraries are permitted to photocopy beyond the limits of U.S. copyright law, for private use of patrons those articles in this volume that carry a code at the bottom of the first page, provided the per-copy fee indicated in the code is paid through the Copyright Clearance Center, 222 Rosewood Drive, Danvers, MA 01923. For other copying, reprint, or republication permission, write to IEEE Copyrights Manager, IEEE Service Center, 445 Hoes Lane, P.O. Box 1331, Piscataway, NJ 08855-1331.

IEEE Catalog Number:	01TH8572
ISBN:	0-7803-7100-3
ISSN:	1099-4742



Advanced Semiconductor Lasers and Applications

Co-Chairs:

Daniel Blumenthal, *UCSB*, Santa Barbara, CA
Bardia Pezeshki, *Santur Corporation*, Mountain View, CA

Technical Program Committee:

D. Deppe, *University of Texas at Austin*, Austin, TX
L. Eng, *Agere Systems*, Allentown, PA
G. Fish, *Agility Communications*, Santa Barbara, CA
J. Kitching, *NIST*, Boulder, CO
D. Kuchta, *IBM TJ Watson Research Center*, Yorktown Heights, NY
R. Mirin, *NIST*, Boulder, CO
P. Morton, *Ciena Corporation*, Linthicum, MD
R. Ram, *MIT*, Cambridge, MA

TABLE OF CONTENTS

Monday, 30 July 2001

MA1.	Spectroscopy & Noise	
MA1.1	Recent Advances in CRDS: Reaching Out beyond Mass Spectrometry.....	N/A
MA1.2	Diode Laser Frequency Control for Cavity Ring-Down Spectroscopy	3
MA1.3	VCSELs in Nonlinear Spectroscopy: Making Optical Magnetometers and Atomic Clocks Practical	5
MA1.4	Performance of Single Mode Laser Components using 2D Photonic Lattice Reflectors	7
MA1.5	Mode Partition Noise in Vertical Cavity Surface Emitting Lasers.....	9
MA1.6	Current Noise in Semiconductor Lasers.....	11
MA2.	Long Wavelength VCSELs I	
MA2.1	Progress on Long Wavelength VCSEL.....	13
MA2.2	GaAsSb/GaAs 1.3- μ m-VCSELs for 10G-Ethernet.....	15
MA2.3	Quantum Dot Vertical Cavity Lasers	17
MA3.	Long Wavelength VCSELs II	
MA3.1	Vertical Cavity Lasers for Telecommunications Networks: Prospects and Challenges	19
MA3.2	Long Wavelength InGaAsN/GaAs Edge Emitting Lasers with Low Threshold Current Density Grown by MOCVD	21
MA3.3	GaInNAs, a New Material for Long Wavelength VCSELs.....	23

Tuesday, 31 July 2001

TuA1.	Tunable Lasers I: VCSELs	
TuA1.1	Network Architectures and Requirements for Widely Tunable Lasers.....	27
TuA1.2	Electrically-Pumped Directly-Modulated Tunable VCSEL for Metro DWDM Applications.....	29
TuA1.3	High Power MEMs-Tunable Vertical-Cavity Surface-Emitting Lasers	31
TuA2.	Tunable Lasers II: DBR Based Devices	
TuA2.1	Tunable Lasers using Sampled Grating DBRs	33
TuA2.2	GCSRs and other Widely Tunable Lasers	35
TuA2.3	Fully Functional Wavelength Selectable DWDM Transmitter.....	37
TuA3.	Tunable Lasers III: External Cavity & Arrays	
TuA3.1	External Cavity Tunable Lasers for Network Deployment.....	39
TuA3.2	Widely Tunable External Cavity Diode Laser using a MEMS Electrostatic Rotary Actuator	41
TuA3.3	Wavelength Selectable Microarray Light Sources	43

Wednesday, 1 August 2001

WA1.	Communication Lasers	
WA1.1	High Speed Uncooled Spot-Size-Converted Distributed Feedback Lasers Suitable for Passive Alignment and 2.5 Gb/s Operation at 85C	47
WA1.2	VCSEL Modulation at 20Gb/s over 200m of Multimode Fiber using a 3.3v SiGe Laser Driver IC	49
WA1.3	Single Mode, Low Impedance 850-nm VCSELs with Integrated Mode Filters	51

Advanced Semiconductor Lasers and Applications

Monday, 30 July 2001

- MA1: Spectroscopy & Noise
- MA2: Long Wavelength VCSELs I
- MA3: Long Wavelength VCSELs II

Monday Missing Paper

- MA1.1 "Recent Advances in CRDS: Reaching Out beyond Mass Spectrometry"
B. Paldus, *Informed Diagnostics Inc., Sunnyvale, CA, USA.*

Diode Laser Frequency Control for Cavity Ring-down Spectroscopy

R. W. Fox and L. Hollberg

National Institute of Standards and Technology, 325 Broadway, Boulder, CO

Here we describe a system consisting of an extended cavity laser electronically locked to a high-finesse ($\Delta\nu \sim 6$ kHz) cavity. The Pound-Drever-Hall technique¹ is used, with the side-bands applied at 30 MHz and a servo bandwidth of nearly 3 MHz. Repetitive locking and un-locking is accomplished by the use of high-speed analog switches at a number of positions in the feedback circuit.

Cavity ring-down spectroscopy is often used to measure low levels of absorption in laboratory settings. The technique relies on the accurate determination of the exponential decay of power from a high-finesse cavity. If a difference in the decay time constant can be measured both with and without an intra-cavity absorber present, the loss due to the absorption over an effective path of tens of kilometers can be calculated. This results in exceedingly sensitive absorption measurements. In our work we have used a 25 cm long cavity with a ring-down time of 25 μ s, which corresponds to a cavity finesse of 90,000 and an effective path length of about 15 km.

Both pulsed and cw lasers are used by research groups in this field. Typically the ring-down event is digitized by a fast A/D board, and subsequently the decay time is extracted by a least-squares fit to the data. Noise in the data can be reduced by averaging if each event has the same time constant, even if the individual decay traces begin from differing intensity levels. Consequently it is often systematic errors which limit the accurate measurement of the decay time. For instance pulsed lasers, depending on the bandwidth, will generally couple to many cavity modes. This leads to beating between modes and departures from an exponential decay. CW excitation has been recognized as superior to pulsed excitation, since the decay is from a single mode and high intensity levels are possible at the start of the ring-down.² The ideal lasers for ring-down instruments would be widely tunable, but also have sufficiently narrow line-widths so that most of the power could be locked to a narrow cavity.

The cavity ring-down is measured in transmission by quickly switching the laser frequency off of the cavity resonance, instead of using an acousto-optic switch to divert the beam from the cavity. We are presently investigating the circumstances in which this approach results in an acceptable decay time measurement. The simplicity and cost of the system is significantly reduced by the absence of the AO modulator and drive electronics.

To measure the ring-down, the feedback is switched off and simultaneously the laser is switched off-resonance by shunting a portion of the injection current to ground. The intensity decay lasts approximately 10τ before becoming comparable to the detector noise. (τ is the cavity time constant, about 25 μ s). To monitor the laser frequency we use a separate reference cavity with a 10 MHz line-width (see fig 1.).

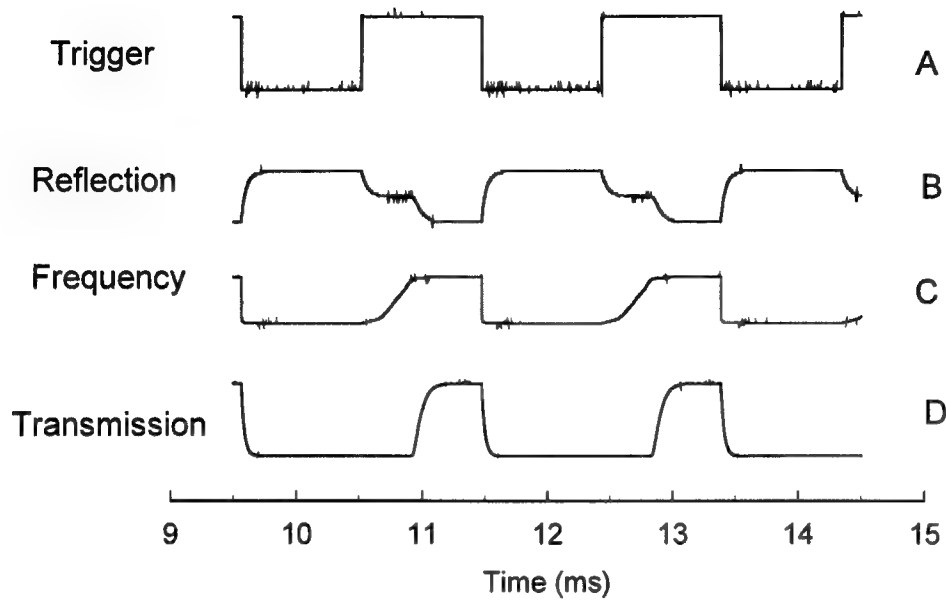


Fig. 1 The top square wave is a 500 Hz trigger square wave. The cavity ring-down occurs at the falling edge, as shown in the Transmission trace on the bottom. The second trace shows the cavity reflection, and the third is an indication of the laser's frequency as measured by a separate reference cavity. On a negative going trigger, current is shunted away from the laser such that it moves about 5 MHz in frequency within 2 μ s. On a positive going trigger the laser current is restored, and the frequency is pulled back to the resonance by the servo.

The 3 MHz servo bandwidth is more than sufficient to tightly lock the extended cavity laser to the ring-down cavity. This control bandwidth is limited by phase shift in the laser chip itself, and was obtained by properly adding phase compensation at a number of points in the feedback loop.

Contribution of the US Government, not subject to copyright.

¹ R. W. P. Drever, J. L. Hall, F. V. Kowalski, J. Hough, G. M. Ford, A. J. Munley, and H. Ward, "Laser Phase and Frequency Stabilization Using an Optical Resonator", *Appl. Phys.* **B31**, 97-105 (1983).

² B. A Paldus, C. C. Harb, T. G. Spence, B. Wilke, J. Xie, J. S. Harris, and R. N. Zare, "Cavity-locked ring-down spectroscopy," *J. Appl. Phys.* **83**, 3991-3997 (1998).

VCSELs in Nonlinear Spectroscopy: Making Optical Magnetometers and Atomic Clocks Practical

R. Wynands, C. Affolderbach, L. Hollberg¹,
J. Klitching¹, S. Knappe, M. Stähler

Institute for Applied Physics, Bonn University, D-53115 Bonn, Germany

¹ *National Institute of Standards and Technology, Boulder, CO 80503, USA*

Tel +49-228-733483, Fax +49-228-733474, E-mail:

wynands@iap.uni-bonn.de

We have experimentally investigated the potential of narrow coherent population trapping (CPT) resonances [1] for precision applications like magnetometry [2, 3], miniaturized atomic frequency standards [4, 5], and the determination of atomic g -factors [6] using the D lines in thermal Cs or Rb vapor. These narrow resonances (widths smaller than 100 Hz are routinely achieved) are probed by a bichromatic laser light field with a frequency difference in the GHz range (9.2 GHz, 6.7 GHz, and 3.0 GHz for Cs, ^{87}Rb , and ^{85}Rb , respectively). This light field can conveniently be derived from a current-modulated single-mode VCSEL, using the carrier and one of the modulation sidebands [7]. This allows for the construction of extremely compact setups with not more than a few 100 mW of electrical power consumption.

When a small magnetic offset field is applied the CPT resonance splits into several Zeeman components. The magnetometer works by monitoring the position of the Zeeman-shifted outermost resonance component. The central Zeeman component is well suited for frequency standard applications because its position is shifted by magnetic fields only in second order. Certain other components lend themselves readily for a determination of the ratio of electronic and nuclear magnetic moments in the atom (g -factor ratio). Picotesla sensitivity for a magnetometer and 10^{-12} relative instability for a finger-sized clock have been achieved in this way (Fig. 1), and a relative inaccuracy of the g -factor ratio of better than 10^{-6} is envisioned for the near future.

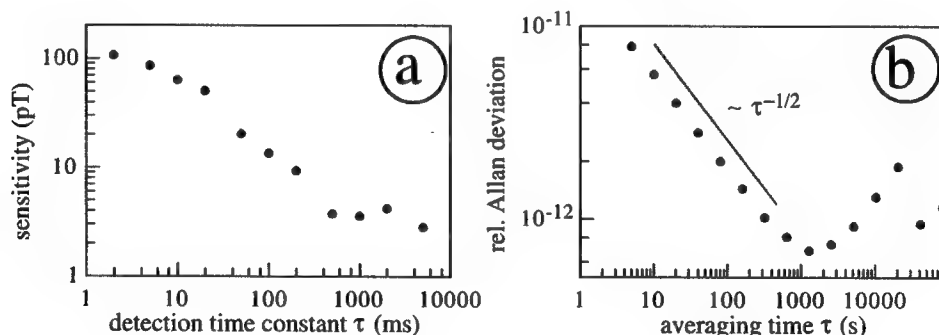


Fig. 1. (a) Magnetometric sensitivity of the Cs dark resonance magnetometer [3]. (b) Allan standard deviation of a compact Cs dark resonance clock [3].

The common problem for all such precision measurements is to gain a thorough understanding of possible systematic effects and of the noise processes limiting the precision. Apart from "the usual suspects" in that context we have identified a new noise source connected to optical hyperfine pumping [8]. Fig. 2 shows the measured detection noise power spectral density (dots) as a function of laser detuning from resonance with the optical transitions. The dashed line is a calculation based on the measured frequency (FM) and amplitude (AM) noise of the laser. The peculiar shape reflects

the absolute value of the slope of the Doppler-broadened optical absorption line: laser FM noise is converted at this slope into AM noise behind the vapor cell. Surprisingly, the whole curve is shifted by about 40 MHz from the center of the optical absorption spectrum. When this shift is included the calculation agrees very well with the experimental data (solid line in Fig. 2).

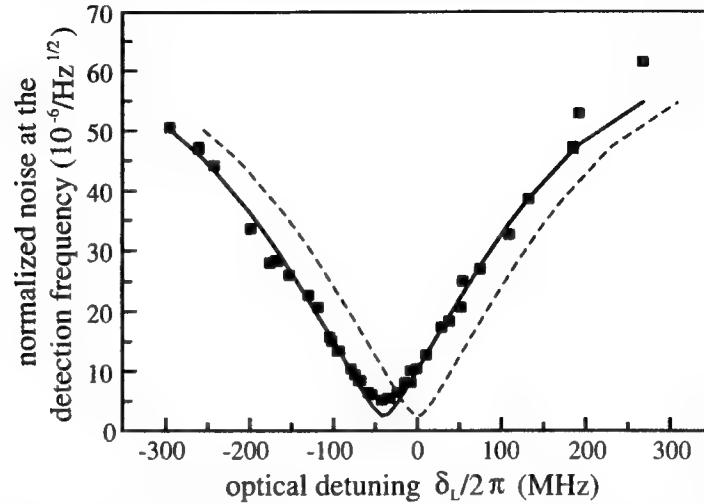


Fig. 2. Detector noise power spectral density as a function of detuning of the laser frequencies from optical resonance (dots: experimental data, dashed line: calculation using the FM and AM noise of the laser, solid line: frequency-dependent optical pumping included) [3].

The shift can be explained and modeled by considering the dependence of the optical hyperfine pumping on the Fourier frequency of the noise. This model further predicts the presence of an additional noise term that is also responsible for the fact that the noise minimum lies somewhat higher than the shot and laser AM noise level. This excess noise should also occur in other types of atomic clocks that involve optical pumping. Furthermore, the shift of the noise minimum with respect to the optical absorption maximum implies a similar shift of the optimum operating point of the dark resonance magnetometer or clock.

The newly-discovered excess noise as well as the general performance of the devices is mainly limited by the FM noise of the VCSEL. The development of VCSELs with smaller linewidths but large modulation bandwidth is therefore highly desirable for these applications.

References

1. E. Arimondo, "Coherent population trapping in laser spectroscopy", *Progress in Optics* **35**, 257 (1996)
2. A. Nagel *et al.*, "Experimental realisation of coherent dark state magnetometers", *Europhys. Lett.* **44**, 31 (1998).
3. M. Stähler *et al.*, "Picotesla magnetometry with coherent dark states", *Europhys. Lett.*, in the press.
4. J. Kitching *et al.*, "A microwave frequency reference based on VCSEL-driven dark line resonances in Cs vapor", *IEEE Trans. Instrum. Meas.* **49**, 1313 (2000)
5. S. Knappe *et al.*, "Characterization of coherent population trapping resonances as atomic frequency references", *J. Opt. Soc. Am. B*, in the press.
6. A. Nagel *et al.*, "Influence of excited state hyperfine structure on ground state coherence", *Phys. Rev. A* **61**, 012504 (2000).
7. C. Affolderbach *et al.*, "Nonlinear spectroscopy with a vertical-cavity surface-emitting laser (VCSEL)", *Appl. Phys. B* **70**, 407 (2000).
8. J. Kitching *et al.*, "Optical pumping noise in vapor-cell frequency references", submitted for publication.

Performance of Single Mode Laser Components using 2D Photonic Lattice Reflectors

M.Hill, A.Massara*, M.Gioannini, R.V.Penty and I.H.White

Centre for Communications Research, University of Bristol, Queens Building, Bristol, BS8 1TR, UK

*now at Agilent Technologies, Ipswich, UK

Abstract: *This paper will report studies of the placement of 2D photonic gratings on either side of the ridge in a Fabry Perot laser device in order to cause single mode emission. Using this approach, side mode suppression ratios of up to 30 dB are achieved, the emission remaining single mode even under 10 Gb/s large signal modulation. It is found that the use of the grating not only causes spectrally dependent reflection but in addition can lead to transverse mode fluctuations. The action of the grating has been studied not just in terms of its edge emission where conversion of the transverse modes is achieved, but also through measurement of the vertical emission from the structure where strong filtering action is observed.*

There is currently much interest in the development of low cost techniques for fabricating single mode laser diodes for data communication applications. As a result, techniques using strongly coupled 1D air gratings have been studied as these allow gratings to be achieved without the use of overgrowth. More recently 2D gratings have been studied. These studies show that strong single mode operation can be achieved without mode hopping being observed.

In order to study the properties of 2D photonic gratings, in this work, focussed ion beam etching has been used to etch a close packed hexagonal lattice of holes in the trench region alongside the ridge in a 1.3 μ m wavelength ridge waveguide MQW Fabry Perot laser diode (figure 1). Typically the holes are etched in a 50 micron long region near one of the facets of the laser, the holes having been etched down to near the active region. To allow a formal study to be initiated, etches have been carried out on a range of ridge laser structures including those with different combinations on cleaved, anti-reflection coated and highly-reflecting facets.

Prior to etching, the Fabry Perot devices exhibit multimode optical spectra. This performance changes strongly however after formation of the hole lattice, at which point side mode suppression ratios of up to 30 dB can be achieved (figure 2). This single mode behaviour remains for a current range from threshold to 3.5 times threshold. The side mode suppression ratio is limited by the residual Fabry Perot modes of the lasing cavity which remain particularly in uncoated devices. To verify the cause of these residual modes, transmission matrix modelling has been conducted, the theoretical results showing excellent agreement with experiment (figure 3). The model further indicates that the side mode suppression ratio will be greatly enhanced by the use of coating on the facet near the 2D lattice reflector.

The lasing wavelength varies at a rate of 0.009nm/mA reduced greatly from the previous Fabry Perot value. There is no evidence of mode hopping. The small signal performance of the device as measured at 20°C for an increasing DC bias current shows the -3dB bandwidth increasing at a rate of 1.4GHz/ $\sqrt{\text{mA}}$, along with a maximum 3dB bandwidth of in excess of 11GHz. The device has been successfully modulated at 10Gbits/s with NRZ data ($2^{23}-1$ PRBS), biased at 70mA with a swing of 40mA giving rise to an extinction ratio of 6.5 dB. This is limited by the original dynamics of the FP laser diode.

Detailed studies of the near field performance of the component have been carried out along with the measurement of the emission vertically from the grating region. Vertical emission from the device, not operating in the lasing single mode regime, clearly shows the strong spectral dependence of the reflection (figure 4), only a narrow wavelength region being selected. In addition to the spectral properties of the grating however, it can be observed from near field measurements that within the grating region, the lasing mode splits into two parts (figure 5), near the holes, this indicating that the grating is sufficiently strong to modify the transverse modal structure. Further results concerning these new observations will be presented at the conference.

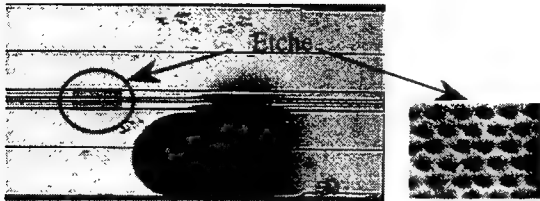


Figure 1 Plan view of the laser and a close up of the 2D lattice etched region

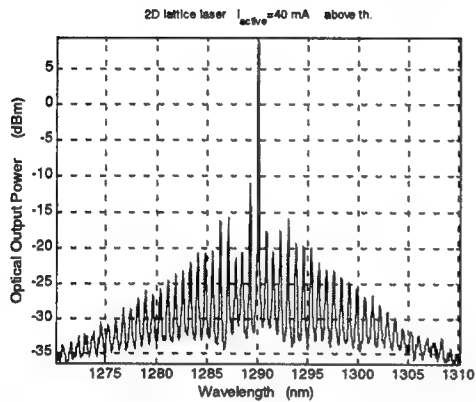


Figure 2 Measured spectra for etched FP laser with cleaved facet

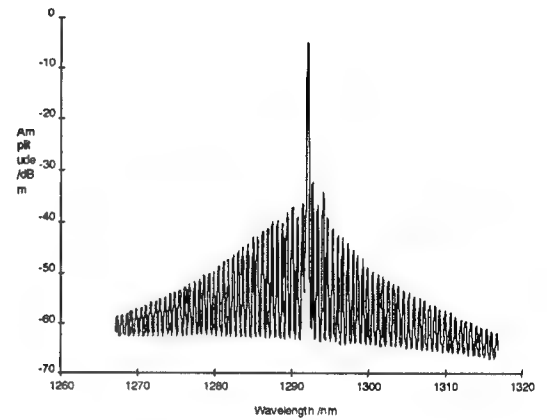


Figure 3 Simulated spectra for etched FP laser with cleaved facet

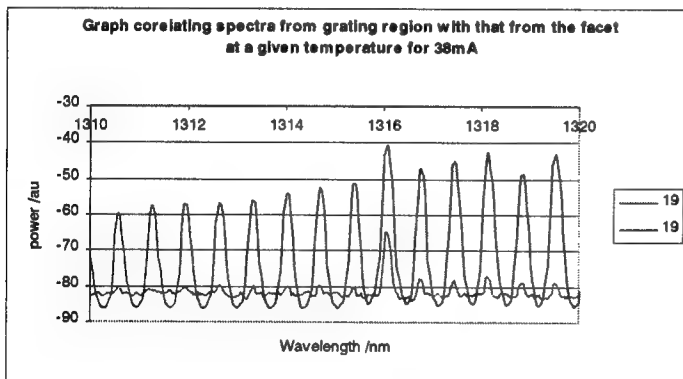


Figure 4 Measured Facet spectra compared with grating emitted light

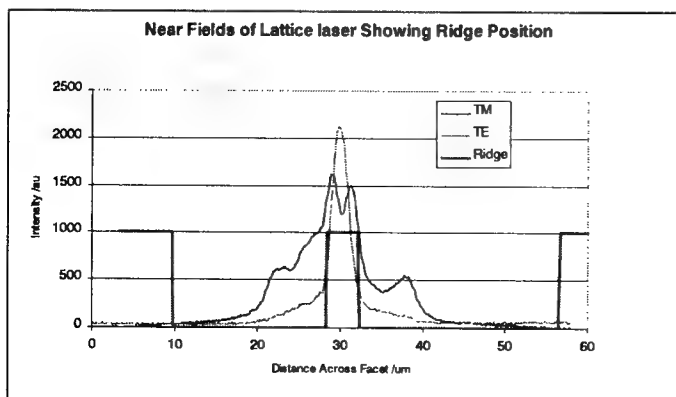


Figure 5 Near fields of etched laser with superimposed facet position, the intensities are not relative to each other.

Mode Partition Noise in Vertical Cavity Surface Emitting Lasers

H. L. T. Lee and R. J. Ram

Research Laboratory of Electronics, Massachusetts Institute of Technology, Room 26-459, Cambridge MA, 02139
phone: (617)258-0273, fax: (617)258-7864, email: harrylee@mit.edu

In vertical cavity surface emitting lasers (VCSELs), a single longitudinal mode is supported in a cavity that can allow multiple transverse modes. In contrast to edge emitting lasers where multiple modes are longitudinal with nearly identical transverse profile, transverse modes can have significant differences in their coupling efficiency. Hence, mode selective loss (MSL) is easily introduced and mode partition noise (MPN) is more significant to the intensity noise of VCSELs. In this paper, we discuss the relevant time scales of the mode partition dynamics of VCSELs and explain the low frequency dependence of the relative intensity noise (RIN) spectrum.

Mode partition noise is often explained in terms of a disruption in the anti-correlation that exists between the individual modes due to their mutual coupling through the carrier density [1-3]. It is argued that a positive fluctuation in one mode saturates the gain for all of the modes and hence their fluctuations are anti-correlated. However, this explanation does not account for the time scale of this interaction and hence cannot explain the frequency dependence of the MPN spectral density shown in Fig. 1 (solid line.) A more careful examination of the dynamics of two modes when one is perturbed can elucidate the time scales important in the dynamics. Fig. 2 shows the time domain perturbation response for a single node (zero space dimensions), two mode model, with a side mode suppression ratio of 18dB calculated by perturbing the main mode by 10% and following the subsequent evolution back to the steady state operating point. This model describes a situation where the multiple modes are strongly coupled. The top plot shows the perturbation response for short time scales, on the order of a relaxation oscillation period. Note that the side mode response is two orders of magnitude smaller than the main mode response and left and right axes have been scaled and shifted to emphasize that the perturbation response of the modes on this time scale is *positively* correlated because their time evolutions track each other. The bottom plot shows the perturbation response for long time scales, on the order of the ratio of the side mode photon density to the spontaneous emission rate into the side mode, or the reciprocal of the gain defect. Here both perturbation responses are of equal magnitude and are clearly *negatively* correlated as their time evolutions are opposing. This is the anti-correlation that leads to a large increase in the low frequency noise power spectral density (PSD) when mode selective loss disrupts the cancellation between these two long time scale responses. At high frequencies near the relaxation oscillation resonance, because the modes are positively correlated and the main mode response dominates the side mode response, the resonant intensity noise is insensitive to MSL. The reasoning from the time domain perturbation analysis is consistent with calculations of the mode cross-correlations, which are negative for low frequencies and positive at the relaxation oscillation resonance as shown in Fig. 3. Physically, at short time scales, the total photon density is out of equilibrium with the carrier density and the laser behaves as a single mode laser. That is, the carrier density and total photon density undergo relaxation oscillations until the carrier density returns to its steady state value. At this point, while the total photon density has returned to its steady state value, the photon density of the individual modes are not in equilibrium and it is the inter-modal evolution towards steady state that is anti-correlated.

The single node model described above applies in situations where the modes are strongly coupled. For a VCSEL with weakly overlapping modes, a different type of inter-modal interaction can occur because the modes can interact with their own individual and a shared region of carrier density. This type of response is characterized by an oscillatory long time scale response and consequently, a noise PSD that has a low frequency oscillation peak as shown in the dashed line of Fig. 2 which was calculated with a 32 node model with a side mode suppression of 6dB. This type of behavior in VCSELs has been pointed out and observed in the past [4] and has been interpreted as relaxation oscillation peaks in the side modes. However, similar to the discussion above, there is a single relaxation oscillation resonance that characterizes the laser as a whole, where the modes are positively correlated. The other resonance peak is the anti-correlated interaction between modes as they settle towards their own equilibrium and is accentuated in the intensity noise spectrum by MSL.

With the qualitative understanding of the time scales that govern MPN in the RIN spectrum, it is possible to develop simple analytical expressions to estimate the mode partition noise at frequencies below the relaxation oscillation resonance. Preliminary results indicate that for the case of strongly coupled modes and a weak side mode, the low frequency cutoff frequency is equal to the side mode gain defect, which can be expressed as the difference between

the side mode photon lifetime and modal gain, or the ratio between the spontaneous emission number rate into the mode and the photon number in the mode. For VCSELs, this is on the order of 10 MHz. Also of interest in estimating the influence of mode partition noise on the intensity noise is determining the value of the DC or low frequency noise. Preliminary results show that for large mode selective loss (one minus the ratio between the side mode and main mode collection efficiencies), the DC noise is quadratic in the mode selective loss and, for small side mode power, linear in the side mode suppression ratio (ratio between the side mode power and main mode power). The results of the model appear to be consistent with the observed degradation of microwave link performance at frequencies on the order of hundreds of megahertz to one gigahertz [5] and indicate that microwave links using multimode VCSELs are limited by increased intensity noise due to mode partitioning and mode selective loss.

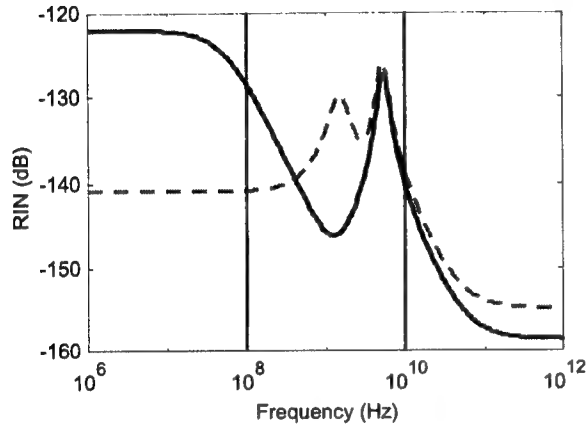


Fig. 1. Calculated relative intensity noise spectra for single node (solid, SMSR = 18dB) and 32 node finite difference (dashed, SMSR = 6dB) model with 50% MSL of the side mode.

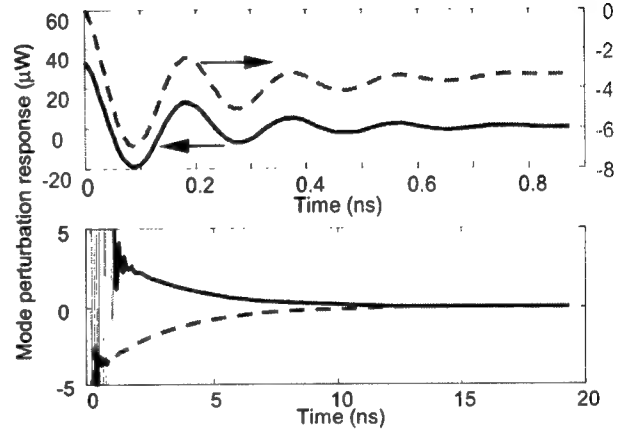
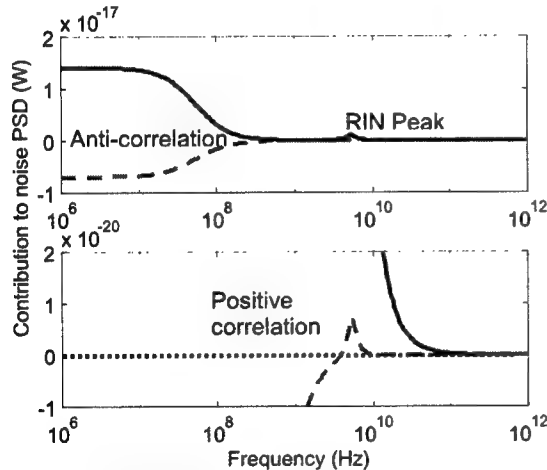


Fig. 2. Time domain perturbation response from a single node, two mode model representing strongly coupled modes where the main mode is increased by 10% at $t=0$. The main (solid) and side (dashed) mode responses are positively correlated at short times while the total photon density equilibrates and are negatively correlated at long time scales while the individual modes equilibrate.

Fig. 3. Main mode autocorrelation (solid) and cross-correlation (dashed) contributions to the noise PSD. In the top plot, the anti-correlation between the main and side mode is indicated by the negative cross-correlation. In the bottom plot, the y-axis is scaled to show the positive cross correlation at the relaxation oscillation frequency.

- [1] G. P. Agrawal, "Mode-partition noise and intensity correlation in a two-mode semiconductor laser," *Phys. Rev. A*, vol. 37, no. 7, pp. 2488-2494, Apr. 1988.
- [2] S. Lathi and Y. Yamamoto, "Influence of nonlinear gain and loss on the intensity noise of a multimode semiconductor laser," *Phys. Rev. A*, vol. 59, no. 1, pp. 819-825, Jan. 1999.
- [3] J. Y. Law and G. P. Agrawal, "Mode-partition noise in vertical-cavity surface-emitting lasers," *IEEE Photon. Technol. Lett.*, vol. 9, no. 4, pp. 437-439, Apr. 1997.
- [4] A. Valle and L. Pesquera, "Relative intensity noise of multitransverse-mode vertical-cavity surface-emitting lasers," *IEEE Photon. Technol. Lett.*, vol. 13, no. 4, pp. 272-274, Apr. 2001.
- [5] H. L. T. Lee, R. V. Dalal, R. J. Ram, and K. D. Choquette, "Dynamic range of vertical-cavity surface-emitting lasers in multimode links," *IEEE Photon. Technol. Lett.*, Vol. 11, No. 11, pp. 1473-1475, Nov. 1999.

Current Noise in Semiconductor Lasers

F. Rana, P. Mayer, R. J. Ram

MIT Research Laboratory for Electronics, 77 Massachusetts Av., Room 26-457, Cambridge, MA 02139
farhan@mit.edu

Accurate modeling of the current noise in semiconductor lasers is desired for many different applications. It is well known that high impedance suppression of the current noise in semiconductor lasers leads to photon number squeezing in the laser output [1,2]. However, the magnitude of the current noise is not well known and, therefore, it is difficult to predict the limits on the amount of squeezing achievable in semiconductor lasers. Accurate modeling of the current noise is also important in semiconductor cascade laser structures in which PN junctions are connected electrically in series [5-8]. In such devices the degree of correlation in photon emission events in different junctions depends on the magnitude of the current noise. In addition, we show in this paper that high frequency current noise measurements can also be used to measure the modulation bandwidth of semiconductor lasers without using any photodetector.

Many laser noise models that have appeared in the literature simply assume statistics for the current noise from the beginning and feed these into the standard laser noise models to calculate the photon noise [5,9]. Such an approach is not self-consistent since a significant portion of the current noise is in fact a circuit response to the carrier density fluctuations inside the active region. In references [1,2] self-consistent models of the current noise in semiconductor lasers have been presented. These models assume from the start a fixed relation between the carrier density fluctuations inside the active region and the fluctuations in the potential difference across the active region. This assumption, although valid for homo-junction semiconductor lasers, does not hold for hetero-junction lasers and overestimates the current noise in the later devices. In addition, all the current noise models ignore the carrier density fluctuations inside the cladding (SCH) regions. The partition noise associated with carrier recombination and carrier leakage in the cladding regions, which as we show sets the upper limit on the amount of photon number squeezing, is consequently neglected.

In this paper we present a detailed model for the current noise in semiconductor hetero-junction lasers and correlate the theoretical results with experimental measurements. The model is fully self-consistent and includes the carrier density fluctuations in the cladding (SCH) regions. The different processes contributing to the current noise are shown in Fig.1. The noise associated with carrier injection into the active region, carrier recombination and leakage in the cladding regions, carrier capture into and carrier emission from the quantum wells, and radiative and non-radiative carrier recombination in the quantum wells is included in the model. In references [1,2] it is shown that the maximum amount of photon number squeezing achievable in semiconductor lasers is $10\log(1-\eta_o)$ dB, where η_o is the laser output coupling efficiency [9]. We show that the partition noise associated with carrier recombination and leakage in the cladding regions limits the maximum amount of squeezing achievable in semiconductor lasers to $10\log(1-\eta_o\eta_i)$ dB, where η_i is the current injection efficiency defined as the fraction of the total number of carriers injected into the active region that recombine in the quantum wells. This result explains the discrepancy between the maximum amount of squeezing observed experimentally (typically $\sim 1-4$ dB after correcting for less than unity detection efficiency) and that which is calculated by ignoring the partition noise (typically $\sim 7-10$ dB) [4]. In reference [3] it has been argued that non-zero current injection efficiency would not lead to increased photon noise since coulomb correlations suppress the noise associated with current partitioning in parallel resistive paths. We show that this argument does not hold in charge neutral active regions of semiconductor lasers. Fig.2 shows the calculated and measured spectral density of photon noise using the model presented in this paper and also using the model presented in references [1,2].

We show both theoretically and experimentally that a significant portion of the current noise in semiconductor lasers is a circuit response to the carrier density fluctuations inside the active region. Current noise measurements can therefore provide important information about the high frequency dynamics inside the laser. Fig.3 shows the experimentally measured high frequency current noise spectra as a function of the bias current in an InGaAsP/InP laser operating at $1.55\ \mu\text{m}$. The current noise spectra show peaks at the laser relaxation oscillation frequency. This is to our knowledge the first observation of relaxation oscillation peaks in the laser current noise. Current noise

measurements can therefore also be used to study the modulation dynamics of semiconductor lasers completely in the electrical domain without using photodetectors. We also show low frequency measurements of the current noise and compare them with the theoretical model.

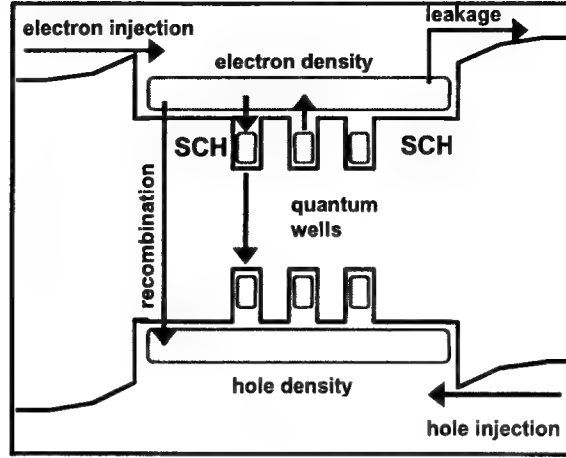


Fig.1 : Energy band diagram of semiconductor quantum well laser showing the various processes contributing to the current noise. The carrier recombination and leakage in the SCH regions also contribute to the current and photon noise.

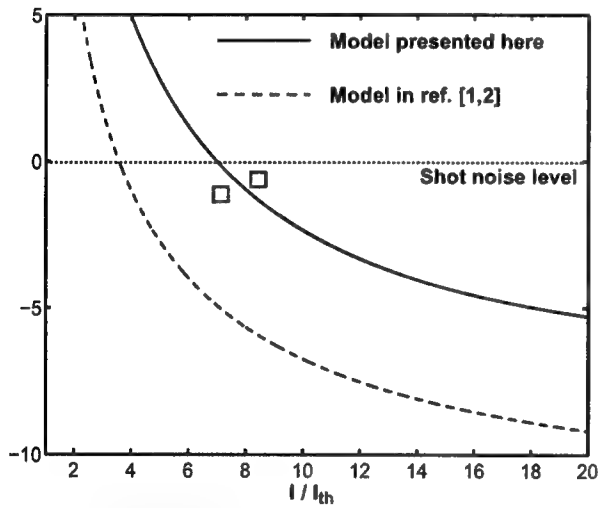


Fig.2 : Spectral density (in dB) of photon noise (normalized to shot noise) of a $1.55 \mu\text{m}$ laser. The inclusion of current partition noise increases the noise level by several dB above that predicted by the model presented in references [1,2]. Boxes are the experimentally measured results in Ref. [10].

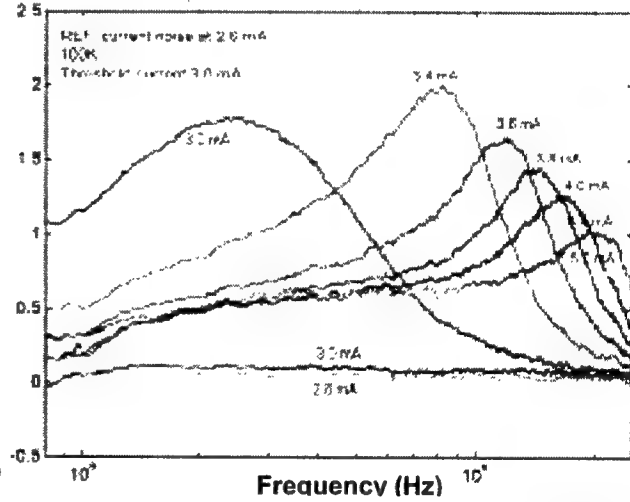


Fig.3 : Spectra (in dB) of current noise measured at different bias currents for a $1.55 \mu\text{m}$ semiconductor laser. The spectra are normalized to the spectrum a little below threshold (measurement bandwidth 100MHz – 2GHz).

References:

1. Y. Yamamoto, N. Imoto, IEEE J. Quantum Electron. **22**, 2032-2042 (1986).
2. Y. Yamamoto, S. Machida, Phys. Rev. A **35**, 5114-5130 (1987).
3. Y. Yamamoto, H. A. Haus, Phys. Rev. A **45**, 6596-6504 (1992).
4. S. Machida, Y. Yamamoto, Optics Lett. **14**, 1045-1047 (1989).
5. G. Bjork, Phys. Rev. A **45**, 8259-8267 (1992).
6. F. Rana, R. Ram, Appl. Phys. Letts. **76**, 1083-1085 (2000).
7. S. G. Patterson, G. S. Petrich, R. J. Ram, L. A. Kolodziejcki, Elec. Letts. **35**, 395-397 (1999).
8. E. Goobar, A. Karlsson, G. Bjork, P-J. Rigole, Phys. Rev. Lett., Jan. 1993, **70**, pp. 437-440.
9. L. A. Coldren, S. Corzine, "Diode Lasers and Photonic Integrated Circuits," John Wiley and Sons, New York (1995).
10. F. Jeremie, C. Chabran, P. Gallion, J. Opt. Soc. Am. B **16**, 460-64 (1999), Appl. Phys. Lett. **75**, 3614-3616 (1999).

Progress on Long Wavelength VCSEL

S. Nakagawa, E. Hall, and L. A. Coldren
Department of Electrical and Computer Engineering and Materials
University of California, Santa Barbara, CA 93106
and
Agility Communications, Inc., 600 Pine Ave., Santa Barbara, CA 93117
e-mail: snakagawa@agility.com

Long-wavelength vertical-cavity surface-emitting lasers (VCSELs) have inherent difficulties in finding appropriate material combinations for implementing both active regions and distributed Bragg reflectors (DBRs) on the same substrates, which are not common problems for 850-980 nm devices. InAlGaAs/InP or InGaAsP/InP quantum wells (QWs) are promising material combinations for long-wavelength active regions. Edge-emitting lasers with these active regions have demonstrated excellent performance, and they are candidate active materials for VCSELs as well. These materials are, however, less promising for DBRs because they lead to small index contrast. These ternary and quaternary materials show low thermal conductivity, and this property is not appropriate for long-wavelength VCSELs, which are sensitive to temperature.

One way to solve these issues is to employ GaAs/AlAs stacks. The wafer-fusion of the mirrors with the InGaAsP/InP actives and the metamorphic GaAs/AlAs mirrors on InP have demonstrated promising results so far [1]-[4], although these approaches are more difficult to fabricate and less reliable compared with the all-epitaxial short-wavelength devices on GaAs. Epitaxial growth of active regions on GaAs produces all-lattice-matched structures with the GaAs-based mirrors, and they promise to provide highly manufacturable and reliable devices much like the shorter-wavelength (850 and 980 nm) GaAs-based VCSELs [5]-[7]. The GaAs-based VCSELs with GaInNAs QWs have demonstrated excellent performances for 1.3 μm [5].

Lattice-matched structures on InP also have been showing promise for 1.55 μm VCSELs. These structures utilize the well-established InAlGaAs or InGaAsP based active regions, although they also inherently exhibit the two material-related problems mentioned above. Two types of approaches have been reported to overcome one of these issues - low index contrast. One is to deploy multiple active regions in order to compensate for the large mirror loss of InAlGaAs-based DBRs [8]. Another approach is to use AlGaAsSb-based materials for highly reflecting DBRs, which show large index contrast [9]. Although these Sb-based DBRs have poor electrical and thermal conductivities, an intracavity-contacted structure with thick InP cladding layers has achieved CW operation output powers $>1\text{mW}$ at 20°C and $>0.1\text{mW}$ at 80°C , differential quantum efficiencies of 23%, and threshold current of $800\mu\text{A}$ [10]. (See Figures 1 and 2.) The thick InP cladding layers allow generated heat and injected current to bypass the AlGaAsSb DBRs, prevent temperature rise in the device, and eventually result in successful long-wavelength VCSELs.

This work was supported by DARPA via the Heterogeneous Optoelectronics Technology Center (HOTC).

References:

- [1] A. Karim, K. A. Black, P. Abraham, D. Lofgreen, Y. J. Chiu, J. Piprek, and J. E. Bowers, "Superlattice barrier 1528-nm vertical cavity laser with 85°C continuous wave operation," *IEEE Photonics Technology Letters*, **12**, pp. 1438-1440, 2000.
- [2] V. Jayaraman, T. J. Goodnough, T. L. Beam, F. M. Ahedo, and R. A. Maurice, "Continuous-wave operation of single-transverse mode 1310-nm VCSELs up to 115 °C," *IEEE Photonics Technology Letters*, **12**, pp. 1595-7, 2000.
- [3] J. Boucart, C. Starck, F. Gaborit, A. Plais, N. Bouche, E. Derouin, L. Goldstein, C. Fortin, D. Carpentier, P. Salet, F. Brillouet, and J. Jacquet, "1-mW CW-RT monolithic VCSEL at 1.55 μm ," *IEEE Photonics Technology Letters*, **11**, pp. 629-31, 1999.
- [4] W. Yuen, G.S. Li, R.F. Nabiev, J. Boucart, P Kner, R.J. Stone, D. Zhang, M. Beaudoin, T. Zheng, C. He, K. Yu, M. Jansen, D.P. Worland, and C.J. Chang-Hasnain, "High-performance 1.6 μm single-epitaxy top-emitting VCSEL," *Electronics Letters*, **36**, pp. 1121-3, 2000.
- [5] A. W. Jackson, R. L. Naone, D. Galt, J. Wasserbauer, J. Smith, J. Beltran, D. W. Kisker, "Materials for 1.3 micron VCSELs on GaAs substrates," *SPIE Photonics West*, Paper No. 4286-04, San Jose, CA, 2001.
- [6] T. Anan, K. Nishi, M. Yamada, K. Kurihara, K. Tokutome, A. Kamei, and S. Sugou, "GaAsSb-based alloys for long-wavelength lasers," *IEEE LEOS 2000*, Paper ThS1, Puerto Rico, 2000.
- [7] J. A. Lott, N. N. Ledentsov, V. M. Ustinov, N. A. Maleev, A. E. Zhukov, A. R. Kovsh, M. V. Maximov, B. V. Volovik, Zh.I. Alferov, D. Bimberg, "InAs-InGaAs quantum dot VCSELs on GaAs substrates emitting at 1.3 μm ," *Electronics Letters*, **36**, pp.1384-5, 2000.
- [8] J. K. Kim, S. Nakagawa, E. Hall, L. A. Coldren, "Near-room-temperature continuous-wave operation of multiple-active-region 1.55 μm vertical-cavity lasers with high differential efficiency," *Applied Physics Letters*, **77**, pp. 3137-9, 2000.
- [9] E. Hall, G. Almuneau, J. K. Kim, O. Sjolund, H. Kroemer, L. A. Coldren, "Electrically-pumped, single-epitaxial VCSELs at 1.55 μm with Sb-based mirrors," *Electronics Letters*, **35**, pp. 1337-8, 1999.
- [10] S. Nakagawa, E. Hall, G. Almuneau, J. K. Kim, D. A. Buell, H. Kroemer, and L. A. Coldren, "1.55 μm , InP-lattice-matched VCSELs with AlGaAsSb/AlAsSb DBRs," *IEEE JSTQE*, **7** (June 2001).

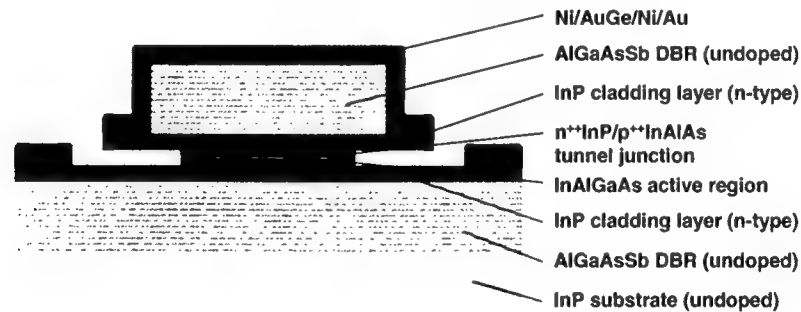


Figure 1. Schematic of double-intracavity contacted VCSEL with thick, n-type InP cladding layers.

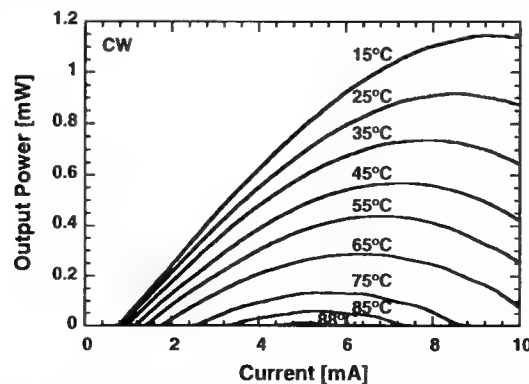


Figure 2. Light output characteristics of double-intracavity contacted VCSEL with 16 μm pillar and 8 μm aperture.

GaAsSb/GaAs 1.3- μ m-VCSELs for 10G-Ethernet

Kenichi Nishi, Takayoshi Anan, Mitsuki Yamada, Kaori Kurihara
*Keiichi Tokutome, *Akio Kamei, and Shigeo Sugou

*Optical Interconnection NEC Laboratory, Real World Computing Partnership
*Photonic and Wireless Devices Research Labs., NEC Corporation
34 Miyukigaoka, Tsukuba, Ibaraki 305-8501, Japan
Phone: +81-298-56-6127 Fax: +81-298-56-6140 Email: k-nishi@cj.jp.nec.com*

Vertical-cavity surface-emitting lasers (VCSELs) emitting at 1.3 μ m are attractive for the use in high-bandwidth fiber communications. GaAs-based long-wavelength VCSELs have been extensively studied using 1.3- μ m light-emitting materials, including GaInNAs[1,2], quantum dots[3], and GaAsSb[4,5]. These material systems can be monolithically formed with low-resistivity GaAs/AlGaAs-distributed Bragg reflectors (DBRs), and these VCSELs can utilize well-established techniques, e.g., current apertures with oxidized layers for very-low-current operations. Out of these candidates, GaAsSb quantum wells (QWs) are believed to be promising for future high-performance and low-cost VCSELs because they are easy to epitaxially grow by either molecular beam epitaxy (MBE) or metal-organic vapor phase epitaxy (MOVPE) [5], even when combined with Al-containing layers. Conventional GaAsSb QWs have realized 1.23- μ m VCSELs with cw-current injection[4] and 1.292- μ m VCSELs under optically pulsed conditions [5]. Thus, it is required for GaAsSb-based VCSELs to extend the lasing wavelength to 1.3 μ m and improve the maximum operating temperature under current injection to meet the 10G-Ethernet specifications. Improving the GaAsSb QW structure as well as designing high-reflective and low-resistive DBRs has recently enabled 1.295- μ m cw operation of GaAsSb VCSELs at up to 70°C[7]. This result encourages the realization of future long-wavelength VCSELs with GaAsSb QWs for 10G-Ethernet.

Figure 1 shows the schematic device structure of a bottom-emitting GaAsSb VCSEL along with its band-lineup in the active region. N-type, Si-doped bottom-DBRs made up of 33.5 pairs of Al_{0.9}Ga_{0.1}As/GaAs were grown on a Si-doped GaAs (001) substrate by MOVPE. A cavity, including the GaAsSb QW active layers, was grown by gas-source MBE, followed by one pair of AlAs/GaAs layers for oxidation. Then, low-resistivity p-type, C-doped DBRs made up of 21 pairs of Al_{0.9}Ga_{0.1}As/GaAs were formed by MOVPE with graded interfaces. Highly strained 6.2-nm-thick GaAs_{0.64}Sb_{0.36} double QWs were used as the active layers with a photoluminescence peak of about 1310 nm.

We made several improvements to achieve high-quality active layers for 1.3- μ m emission. Increasing the growth rate up to 0.8 μ m/h (from 0.4 μ m/h) at a growth temperature of 490°C achieved a good optical quality of GaAsSb QWs with a high Sb-content. In addition, a growth interruption was applied just beneath the second GaAsSb QW to recover surface flatness because the first GaAsSb QW growth resulted in small morphological undulations. To compensate for the highly compressive strain in GaAsSb QWs, 30-nm-thick GaAs_{0.8}P_{0.2} layers were positioned to sandwich the QW active region. The barrier and the adjacent layers of the QWs remained GaAs to maintain the transition wavelength and prevent inhomogeneous hole injection. A 30-nm-thick GaAs barrier layer between the QWs was doped with Be to improve the hole-injection uniformity.

VCSEL devices with the oxide-confined layer having various aperture sizes were fabricated from the wafer. First, 45- μ m ϕ mesas were formed by wet chemical etching. An AlAs oxidation was performed at 400°C for 15 min to form a 6- μ m ϕ current-flowing aperture. The top p-DBR was coated with gold, augmenting the reflectivity of the top-DBRs. The devices were tested under cw conditions.

Figure 2 shows the cw light-current and voltage-current curves of a device with a 6- μ m ϕ oxide aperture at RT with an antireflecting coating. The threshold current was as low as 1.1 mA, and the threshold voltage was 2.0 V. Because of the highly reflective mirror design, the maximum RT-cw output power was about 0.1 mW. Lasing at 1.295 μ m is shown in the inset of Fig. 2. Figure 3 shows the temperature characteristics of a 6- μ m ϕ oxide-aperture device under cw operation. The maximum lasing temperature was 70°C. The characteristic temperature was 139 K, ranging between 20 and 60°C.

Thus, we demonstrated high-performance GaAsSb VCSELs emitting at 1.295 μm with a low threshold current of 1.1 mA and a maximum cw operating temperature of 70°C. After the high-frequency modulation characteristics have been validated, the GaAsSb VCSELs should be viable low-cost light sources for high-bandwidth fiber communications.

- [1] K. D. Choquette, J. H. Klem, A. J. Fischer, O. Blum, A. A. Allerman, I. J. Fritz, S. R. Kurtz, W. G. Breiland, R. Sieg, K. M. Geib, J. W. Scott, and R. L. Naone, *Electron. Lett.* **36**, 1388 (2000).
- [2] G. Steinle, H. Riechert, and A. Yu. Egorov, *Electron. Lett.* **37**, 93 (2001).
- [3] J. A. Lott, N. N. Ledentsov, V. M. Ustinov, N. A. Maleev, A. E. Zhukov, A. R. Kovsh, M. V. Maximov, B. V. Volovik, Zh. I. Alferov, and D. Bimberg, *Electron. Lett.* **36**, 1384 (2000).
- [4] M. Yamada, T. Anan, K. Kurihara, K. Nishi, K. Tokutome, A. Kamei, and S. Sugou, *Electron. Lett.* **36**, 637 (2000).
- [5] F. Quochi, J. E. Cunningham, M. Dinu, and J. Shah, *Electron. Lett.* **36**, 2075 (2000).
- [6] K. Kurihara, K. Nishi, T. Anan, M. Yamada, A. Kamei, A. Gomyo, and S. Sugou, *ICMOVPE-X*, Sapporo, 2000, 359.
- [7] T. Anan, M. Yamada, K. Nishi, K. Kurihara, K. Tokutome, A. Kamei, and S. Sugou, *Electron. Lett.* **37**, 566 (2001).

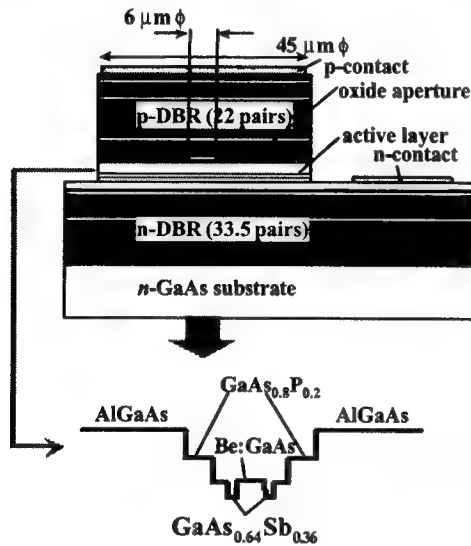


Fig. 1. Schematic device structure of GaAsSb VCSEL along with its band-lineup in the active region.

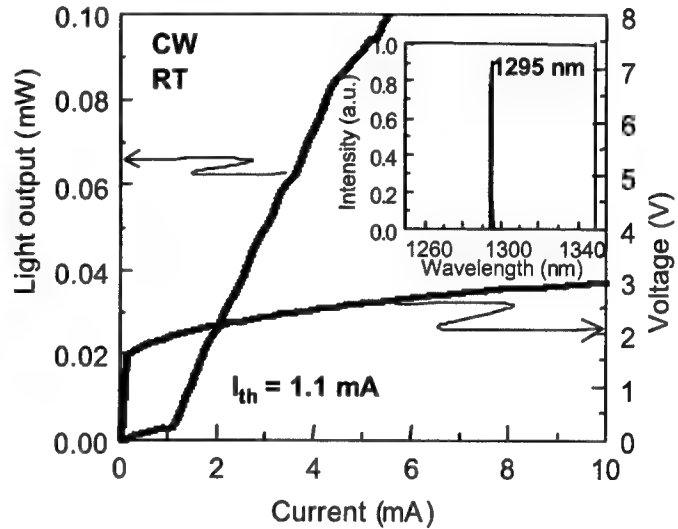


Fig. 2. Light-current and voltage-current characteristics of 6- $\mu\text{m}\phi$ -aperture device under CW operation at room temperature. Inset shows lasing spectrum.

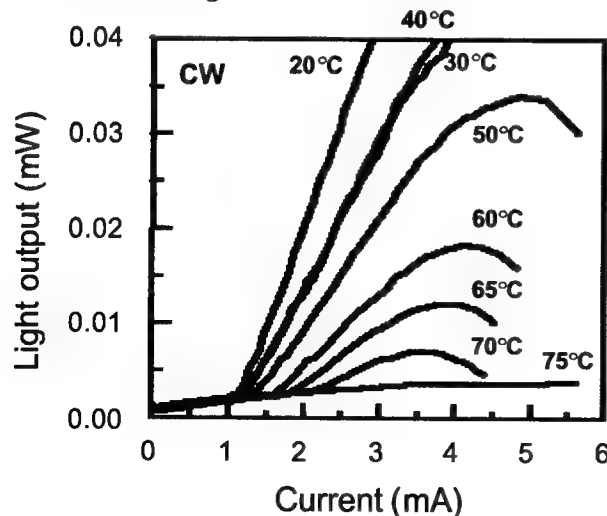


Fig. 3. Temperature dependence of light-current curves of 6- $\mu\text{m}\phi$ -aperture device. CW operation at as high as 70°C was demonstrated.

Quantum Dot Vertical Cavity Lasers

J.A. Lott, N.N. Ledentsov[†], V.M. Ustinov^{*}, and D. Bimberg[†]

Air Force Institute of Technology, Dept. of Electrical and Computer Engineering, Wright-Patterson AFB, Ohio

**A. F. Ioffe Physical Technical Institute of the Russian Academy of Sciences, St. Petersburg, Russian Federation*

[†] Institute for Solid-State Physics, Technical University of Berlin, Berlin, Germany

Vertical cavity surface emitting lasers (VCSELs) emitting from 1.0 to 1.8 μm and integrated with GaAs-based microelectronic circuits have many potential applications in fiber optic communication systems, optical interconnects, and photonic switching fabrics. We first reported VCSELs with quantum dot (QD) active regions emitting near 1.0 μm and with submilliampere threshold currents in 1997 [1]. In 2000 we reported the room temperature (RT) pulsed operation [2] and soon thereafter the RT continuous wave (CW) operation [3] of QD VCSELs on GaAs substrates emitting at 1.3 μm . In our current work we focus on improving the QD VCSEL fabrication process and extending the emission wavelength up to and beyond 1.55 μm . The wavelength extension is accomplished by varying the physical size and composition of sheets of InAs-InGaAs dots grown directly on GaAs substrates. We also investigate tunable QD VCSELs for application in dense wavelength division multiplexing optical communication systems. We study important design and fabrication issues associated with the development of prototype, long-wavelength tunable QD VCSELs. This work includes studies of optically efficient InAs-InGaAs quantum dot gain layers within the microcavity active region, where the size of the QDs is either highly uniform or variable. We investigate the device performance trade-offs associated with ensembles of equal-size and unequal-size quantum dots. As expected, an ensemble of dots with varying physical size extends the gain bandwidth and thus the tuning range but at the expense of overall device efficiency.

An example fabrication process used to make intracavity-contacted QD VCSELs is shown in Figure 1. A series of dry etches is followed by selective wet-oxidation and ohmic metallization. A cross-section diagram of a fabricated QD VCSEL is given in Figure 2. A corresponding plot of the calculated electric-field intensity on resonance for a 1.3 μm QD VCSEL is shown in Figure 3. Figure 4 discloses the real refractive index of AlO versus wavelength obtained from optical measurements on calibration samples. Sheets of quantum dots lie within InGaAs quantum wells, all in a 1.0λ -thick GaAs optical microcavity. The microcavity is surrounded by (p) and (n) $\text{Al}_{0.98}\text{Ga}_{0.02}\text{As}$ layers (less than $\lambda/4$ -thick) followed by 1.0λ or 1.5λ -thick (p) and (n)GaAs current spreading/intracavity contact spacer layers. The spacer layers are followed by distributed Bragg reflectors (DBRs) composed of alternating $\text{Al}_{0.98}\text{Ga}_{0.02}\text{As}$ (wet-oxidized) and $\lambda/4$ -thick GaAs layers. These top and bottom DBRs typically have 5.5 and 7 periods, respectively. The $\text{Al}_{0.98}\text{Ga}_{0.02}\text{As}$ layers in the DBR, as well as those surrounding the optical cavity, are selectively oxidized using water vapor to form AlGaO. The top and bottom $\text{Al}_{0.98}\text{Ga}_{0.02}\text{As}$ DBR layers and the thinner $\text{Al}_{0.98}\text{Ga}_{0.02}\text{As}$ current aperture layers are oxidized simultaneously. The devices have approximately square current apertures of area between 5×5 and $10\times 10\ \mu\text{m}^2$. The devices were tested using a continuous wave current source on a temperature controlled probe station. The room temperature light power-current-voltage (L-I-V) characteristic of an example $10\times 10\ \mu\text{m}^2$ InAs-InGaAs QD VCSEL is shown in Figure 5. To date, the best room temperature, continuous wave 1.3 μm QD VCSELs with a $10\times 10\ \mu\text{m}^2$ current aperture have a threshold current of 1.5 mA, a peak differential slope efficiency of 40 percent, and a maximum output power of 900 μW .

This work supported by the U.S. Air Force Office of Scientific Research (Dr. Howard R. Schlossberg). The views expressed are those of the authors and do not reflect the official policy or position of the U.S. Air Force, the U.S. Department of Defense, or the U.S. Government.

References

1. J.A. Lott *et al.*, *Electronics Letters*, 33(13), p.1150 (1997).
2. J.A. Lott *et al.*, *Proceedings 17th IEEE Int'l Semi. Laser Conference*, Monterey, CA, p. 14 (25-29 Sep 00).
3. J.A. Lott *et al.*, *Proceedings IEEE LEOS 2000*, Rio Grande, Puerto Rico, p. 304 (13-16 Nov 00).

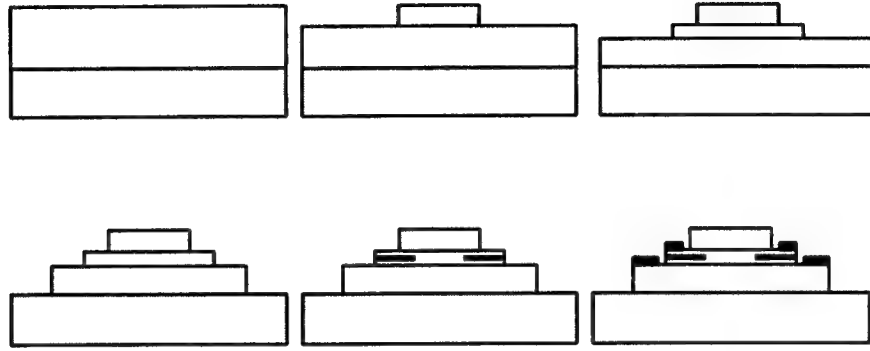


Fig. 1. Schematic overview of fabrication steps for the wet-oxidized QD VCSELs.

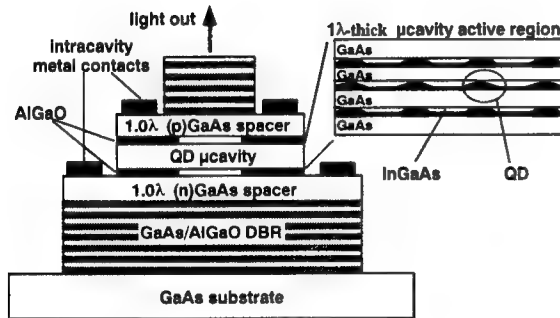


Fig. 2. Schematic of a QD VCSEL.

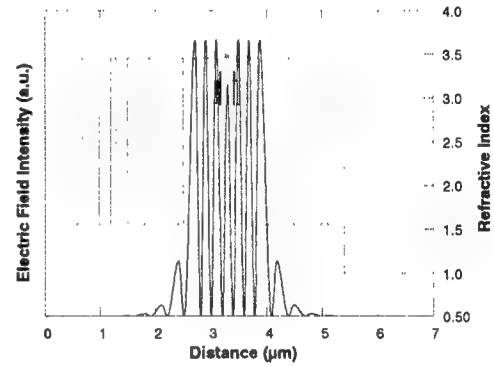


Fig. 3. Calculated QD VCSEL electric-field intensity.

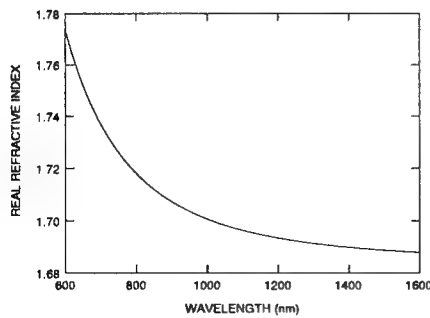


Fig. 4. Measured AlO refractive index dispersion.

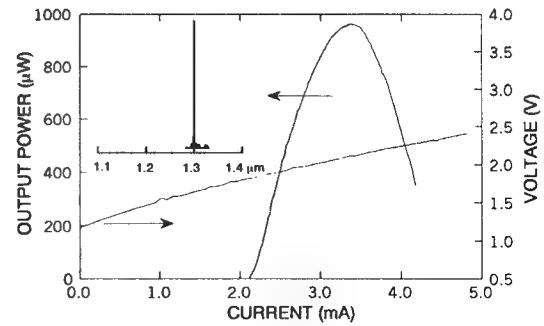


Fig. 5. RT CW L-I-V characteristic for a QD VCSEL.

Vertical Cavity Lasers for Telecommunications Networks: Prospects and Challenges

Adil Karim
Department of Electrical and Computer Engineering
University of California
Santa Barbara, CA 93106
adil@opto.ucsb.edu

Vertical cavity surface emitting lasers (VCSELs) have been studied extensively for use in fiber optic networks and as optical interconnects. The VCSEL offers many potential advantages when compared to the traditional edge-emitting laser. The most recognized advantage of the VCSEL is compatibility with low cost wafer scale fabrication and testing methods. The VCSEL offers several other attractive characteristics that make it well suited for use in fiber optic systems. These include a circularly shaped output beam for high coupling efficiency, high modulation bandwidths at low current levels, single mode operation, low power consumption and the potential for producing integrated modules and arrays on wafer.

Rapid progress in VCSEL development over the last decade has allowed 850 and 980 nm devices to be deployed in data communication networks. However, for extended reach applications, long wavelength (1.3-1.6 μm) laser diodes are required in order to operate with low loss and dispersion. Single mode VCSELs at 1300 nm and 1550 nm are widely anticipated as sources in telecommunications networks. Ten Gigabit Ethernet (10GbE) standards are expected to focus on low cost, high performance laser diodes such as long wavelength VCSELs. Despite the obvious commercial incentives, long wavelength VCSELs have been slower to develop than their short wavelength counterparts. The main limitation has been unsatisfactory high temperature operation. Maximum operating temperatures of 70-85°C are specified for sources in fiber optic networks. The traditional InP/InGaAsP material system is limited in VCSELs by low characteristic temperatures. The lack of a robust aperturing technique on InP similar to the lateral oxidation of AlGaAs on GaAs has limited the operating efficiency. Distributed Bragg reflectors (DBRs) with high thermal conductivity, high reflectivity, and in the case of current injection through the DBR, high electrical conductivity have proven difficult to fabricate on InP. A number of novel designs have been developed to overcome the limitations of the traditional InGaAsP material system. These include GaInNAs active regions on GaAs[1], metamorphic GaAs mirrors grown on InP[2], buried tunnel junctions[3], multiple active regions[4], and antimonide DBRs[5]. The best high temperature results to date have been achieved using wafer bonded GaAs/AlGaAs mirrors in both electrically pumped[6] and integrated optically pumped designs[7].

The high thermal conductivity of GaAs/AlGaAs DBRs has enabled continuous-wave operation up to 105°C with electrical injection and 115°C with a wafer-bonded pump VCSEL. Continuous-wave light-current characteristics for a 1.55 μm VCSEL with two wafer-bonded GaAs/AlGaAs DBRs are shown in Figure 1. Threshold currents as low as 0.8 mA and single mode output powers of 0.7 mW have been measured for these devices.

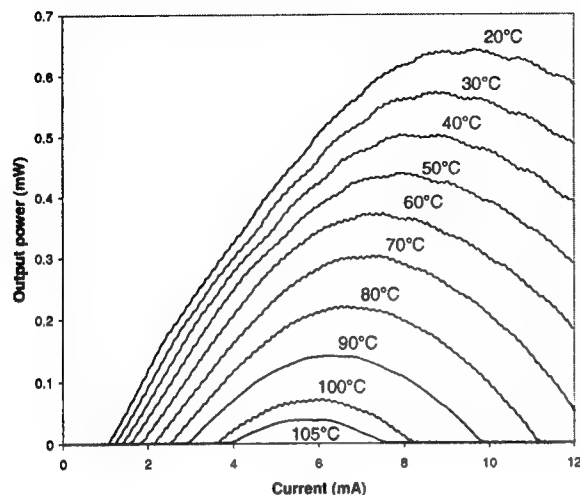


Figure 1 L-I characteristics of wafer bonded 1.55 μm VCSEL

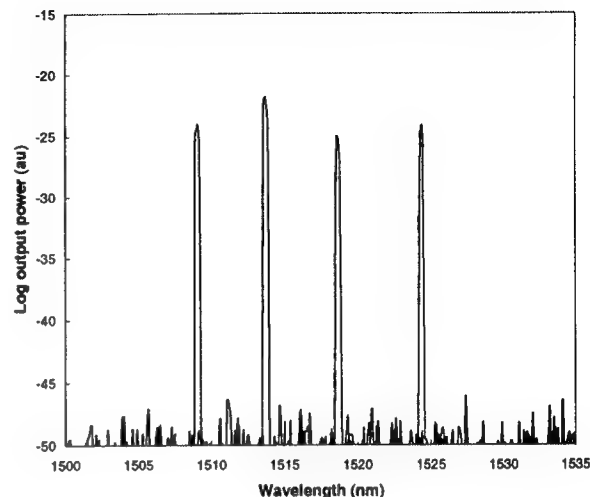


Figure 2 Spectra of WDM VCSEL array

Multiple wavelength VCSEL arrays have been fabricated using an intracavity superlattice[8] to adjust cavity lengths prior to bonding. This technique allows arrays with controlled channel spacing to be repeated over the entire wafer. The output spectrum from a four-channel wafer bonded array is shown in Figure 2. The electrical and optical characteristics are nearly uniform across the array. Each channel may be directly and individually modulated.

Recent advances in long wavelength VCSEL technology have enabled high performance devices based on a number of different approaches. Continued improvements in operating temperature and single-mode output power have made these devices commercially viable. Multiple wavelength VCSEL arrays and tunable VCSELs will add functionality. These sources are expected to dramatically reduce costs and improve performance in local and metropolitan area networks.

References

- [1] K. D. Choquette, J. F. Klem, A. J. Fischer, O. Blum, A. A. Allerman, I. J. Fritz, S. R. Kurtz, W. G. Breiland, R. Sieg, K. M. Geib, J. W. Scott, and R. L. Naone, "Room temperature continuous wave InGaAsN quantum well vertical cavity lasers emitting at 1.3 μm ," *Electronics Letters*, vol. 36, pp. 1388-1390, 2000.
- [2] J. Boucart, C. Starck, F. Gaborit, A. Plais, N. Bouche, E. Derouin, L. Goldstein, C. Fortin, D. Carpentier, P. Salet, F. Billouet, and J. Jacquet, "1-mW CW-RT monolithic VCSEL at 1.55 μm ," *IEEE Photonics Technology Letters*, vol. 11, pp. 629-31, 1999.
- [3] M. Ortsiefer, R. Shau, M. Zigldrum, G. Bohm, F. Kohler, and M. C. Amann, "Submilliamp long-wavelength InP-based vertical-cavity surface-emitting laser with stable linear polarisation," *Electronics Letters*, vol. 36, pp. 1124-6, 2000.
- [4] J. K. Kim, S. Nakagawa, E. Hall, and L. A. Coldren, "Near-room-temperature continuous-wave operation of multiple-active-region 1.55 μm vertical-cavity lasers with high differential efficiency," *Applied Physics Letters*, vol. 77, pp. 3137-9, 2000.
- [5] S. Nakagawa, E. Hall, G. Almuneau, J. K. Kim, D. A. Buell, H. Kroemer, and L. A. Coldren, "88°C continuous-wave operation of apertured, intracavity contacted, 1.55 μm vertical-cavity surface-emitting lasers," *Applied Physics Letters*, vol. 78, pp. 1337-9, 2001.
- [6] A. Karim, P. Abraham, D. Lofgreen, Y. J. Chiu, J. Piprek, and J. Bowers, "Wafer bonded 1.55 μm vertical cavity lasers with continuous-wave operation up to 105°C," *Applied Physics Letters*, vol. 78, pp. to be published, 2001.
- [7] V. Jayaraman, T. J. Goodnough, T. L. Beam, F. M. Ahedo, and R. A. Maurice, "Continuous-wave operation of single-transverse-mode 1310-nm VCSELs up to 115 degrees C," *IEEE Photonics Technology Letters*, vol. 12, pp. 1595-7, 2000.
- [8] V. Jayaraman and M. Kilcoyne, "WDM array using long-wavelength vertical cavity lasers," *Proc. SPIE*, vol. 2690, pp. 325-36, 1996.

Long Wavelength InGaAsN/GaAs Edge Emitting Lasers with Low Threshold Current Density Grown by MOCVD

Chris Murray, Henry Xin and Fred Newman
Emcore Corporation, 10420 Research Rd SE, Albuquerque, NM 87123

An Emcore D180 metalorganic chemical vapor deposition (MOCVD) system is being used to develop 1.3 micron InGaAsN/GaAs vertical cavity surface emitting lasers (VCSELs). Prior to growing a full VCSEL structure, broad area edge emitting lasers (EELs) were grown to investigate the potential of the InGaAsN/GaAs material system for long wavelength VCSELs. The MOCVD source materials were trimethylgallium (TMG), trimethylindium (TMI), AsH₃ and dimethylhydrazine (DMHy). Substrates were 2° off (100) Si-doped GaAs, and Si₂H₆ and DEZn are the n-type and p-type dopants, respectively. The InGaAsN/GaAs double quantum wells (QWs) were grown at 530 ~ 550°C at a total pressure of 50 Torr. The QWs were confined with undoped GaAs waveguides with a bottom cladding of GaInP and a top cladding of AlGaAs. A schematic of the InGaAsN/GaAs edge emitting lasers is shown in Figure 1. The EELs metal widths ranged between 5 and 97 microns and cavity lengths ranged between 450 and 1100 microns. Top and bottom contacts consisted of 200Å Ti/3000Å Au that were annealed at 380°C for 2 minutes.

The growth of InGaAsN EEL was initiated with the growth of In_{0.3}Ga_{0.7}As/GaAs QW EELs, that was proceeded by adding small amounts of nitrogen up to 1% and thus red-shifting the wavelength. To date, the addition of 1% nitrogen has increased the wavelength from 1115 nm (InGaAs with no nitrogen) to approximately 1275 nm. However, the addition of nitrogen decreases the material quality and thus increases the threshold current density of EELs. Figure 2 summarizes the threshold current densities for EELs with various cavity lengths and metal widths. The most recent result is a 1275 nm EEL with a threshold current density of 880 A/cm². Figure 3 is the L-I curve and corresponding laser spectrum for this edge emitter with a DC current of 400 mA. We believe the low slope efficiency is due to particulates that are generated during the growth, which is possibly due to a reaction between the Al precursor and the DMHy.

For a InGaAsN/GaAs QWs EEL with a wavelength of 1235 nm and a threshold current density of 960 A/cm², a characteristic temperature of 138K was obtained between 10° and 70°C. Additional temperature dependent data for longer wavelength EELs will be presented at the conference.

With the recently obtained results of threshold current densities of less than 1 kA/cm², full VCSEL structures have been grown. The 1250 nm VCSEL consists of double GaInNAs/GaAs quantum well and 1λ cavity with a 39 pair bottom n-DBR and a 24 pair top p-DBR. The DBRs consist of dual layers of Al_{0.92}Ga_{0.08}As/GaAs with graded interfaces. Data will be presented on the VCSEL operating characteristics.

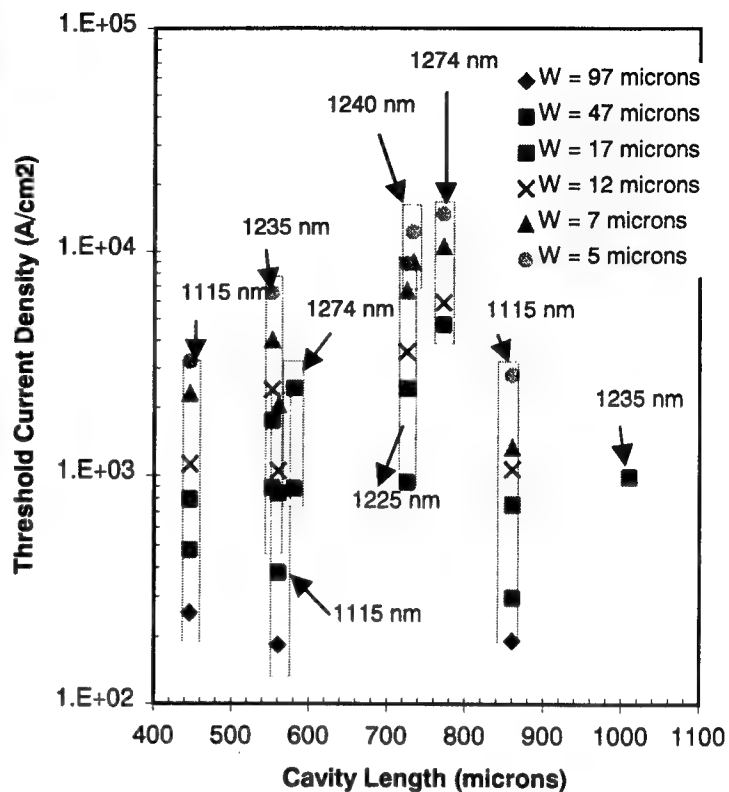
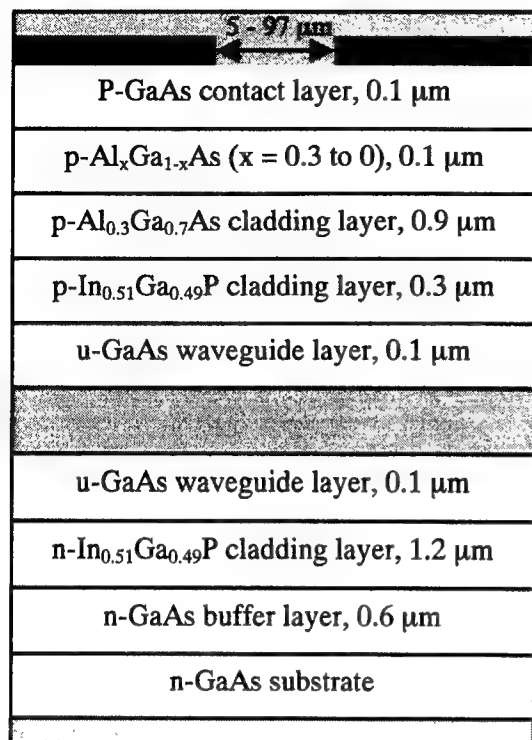


Figure 1: Schematic of InGaAsN/GaAs EEL

Figure 2: Summary of Threshold Current Densities

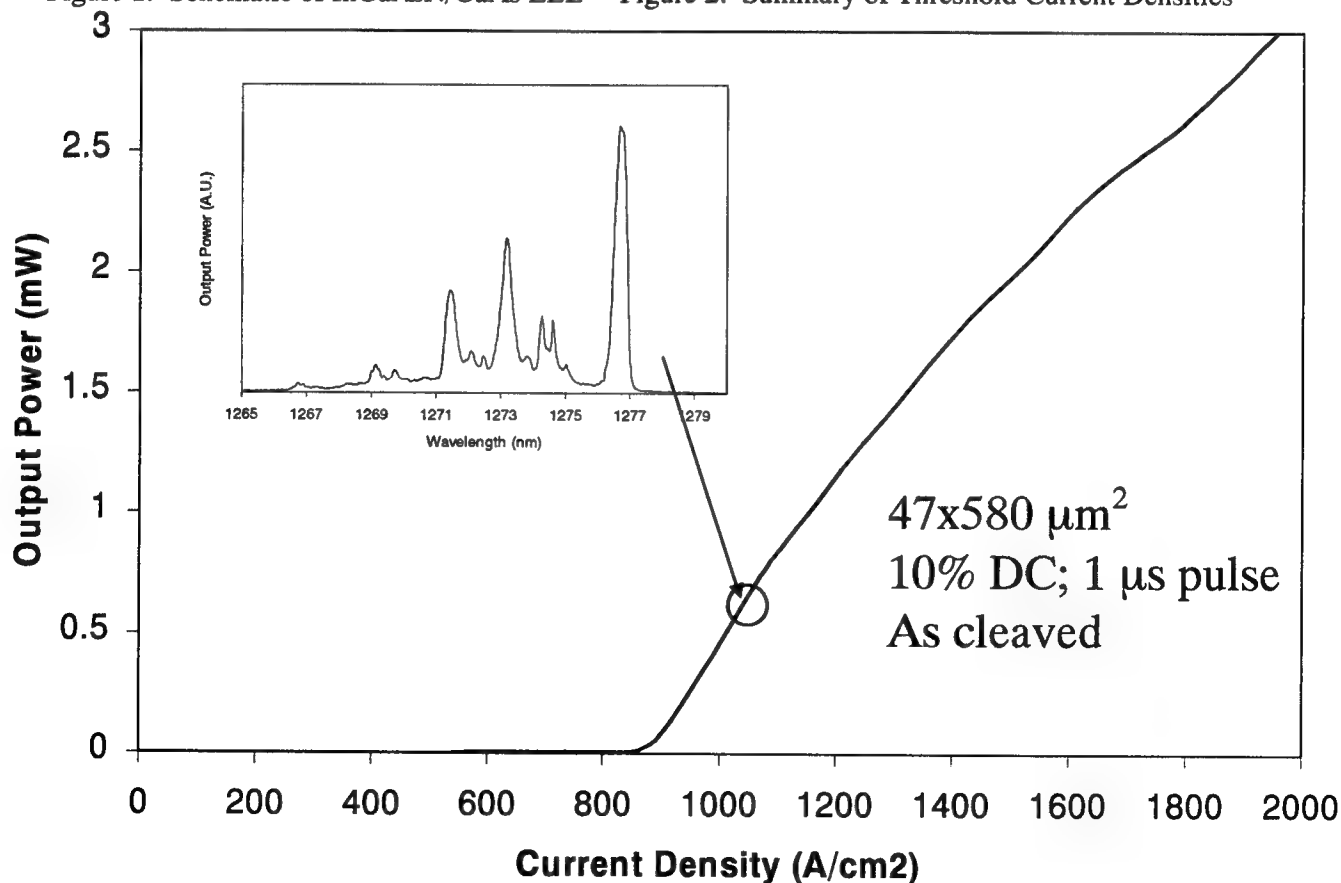


Figure 3: L-I Curve and Laser Spectrum for a 1277 nm InGaAsN/GaAs EEL.

GaInNAs, a new material for long wavelength VCSELs

J. S. Harris, Jr.

Solid State and Photonics Lab, Stanford University, CIS 328, Via Ortega, Stanford, CA 94305

The incredible growth of Internet, cellular, wireless and data communications is pushing the bandwidth requirements for fiber networks and expansion of metro and local area networks at an unprecedented pace. Low cost lasers which are easily packaged and coupled to fiber are needed for the next generation of these networks. Vertical cavity surface-emitting lasers (VCSELs) currently find widespread use for short-haul optical fiber transmission systems. Given the commercial success of GaAs-based 850nm VCSELs, dramatic enhancements in transmission bandwidth and distance can be achieved in conventional single- and multi-mode fiber by extending the emission wavelength to the 1300nm-1550nm range. Extension out to 1.3-1.55 μ m is absolutely essential to achieve 10Gbps Ethernet rates. GaInNAs is a promising active layer material grown on GaAs that can achieve 1300nm emission [1], and electrically pumped, cw GaInNAs VCSELs [2] have been realized.

The GaInNAs materials system provides many challenges as the equilibrium phases of the constituent binary alloys are cubic (GaAs and InAs) and hexagonal (GaN and InN). As shown in Fig. 1, one of the major surprises in MBE growth of GaInNAs is that Nitrogen is incorporated into the alloy with unity sticking coefficient, providing excellent compositional control. GaInNAs is also different from other III-V alloys in observation of significant annealing effects which improved crystalline structure and reduce defects. GaInNAs also appears to have a more favorable conduction band/valence band offset division, providing greater confinement of electrons, resulting in higher temperature and power capabilities for GaInNAs. The key challenge in this materials system is the increasing density of non-radiative defects with increasing N content, thus limiting how far into the infrared that emission can be pushed.

Our VCSEL design is shown schematically in Fig. 2. The bottom mirror consists of a 22.5-period n-doped GaAs/AlAs distributed Bragg reflector (DBR) with a center wavelength near 1200nm, the top mirror is a 22-period p-doped DBR whose reflectance is enhanced by a Ti/Au contact electrode, and the GaAs λ cavity contains three 70Å Ga_{0.3}In_{0.7}N_{0.02}As_{0.98} quantum wells (QWs) separated by 200Å GaAs barriers. The structures were grown by molecular beam epitaxy using solid-source arsenic and a rf nitrogen plasma source. Lateral AlAs oxidation was used to produce current apertures. The output power and voltage vs. injection current for a 5 μ m x 5 μ m device operating CW at room temperature is shown in Fig. 3. Fig. 4 shows emission spectra at threshold, with a lasing wavelength of 1201.54 nm, and at 2.6 times threshold. The device lased in a single transverse and longitudinal mode, even far above threshold, the side mode suppression ratio was in excess of 40 dB. CW laser operation was achieved for devices ranging from 3.6 μ m to 6.4 μ m, with threshold currents from 0.94 to 2.3 mA and a slope efficiency as high as 0.049 W/A.

A key element for long wavelength operation is quantum well design and stability of the metastably grown GaInNAs. Using GaNAs barriers rather than GaAs barriers reduces N outdiffusion and maintains wavelength after anneal. The L-I curve for a 1.34 μ m edge emitting laser with GaNAs barriers is shown in Fig. 5 and the spectral response in Fig. 6. Thermal measurements of edge emitting lasers with GaNAs barriers exhibit a $T_0 = 146^\circ\text{K}$.

In summary, we have demonstrated low-threshold GaInNAs VCSELs operating cw at room temperature, with an emission wavelength of 1200 nm. Higher output power will be possible by reducing the resistance of the p-DBR, and 1300 nm VCSEL emission will be achieved by increasing the indium and/or nitrogen content of the GaInNAs/GaAs multiple quantum well active layer, use of GaNAs barriers and optimized growth and annealing conditions. This work was supported by ONR under contract N00014-01-1-010 and by DARPA and ARO under contract DAAG55-98-1-0437.

[1] M. Kondow, et al., IEEE J. Selected Topics in Quantum Electronics 3, pp.719-730, 1997.

[2] C.W. Coldren, M.C. Larson, S.G. Spruytte, J.S. Harris, IEEE Photon. Techn. Lett.,

[3] C.W. Coldren, M.C. Larson, S.G. Spruytte, H.E. Garrett, J.S. Harris, CLEO '00, 2000.

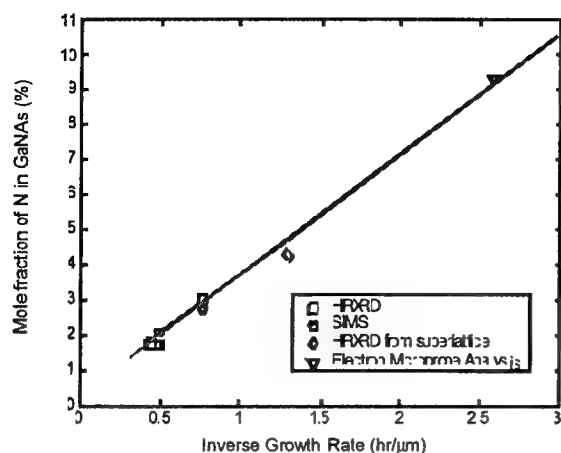


Fig. 1. Nitrogen Content vs Inverse Growth Rate Illustrating unity N sticking coefficient

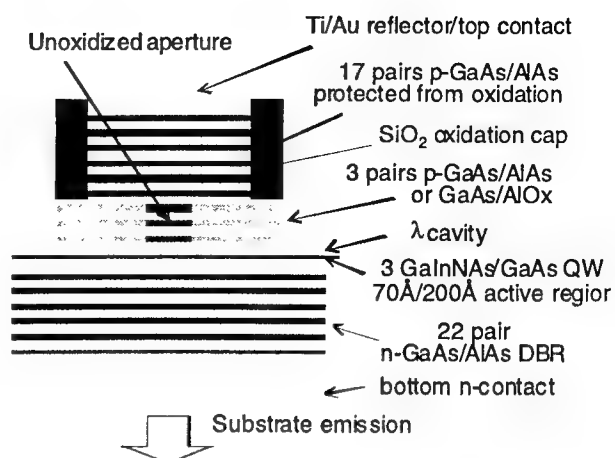


Fig.2. VCSEL Schematic Diagram

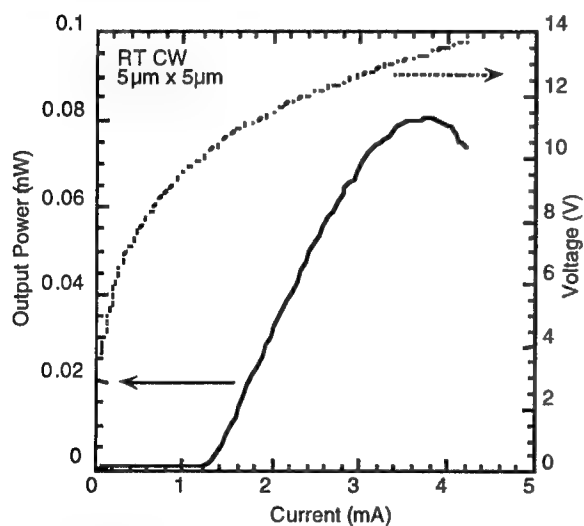


Fig. 3. Light-Current and Voltage-Current Data for cw operation of 1.2μm VCSEL

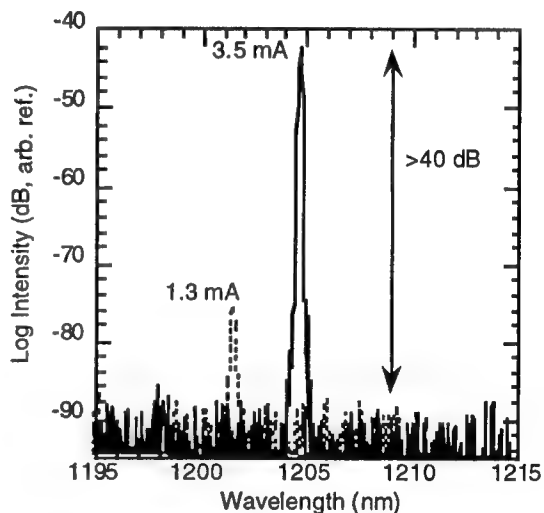


Fig. 4. Emission Spectra at $\sim I_{th}$ and $2.6 I_{th}$

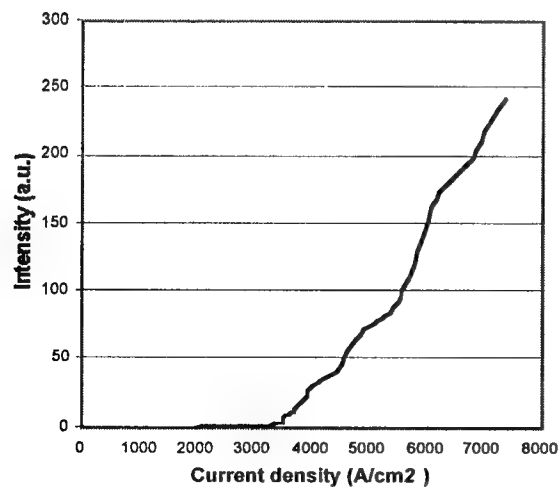


Fig. 5. Edge Emitter Power vs. Current

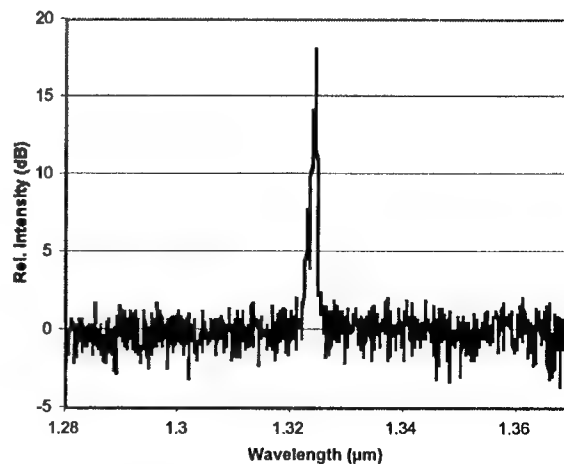


Fig. 6. Emitted Spectrum of Edge Emitter

Advanced Semiconductor Lasers and Applications

Tuesday, 31 July 2001

- TuA1: Tunable Lasers I: VCSELs**
- TuA2: Tunable Lasers II: DBR Based Devices**
- TuA3: Tunable Lasers III: External Cavity & Arrays**

Network Architectures and Requirements for Widely Tunable Lasers

David W. Jenkins and Roger P. Holmstrom
Tellabs Operations, Inc.
1000 Remington Blvd.
Bolingbrook, IL 60440

Long Haul Networks

The telecommunications industry is advancing in the use of optical technologies and in the deployment of new networks to accommodate the ever-increasing traffic demands on service providers. For several years, dense wave division multiplexing (DWDM) has been used cost effectively in long haul telecommunications. The enabling technologies for DWDM are the advent of narrow line width distributed feedback lasers (DFB) and erbium doped fiber amplifiers (EDFA). The networks that use DWDM generally have long fiber links, that is greater than 50 km. Recently there are DWDM products tailored for metro markets where the fiber links are generally shorter than 50 km. The enabling technologies for this type of network differ from those of the long haul network.

In the long haul network, the dominant cost of the infrastructure is the fiber and the optical repeaters necessary for long distance transmission. Without the use of DWDM, a long fiber link required electronic repeaters or 3R regeneration (retiming, reshaping, and recovery) roughly every 25 miles. The use of DWDM with EDFA's allows the amplification of the signal without conversion into the electrical domain. EDFA's are spaced at greater distances than 3Rs and can amplify several WDM channels simultaneously. Thus, several electronic repeaters are replaced with one EDFA. This is the major cost savings realized in a long-haul network.

In the long haul network, the optical links consist of transmitter-receiver pairs on each end of a pair of fibers, for bi-directional traffic, with erbium doped fiber amplifiers interspersed on the link. In any optical network in North America, service providers use the SONET protocol for transport. SONET architecture is in the form of rings where diverse path routing is used for protection purposes. In a ring-based system, traffic that is originated at one node on the ring and terminated at another node on the ring, passes through intervening nodes. Similarly, in a WDM architecture, traffic may be groomed onto wavelengths that pass (optically) through intervening nodes.

The use of tunable lasers in a long haul network has two applications: sparing and optical networking. The justification for sparing is that the use of tunable lasers reduces the number of extra transponders (one for every wavelength) that service providers must stock. Several applications are covered in the term "optical networking". In general, wavelengths are changed remotely at any site in the network. This is important at nodes that are interconnections between rings called hub nodes. Inter-ring traffic may experience wavelength blocking. If traffic within a ring is color coded for origin and destination, then it is possible to have traffic coded by one wavelength from the origin on one ring to a hub node on that ring to a node on a different ring *using a different wavelength on the second ring*. Tunable lasers allow the quick change to any available wavelength on the ring while avoiding costly electronic intervention. In addition, wavelengths are managed on a ring basis rather than a network basis. Coupled with optical switching, tunable lasers can be used for 1:N wavelength protection, dynamic wavelength provisioning, and

configurable add-drop. Optical networking has great value because it prevents "stranded bandwidth"; bandwidth that cannot be used within the network because of wavelength blocking.

The specifications for long haul tunable lasers are very similar to those of fixed wavelength lasers. The extra parameter to be specified is switching speed (between wavelengths) which is important for optical networking but not sparing.

Metro Networks

In a metro network, the optical fiber links are generally short enough that optical regeneration or amplification is not generally required. The cost justification that drove service providers to DWDM in the long haul network is less important in the metro networks. The trade off for the service providers is DWDM equipment verses the cost of adding more fibers. In the metro network, there is great variance in the cost of laying new fiber depending on the location and spare capacity in existing fiber duct. This may not be enough to justify deployment of DWDM in the metro network. What can be done to help lower the cost of the network is to eliminate the OEO conversions in the network?

Studies at Tellabs on real customer metro networks show that roughly 25-30 % of traffic flowing into a node will terminate at that node. The remainder passes through to other nodes in the network. One way to lower the cost of the network is to pass the "pass-through" traffic optically (without OEO regeneration). Passing the appropriate wavelengths through from the ingress DWDM multiplexer directly to the egress DWDM multiplexer can do this. In this way, roughly 70% of the OEO regeneration cards are eliminated. The trade off in this architecture is that amplifiers must be used.

The justifications for tunable lasers are the same in metro networks as in long haul networks. The performance requirements for tunable lasers used in metro networks maybe quite different. Typically, a metro network will have more nodes and shorter spans, and traffic may transfer through several rings.

If optical pass-through exists, then wavelengths may pass through several multiplexer/demultiplexer pairs and experience the loss of many thin-film filters. On a per-channel basis, this accumulated loss may be very different. Thus, the specification of total wavelength drift of the laser is more stringent than 30 GHz.

In addition, with optical pass through, care must be taken to maintain uniform power distribution within the network. Variations in loss between wavelengths in passive components and possible channel unfairness in amplifiers can skew the power levels between channels to limit the number of nodes a given signal can transit. Consequently, there are more rigid power requirements on both a single channel drift and variations between channels.

Another aspect of a metro network is the possibility of protection switching for non-SONET traffic. SONET provides protection switching at the optical layer however, other protocols, IP, ATM or FCON do not. Traffic may be required to switch from one wavelength to another wavelength with a few milliseconds. For this type of switching to be effective, the output light must transition from one wavelength to another wavelength without emitting light in any of other wavelength.

Electrically-Pumped Directly-Modulated Tunable VCSEL For Metro DWDM Applications

W. Yuen, G. S. Li, R. F. Nabiev, M. Jansen, D. Davis, C. J. Chang-Hasnain

Bandwidth9 Inc., 46410 Fremont Blvd., Fremont, CA 94538; email: wyuen@bw9.com

Introduction

Vertical cavity surface emitting lasers (VCSELs) offer advantages of being very cost effective and mass manufacturable. By integrating a VCSEL with a micro-electro-mechanical (MEM) cantilever, a tunable VCSEL with wide and continuous wavelength tuning can be obtained. Previous demonstrations of this concept were achieved in the short-wavelength (900-980 nm) regime¹.

In this paper, we report the first electrically pumped tunable VCSELs with continuous tuning in 1530-1620 nm wavelength regime. The VCSELs are directly modulated at 2.5 Gbps (OC-48) rates and show error-free transmissions. Wavelength locking to ITU-grids are accomplished in ~200 μ S.

Tunable Cantilever-VCSEL Design

Figure 1 shows the schematic of a tunable VCSEL, hereinafter referred to as cantilever-VCSEL or c-VCSEL. The device consists of a bottom n-DBR, a cavity layer with an active region, and a top mirror. The top mirror, in turn, consists of three parts (starting from the substrate side): a p-DBR, an airgap, and a top n-DBR. The top n-DBR is freely suspended above the laser cavity and is supported by the cantilever structure. The hetero-structure is similar to that described in our previous report of electrically pumped long-wavelength VCSEL^{2,3}. It is grown in one single epitaxy step, resulting in highly accurate and predictable tuning characteristics.

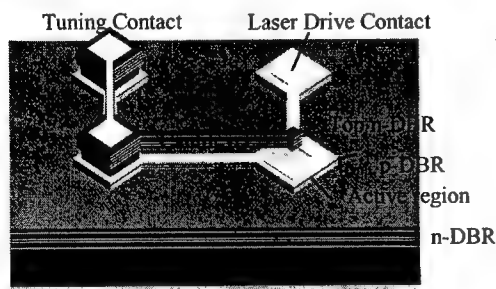


Figure 1 Schematic of a tunable cantilever-VCSEL

Electrical current injection is conducted through the middle contact via the p-DBR. An oxide aperture is formed on an Al-containing layer in the p-DBR to provide current and optical confinement. A tuning contact is fabricated on the top n-DBR. The processing steps include cantilever formation and release.

Continuous Tuning

Wavelength tuning is accomplished by applying a reverse voltage bias to the top n-DBR and p-DBR, across the airgap. The applied voltage creates electrostatic force, which attracts the cantilever toward the substrate and blue shifts the lasing wavelength. Due to the extremely short cavity thickness of the VCSEL, the cantilever movement results in truly continuous wavelength tuning. Continuous tuning allows these VCSELs be used in systems with any channel spacings and provides wavelength sweeping capability that is important for channel monitoring applications. The mechanical movement is completely elastic; there is no hysteresis in the tuning curve. The resonant frequency of the cantilever is about 80 kHz, providing immunity against noise in typical operation environments.

Figure 2 shows a typical c-VCSEL tuning curve. Each of the data point is an ensemble of ~2000 measurements. The continuous, repeatable, and hysteresis-free tuning characteristics as shown here enables the transmission system to lock onto a channel well ahead of its data transmission, known as dark tuning. Dark tuning is crucial for reconfigurable metro networks when activation and redirection of broadband optical signal must be accomplished without interference to other operating channels.

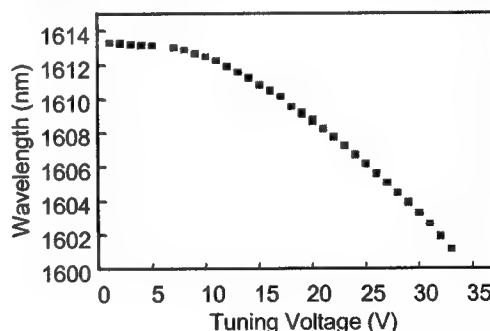


Figure 2 c-VCSEL wavelength vs. tuning voltage

Figure 3 shows the emission spectra of a c-VCSEL, tuned across 20 channels of C-band at 100 GHz ITU spacings. Single mode lasing with great than 45 dB side mode suppression ratio (SMSR) is obtained throughout tuning. The tuning range shown is 16nm. Extension of the tuning range to cover the entire C- or L- band is expected with simple design variations.

The combination of monolithic integration and direct current injection gives c-VCSELs the unique advantage of being direct-modulatable at high data

rates. Such direct modulated lasers eliminate the cost of external modulators, and are ideal for metro-DWDM applications where cost sensitivity is high. Figure 4 shows a typical eye-diagram for a c-VCSEL under direct modulation at 2.5Gbps (OC-48). A SONET mask is also shown to illustrate that there are no errors. An open and error-free eye diagram is obtained over the full tuning range.

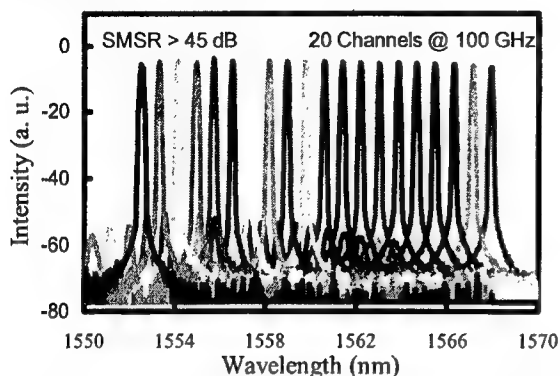


Figure 3 c-VCSEL emission spectra. 20 channels at 100 GHz spacing in C-band



Figure 4: Eye diagram for a c-VCSEL directly modulated at 2.5 Gb/s shows error-free operation

Fast and Precise Wavelength Locking

The continuous wavelength-tuning characteristic enables a simple and cost-effective design of a universal wavelength locking mechanism that does not require individual adjustments or calibration for each laser. It also enables rapid locking, resulting in a fast usable tuning speed.

A typical c-VCSEL with a closed-loop feedback locking can be tuned over multiple channels on the 100 GHz ITU grid and locked to within 2.5 GHz accuracy in ~200 μ s (see Figure 5). In this case, the locker consists of a reference wavelength filter for identification of the absolute wavelength and a comb filter for ITU-grid locking. We expect the locking time to improve to less than 100 μ s for tuning across the entire C- or L- band.

A continuous tuning curve further implies that a tunable transmitter that is set at a given ITU-grid spacing can be easily programmed to lock onto a

denser spacing without concerns of mode hopping or significant changes in hardware. This enables a WDM system built with such transmitters to upgrade gracefully and cost-effectively in both channel counts and wavelength plans.

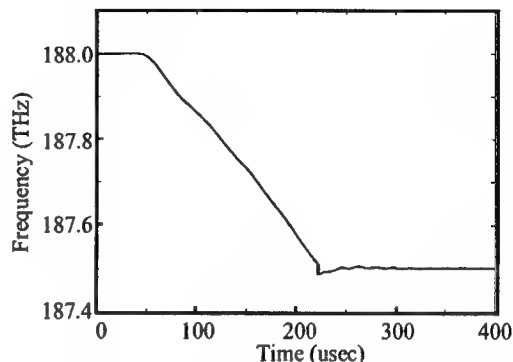


Figure 5: Optical frequency vs. time. The VCSEL is tuned to within 2.5 GHz accuracy in ~200 μ s

Summary

The monolithic integration of MEMS and VCSEL has successfully combined the best of both devices and led to an unprecedented capability in wavelength-tunable lasers. The electrically pumped cantilever-VCSELs can be directly modulated at high data rates. They have a simple monotonic tuning curve for easy wavelength locking and dark tuning, and have a fast usable tuning speed. The tuning range can be designed to cover an entire S-, C- or L-band, and potentially more than one full band. The entire epitaxy structure is grown in one-step epitaxy, which leads to high accuracy and reproducibility of the tuning wavelengths.

The c-VCSELs can be batch processed and tested, which is an essential characteristic for mass production. Furthermore, they can be locked via a universal locker without custom tailoring.

Tunable VCSELs are expected to reshape the horizon of metropolitan area networks by enabling a wide range of exciting new system functionalities. These functionalities will in turn bring the most cost-effective, flexible, on-demand, broadband services to the end users.

References

- [1] C. J. Chang-Hasnain, "Tunable VCSEL," IEEE Journal of Selected Topics in Quantum Electronics, 6 (2000), p. 978-987.
- [2] W. Yuen et al. Electron. Lett., 36(2000) p.1121-1123.
- [3] R. Stone et al. Electron. Lett., 36(2000) p. 1793-1794.

High Power MEMs-Tunable Vertical-Cavity Surface-Emitting Lasers

K.J. Knopp, D. Vakhshoori, P.D. Wang, M. Azimi, M. Jiang, P. Chen, Y. Matsui, K. McCallion, A. Baliga, F. Sakhtab, M. Letsch, B. Johnson, R. Huang, A. Jean, B. DeLargy, C. Pinzone, F. Fan, J. Liu, C. Lu, J. Zhou, H. Zhu, R. Gurjar, P. Tayebati, D. MacDaniel, R. Baorui, R. Waterson, G. VanderRhodes

Nortel Networks

299 Ballardvale Street, Wilmington, Massachusetts, 01887

Tel: (978) 570-1200, Fax: (978) 570-1300, kknopp@nortelnetworks.com

Tunable sources are a fundamental component needed for the reduction of overall DWDM transmission system costs and for its evolution to an agile and intelligent optical network. The cost benefit of eliminating the required supply management of the rapidly growing part inventories necessary to support the ever-increasing numbers of desired ITU channels is tremendous. This cost impact is evident from the reduction of the needed sparing provisions to the ability to accelerate the shipment of systems to the customer. Furthermore, their offering of wavelength routing, wavelength protection, and wavelength on demand capability will aid in the realization of more flexible and reconfigurable, as well as, scalable optical network architectures.

One such tunable source is Nortel Network's widely tunable micro-electromechanical vertical-cavity surface-emitting laser (MEM-VCSEL). MEM-VCSELs offer mode-hop-free and single transverse-mode operation with high side-mode suppression and polarization extinction across a wide tuning range. MEM-VCSEL chips are capable of coupling in excess of 20 mW of optical power into a single-mode optical fiber while continuously tuning across the C-band.

The technology is based on a micro-electromechanical vertical-cavity tunable laser that is optically pumped by a co-packaged 1310 nm pump source and controlled by a co-packaged broadband wavelength locker and power monitor. A schematic of the MEM-VCSEL device discussed in this work is given in Fig. 1. The spot size of the fundamental lasing mode is measured to be $\sim 10 \mu\text{m}$. Single-mode operation is obtained for all pump powers across the tuning range in part through the excellent match between the imaged pumped spot size and that of the TEM_{00} mode of MEM-VCSEL resonator. Details on the fabrication process of the MEM structure can be found in our earlier work [1, 2].

Figure 2 shows the fiber-coupled output of a MEM-VCSEL chip as a function of the launched 1310 nm optical pump power for a tuning voltage of zero. An equivalent wall plug efficiency of $\sim 0.1 \text{ W/A}$ and $>20 \text{ mW}$ of VCSEL power is illustrated. Figure 3 shows the MEM-VCSEL emission wavelength as a function of tuning voltage. The quadratic dependence of the lasing wavelength on applied voltage is observed due to the mechanics of the translation of the top mirror. A continuous mode-hop free tuning range of 27 nm is illustrated. Tuning response times are on the microsecond time scale with the limit imposed by the mechanical resonance observed at 700 kHz. Figure 4 shows that operating the device in a constant output power mode (variable pump power), 20 mW can be maintained over the tuning range. Additionally, devices having 10 mW of output over an extended tuning range of 65 nm have also been demonstrated. For typical devices, the instantaneous linewidth is $<5 \text{ MHz}$, the polarization extinction ratio is $>20 \text{ dB}$, and the RIN is $<-140 \text{ dB/Hz}$ across the transmission frequencies. The SMSR is typical $>50 \text{ dB}$ throughout the tuning range and the OSNR is typically $>50 \text{ dB}$.

A photograph of a completed Nortel Gen-HP tunable source showing the 26-pin hermetic package containing the MEM-VCSEL, pump laser, broadband wavelength locker, power monitor, and coupling optics is in Fig. 5. The product specifications for this package are $>10 \text{ mW}$ in the fiber and continuous tuning over $>16 \text{ nm}$. The spectral output of 20 locked channels with a $\pm 2.5 \text{ GHz}$ locking accuracy is shown in Fig. 6. The high spectral fidelity of the package's output is shown.

- [1] D. Vakhshoori, P. Tayebati, Chih-Cheng Lu, M. Azimi, P.D. Wang, Jian-Huai Zhou, and E. Canoglu, "2mW CW singlemode operation of a tunable 1550nm vertical cavity surface emitting laser with 50 nm tuning range," *Electron. Lett.*, vol. 35, no. 11, pp. 1-2, 1999.
- [2] P. Tayebati, P.D. Wang, M. Azimi, L. Meflah, D. Vakhshoori, "Microelectromechanical tunable filter with stable half symmetric cavity," *Electron. Lett.*, vol. 34, no. 20, pp. 1967-1968, 1998.

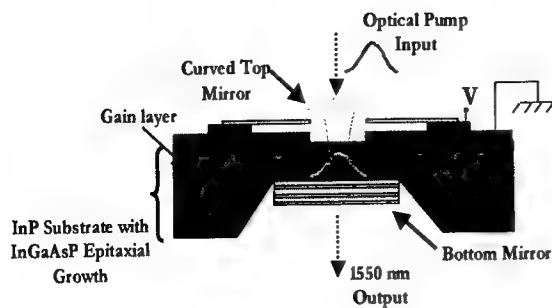


Figure 1. Schematic of the MEM-VCSEL device. Tuning is achieved by applying a bias voltage between the curved top mirror and the InP substrate.

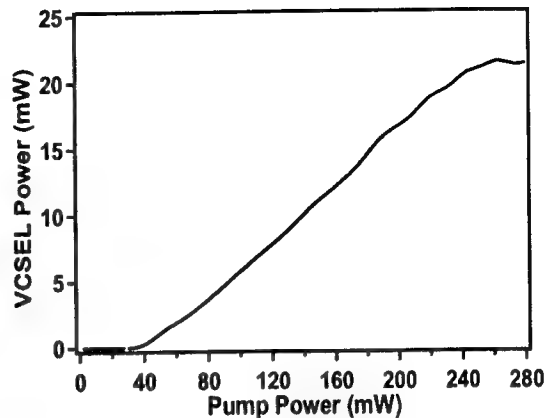


Figure 2. VCSEL output versus launched 1310 nm pump power at 1570 nm.

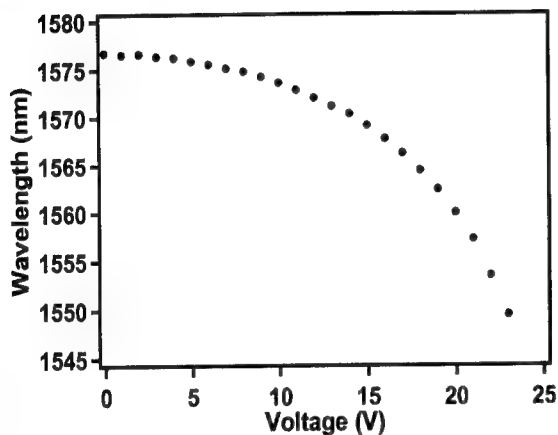


Figure 3. MEM-VCSEL emission wavelength versus applied tuning voltage.

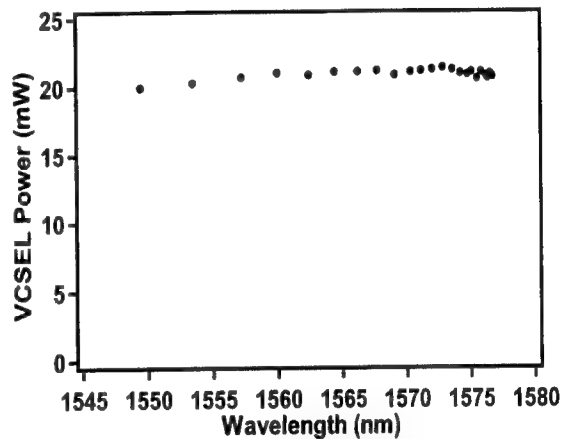


Figure 4. MEM-VCSEL output power through the tuning range.

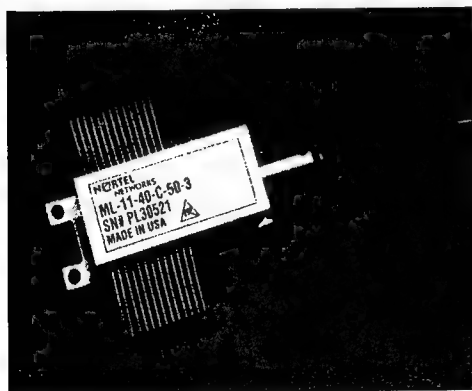


Figure 5. Completed Nortel Gen-HP tunable source showing the package containing the MEM-VCSEL, pump laser, broadband wavelength locker, power monitor and coupling optics.

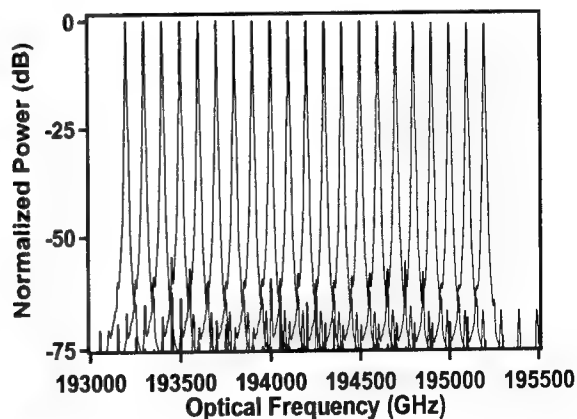


Figure 6. The spectral output for 20 locked channels from the Gen-HP package.

Tunable Lasers using Sampled Grating DBRs (Invited)

Jonathon Barton, Larry Coldren

Materials Dept., University of California, Santa Barbara

Greg A. Fish

Agility Communications, Inc., 600 Pine Ave, Santa Barbara, CA 93117

Tunable lasers are desirable for both long-haul and metro optical networks to reduce inventory associated with sparing, and to add improved network configurability. A marketable tunable laser would have low cost, high output power ($>10\text{mW}$ fiber-coupled)[4], ultra-wide tuning range ($>35\text{nm}$ C Band), direct or integrated modulation ($>2.5\text{Gbit/s}$)[2,5], and high reliability (>20 year MTTF). These criteria have been met with monolithic Sampled Grating Distributed Bragg Reflector lasers (SGDBRs). A number of different tunable laser technological approaches have also been proposed, but none offer the simplicity of the SGDBR platform for integration with modulators, amplifiers or other components. This presentation will focus on the latest advances in the design of monolithic SGDBR lasers and integrated photonic devices.

SGDBRs hold high promise in meeting the above requirements and desires. The monolithic SGDBR fabrication approach does not require moving parts and imparts similar device reliability as Distributed Feedback lasers (DFBs). High speed switching ($>10\text{ms}$) is possible since temperature tuning is not required. Ultimately, The SGDBR enables a plethora of integrated device possibilities. Previous work in SGDBR design has focused on extending the tuning range of these devices resulting in demonstrated tuning ranges as high as 72nm [5] However, as recent as a few years ago, output power from monolithically tunable lasers has been lacking in comparison with single wavelength DFBs. Recent advances in cavity design – that focus on optimizing the output power in addition to covering $40\text{-}50\text{nm}$ of tuning – yield fiber-coupled output powers exceeding 10mW [7]. A schematic of a device structure that incorporates an integrated SOA and the fiber-coupled power output over the tuning range are shown in fig. 1. Not only has the power output increased, additionally, the unlevelled power

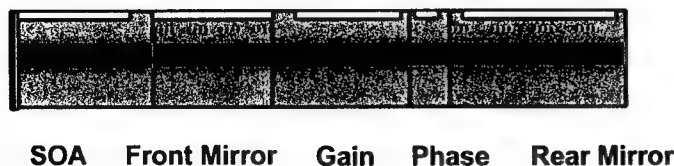
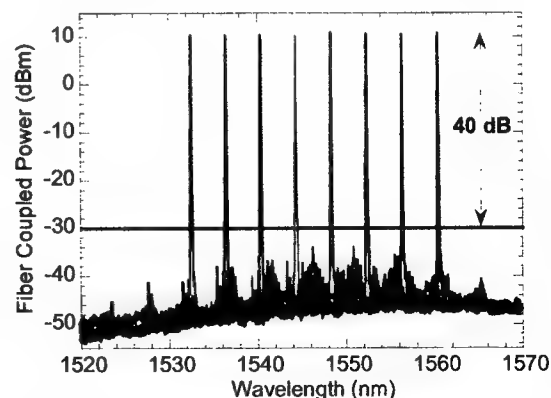


Fig. 1 Device structure



Fiber-coupled power for integrated SOA-SGDBR laser

variation across the tuning range is improved to less than 4dB across the 44nm tuning range.

The most compelling advantage of the SGDBR design is its capability to provide a simple platform for the integration of modulators and semiconductor optical amplifiers [1,2,3,5]. This lowers the coupling losses inherent in hybrid coupling schemes and ultimately, reduces the overall cost of the device. In addition, integration provides far more exotic device functionality – enabling wavelength converters, biosensors, and wavelength monitors, to name a few. This can be achieved through a single regrowth step with a versatile offset QW structure. Integration of semiconductor optical amplifiers benefits the system twofold – firstly the SGDBR design can be designed for higher tunability as the SOA will compensate for increased absorption loss in the mirrors at high tuning currents. Secondly, the output power is decoupled from the tuning control.

The main challenges to the widespread availability of SGDBRs is the development of feedback control circuitry involving wide-tuning range wavelockers, and high volume production of devices that must meet specifications for high power over all channels as well as for enhanced capabilities such as modulation. Also, facets must have adequate AR coating ($<10^{-4}$) to prevent spurious degradation of tunability or amplification. The use of an angled waveguide has been explored to reduce the AR coating requirements. SGDBRs have been demonstrated with high power, integrated photonic devices have been demonstrated with $>2.5\text{Gbit/s}$ modulation in separate experiments. The next challenge is to integrate high power devices with improved modulation capabilities simultaneously.

Acknowledgements

This work was supported by the office of naval research.

References

- [1] B. Mason, J. Barton, G.A. Fish, L.A. Coldren, and S.P. DenBaars, "Design of Sampled Grating DBR Lasers with Integrated Semiconductor Optical Amplifiers," *IEEE Photon. Tech. Letters*, 12, (7) 762-764, July 2000.
- [2] B. Mason, G. A. Fish, S. Denbaars, And L.A. Coldren, "Widely tunable sampled grating DBR laser with integrated electro-absorption modulator", *IEEE Photon. Tech. Letters*, 11,(6), p. 638-640, June 1999.
- [3] L.A. Coldren, Y.H. Jan, B. Mason, M. E. Heimbuch, S.P. Denbaars, "Properties of widely-tunable integrated WDM sources and receivers, *LEOS* 97, p. 331-2 vol.1. 2
- [4] P.J. Williams, D. J. Robbins, F.O. Robson, N.D. Whitbread, "High Power and Wide Quasi-Continuous Tuning, SG-DBR Lasers, *Proceedings of ECOC 2000*, Munich, Germany, Sept 2000.
- [5] B. Mason G. A. Fish, J. Barton, V. Kaman, L.A. Coldren, S.P. DenBaars, J. Bowers, "Characteristics of Sampled Grating DBR Lasers with Integrated Semiconductor Optical Amplifiers and Electroabsorption Modulators," *Proceedings of OFC 2000*.
- [6] Delorme, F. , Alibert, G., Ougier, C. , Siempkes, S., S., Nakajima, H., "Sampled-grating DBR lasers with 101 wavelengths over 44nm and optimized power variation for WDM applications". *Electronic Letters*, 34,(3), 5 Feb 1998. p. 279-81.
- [7]G. A.Fish, "Monolithic, Widely-Tunable, DBR Lasers", *Proceedings OFC 2001*.

GCSRs and other Widely Tunable Lasers

Jan-Olof Wesström, Johan Bergerengen, Gert Sarlet, Ylva Gustafsson, Peter Szabo, and Björn Broberg

ADC Inc.
PO Box 911, SE-175 29 Jarfalla, Sweden

Tunable lasers offer an extra degree of freedom in WDM systems¹, which facilitates fast optical switching, flexible reconfiguration of networks, and reduced inventories. The savings are evident as a single component can be used to reach any frequency in a given channel plan. Several candidate components give the required tuning: external cavity lasers, micro-electromechanically tuned vertical cavity lasers², temperature-tuned DFB arrays³, and monolithic edge-emitting DBR-type (Distributed Bragg Reflector) lasers⁴, tuned by carrier injection. Of these only the DBR-type lasers achieve the fast frequency switching^{5,6} required for packet switching. The reason is the small time constants for carrier recombination of the order of 10ns.

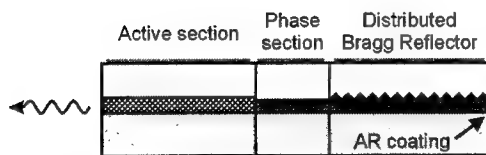


Fig. 1 Three-section DBR laser

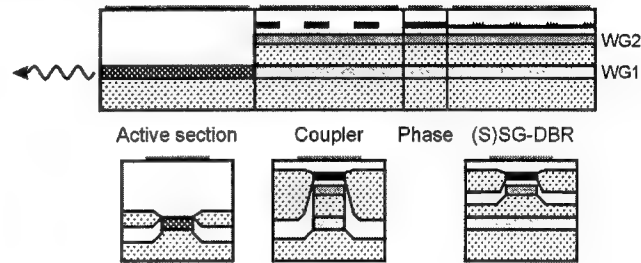


Fig. 2 GCSR laser

The three-section DBR laser⁷ in Fig. 1 uses a Distributed Bragg Reflector (DBR) as a tunable frequency selective element. The active section is used to produce the optical gain. By injecting current into the DBR section the laser can be tuned 1-2 THz.⁸ The phase section is used to align a cavity mode with the reflection peak, and thus do the fine-tuning. The tuning range can be enhanced by an appropriate choice of tuning material, doping, and geometry.⁹ Approximately 2 THz is however the widest tuning range reported. This is just half of what is required to cover the C-band (192.1 – 196.0 THz). To meet this requirement, four-section DBR-type lasers have been developed. The Sampled Grating DBR laser¹⁰ (SGDBR) and the Grating Coupler Sampled Reflector laser¹¹ (GCSR) are two such designs that greatly enhance the tuning range by the use of reflectors with multi-peak reflection spectra.⁴ See Fig. 3.

The SGDBR uses two such sampled gratings, one at the front and one at the rear. The peak separations of the two gratings are slightly different and the idea is to use the Vernier effect to select the reflection peak for lasing. By tuning the two reflector sections and the phase section, any frequency within a wide range can be reached.

In the GCSR laser, Fig. 2, the transmission peak through the grating assisted coupler is instead used to select the appropriate reflection peak for lasing. The coupler is thus used for coarse tuning, the reflector is used for intermediate tuning, and the phase section is used for fine-tuning of the laser so that any frequency within the tuning range can be reached.

For most applications it is practical to supply the laser with the necessary control electronics including a microprocessor and an EPROM where an arbitrary number of factory calibrated channels are stored. The main advantage is the ease of use. Instead of feeding the laser with a set of four currents, the user selects a channel number through the digital interface. A second advantage is that the integrated modules are interchangeable although they contain laser chips that may differ. In Fig. 4 we see an example of an integrated module, the NYW-50 built around a GCSR laser. In the calibration process, the currents needed for each channel are stored in the EPROM. Finding those currents must be done in an efficient way.^{12,13} In mass production, the measurements should not take more than minutes, while scanning through the whole four-dimensional space of currents takes many orders of magnitude longer. One approach to reduce measurement time is to avoid slow frequency measurements as much as possible and instead use frequency dependent filters to detect the mode hops as changes in power, and then select operation points far from those.

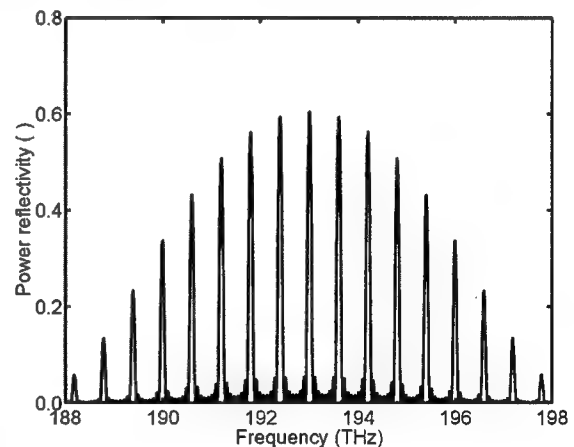


Fig. 3 Simulated reflection spectrum from a sampled grating

The long-term stability is one of the most important issues for any component in a telecommunication system. In an unstable tunable laser, the frequency may drift and in worst case mode hops occur. This is of course unacceptable. Fortunately, stability is achievable after proper burn in. Good results have been reported for DBR lasers.^{14,15} In GCSR lasers, lower tuning currents are used which further reduces degradation. Long-term stability is also what we observe in our accelerated-aging studies. As an extra precaution, various stabilization algorithms can be applied to lock the frequency to an external reference. Mode hops can be avoided by monitoring for example the slope vs. tuning currents of the output power¹⁶ or of the gain-section voltage.¹³ We have developed a frequency and mode stabilization that yields good results. In a test with accelerated aging on GCSR lasers without prior burn in, the frequency drift and Side-Mode Suppression ratio (SMSR) were compared for operation with and without stabilization. Even though non-stabilized lasers mode hopped or drifted up to 10 GHz, with stabilization the same lasers showed no mode hops, negligible frequency drift and small variations of the SMSR.



Fig. 4 The ADC NYW-50 integrated module

In summary, the natural choice for fast widely tunable lasers, user-friendly integrated modules with GCSR or SGDBR lasers, are turning into mature components as burn-in procedures make them very stable and frequency and mode stabilization schemes are developed to take care of the residual degradation.

¹ R. Plastow, "Emerging tunable laser applications in optical networks," *Lightwave Magazine*, vol 17, no. 3, March 2000.

² D. Vakhshoori, P.D. Wang, M. Azimi, K.J. Knopp, and M. Jiang, "MEMs-Tunable Vertical-Cavity Surface-Emitting Lasers," *Proc. OFC '01*, paper TuJ1, Anaheim, CA, USA, March 2001.

³ K. Yashiki, K. Kudo, T. Morimoto, S. Sudo, Y. Muroya, T. Tamanuki, M. Ishizaka, T. Hosoda, Y. Furushima, H. Hatakeyama, Y. Yokoyama, K. Mori, T. Sasaki, and M. Yamaguchi, "Multi-Range Wavelength-Selectable Microarray Light Sources with Detuning Adjustable EA-Modulator," *Proc. ECOC '00*, pp. 159-161, paper 6.3.2, vol 2, Munich, Germany, September 2000.

⁴ An excellent overview of DBR-type lasers can be found in M.-C. Amann, and J. Buus, *Tunable laser diodes*, Artech House, Norwood, MA, USA, 1998.

⁵ K. Shrikhande, I. M. White, M. S. Rogge, F.-T. An, A. Srivatsa, E. S. Hu, S. S.-H. Yam, and L. G. Kazovsky, "Performance Demonstration of a Fast-Tunable Transmitter and Burst-Mode Packet Receiver for HORNET," *Proc. OFC '01*, paper ThG2, Anaheim, CA, USA, March 2001.

⁶ Olga A. Lavrova and Daniel Blumenthal, "Detailed Transfer Matrix Method-Based Dynamic Model for Multisection Widely Tunable GCSR Lasers," *J. Lightwave Technol.*, vol. 18, no. 9, pp. 1274-1283, September 2000.

⁷ S. Murata, I. Mito, and K. Kobayashi, "Over 720 GHz (5.8 nm) frequency tuning by a 1.5 μ m DBR laser with phase and Bragg wavelength control regions," *Electron. Lett.*, vol. 23, no. 8, pp. 403-405, April 1987.

⁸ H. Debrégeas-Sillard, A. Voung, F. Delorme, J. David, V. Allard, A. Bodéré, O. LeGouezigou, F. Gaborit, J. Rotte, M. Goix, V. Voirot, and J. Jacquet, "DBR Module with 20-mW Constant Coupled Output Power, Over 16 nm (40 x 50-GHz Spaced Channels)," *IEEE Photonic. Tech. L.*, vol. 13, no. 1, January 2001.

⁹ J. P. Weber, "Optimization of the carrier-induced effective index change in InGaAsP waveguides - Application to tunable Bragg filters," *IEEE J. Quantum Electron.*, vol 30, no. 8, pp. 1801-1816, August 1994.

¹⁰ V. Jayaraman, Z.-M. Chuang, and L.A. Coldren, "Theory, design and performance of extended tuning range semiconductor lasers with sampled gratings," *IEEE J. Quantum Electron.*, vol. 29, no. 6, pp. 1824-1834, June 1993.

¹¹ J. Willems, G. Morthier, and R. Baets, "Novel widely tunable integrated optical filter with high spectral selectivity," *Proc. ECOC '92*, pp. 413-416, paper WeB9.2, Berlin, Germany, September 1992.

¹² T. Farrell, J. Dunne, and R. O'Dowd, "Complete wavelength control of GCSR lasers over EDFA band," *Proc. LEOS '99*, pp. 329-330, paper TuY1, San Francisco, CA, USA, November 1999.

¹³ G. Sarlet, G. Morthier, and R. Baets, "Control of widely tunable SSG-DBR lasers for dense wavelength division multiplexing," *J. Lightwave Technol.*, vol. 18, no 8, pp. 1128-1138, August 2000.

¹⁴ F. Delorme, G. Terol, H. de Baillencourt, S. Grosmaire, and P. Devoldere, "Long-term wavelength stability of 1.55- μ m tunable distributed Bragg reflector lasers," *IEEE J. Selected Topics Quantum Electron.*, vol. 5, no. 3, pp. 480-486, May 1999.

¹⁵ H. Mawatari, M. Fukuda, F. Kano, Y. Tohmori, Y. Yoshikuni, and H. Toba, "Lasing wavelength changes due to degradation in buried heterostructure distributed Bragg reflector lasers," *J. Lightwave Technol.*, vol. 17, no. 5, pp. 915-923, May 1999.

¹⁶ D. A. Ackerman, K. F. Dreyer, U. Koren, J. W. Stayt, S. L. Broutin, W. A. Asous, J. E. Johnson, L. J.-P. Ketelsen, K. K. Kamath, S. O'Brien, W. J. Shakespeare, M. A. Eshelman, M. M. Meyers, D. A. Snyder, and E. S. Mak, "Wavelength, Modal and Power Stabilization of Tunable Electro-Absorption Modulated, Distributed Bragg Reflector Lasers," *Proc. IEEE 17th International Semiconductor Laser Conference 2000*, pp. 49-50, paper TuB3, Monterey, CA, USA, September 2000.

Fully functional wavelength selectable DWDM transmitter

D. A. Ackerman, J. E. Johnson, L. J-P. Ketelsen, J. M. Geary[†], W. A. Asous[†], F. S. Walters[†], J. M. Freund[†], M. S. Hybertsen, K. G. Glogovsky[†], C. W. Lentz[†], C. L. Reynolds[†], R. B. Bylsma[†], E. J. Dean[†] and T. L. Koch[†]

Agere Systems, 600 Mountain Avenue, Murray Hill, NJ 07974 USA
[†]9999 Hamilton Blvd., Breinigsville, PA 18031 USA

A wavelength selectable transmitter for 2.5 or 10Gb/s dense wavelength division multiplexed (DWDM) systems must tune across a substantial number of channels while meeting rigorous system specifications in each channel. Moreover, a tunable transmitter must feature the same level of stability, reliability and ease of use compared to single wavelength counterparts. We examine a 20-channel transmitter designed to meet the needs of high bit-rate DWDM systems.

Introduction

Dense wavelength division multiplexed systems operating over long distances at high bit rates require stable, low-chirp optical sources to transmit closely spaced channels. Externally modulated distributed feedback (DFB) lasers and monolithically integrated electro-absorption modulated DFB lasers (EMLs) serve as sources in 2.5 and 10Gb/s transmitters. EMLs are compact, while DFB lasers coupled to lithium niobate modulators are bulkier but tend to operate with slightly lower chirp. In both cases, single channel transmitters require burdensome inventory for systems of many DWDM channels. Wavelength selectable transmitters relieve inventory requirements, while meeting, in every channel, the rigorous performance and reliability specifications met by single wavelength transmitters.

Various approaches achieve wavelength selectable functionality. DFB laser arrays offer time-tested stability and reliability at the cost of large device size [1]. Output power is sacrificed in array element combiners, but wavelength control of each element is simple. Edge-emitting distributed Bragg reflector (DBR) lasers offer compact size and attendant lower cost at the expense of complicated wavelength and modal control. Tunable VCSELs, coupled with integrated moving mirrors offer compactness without risk of mode hopping [2], but questions of long-term-reliability and cost remain. Our approach has been to develop a highly integrated InP chip comprising a DBR laser coupled to a semiconductor optical amplifier (SOA), power monitor and electro-absorption (EA) modulator [3]. Hardware for closed-loop feedback ensuring wavelength and modal stability is incorporated into the small form factor transmitter package [4]. We report on fully functional high bit rate versions of this EA-DBR source capable of error-free transmission at 2.5Gb/s over 680km [3] and 10Gb/s over 80km [5] of standard fiber on each of twenty 50GHz-spaced DWDM channels.

Device

A schematic representation of the EA-DBR laser is shown in Figure 1. A 420 μ m gain section, chosen to give 100GHz mode spacing, and 250 μ m DBR tuning section form a DBR laser which is coupled to a 450 μ m SOA, a short power monitor and an EA modulator. Modulator lengths are 235 and 135 μ m for 2.5 and 10Gb/s, respectively. Trenched isolation regions separate the five sections of the 1700 x 500 μ m chip. The SOA compensates for on-state modulator loss and free carrier absorption in the tuning section. A forward power tap after the SOA enables closed-loop control of the fiber coupled output power in the 2.5Gb/s design, and will be added to the 10Gb/s design.

A dual waveguide integration scheme allows independent optimization of DBR laser, amplifier and modulator performance. The active-passive integration scheme [6], shown in Figure 1, consists of an upper waveguide that contains the multiple quantum well active layers and a lower waveguide that is thicker in the tuning section. Two short lateral tapers in the upper waveguide adiabatically transfer the guided mode between upper and lower waveguides. High modal gain in the active sections and tight optical confinement in the tuning section yield efficient tuning, low radiation loss, and low optical back-reflection at the interfaces.

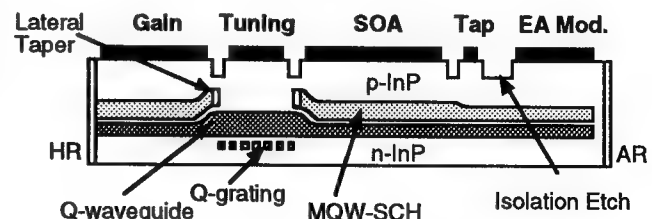


Figure 1: Schematic of EADBR laser

Results and Discussion

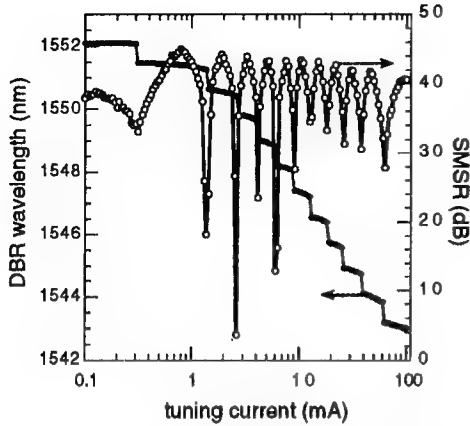


Figure 2: Tuning and SMSR characteristics

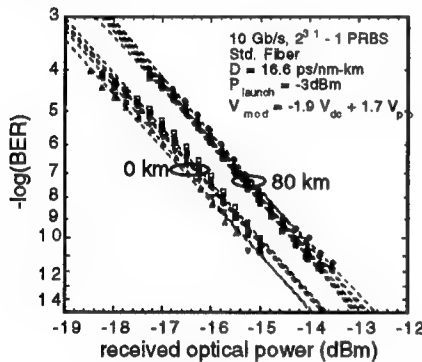


Figure 3: 10Gb/s transmission results

The small-signal bandwidth of the 10Gb/s EA-modulator is 19.7GHz at a bias of $-1.5V$. RF extinction ratio is $> 14\text{dB}$ for the 2.5Gb/s modulator for $V_{\text{mod}} = 2.0V_{\text{p-p}}$, and $> 8.5\text{dB}$ for the 10Gb/s modulator for $V_{\text{mod}} = 1.7V_{\text{p-p}}$. Peak-to-peak device chirp, measured by time-resolved spectroscopy is typically $< 0.20\text{\AA}$, attributable to isolation trenching and good AR coatings on the chip as well as careful package design to minimize electrical cross-talk.

The fiber transmission system used in the experiment consisted of the EA-DBR transmitter followed by up to 8 spans of conventional single-mode fiber with an average dispersion of 17 ps/nm-km . EDFAs boosted the launched power into each span to $+7\text{dBm}$. After the final span, the optical signal was bandpass-filtered to remove ASE, passed through a variable attenuator, and coupled into a receiver/regenerator. Good transmission characteristics were obtained at 2.5 Gb/s over 681 km. The EA modulator was driven by a 2.5 Gb/s 2^{23} -1 PRBS signal with a $2.0V_{\text{pk-pk}}$ drive. The measured power penalty at $\text{BER} = 10^{-9}$ was $\sim -0.5\text{ dB}$ for the worst channel with wavelength and mode stabilization control loops engaged. No error floors were observed. The dispersion penalty is slightly higher for the low frequency channels because the higher FM efficiency of the tuning section at low tuning current makes it more sensitive to power supply noise and electrical crosstalk with the integrated modulator [10]. At 10Gb/s, dispersion penalties less than 1.3dB without error floors were achieved using a 2^{31} -1 PRBS signal for all 20 operating wavelengths of the device over a single 80 km span of standard fiber, as shown in Figure 3.

References:

- [1] K. Kudo et al., Opt. Fiber Comm. Conf., Baltimore, MD USA, 2000. [2] D. Vakhshoori et al., Opt. Fiber Comm. Conf., Anaheim, CA USA, 2001. [3] L. Ketelsen et al., Opt. Fiber Comm. Conf., Baltimore, MD USA, 2000. [4] D. Ackerman et al., IEEE 17th Int. Semiconductor Laser Conf., Monterey, CA USA, 2000. [5] J. Johnson et al., Opt. Fiber Comm. Conf., Anaheim, CA USA, 2001. [6] J. Johnson et al., *IEEE J. Selected Topics Quantum Electron.*, vol. 6, no. 1, pp. 19-25, Feb., 2000. [7] S. Woodward et al., *IEEE Photon. Tech. Lett.*, vol. 4, no. 5, pp. 417-419, 1992. [8] F. Delorme et al., *IEEE J. Selected Topics Quantum Electron.*, vol. 3, no. 21, pp. 607, Apr., 1997. [9] D. Ackerman et al., IEEE 17th Int. Semiconductor Laser Conf., Monterey, CA USA, 2000. [10] J. Johnson et al., Int. Photon. Res. Conf., Quebec, Canada, 2000.

External Cavity Tunable Lasers for Network Deployment

Dr. Timothy Day

New Focus, Inc., 5215 Hellyer Avenue, San Jose, CA 95138

Abstract: We report a high-performance tunable laser for line card deployment. The device utilizes an external cavity approach to achieve high output power, wide tuning range, and high side-mode suppression ratio.

There are four primary approaches to providing tunability with semiconductor lasers¹—each with distinct advantages and disadvantages. Tunable DFB (Distributed FeedBack) lasers use temperature to tune the wavelength over a limited range of 2 nm with output power of 13 dBm². Additional gain sections on the same semiconductor can extend the tuning range to 15 nm³.

Tunable Distributed Bragg Reflector (DBR) lasers have emerged as an alternative to achieve wider tunability. Several varieties of DBR lasers have been demonstrated. SG-DBR (Sampled Grating Distributed Bragg Reflector)^{1,4,5}, SSG-DBR (Super-Structure Grating Distributed Bragg Reflector)^{1,4}, and GCSR (Grating assisted Co-directional with Sampled Reflector)^{1,6} can all be tuned over a range exceeding 30 nm. However, the Bragg reflectors and other tuning sections result in substantial loss thus lowering the overall output power to less than 5 mW. The addition of a semiconductor optical amplifier (SOA) increases the output power to 10 mW at the expense of higher background noise.⁷

Yet another approach uses a vertical-cavity surface-emitting laser (VCSEL) with a MEMS (Micro-Electrical Mechanical Systems)-based movable top mirror. Tuning ranges up to 35nm have been demonstrated with tunable VCSELs^{8,9,10} but the output power of electrically-pumped devices remains low (< 1 mW).

At New Focus, we have concentrated on External-Cavity Diode Laser (ECDL) technology in order to provide wider tuning ranges (~100 nm) with higher output powers.¹¹ In this type of laser, the resonant cavity is external to the laser diode which acts as a gain medium only. Littman-Metcalf and Littrow cavity configurations are examples of single-sided ECDL sources in which gratings are used to provide optical feedback and to tune the wavelength.^{12,13}

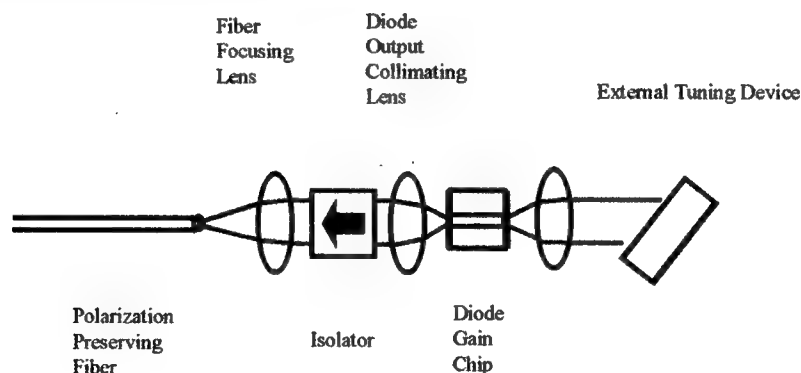
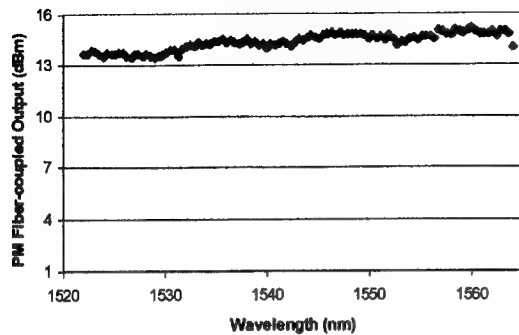


Figure 1. A two-sided ECDL configuration.

Additional flexibility is possible using a two-sided ECDL configuration (Fig. 1). In this implementation one facet of the laser diode, uncoated or coated to be a partial reflector, acts as an output coupler. Light transmitted from the output-coupling facet is collimated, passed through a Faraday isolator and focused into an output fiber. The other side of the laser diode is anti-reflection coated to minimize optical feedback and a lens is positioned to couple the light into the external cavity. Various optical tuning elements may be used in the external cavity including gratings and etalons. By proper choice of cavity configuration and parameters, the laser can be made to emit light at discrete ITU wavelengths with excellent wavelength accuracy and stability, and the problem of mode-hopping is also eliminated.

The resulting tunable lasers provide excellent optical output for DWDM transmission in optical networks. For example, with such an ECDL, high output power (>13 dBm) is achieved over the entire C-band (Fig. 2). Other advantages of ECDLs include a side-mode suppression ratio (SMSR) better than -50 dB (Fig. 3), RIN values of -150 dBc/Hz, and narrow intrinsic linewidth of less than 1 MHz.



>13dBm over the entire C-band

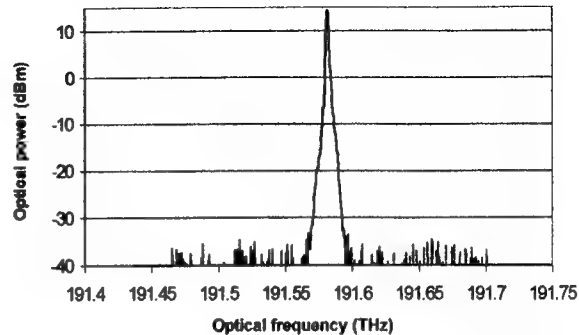


Figure 3. Optical spectrum of a New Focus ECDL showing SMSR better than -50 dB.

In addition, ECDLs employ inexpensive, Fabry-Perot laser diodes that exhibit long lifetimes with stable performance characteristics. Tuning mechanisms are designed for accuracy and stability, using proven technology for the reliability required in telecom applications.

In summary, with these recent advances, widely tunable lasers have become a viable technology for deployed optical networks exceeding optical performance and reliability requirements. The implementation of such lasers will not only eliminate the logistical and inventory problems that result from fixed-wavelength transmitters, but will also enable novel network architectures with dynamic functionality.

The author would like to acknowledge William Chapman, William Kozlovsky, Paul Zorabedian, Tim Bodenhamer, Herman Chui, Nadim Maluf, and Kathryn D. Li Dessau for contributions to this article and work.

¹ "Tunable laser Diodes", M-C Amann and J. Buus, Artech House, 1998, pg. 114.

² "Alcatel Optronics Division Delivers First Tunable, Wavelength-locked Laser", August 9, 2000, Alcatel Optronics, www.alcatel.com

³ "Nortel Networks Announces World Leading technology With 15nm Tunable Laser", February 22, 1999, Nortel Networks, www.nortelnetworks.com

⁴ "Directly modulated Sampled Grating DBR lasers for long-haul WDM communications systems," B. Mason, S.L. Lee, M.E. Heimbuch, and L. A. Coldren IEEE Photonics Technology Letters vol. 9, pp. 377-379, 1997.

⁵ "Design of Sampled Grating DBR Lasers with Integrated Semiconductor Optical Amplifiers", Beck Mason, Jonathan Barton, Greg A. Fish, Larry. A. Coldren, Steven P. DenBaars, IEEE Photonic Technology Letters. Vol. 12, No. 7, July 2000.

⁶ Altitun NYW-60, October 2000, www.altitun.com

⁷ "Optical Fiber Communication Systems", L. Kazovsky, et al, Artech House, 1996, pp. 419-426.

⁸ "Error-free 2.5 Gb/s transmission of a c-band tunable 8 dBm vertical cavity surface emitting laser over 815 km of conventional fiber", M. Jiang, C-C Lu, P. Chen, J.H Zhou, J. Cai, K. McCallion, K. J. Knopp, P. D. Wang, M. Azimi, P. Tayebati, D. Vakshoori, presented at NFOEC 2000, August 27-31, 2000.

⁹ "Top-emitting micromechanical VCSEL with a 31.6 nm tuning range", M.Y. Li, W. Yuen, G.S. Li, and C.J. Chang-Hasnain, IEEE Photonics Technology Letters vol. 10, pp. 18-20, 1998.

¹⁰ "High-Performance 1.6μm Single-Epitaxy Top-Emitting VCSEL", W. Yuen, J. Boucart, P. Kner, R. J. Stone, D. Zhang, M. Bea, T. Zheng, C. He, K. Yu, M. Jansen, D. P. Worland, C. J. Chang-Hasnain, Presented at Conference on Lasers Electro-Optics (CLEO), May 7-12, 2000 San Francisco, CA.

¹¹ "Continuously Tunable Diode Lasers," T. Day, F. Luecke, and M. Brownell, Lasers & Optronics, June 1993.

¹² P. Zorabedian and W. R. Trutna, Optical Letters, vol. 13, pp. 826-828, 1988

¹³ "Synchronous Cavity Mode and Feedback Wavelength Scanning in Dye Laser Oscillators with Gratings," P. McNicholl and H. J. Metcalf, Applied Optics vol. 24, No. 17 pp. 2757-2761 1 Sept. 1985

Widely tunable external cavity diode laser using a MEMS electrostatic rotary actuator

Jill D. Berger, Yongwei Zhang, John D. Grade, Howard Lee, Stephen Hrinia,
Hal Jerman, Al Fennema, Alex Tselikov and Doug Anthon

Iolon, Inc., 1870 Lundy Ave., San Jose, California 95131
Voice: 408-952-5039, Fax: 408-952-5006, danthon@iolon.com

Widely tunable semiconductor lasers are useful in dense wavelength division multiplexing (DWDM) applications such as wavelength conversion, optical network routing and multi-wavelength sparring. Several types of widely tunable lasers have been demonstrated, including multisection DFBs [1], sampled grating DBRs [2], and MEM-VCSELs [3]. Tunable external cavity diode lasers (ECL) with wide continuous tuning ranges, high output power, narrow linewidth, and excellent wavelength accuracy and side mode suppression have been widely used in test equipment, but the size and cost of the large opto-mechanical assemblies have generally precluded their use in telecommunications[4,5]. We describe a high power, widely tunable micro-external cavity diode laser with a MEMS electrostatic actuator that matches the performance of conventional ECL's, in a low cost, 5mm×5mm form factor.

The MEM-ECL shown in Fig. 1 consists of a InGaAsP/InP multiple quantum well laser diode with an 80 nm gain bandwidth centered at 1550 nm placed in a Littman/Metcalf tunable resonator [6]. The output from the antireflection-coated diode facet ($R = 2 \times 10^{-4}$) is collimated by a diffraction-limited silicon microlens, and split almost equally by the grazing-incidence grating into the directly reflected, zero-order output beam, and the first-order diffracted beam that is reflected by the mirror back to the laser diode. This produces an intracavity optical filter with a 3 dB passband comparable to the 0.2 nm mode spacing of the resonator. The laser wavelength corresponds to the cavity mode closest to the center of the filter, and optimum performance will occur if the mode is centered on the passband. The mirror is mounted on an electrostatic comb-drive actuator where an applied voltage of ± 140 V rotates the mirror by $\pm 1.4^\circ$ about a virtual pivot, synchronously tuning the passband and the cavity modes to give continuous tuning without mode hops [7]. The 85- μm thick actuator is fabricated from single-crystal silicon using Deep Reactive Ion Etching (DRIE) [8], producing a MEMS structure with greater out-of-plane stiffness and actuator force than is possible with surface micromachining techniques. The MEM-ECL is assembled on a ceramic substrate, mounted to a thermoelectric cooler and packaged in a 14-pin butterfly package where the output is coupled through a 30 dB isolator to polarization maintaining fiber with 70% efficiency.

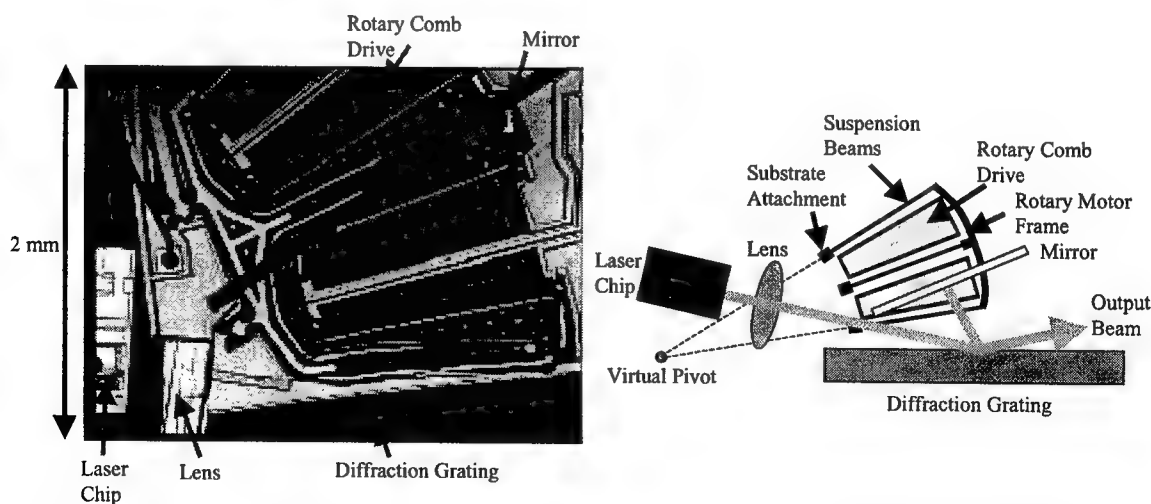


Fig. 1. Photograph and schematic of the MEM-ECL.

The series of lasing spectra in Fig. 2(a) shows a +7 dBm fiber-coupled output from the MEM-ECL, with 55 dB side mode suppression over a 40 nm range. Fig. 2(b) shows the L-I curve and a free-space output of 14

mW. The MEM-ECL exhibits a relative intensity noise (RIN) of less than -145 dB/Hz from 1 MHz to 10 GHz, a polarization extinction ratio better than 20 dB, and a spontaneous emission background 40 dB below the laser peak value. The fundamental laser linewidth due to spontaneous-emission-induced phase noise depends on cavity length and, at less than 1 MHz, is narrower for a MEM-ECL than for a DFB or DBR laser. Mechanical vibrations broaden the observed time-averaged linewidth, and a homodyne measurement with a 25 μ s delay gave a time-averaged 3 dB linewidth of 2 MHz.

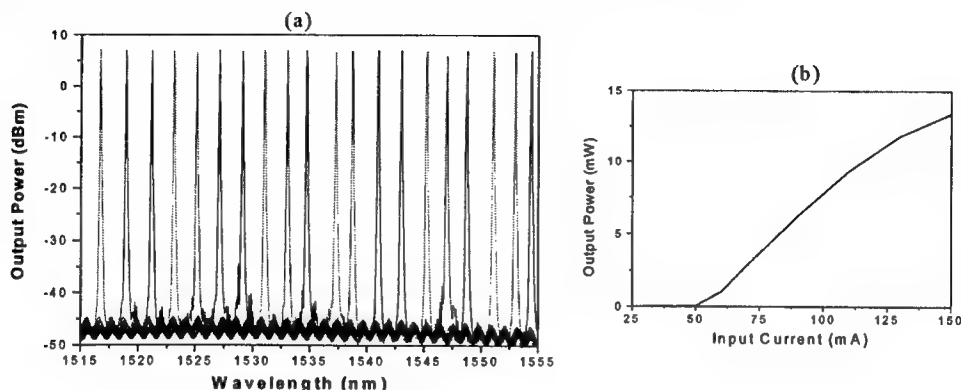


Fig. 2. (a) MEM-ECL lasing spectra exhibiting 40 nm tuning range, +7 dBm fiber coupled output power, and > 50 dB side mode suppression ratio. (b) L-I curve demonstrating 14 mW free-space output power.

Changing the actuator voltage tunes the laser, and an accuracy of 100 pm can be obtained with open-loop control. DWDM systems with 50 GHz channel spacings typically require a wavelength accuracy of 20 pm, which is achieved by sending a portion of the output signal to an etalon wavelength locker and using the error signal to make fine adjustments to the mirror position. Without servo control, temperature variations caused the laser wavelength to vary over 100 pm. With the servo enabled, the wavelength is stabilized to within 10 pm. The time to tune between any two channels is less than 15 ms.

In summary, the DRIE-MEMS actuators have enabled a small form factor, low cost tunable laser source ideal for many DWDM applications. The performance of the MEM-ECL meets telecommunications requirements for optical power, side mode suppression, polarization extinction ratio, relative intensity noise, and linewidth. The required wavelength accuracy of 2.5 GHz has been demonstrated using simple closed loop control of the MEMS actuator voltage.

References

1. Jin Hong, Hyung Kim, and Toshi Makino, "Enhanced wavelength tuning range in two-section complex-coupled DFB lasers by alternating gain and loss coupling," *IEEE J. Light. Tech.* **16**, 1323-1328 (1998).
2. B. Mason, G.A. Fish, S.P. DenBaars, and L.A. Coldren, "Widely tunable sampled grating DBR laser with integrated electroabsorption modulator," *Photon. Tech. Lett.* **11**, 638-640 (1999).
3. D. Vakhshoori, P. Tayebati, Chih-Cheng Lu, M. Azimi, P. Wang, Jiang-Huai Zhou and E. Canoglu, "2 mW CW single mode operation of a tunable 1550 nm vertical cavity surface emitting laser with 50 nm tuning range," *Electron. Lett.* **35**, 1-2 (1999).
4. T. Day, F. Luecke, and M. Brownell, "Continuously tunable diode lasers," *Lasers and Optonics*, (June 1993).
5. P. Zorabedian, "Tunable External Cavity Semiconductor Lasers," in "Tunable Laser Handbook," (F.J. Duarte Ed.), Academic Press, San Diego, 1995.
6. M. Littman and H. Metcalf, "Spectrally narrow pulsed dye laser without beam expander," *Appl. Opt.* **17**, 2224-2227 (1978).
7. K. Liu and M. Littman, "Novel geometry for single-mode scanning of tunable lasers," *Opt. Lett.* **6**, 117-118 (1981).
8. J.D. Grade, H. Jerman, and T.W. Kenny, "A large-deflection electrostatic actuator for optical switching applications," *Technical Digest 2000 Solid State Sensor and Actuator Workshop*, Hilton Head, SC, June 2000, pp. 97-100.

Wavelength Selectable Microarray Light Sources

Tatsuya Sasaki and Koji Kudo
Photonic and Wireless Devices Research Laboratories, NEC Corporation
2-9-1, Seiran, Ohtsu, Shiga 520-0833, Japan
e-mail: t-sasaki@dn.jp.nec.com

1. Introduction

The rapid increase in the transmission capacity of dense wavelength division multiplexing (DWDM) optical communication systems requires advanced wavelength tunable or selectable light sources. Wavelength selectable light sources (WSLs) will be key components because they offer a cost-effective solution to the problem of supplying stand-by sources for restoring failed channels. They are also attractive for use in reconfigurable all-optical networking systems. WSLs for these applications should have not only fine wavelength selectability and tunability, but also at least comparable characteristics to conventional single-wavelength transmitters. Their optical output power should therefore be high, they should be stable single-mode devices, and their wavelengths should be reliable. Because cost is also an important issue, it should be possible to make these WSLs by using a simple process. And testing and packaging costs can also be kept low if these devices use a simple tuning scheme.

A DFB-LD array-based WSL is promising because wavelengths it provides are stable and reliable. A desired wavelength is selected simply by injecting current into one of the DFB-LDs and using a thermo-electric cooler to control device temperature. Also advantageous are the high side mode suppression ratio (SMSR) and low spectral linewidth of DFB-LDs. Disadvantageous, however, are that so far they have needed to contain an optical combiner and a semiconductor optical amplifier (SOA), and this complicates the fabrication process and increases chip size.

DFB-LD array-based WSLs with practical solutions to these problems have been reported recently [1-5]. They contain four to eight DFB-LDs provide wavelengths tunable from 8 to 22nm. Sophisticated fabrication processes and reduced chip size are very promising for cost reduction. In this paper, recent demonstrations of our WSLs are presented.

2. Design and Fabrication

The device structure of a WSL as a CW light source is shown schematically in Figure 1 [5]. The device consists of four $\lambda/4$ -shifted DFB-LDs, one 4x1 MMI optical combiner and a SOA. Our approach to reducing chip size is to array the LDs densely. With a LDs spacing of only $10\ \mu\text{m}$, this "microarray" structure reduces the length of the MMI combiner without requiring the use of access bent waveguides. Consequently, the device is only 2mm long and 0.4mm wide.

Device fabrication process is also strongly related to device yield and cost. Active layers of the DFB-LD array and the SOA should be connected to a core layer of the MMI waveguide with sufficiently low optical reflection. We do this by using selective epitaxial growth so that these active and passive layers can be grown in a single step. Waveguides smoothly connected at the joints also help eliminate optical reflectivity. In growing the active layers for this microarray DFB-LD, we use a novel microarray selective epitaxy (MASE) technique which enables densely arrayed active waveguide stripes to be formed simultaneously without etching the semiconductor layers [1].

Since each gain peak wavelength of the active layer can also be controlled by using this selective growth technique, the entire C-band can be covered by a few WSLs fabricated simultaneously on a one

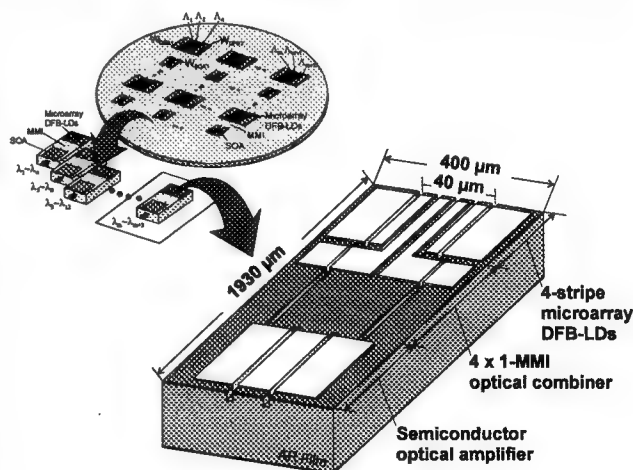


Fig.1 WSL structure

wafer. We designed to cover the entire C-band, from 1530.334nm to 1561.826nm, by five WSLs (C1~C5), each covered eight 100GHz-spaced ITU-T grids. The lasing wavelengths of neighboring DFB-LDs were designed to have an overlap of approximately 0.4nm, and ranges of neighboring WSLs were designed to have an overlap of approximately 2.5nm.

Gratings with different pitches were first formed by EB lithography on a n-InP substrate, then a SiO₂ mask pattern for selective growth was formed on the substrate, and the active and passive MQW waveguide layers were selectively grown by atmospheric-pressure MOVPE. The grating pitch of each DFB-LD was determined from the assigned lasing wavelength and estimated effective refractive index. Gain-peak wavelengths of the DFB-LD array and the SOA for each WSLs were also adjusted to the desirable range after investigation of growth simulation [6]. After the active and passive waveguide layers were grown, current-blocking layers and a p-InP cladding layer were grown to form a conventional BH structure in the DFB-LD and SOA regions. Each DFB-LD in the array was electrically isolated by trenches formed using inductively-coupled plasma etching. The number of growth steps can be reduced from three to two by instead using only a p-InP overcladding layer to cover the MQW layer. A ridge waveguide structure was formed in the MMI combiner region. After the growth, electrodes were formed and facets were coated with anti-reflection films. We also form a window structure at both the facets, and the optical reflectivity was estimated to less than 0.04%.

3. Characteristics

The controllability of the bandgap energy of the MQWs simultaneously grown on the five WSLs was investigated by comparing photoluminescence (PL) peak wavelengths and lasing wavelengths, and the difference between them was sufficiently less than 10nm. We confirmed uniform threshold currents of 8.3 ± 1.2 mA at 25°C, which resulted from fine gain-peak wavelength control made possible by the selective growth technique. Figure 2 shows superposed lasing spectra for five WSLs enabling precise tuning to 32 ITU-T grids with 100GHz spacing. Thus the entire C-band was covered with five devices. In the measurements, device temperature was varied between 15 and 40°C. Stable single-mode operation with a SMSR greater than 45dB was obtained. Fiber-coupled power between 8 and 15mW were obtained between 15 and 40°C when the DFB injection current was 75mA. The fiber coupling loss was typically around 4.4dB. The fiber output power will be improved by optimizing the device structure.

4. Conclusions

The DFB-LD array-based WSL is a very promising for DWDM applications because of its fine wavelength tunability and stability and its simple tuning scheme. And the advanced simple fabrication process used to produce this device is an effective one. Further optimizations of device structure make this type of device a practical light source for DWDM transmission systems.

Acknowledgements

We thank K. Yashiki, T. Morimoto, S. Sudo, Y. Hisanaga, Y. Muroya, T. Tamanuki and H. Hatakeyama for their cooperations in this work. We also thank K. Mori, M. Yamaguchi, T. Torikai, K. Kobayashi, M. Fujiwara, and T. Uji for fruitful discussions and support.

References

- [1] K. Kudo et al., IEEE J. of Sel. Topics in Quantum Electron., Vol. 5, pp. 428, 1999.
- [2] M. Bouda et al., Proc. OFC'2000, paper TuL1, 2000.
- [3] B. Pezeshki et al., Electron. Lett., Vol.36, pp.788, 2000.
- [4] K. Yashiki et al., Proc. ECOC'2000, paper 6.3.2, 2000.
- [5] K. Kudo et al., Proc. OFC'2001, paper TuB4, 2001.
- [6] S. Sudo et al., J. Crystal Growth, Vol.221, pp. 189, 2000.

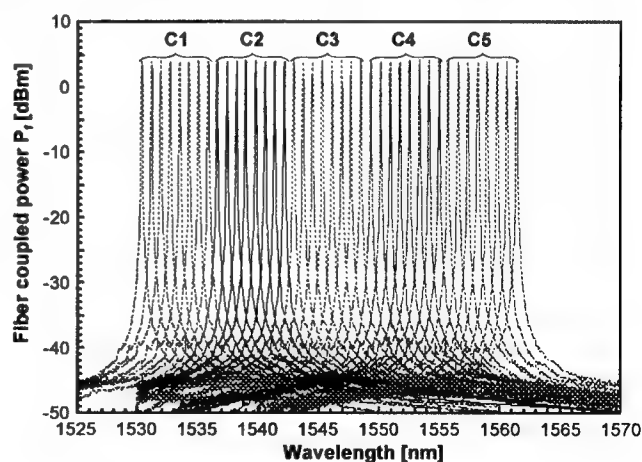


Fig.2 Superposed lasing spectra obtained from five WSLs

Advanced Semiconductor Lasers and Applications

Wednesday, 1 August 2001

WA1: Communication Lasers

High Speed Uncooled Spot-Size-Converted Distributed Feedback Lasers Suitable for Passive Alignment and 2.5 Gb/s Operation at 85C

D. Klotzkin, S. Ustin, N. Gleason, M. Chien, E. Michel, S. Roycroft, P. Kiely, K. Kojima, L. Ketelsen
Agere Systems, Optoelectronics, 9999 Hamilton Boulevard, Breinigsville, PA 18031-9359
 Corresponding Author: klotzkin@agere.com, 1-484-397-3219 (Tel), 1-484-397-2236 (Fax.)

The trend in the optoelectronics industry is towards integrating more functionality into smaller packages. Multi-gigabit transponder and transceiver modules that accept many low-speed data inputs and perform the packet encoding and decoding are being offered by different vendors. A packaged solution that incorporates the multiplexing and demultiplexing electronics, and lasers and receivers, is an attractive, low-cost way for systems vendors to develop high-speed systems.

The development of these integrated systems is also motivating the development of new laser technology^{1,2}. In a complete packaged transceiver or transponder, it is highly desirable to include the laser as a bare chip passively coupled to the fiber, rather than as a separately packaged pigtailed laser device. This eliminates additional packaging costs, eliminates alignment time, removes the bulky lenses and optics, and removes many of the high speed limitations associated with the laser package. This unpackaged laser must be designed to have a small far-field angle in order to be able to couple a large fraction of the emitted light and still have performance equivalent to standard high-performance buried heterostructure (BH) devices. Lasers with narrow far-fields are also highly desirable in a completely passive alignment scheme because they have relaxed alignment tolerances to the fiber compared with standard devices. These transponder/transceiver modules with high power densities are designed to operate uncooled, requiring the laser to have good high temperature performance and excellent aging characteristics.

High speed, uncooled, error-free transmission has already been demonstrated with spot-size-converted (SSC) Fabry-Perot lasers³. In this work, we demonstrate spot-size-converted distributed feedback lasers (DFB) lasers with narrow far fields capable of high coupling efficiency directly into flat cleaved fiber. We also report, to our knowledge for the first time, 2.5Gb/s transmission at 85C using a DFB-SSC device.

Fig. 1 shows the basic design of the SSC device. The active region consists of a strained multiquantum-well (MQW) InGaAsP standard BH laser operating at 1.3 μ m. The expander section consists of a quaternary InGaAsP waveguide surrounded by an InP cladding. By careful design, the degradation in the active laser performance due to the presence of the expander is minimized, and the DC laser properties are comparable to standard BH lasers. The waveguide extends under the active region of the device, and the mode transfer of the light from the active quantum wells to the underlying waveguide is accomplished through a lateral taper etch removal of the active MQWs⁴. The underlying waveguide layer is grown with selective area growth (SAG), in order to get a thick waveguide at the mode transition region while maintaining a thin waveguide at the expander facet to achieve a large spot size. The device includes a holographically fabricated grating underneath the coupling waveguide. The thickness and composition of the grating layer are chosen for high coupling ($\kappa L \sim 1$) despite the distance from active region.

The SSC wafers are grown using metal organic chemical vapor deposition and fabricated using standard metallization and wet and dry etching techniques. The devices are then separated into bars, HR/AR coated, and then mounted into fixtures suitable for high-speed and high-temperature testing.

At room temperature, the slope efficiency is about 0.37 W/A with a threshold of 7-9mA, with slope efficiency of about 0.20W/A and thresholds of 40-45mA at 85C (Fig. 2). The side mode suppression ratios is typically >40dB at 25C. Typical full-width-half-maximum far fields of the emitted light of 8-10 X 13-16 degrees are obtained (Fig. 3). These far fields enable coupling as much as 50% of the light directly into flat cleaved fiber, and typical median coupling efficiencies of about 16% are obtained using completely passive alignment of the laser to a fiber in a V-groove on a Si submount.

At 85C, 2.5Gb/s transmission was demonstrated with dispersion penalty of 0 to 0.2dB over 14km of standard single mode fiber, with no error floor down to 10⁻¹² error rates. Figure 4 shows the eye pattern taken at 85C at a bias current of about 20mA above threshold and a 10dB extinction ratio, filtered by the standard OC48 filter. The eye is wide open and shows no mask test failures in 1000 waveforms. Figure 5 shows the small-signal modulation bandwidth of the device demonstrating bandwidths of >10GHz and D-factors of 1.7GHz/mA^{1/2} at room temperature. Bandwidths at 85C were 7-8GHz. Aging characteristics of this device are also similar to our standard BH device, with median aging rates of 2%/khr at 85C and FIT rates of 15 at 50C over a ten year life, using a standard failure criteria of 50% increase in driving current for a 10mW output.

Despite the tradeoffs inherent in including an expander, a spot-size converted DFB laser has been developed which can be used for uncooled, high-speed operation of 2.5 Gb/s at 85C. The expanded beam was demonstrated with both F-P and DFB devices. The development of these spot size converted devices is an important enabling technology for integrated module systems.

[1] M. Kito, et. al, *IEEE JQE*, vol. 35, pp.1765-1770, Dec. 1999.

[2] Y. Okunuki, et. al, Technical Digest of *Optical Fiber Conference 2000*, WM26-3, March 2000.

[3] D. Klotzkin, et. al, *IEDM Technical Digest*, 24.3.1, December 2000.

[4] J. Johnson, et. al., *IEEE JSTQE*, vol. 6, pp.19-25, Jan. 2000.

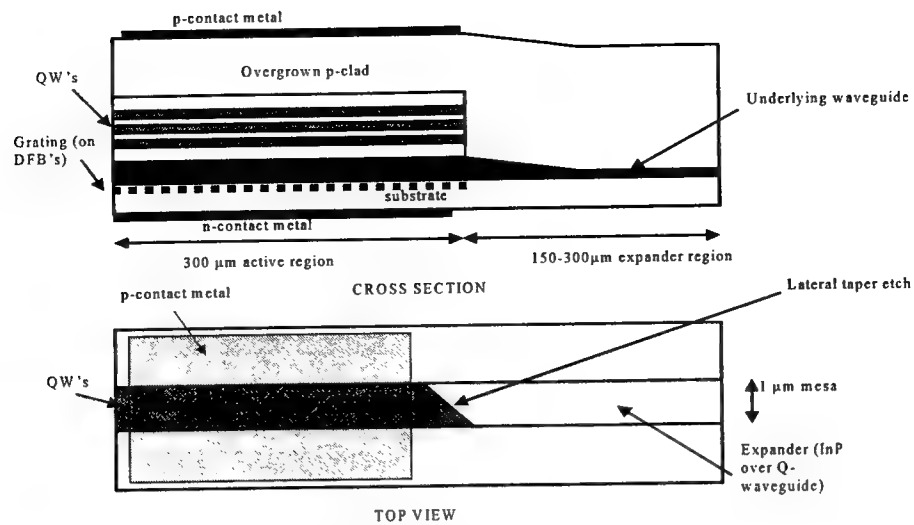


Fig 1: Diagram of SSC Fabry-Perot and distributed feedback laser device structure.

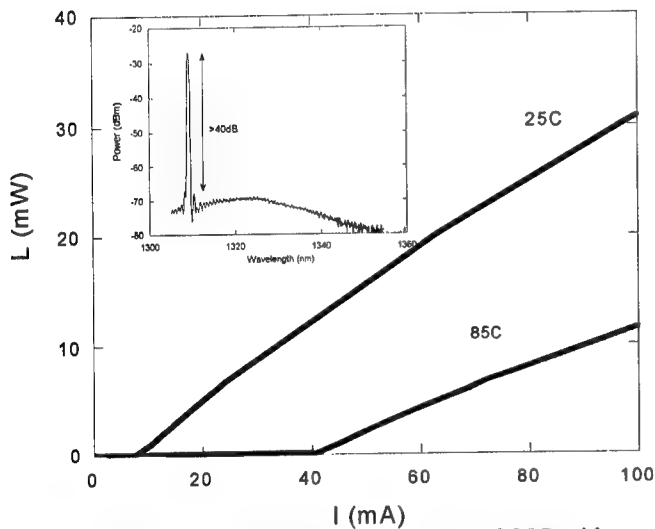


Figure 2: L-I of SSC-DFB at 25C and 85C with a spectral inset

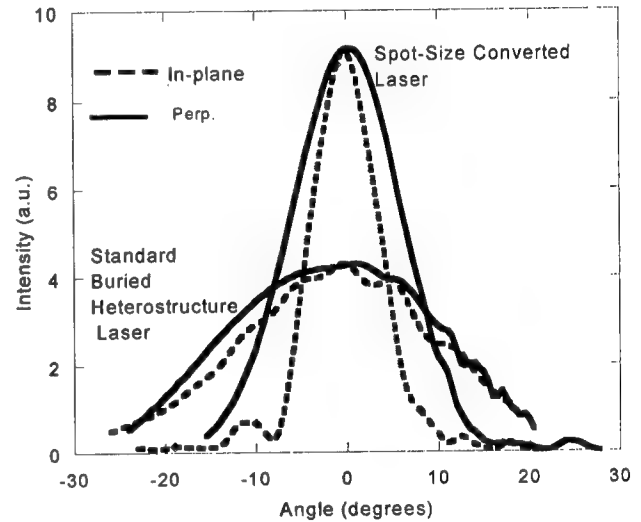


Figure 3: Far field of SSC laser with, for comparison, far fields of standard BH lasers

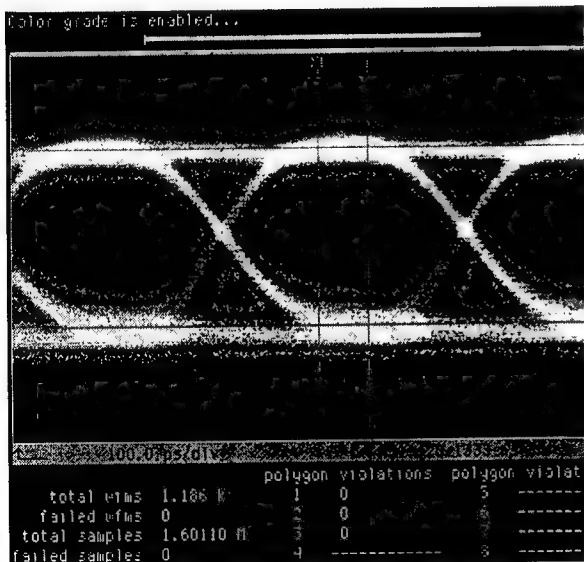


Fig 4: Filtered eye pattern of SSC-DFB at 85C at a 10dB extinction ratio

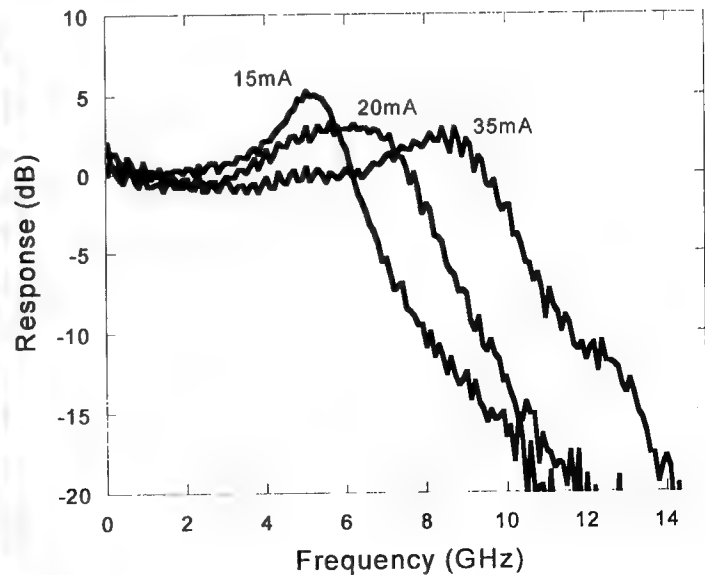


Fig 5: Bandwidth of SSC-DFB at 25C showing >10GHz BWs

VCSEL Modulation at 20Gb/s over 200m of Multimode Fiber using a 3.3v SiGe Laser Driver IC

Daniel M. Kuchta, Petar Pepeljugoski, and Young Kwark

IBM T. J. Watson Research Center

P. O. Box 218

Yorktown Heights NY 10598

kuchta@us.ibm.com

The data communications industry has developed optical link standards options for 10 Gbit/s using VCSEL based transmitters, and the next step is cost effective 40 Gbit/s links. Parallel link options [1] have been proposed, but the 10 Gbit/s link experience has taught that if serial links can be made they will be most cost effective, and being closer to serial is better than being slower and wider. This raises the question of achieving 40Gb/s using two VCSELs at 20Gb/s each as a possible cost effective solution. Numerous groups have demonstrated large signal modulation of VCSELs up to 12.5Gb/s (i.e. [2], [3]) and up to 15.6Gb/s [4]. This paper reports on experiments driving VCSEL based optical links to 20Gb/s which is the fastest known VCSEL link driven by 3 volt IC's and operating over premises length multimode fiber.

The VCSEL used in this experiment is an oxide confined device with an 8 μ m oxide aperture. The device is fabricated on a semi-insulating substrate with two planar topside contacts. At room temperature the threshold current is 0.3mA and the slope efficiency is 0.29mW/mA. Thermal rollover begins at 6.2mA due to the high thermal impedance of 1700 K/W. The maximum cw optical power is 1.3 mW. The series resistance in the range of operation is 145 Ohms. The device is primarily single mode at 843nm although three side modes exist at -10, -11 and -18dB down respectively under cw and ac conditions. Figure 1 is a plot of the small signal response as a function of bias. At 6.2mA the -3dB frequency is 15.4GHz. The modulation efficiency is 13.7 GHz/root(mW) up to 1.2mA(10GHz) and then begins to saturate. The device is directly connected to a driver IC through two short (500 μ m) wirebonds. The VCSEL driver is implemented in a 0.5 μ m 50GHz f_T SiGe bipolar technology. The driver utilizes fully differential circuits including an on-chip AC coupling network to the VCSEL load. DC bias control is also provided on the driver thereby eliminating the need for any external passives between the driver and VCSEL. This permits the use of an unterminated network between the two parts since the lack of any off-chip passives allows for very small physical separations. The total power dissipation running at 20Gb/s is typically 180mW at 3.3v. To optimize the circuit design, a rate equation based model of the VCSEL including an impedance model similar to [5] implemented in spice was used.

Figure 2 shows the back to back optical eye diagram from the VCSEL (top trace) and the electrical signal that is fed to the driver IC (bottom trace). The deterministic jitter (DJ) of the source is 9.5ps, the rise and fall times (20-80) are 20 ps (undeconvolved from 13ps oscilloscope 10-90 risetime) and the intersymbol interference (ISI) is 0.93dB. At 2m, the DJ from the VCSEL is 15.5ps and the ISI is 2.64dB. Some eye closure (ISI) is expected from the VCSEL as the 15GHz bandwidth of the device attenuates much of the high frequency part of the driving signal. Figure 3 shows the averaged eye diagram at 200m. The additional accumulated ISI over 200m is only 1dB and the final DJ is 20.2 ps. The properties of this fiber are described in [4].

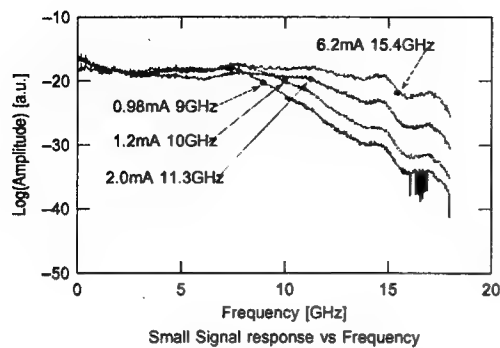


Figure 1. VCSEL small signal response vs. bias

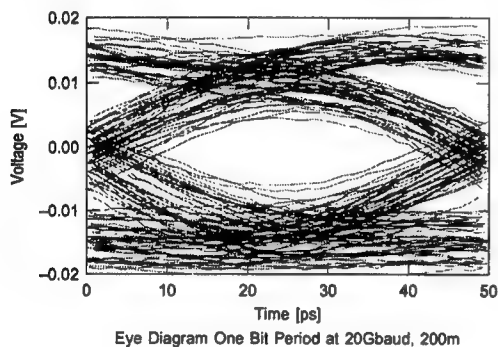


Figure 3. Averaged eye diagram after 200m of 50/125 multimode fiber

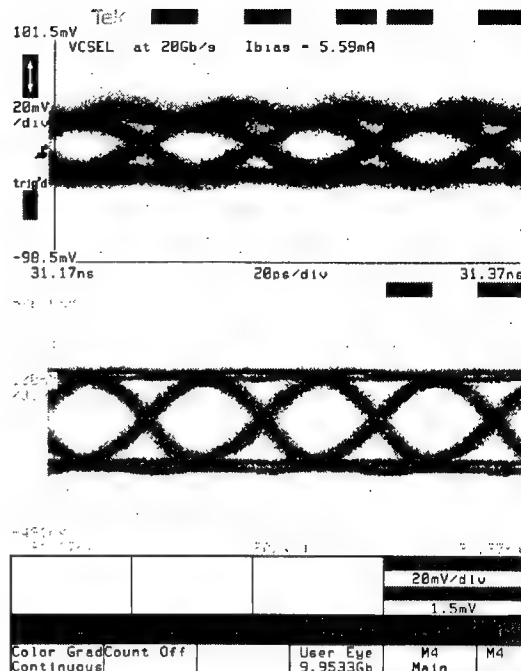


Figure 2. (top)VCSEL eye diagram at 20Gb/s , (bottom) Electrical input waveform

- [1] R. Michalzik, G. Giaretta, K. W. Goossen, J. A. Walker, and M.C. Nuss, "40Gb/s Coarse WDM Data Transmission with 825nm Wavelength VCSELs over 310m of High Performance Multimode Fiber" *26th European Conference on Optical Communication (ECOC 2000)* vol. IV, pp. 33.
- [2] M. Kicherer, R. Jager, R. King, F. Mederer, H. J. Unold, and K. J. Ebeling, "Single- and Multi-Mode VCSELs for 12.5Gb/s Data Links", in *Lasers and Electro-Optics Europe, 2000 Conference Digest paper CTuG2*.
- [3] M. Webster, R. V. Penty, I. H. White, M. R. T. Tan, and S. W. Corzine, "Performance of 10Gbit/s VCSELs operating at 85C," in *Conference on Lasers and Electro-Optics (CLEO) 2000*, pp.201-202.
- [4] P. Pepeljugoski, D. Kuchta, Y. Kwark, P. Pleunis, and G. Kuyt, "15.6Gb/s Transmission over 1km of Next Generation Multimode Fiber", Submitted to ECOC 2001.
- [5] K.L Lear, M. Ochiali, V. M. Hietala, H. Q. Hou, B. E. Hammons, J. J. Banas, and J. A. Nevers, "High-speed vertical cavity surface emitting lasers," in *1997 Tech. dig. IEEE/LEOS Summer Topical Meetings: Vertical Cavity Lasers, 1997*, pp. 53-54.

Single Mode, Low Impedance 850-nm VCSELs with Integrated Mode Filters.

E. M. Strzelecka, R. A. Walterson, E. L. Kalweit, T. M. Marta, T. Wang*, and J. A. Cox
VCSEL Products Division, Honeywell, 12001 State Highway #55, Plymouth, MN 55441

*Corresponding author

Single mode VCSELs with a few milliwatts of output power will find use in data storage, data communication, sensor, and spectroscopy applications. Typically, small diameter single mode VCSELs (i.e., 2 to 3 microns diameter oxide confined devices), have a maximum output power limited to approximately 2 mW. Such devices also have a large series resistance. Larger-diameter VCSELs have lower resistances, but typically support multiple transverse modes. Many techniques have been investigated to prevent higher order modes from lasing. These techniques include metal spatial filters¹, e-beam etched features in the top surface², antiguided structures³, extended⁴ or external cavities⁵, combinations of implant and oxide apertures⁶, etc.

We present very simple implementations of mode filters that allow single mode operation of oxide-confined VCSELs with diameters 6 to 15 μm . One implementation favored the fundamental mode by introducing mode selective reflectivity. The output mirror stack was terminated with an additional dielectric mirror pair ($\text{SiO}_2/\text{Si}_3\text{N}_4$) in the center and with a quarter-wave dielectric (Si_3N_4) in the outer region of the device. This mode filter was made by standard lithography and a selective etch. The second implementation favored the fundamental mode by introducing mode selective gain. While the oxide aperture defined the mode diameter, an additional current aperture provided gain to the center of the device only. This mode filter was made by standard lithography and a deep proton implant.

In the study, we varied the mode filter diameter from well inside the oxide aperture to slightly outside the oxide aperture. Fig. 1 shows a series of 10-micron-diameter oxide devices, with the dielectric mode filters. The threshold increased and the power decreased with decreasing mode filter diameter. The smaller mode filters provided excellent suppression of higher order transverse modes, > 30dB. Devices with mode filters < 6.5 μm , were single mode and single polarization over their entire operating range. Larger mode filters suppressed the onset of higher order modes in a limited current range above threshold. The largest mode filters, >9 μm , did not provide significant mode suppression. The optimum mode filter diameter coincided with the $1/e^2$ diameter of the mode ($\sim 6.5 \mu\text{m}$). VCSELs with optical power of 3.2 mW and a series resistance of 50 Ω were demonstrated (12.5 μm oxide and 6.5 μm mode filter diameter).

We made 2xN arrays of VCSELs with mode filters to verify that the process is uniform and robust enough for manufacturing. The process introduced one critical lithography step (alignment of the mode filter) and one non-critical step (via etch). The uniformity of an array with a 6- μm oxide and 3.8- μm mode filter diameter is illustrated in Fig. 2.

The increased threshold current with the mode filter is in part due to a scattering loss introduced at the edge of the dielectric disc. A smooth transition (sloped dielectric etch) would reduce this effect. The single mode power in the dielectric mode filter design was limited to little over 3 mW, practically regardless of the diameter of the oxide aperture. The limited single mode power is attributed in part to nonuniform current injection at higher bias, when most of the current flows in the perimeter of the device and where the fundamental mode is diminished. In Fig. 3, the far field and spectral characteristics of two 12.5-micron-diameter oxide VCSELs driven at 15 mA (near rollover) are shown. One of them does not have a mode filter and lases in a high order mode with no light in the center. A similar device with a mode filter has a dramatically different far field, with a single central lobe and a divergence of 9.2°.

With a separate current aperture in our gain selective mode filter design, the fundamental mode was pumped more efficiently, while the higher order modes were suppressed due to absorption in the unpumped portion of the quantum wells. With this design, we achieved 4.3 mW of single mode power from a VCSEL with a 12.5- μm oxide 6.5- μm gain diameter. The series resistance was 140 Ω .

In conclusion, we have demonstrated single mode operation of large diameter oxide-confined VCSELs using simple and manufacturable fabrication techniques.

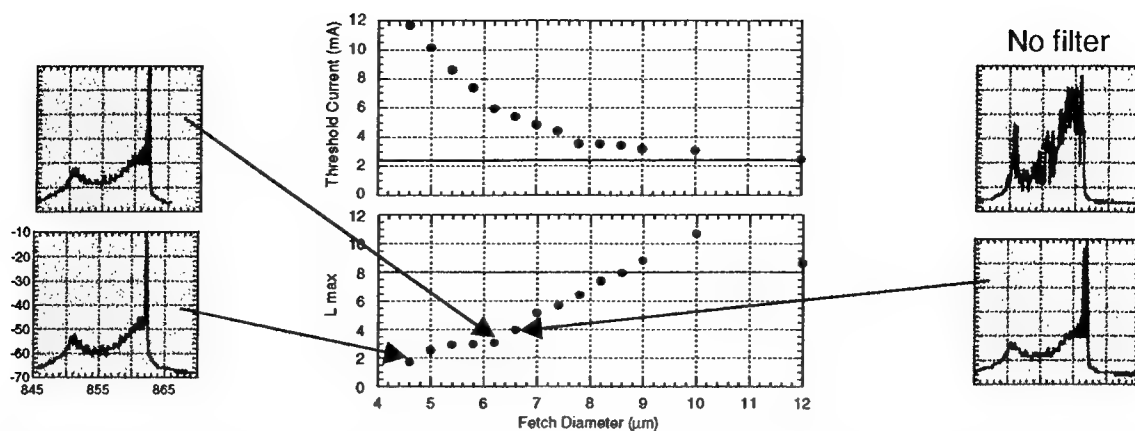


Fig. 1. Threshold current and maximum output power as a function of mode filter diameter for a 10-micron oxide aperture device. Spectra taken at 16 mW (near rollover) are shown on a log scale (10 dB/div) vs. wavelength in nm (5 nm/div). Devices with filter etch (fetch) diameter $< 6.5 \mu\text{m}$ were single mode and single polarization.

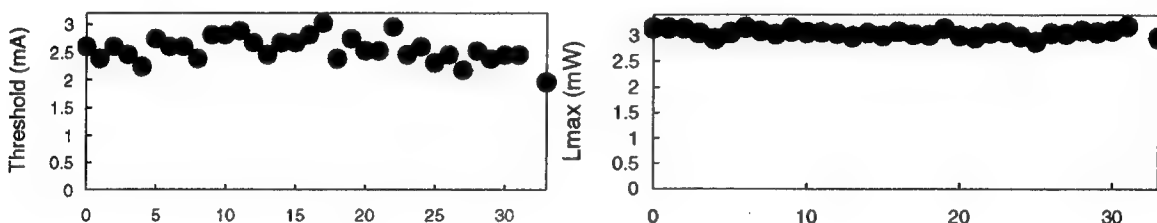


Fig. 2. Uniformity of threshold current and maximum output power of a 2x34 array of single mode lasers on a 75-micron pitch plotted vs. device number. The devices had a 6.5- μm oxide and a 3.8- μm diameter dielectric filter. They were all single mode and linearly polarized.

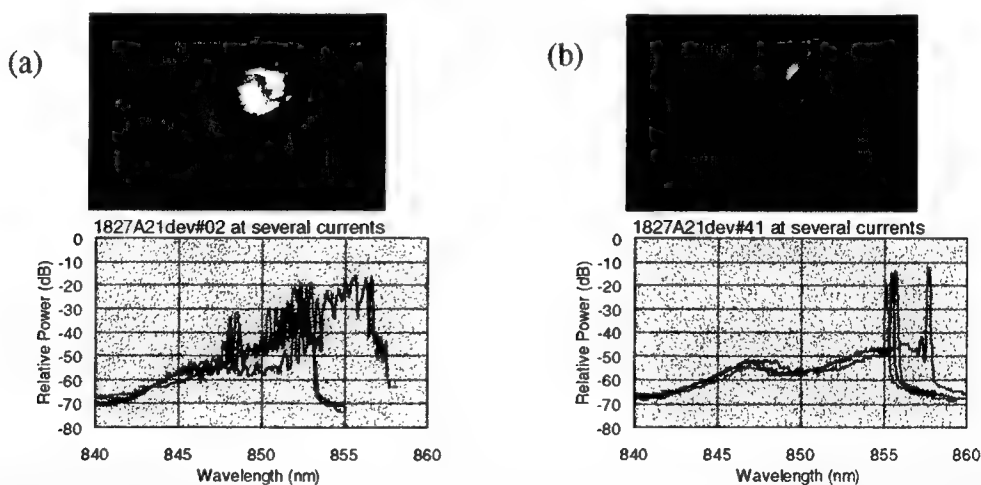


Fig. 3. Far fields and spectra of two 12.5-micron oxide aperture devices driven at 15 mA (near maximum power), (a) without a mode filter, (b) with a mode filter. The red-most shifted spectra are near maximum (15mA).

REFERENCES

1. R. A. Morgan, et al., *IEEE Photon. Technol. Lett.*, 4 (4), 374-377 (1993)
2. H. Martinsson, et al., *IEEE Photon. Technol. Lett.*, 11 (12), 1536-1538 (1999)
3. K. D. Choquette, et al., paper CTuL6, CLEO, San Francisco, CA (2000)
4. H. J. Unold, et al., *Electron. Lett.*, 37, (3)178-179 (2001).
5. M. A. Holm, et al., *IEEE Photon. Technol. Lett.*, 11 (12), 1551-1553 (1999)
6. T.-H. Oh, et al., *IEEE Photon. Technol. Lett.*, 10 (8), 1064-1066 (1999)

AUTHOR INDEX

Ackerman, D.	TuA2.3	Kitching, J.	MA1.3
Affolderback, C.	MA1.3	Klotzkin, D.	WA1.1
Anan, T.	MA2.2	Knappe, S.	MA1.3
Anthon, D.	TuA3.2	Knopp, K.	TuA1.3
Asous, W.	TuA2.3	Koch, T.	TuA2.3
Azimi, M.	TuA1.3	Kojima, K.	WA1.1
Baliga, A.	TuA1.3	Kuchta, D.	WA1.2
Baorui, R.	TuA1.3	Kudo, K.	TuA3.3
Barton, J.	TuA2.1	Kurihara, K.	MA2.2
Berger, J.	TuA3.2	Kwark, Y.	WA1.2
Bergerengen, J.	TuA2.2	Ledentsov, N.	MA2.3
Bimberg, D.	MA2.3	Lee, H.	TuA3.2
Broberg, B.	TuA2.2	Lee, H.	MA1.5
Bylsma, R.	TuA2.3	Lentz, C.	TuA2.3
Chang-Hasnain, C.	TuA1.2	Letsch, M.	TuA1.3
Chen, P.	TuA1.3	Li, G.	TuA1.2
Chien, M.	WA1.1	Liu, J.	TuA1.3
Coldren, L.	MA2.1	Lott, J.	MA2.3
Coldren, L.	TuA2.1	Lu, C.-C.	TuA1.3
Cox, J.	WA1.3	MacDaniel, D.	TuA1.3
Davis, D.	TuA1.2	Marta, T.	WA1.3
Day, T.	TuA3.1	Massara, A.	MA1.4
Dean, E.	TuA2.3	Matsui, Y.	TuA1.3
DeLargy, B.	TuA1.3	Mayer, P.	MA1.6
Fan, F.	TuA1.3	McCallion, K.	TuA1.3
Fennema, A.	TuA3.2	Michel, E.	WA1.1
Fish, G.	TuA2.1	Murray, C.	MA3.2
Fox, R.	MA1.2	Nabiev, R.	TuA1.2
Freund, J.	TuA2.3	Nakagawa, S.	MA2.1
Geary, J.	TuA2.3	Newman, F.	MA3.2
Gioannini, M.	MA1.4	Nishi, K.	MA2.2
Gleason, N.	WA1.1	Paldus, B.	MA1.1
Glogovsky, K.	TuA2.3	Penty, R.	MA1.4
Grade, J.	TuA3.2	Pepeljugin, P.	WA1.2
Gurjar, R.	TuA1.3	Pinzone, C.	TuA1.3
Gustafsson, Y.	TuA2.2	Ram, R.	MA1.5, MA1.6
Hall, E.	MA2.1	Rana, F.	MA1.6
Harris, J.	MA3.3	Reynolds, C.	TuA2.3
Hill, M.	MA1.4	Roycroft, S.	WA1.1
Hollberg, L.	MA1.2, MA1.3	Sakhitab, F.	TuA1.3
Holmstrom, R.	TuA1.1	Sarlet, G.	TuA2.2
Hrinya, S.	TuA3.2	Sasaki, T.	TuA3.3
Huang, R.	TuA1.3	Staehler, M.	MA1.3
Hybertsen, M.	TuA2.3	Strzelecka, E.	WA1.3
Jansen, M.	TuA1.2	Sugou, S.	MA2.2
Jean, A.	TuA1.3	Szabo, P.	TuA2.2
Jenkins, D.	TuA1.1	Tayebati, P.	TuA1.3
Jerman, H.	TuA3.2	Tokutome, K.	MA2.2
Jiang, M.	TuA1.3	Tselikov, A.	TuA3.2
Johnson, B.	TuA1.3	Ustin, S.	WA1.1
Johnson, J.	TuA2.3	Ustinov, V.	MA2.3
Kalweit, E.	WA1.3	Vakhshoori, D.	TuA1.3
Kamei, A.	MA2.2	VanderRhodes, G.	TuA1.3
Karim, A.	MA3.1	Walters, F.	TuA2.3
Ketelsen, L.	TuA2.3, WA1.1	Walterson, R.	WA1.3
Kiely, P.	WA1.1	Wang, P.	TuA1.3

Wang, T.-Y.	WA1.3	Yamada, M.	MA2.2
Waterson, R.	TuA1.3	Yuen, W.	TuA1.2
Wesstrom, J.-O.	TuA2.2	Zhang, Y.	TuA3.2
White, I.	MA1.4	Zhou, J.	TuA1.3
Wynands, R.	MA1.3	Zhu, H.	TuA1.3
Xin, H.	MA3.2		

**2001 IEEE/LEOS
Summer Topical Meeting**

30 July – 1 August 2001

**Ultraviolet and Blue Lasers
and their Applications**

**Copper Mountain Resort
Copper Mountain, CO**

IEEE Catalog Number: 01TH8572

ISBN: 0-7803-7100-3

ISSN: 1099-4742

The papers in this book comprise the digest of the meeting mentioned on the cover and title page. They reflect the authors' opinions and are published as presented and without change in the interest of timely dissemination. Their inclusion in this publication does not necessarily constitute endorsement by the editors, the Institute of Electrical and Electronics Engineers, Inc.

© 2001 by the Institute of Electrical and Electronics Engineers, Inc. All rights reserved.

Copyright and Reprint Permissions: Abstracting is permitted with credit to the source. Libraries are permitted to photocopy beyond the limits of U.S. copyright law, for private use of patrons those articles in this volume that carry a code at the bottom of the first page, provided the per-copy fee indicated in the code is paid through the Copyright Clearance Center, 222 Rosewood Drive, Danvers, MA 01923. For other copying, reprint, or republication permission, write to IEEE Copyrights Manager, IEEE Service Center, 445 Hoes Lane, P.O. Box 1331, Piscataway, NJ 08855-1331.

IEEE Catalog Number:	01TH8572
ISBN:	0-7803-7100-3
ISSN:	1099-4742



Ultraviolet and Blue Lasers and their Applications

Co-Chairs:

J. Gary Eden, *University of Illinois, Urbana, IL*
Gregory Quarles, *VLOC Incorporated, New Port Richey, FL*
Richard Scheps, *SPAWAR Systems Center, San Diego, CA*

Technical Program Committee:

A. Petersen, *Spectra Physics Lasers, Inc, Mountain View, CA*
J. Rocca, *Colorado State University, Fort Collins, CO*
K. Schaffers, *Lawrence Livermore National Laboratory, Livermore, CA*

TABLE OF CONTENTS

Monday, 30 July 2001

MB1.	Advances in Short Wavelength Sources & Optics I	
MB1.1	Spatially Coherent Tabletop Soft-X-Ray Laser Sources with Milliwatt Average Power	3
MB1.2	Phase Matching Techniques in the UV - EUV	5
MB2.	Advances in Short Wavelength Sources & Optics II	
MB2.1	Advances in the Generation of High Order Harmonics using Few-Optical-Cycle Pulses	7
MB2.2	Quantum Electrodynamics Treatment of Optical High Order Harmonic Generation	9
MB2.3	High Reflectivity Optics for the Extreme Ultraviolet and Soft X-Ray Spectral Regions	11
MB3.	Photolithography	
MB3.1	Short Wavelength Sources for Microlithography	13
MB3.2	DUV and VUV Lithography Application of Excimer Laser Systems.....	15
MB4.	Nonlinear Solid State UV Sources	
MB4.1	Development on the Generation of Coherent UV Light from Nonlinear Optical Borate Crystals.....	17
MB4.2	Solid-State 263-nm Laser for Triggering High-Voltage Switches at Sandia's Z-Accelerator	19
MB4.3	Diode Pumped UV Lasers for Electronics Applications.....	N/A

Tuesday, 31 July 2001

TuB1.	Development and Applications of UV and VUV Lasers	
TuB1.1	TBD	N/A
TuB1.2	TBD	N/A
TuB1.3	DUV Lasers applied to Semiconductor Wafer Inspection and Optical Disk Mastering	23
TuB1.4	F ₂ Lasers: Precise Shaping and Trimming of Photonic Components.....	25
TuB1.5	Progress in Dense Plasma Interferometry with Table-Top Soft X-Ray Laser	27

Wednesday, 1 August 2001

WB1.	Visible Solid State Lasers and Amplifiers	
WB1.1	Solid-State Blue Laser Technology	31
WB1.2	Upconversion Green Fiber Amplifier	33
WB2.	Novel Incoherent Sources	
WB2.1	Curing with UV Lamps.....	N/A
WB2.2	Microdischarge Arrays: A New Family of UV Sources	35

Ultraviolet and Blue Lasers and their Applications

Monday, 30 July 2001

- MB1: Advances in Short Wavelength Sources &
Optics I**
- MB2: Advances in Short Wavelength Sources &
Optics II**
- MB3: Photolithography**
- MB4: Nonlinear Solid State UV Sources**

Monday Missing Paper

MB4.3 “Diode Pumped UV Lasers for Electronics Applications”, A. Petersen,
Spectra Physics Lasers, Inc., Mountain View, CA, USA.

Spatially coherent tabletop soft-x-ray laser sources with milliwatt average power

J.J. Rocca, B. Benware, J. Filevich, M. Frati, M.C. Marconi^a, M. Seminario, H.L. Mancini^b, E. Hammersten, E. Jankowska, B. Luther, D. Braley, I.A. Artiukov^c, A. Vinogradov^c, and V.N. Shlyaptsev^d

*Department of Electrical and Computer Engineering, Colorado State University, Fort Collins, CO 80523
Tel: (970)491-8659, Fax: (970) 491-8671, E-mail: rocca@engr.colostate.edu*

Abstract: We summarize the development status of milli-Watt average power tabletop soft x-ray lasers based on fast capillary discharges with essentially full spatial coherence, and give examples of their use in dense plasma interferometry, soft x-ray reflectometry, laser ablation, and plasma generation.

For many years researchers have envisioned the development of compact high repetition rate soft x-ray lasers with high spatial coherence that could be routinely used in numerous applications. With demonstrated average powers of several mW and millijoule-level pulse energy at 46.9nm the Ne-like Ar capillary discharge-pumped laser is the first compact laser to reach this goal [1]. Herein we summarize the development status of tabletop soft x-ray lasers based on capillary discharge excitation, and give examples of their successful use in dense plasma interferometry, soft x-ray reflectometry for the determination of optical constants, characterization of diffraction gratings, laser ablation of materials, and plasma generation. Lasing at 52.9nm line in Ne-like Cl [2], and the prospects for lasing at shorter wavelengths [3] are also discussed.

Table 1 summarizes the output parameters of the Ne-like Ar laser, and Fig. 1 illustrates its size (occupies a table space of 0.4 m × 1 m). Operation of a 34.5 cm long discharge at 4 Hz repetition rate yielded an average laser pulse energy of 0.88 mJ, corresponding to an output power of ~3.5 mW ($> 8 \times 10^{14}$ photons/sec), and a peak power of ~0.6 MW. More than 5000 laser shots were obtained from one capillary. Measurements of the spatial coherence indicate that full spatial coherence is approached with 36 cm long capillaries, and the peak spectral brightness of $\sim 2 \times 10^{25}$ photons/(s mm² mrad² 0.01 % bandwidth) [4] makes it one of the brightest soft x-ray sources available. We have also recently obtained lasing at 52.9 nm (23.4 eV) in the 3p¹S₀-3s¹P₁ transition of Ne-like Cl. Laser pulses with energy up to 10 μJ were measured at repetition rates between 0.5 and 1 Hz [2].

Table 1. Summary of 46.9nm Ne-Like Ar capillary discharge table-top soft X-ray laser parameters

Laser Parameter		Ref.
Pulse Energy	0.88 mJ @ 4Hz	1
Average Pulse Power	3.5 mW	1
Peak Pulse Power	0.6 MW	1
Divergence	~ 4.6 mrad	1
Pulse Width	1.2-1.5 ns	1
Peak Spectral brightness	2×10^{25} photons/(s mm ² mrad ² 0.01 % bandwidth)	4

The laser output characteristics of Table 1 have allowed the use of the Ne-like Ar laser in several applications. It was used in combination with an amplitude-division diffraction grating interferometer to map the electron density evolution of large scale laser-created plasmas. Figs. 2a and b are examples of interferograms without and with plasma present respectively. Measurements for a 1.8 mm long line-focus plasma created by 0.6 J Nd:YAG laser pulses probed electron densities up to 1×10^{20} cm⁻³. Ray tracing computations show that these measurements would be difficult to realize with an UV laser probe due to strong refraction [5]. In a different application we took advantage of the high repetition rate to perform reflectometry measurements. Reflectance data was obtained as a function of incident angle for Si, GaP, InP, GaAs, GaAsP and Ir. Optical constants at 26.5eV were obtained by fitting the angular dependence of the reflectivity with the Fresnel formula [6]. Measurement of samples with different surface layers showed that the optical constants for the bulk material can be reliably obtained in the presence of surface layer contaminants. A similar reflectometry setup was used to characterize Si/Sc multi-layer mirrors designed for use at 46.9 nm, and the diffraction efficiency of gratings.

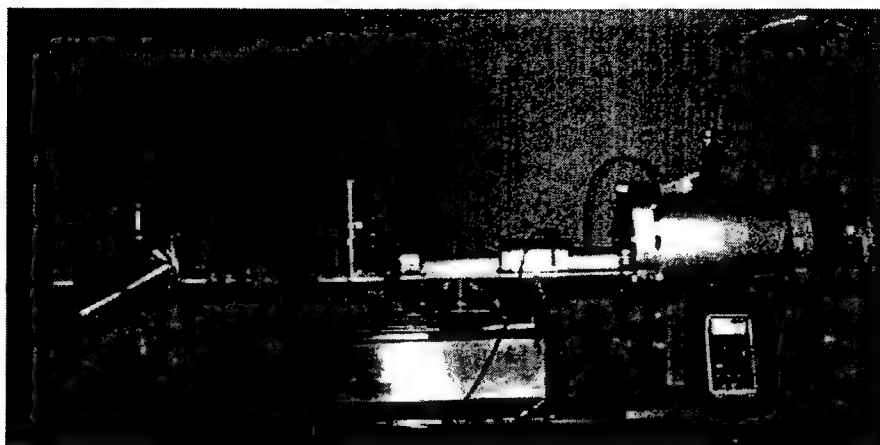


Fig. 1. Photograph of capillary discharge soft x-ray laser (right) and application chamber (left). The multimeter shown in front of the laser provides size reference.

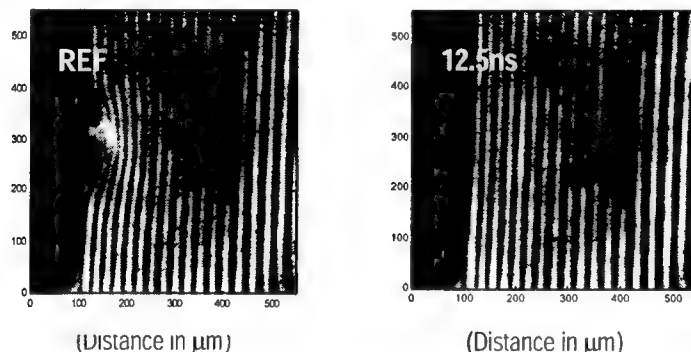


Fig. 2. (a) Soft X-ray interferogram without the plasma present. (b) Interferogram of a 2.7mm long line focus plasma generated by a Nd:YAG laser pulse ($\lambda=1.06$ nm, 0.36 J, 13 ns FWHM) acquired 12.5ns after the beginning of the Nd:YAG laser pulse. (c) Calculated density profile corresponding to the interferogram on (b)

In a different experiment the output of the 46.9nm Ne-like Ar laser beam was focused by a spherical ($R=10$ cm) Si/Sc multilayer mirror of ~ 40 % reflectivity. The focused laser beam was observed to ablate aluminum, stainless steel and brass when the samples were positioned within several hundred μm from the focus. The average intensity within a 2 μm diameter region at the focus is estimated $>1 \times 10^{11} \text{ W/cm}^2$. The minimum spot size was limited by the spherical aberration [7]. The high intensity of the focused beams was used to generate laser-created plasmas in Al, C, Cu and Sn. A critical density of $5 \times 10^{23} \text{ cm}^{-3}$ and the single photon ionization of the target atoms differentiates these plasmas from conventional laser-created plasmas. These proof-of-principle experiments in materials science, plasma physics, and EUV optics characterization, show that tabletop capillary discharge lasers are new practical sources of coherent short-wavelength radiation that can impact numerous fields.

1. C. D. Macchietto, B. R. Benware and J. J. Rocca, *Opt. Lett.*, **24**, 1115 (1999)
2. M. Frati, M. Seminario and J.J. Rocca. *Opt. Lett.* **25**, 1022 (2000)
3. M. Frati, F.G. Tomasel, B. Bowers, J.J. Gonzalez, V.N. Shlyaptsev, and J.J. Rocca. "Generation of highly ionized cadmium plasma columns for a discharge-pumped Nickel-like Cd laser". *Proc. 8th Int Conf. on X-ray lasers*. Saint Malo, France (2000).
4. Y. Liu, M. Seminario, F.G. Tomasel, C. Chang, J.J. Rocca, and D.T. Attwood, *Phys. Rev A*, in press (2001).
5. J. Filevich, K. Kanizay, M. C. Marconi, J. L. A. Chilla, and J. J. Rocca, *Opt. Lett.* **25**, 5, 356 (2000)
6. I.A. Artiukov, B.R. Benware, J.J. Rocca, M. Forsythe, Yu. A. Uspenskiia and A.V. Vinogradov. *IEEE J. Sel. Topics in Quant. Elect.* **5**, 1495, (1999).
7. B.R. Benware, A. Ozols, J.J. Rocca, I.A. Artiukov, V.V. Kondratenko and A.V. Vinogradov, *Optics Lett.* **24**, 1714, (1999).

Work supported the National Science Foundation, and the US Department of Energy · Universidad de Buenos Aires, Argentina

^bUniversidad de Navarra, Spain; ^cLebedev Physical Institute, Moscow, Russia; ^dUniversity California Davis at Livermore; ^aUniversidad de Buenos Aires, Argentina; ^bUniversidad de Navarra, Spain, ^cLebedev Physical Institute, Moscow, Russia ^dUniversity California Davis at Livermore

Phase matching techniques in the UV - EUV

Sterling Backus, Ra'anan Tobey, Lino Misoguti, Randy Bartels, Henry Kapteyn, and Margaret Murnane
*JILA, National Institute of Standards and Technology, and the University of Colorado at Boulder,
Boulder CO 80309*

The efficient upconversion of laser light into the UV and EUV regions of the spectrum has two major requirements: 1) the ability to generate photons in the required energy range through the nonlinear laser-atom interaction; and 2) the ability to *coherently* add, without absorption, the signal from a large number of radiating atoms. In past work using a hollow-waveguide geometry for frequency conversion, we demonstrated that it is possible to achieve high efficiency conversion into the UV and soft-x-ray (XUV) regions of the spectrum.[1,2] In this work, we show that this high efficiency allows us drive cascaded nonlinear upconversion processes from the visible to the VUV region of the spectrum with macroscopic conversion efficiencies. We also observe a type of quasi-phasesmatching in the deep-UV region of the spectrum for the first time.[3] Finally, we use coherent control techniques to selectively enhance a single harmonic order, to generate transform-limited EUV pulses for the first time.[4,5]

High-harmonic generation is one of the most extreme nonlinear-optical processes observed to date. By focusing an intense laser pulse into a gas, the light-atom interaction that occurs during the process of ionising the atoms results in the generation of harmonics of the driving laser frequency, that extend up to order ~ 300 (corresponding to photon energies from 4 to $>500\text{eV}$). Because this technique is simple to implement and generates coherent, laser-like, soft-x-ray beams, it is currently being developed for applications in science and technology including probing of dynamics in chemical and materials systems and for imaging. In this work we demonstrate that by carefully controlling the shape of intense light pulses of 6-8 optical cycles, we can control the interaction of light with an atom as it is being ionized, in a way that improves the efficiency of x-ray generation by an order of magnitude. Furthermore, we demonstrate that it is possible to control the spectral characteristics of the emitted radiation and to "channel" the interaction between different-order nonlinear processes. The result is an increased utility of harmonic generation as a light source, as well as the first demonstration of optical pulse-shaping techniques to control high-order nonlinear processes. The mechanism underlying the enhancements observed is a new type of "single-atom" phase matching, as shown in Fig. 1.

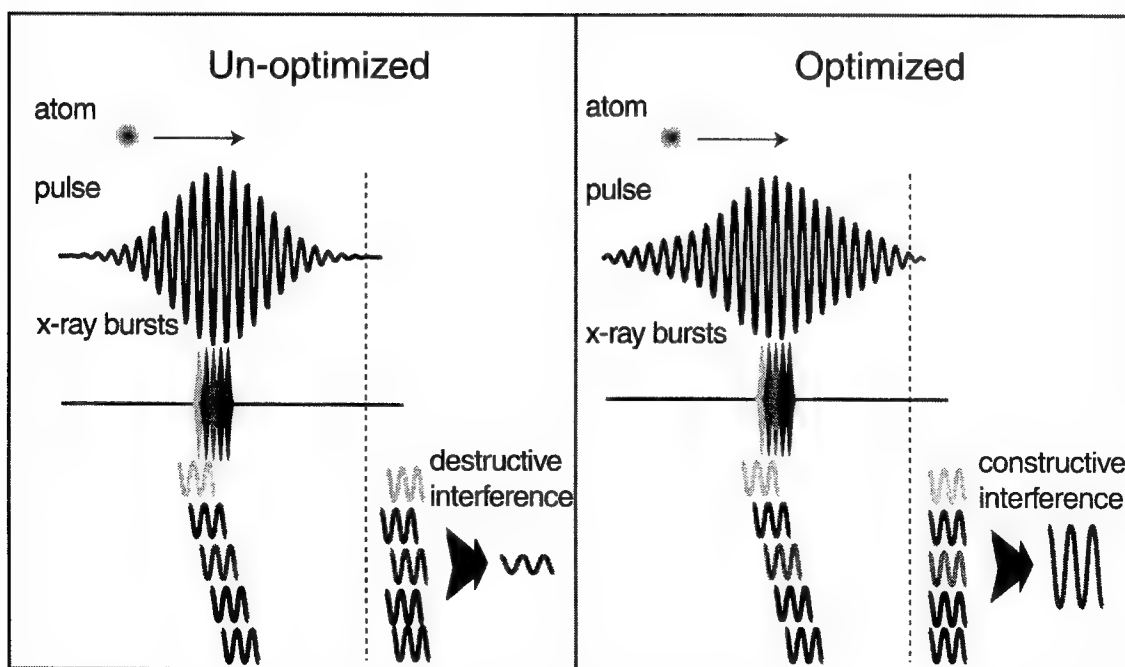


Figure 1: Schematic representation of intra-atomic phase matching.

We also investigated power scaling of the generated UV and EUV light. In the UV region of the spectrum, efficiencies approaching 40% have been obtained for conversion into the third harmonic using a 1mJ, 1kHz, 20fs laser system. At shorter wavelengths around 27nm, conversion efficiencies are approximately 10^{-5} per harmonic, while at wavelengths between 9 and 17nm, efficiencies are approximately 10^{-7} per harmonic. This corresponds to pulse energies of nJ per harmonic at 27nm, or average powers of microwatts per harmonic when driven by a few hundred microjoules of laser energy at 1kHz repetition rates.

To extend the average flux to mW per harmonic, we use a cryo-cooled, single-stage, ultrafast laser amplifier system capable of generating 700μJ-1mJ of energy, at repetition rates of 1-10kHz, with pulse durations of 20fs.[6] In combination with optimization techniques, this laser system can increase the average powers available from high harmonic sources by 1 – 2 orders of magnitude. We will also present measurements on the beam quality (M^2) of the generated UV and EUV beams.

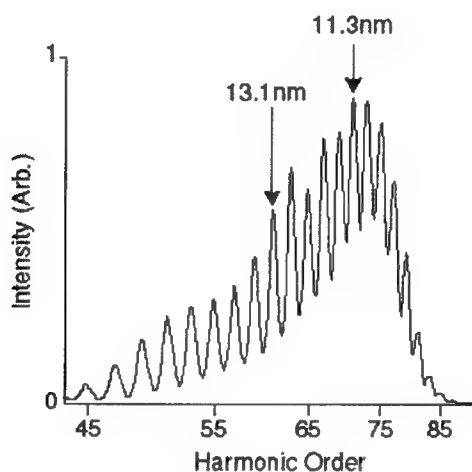


Figure 2. Harmonic spectrum from He generated in hollow core fiber, at a phased matched pressure of 340 Torr and an overall efficiency of 2×10^{-7} .

References

1. C. Durfee, S. Backus, M. Murnane H. Kapteyn, "Ultrabroadband phase-matched optical parametric generation in the uv using guided waves", *Optics Letters* **22**, 1565 (1997).
2. Rundquist, C. Durfee, Z. Chang, C. Herne, H. Kapteyn and M. Murnane, "Phase Matching of Soft-X-Ray Harmonic Emission in Hollow-Core Fibers", *Science* **280**, 1412 (May 29, 1998).
3. L. Misoguti, S. Backus, C. Durfee, R. Bartels, M. Murnane and H. Kapteyn, "Generation of broadband VUV light using third-order cascaded processes", submitted to *Physical Review Letters*.
4. R. Bartels, S. Backus, E. Zeek, L. Misoguti, G. Vdovin, I. P. Christov, M. M. Murnane, H. C. Kapteyn, "Shaped-pulse optimisation of coherent soft-x-rays," *Nature* **406**, 164-166, 2000.
5. I.P. Christov, M. M. Murnane and H.C. Kapteyn, "Attosecond time-scale intra-atomic phase matching of high harmonic generation", submitted to *Physical Review Letters*
6. S. Backus, R. Bartels, S. Thompson, R. Dollinger, H. C. Kapteyn, M. M. Murnane, "High efficiency, single-stage, 7 kHz high average power ultrafast laser system", *Optics Letters* (April 2001).

Advances in the generation of high order harmonics using few-optical-cycle pulses

P. Villoresi¹, M. Nisoli², G. Cerullo², M. Pascolini¹, L. Poletto¹, E. Priori², S. Stagira²

Istituto Nazionale Fisica della Materia,

¹*Laboratorio di Elettronica Quantistica, D.E.I., Università di Padova, Padova (Italy)*

via Gradenigo 6a, 35131 Padova, Italia; e-mail: Paolo.Villoresi@dei.unipd.it

²*Dipartimento di Fisica, Politecnico, Milano (Italy)*

P.za Leonardo da Vinci 32, 20133 Milano, Italia.

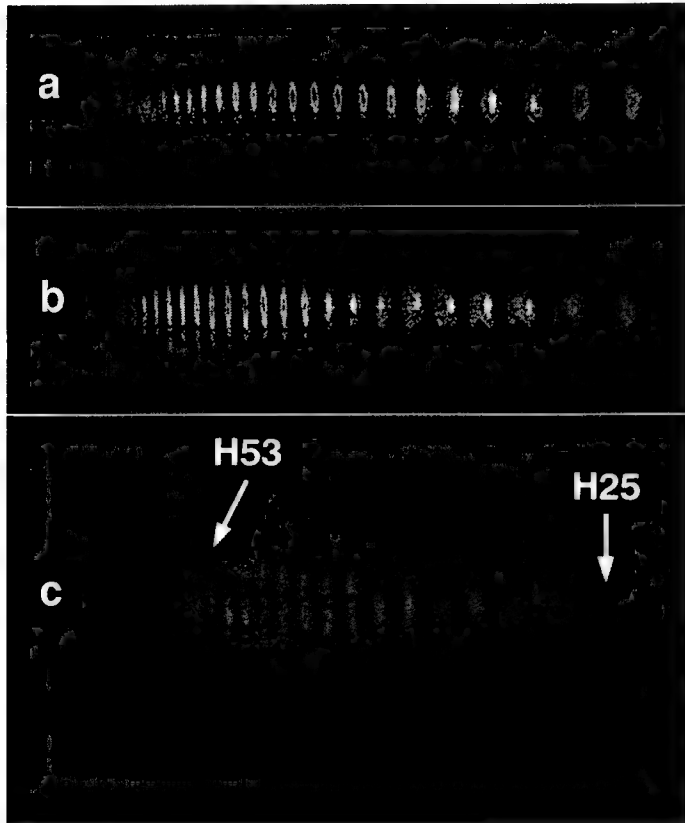
The coherent nonlinear effects induced by ultrashort pulses have highlighted different regimes of the laser-matter interaction with respect to nanosecond or even picosecond excitation. The electron dynamics in these latter contexts are generally dominated by collective motion and plasma effects. When the stimulus provided by the laser is restricted to a time interval of the order of the electron orbital period, the matter's response shows up a single-particle nature, eventually evidencing the quantum interference between different paths yielding to the same transition. The physics of both above threshold ionization and high order harmonics (HOHs) generation in the femtosecond temporal regime has now a sound interpretation in this sense, which has united the efficacy of the predictions with the beauty of the unification.

Moreover, the HOHs have a direct application as short-wavelength sources, since their generation is actually the coherent frequency conversion from the near infrared to the extreme-ultraviolet and soft X-ray up to the water window region. In particular, the generation of high-order laser harmonics using sub-10 fs pulses takes place in a condition where the amplitude of the laser electric field varies significantly over each optical cycle. Thus, modeling of the process can not be carried out using the adiabatic approximation. Therefore, there is a claim for experimental evidences of this new generation regime. Moreover, most of the prediction formulated for the characteristics of the generation in the long-pulse regime have to be verified and eventually corrected for short pulses.

The laser pulse used in the experiment is a Ti:sapphire source, with a duration of 25 fs and an energy per pulse of 0.8 mJ, which is compressed to 5-7 fs by using the hollow fiber technique. The amplitude and phase of the compressed pulses have been measured with spectral phase interferometry for direct electric field reconstruction (SPIDER). Peak intensities up to $1 \cdot 10^{15}$ W/cm² can thus be achieved in the interaction region. The spectral and spatial distribution of the harmonics beam have been analyzed with a XUV flat-field spectrograph and a bidimensional detector.

We have performed measurements of the harmonic spatial profiles as a function of the nonlinear order and of the position of the gas jet relative to the laser focus. Hereafter such relative position will be called z , and will be taken as positive when the laser beam is focused before the gas jet. The spectra show discrete and well resolved harmonics; moreover the harmonic beam is characterized by regular spatial profiles, with small divergence even when the gas jet is located before and around the laser focus, without any evidence of annular profiles. The harmonic divergence continuously increases upon increasing the z value. The spectra in neon generated for three positions of the gas jet with respect to the laser focus is shown in the Figure: (a) $z = -1$ mm, (b) $z = 0$, (c) $z = 3$ mm. The vertical direction shows the spatial profile. From the focalplane spatial distribution we estimated the divergence of the HOHs beam.

Divergence increases with harmonic order in the plateau and slowly decreases in the cut-off region. Similar results have been obtained using helium as nonlinear medium. The developed sub-10-fs-pulse-driven neon harmonic source emits about 10^6 photons/pulse per harmonic (in the plateau region), and within an estimated time interval of about 3 fs.



The measured brightness for plateau harmonics and position around the focus is of $6 \cdot 10^{13}$ W/cm²srad (we have assumed a spot size of the emission area ranging from 13 to 25 μ m for the different harmonic orders).

The reported measurements clearly demonstrate novel spatial properties of the harmonic emission: regular harmonic spectral profiles, with small divergence, can be generated not only when the gas jet is located significantly after the laser focus, where conversion efficiency is not optimal, as previously observed, but in a considerably larger range of positions around the laser focus, including that corresponding to the maximum conversion efficiency. This result is particularly significant for applications where high XUV brightness is required.

We have then performed a theoretical study of the spatial properties of high-order harmonic radiation, using

a nonadiabatic three-dimensional numerical propagation model, and the same parameters used in the experiments. This model can reproduce correctly the spectral characteristics of the harmonic beam, namely: the emission spectrum, the linewidth of the harmonic peaks as a function of the harmonic order, and the spectral shift of the harmonic peaks as a function of the gas jet position with respect to the laser focus. We have then used the same numerical model to investigate the spatial properties of the harmonic beam. The angular distributions have been calculated by integrating the two-dimensional profile of the harmonic beam over one direction, in order to reproduce the operation of the spectrometer. In this case, the numerical simulation presents a qualitative agreement with experimental data; in particular, the divergence correctly increases upon increasing the z value. Moreover, in agreement with the experimental results, the calculated harmonic beam displays regular spatial profiles even when the gas jet is moved near the laser focus. The remarkably different spatial behavior of the harmonic emission observed using a fundamental beam with Bessel profile instead of one with Gaussian profile, can be understood in terms of the peculiar properties of a truncated-Bessel beam.

In conclusion, we have shown that the angular distribution of high-order harmonics strongly depends on the spatial properties of the fundamental beam. The use of fundamental beams with Bessel intensity profile allows to significantly improve the spatial quality of the harmonic beam.

References on results: P. Villorresi et al., PRL vol. 85 p. 2494 (2000), E Priori et al., PRA vol. 61 p. 063801, C. Altucci et al. PRA vol 61 p. 021801 (2000), **on methods:** M. Nisoli et al. APL vol 68 p. 2793 (1996), L. Poletto et al., Rev. Sci. Instrum., to appear 2001.

Quantum Electrodynamics Treatment of Optical High Order Harmonic Generation

J. GAO

University of Illinois, Urbana-Champaign

Optical high order harmonic generation (HHG) is one of the most promising ways to generate the coherent EUV and soft X-ray radiation required by next the generation of photolithography. It is of equal significance in basic research for understanding the laser-matter interaction. The most intriguing characteristic of HHG spectra is the display of a plateau region, in which the harmonic intensity is relatively insensitive to the harmonic order q , following rapid intensity fall for the lowest harmonics [1]. Several theoretical methods have been explored to describe the nonperturbative behavior of harmonic generation in intense optical fields ($>10^{13}$ W/cm²), which have the unifying theme of calculating dipole radiation from an electron under the influence of the optical field. The interpretation of HHG can be summarized by a two-step model [2,3]: bound electrons tunnel into the continuum under the influence of the optical field, accelerate to a maximum energy of approximately three times the ponderomotive potential (U_p), and subsequently recombine with the parent ion to generate short-wavelength generation.

An alternative framework based on the quantum electrodynamic (QED) formalism for describing HHG was recently introduced [4] in which the atom and the quantized high optical field was treated as an isolated system with well-defined energy and momentum. The electron-laser interaction is described nonperturbatively by quantized field Volkov states which are modified in a perturbative manner to introduce a harmonic field. As a result, radiation is produced by transitions between quantized Volkov states that experience a phase shift during the process. Such a dressed continuum-to-continuum transition is different from dipole transitions and highlights a direct photon-conversion process in which q fundamental photons are annihilated to produce a single harmonic ($q\omega$) photons with the electron energy unchanged. In this picture, the fundamental optical field plays the active role by first producing photoelectrons through

above threshold ionization (ATI) and then interacting with the electron to form Volkov states, subsequently generating discrete radiation with harmonic energies that are equal to the spacing between quantized Volkov states. The transition matrix that describes each sub-process is developed based on the formal scattering theory, and the explicit expression for the matrix elements is obtained for a general elliptically polarized optical fields, allowing us to compare with all aspects of experiments, including harmonic spectra and polarization data [5,6]. Also, recent calculations of the spectral lineshapes of individual harmonics are presented and compared with published measurements.

Throughout the calculations the discrete, nonzero energies of the ATI photoelectron are maintained and a clear connection between HHG and above threshold ionization is drawn. For experiments in which the laser pulse width is 100-150 fs, only the lowest ATI photoelectron orders contribute significantly to harmonic generation, whereas higher-energy electrons escape from the parent atom during the pulse risetime. As the duration of the fundamental field is decreased, the rapid rise of the field intensity to its peak value effectively traps more energetic photoelectrons, thereby extending the harmonic response to shorter wavelengths.

References:

- [1] Citing just one of many excellent experimental works from various groups: X. F. Li, L'Huillier, M. Ferray, L. A. Lompre, G. Mainfray, *Phys. Rev. A* **43**, 1669 (1991).
- [2] K. C. Kulander, K. J. Schafer, and J. L. Krause, in *Super-Intense Laser-Atom Physics*, edited by B. Piraux.
- [3] P. B. Corkum, *Phys. Rev. Lett.* **71**, 1994 (1993).
- [4] J. Gao, F. Shen and J. G. Eden, *Phys. Rev. Lett.* **81**, 1833 (1998).
- [5] J. Gao, F. Shen and J. G. Eden, *J. Phys.* **B32**, 4153 (1999).).
- [6] J. Gao, F. Shen and J. G. Eden, *Phys. Rev.* **A61**, 043812 (2000).

High Reflectivity Optics for the Extreme Ultraviolet and Soft X-Ray Spectral Regions

A.V.Vinogradov

Lebedev Physical Institute, Lenensky Prospekt 53, Moscow 119991, Russia

vinograd@sci.lebedev.ru

The wavelengths in the region between 35nm and 50nm are too short to be reflected at normal incidence by any bulk material and too long for standard multilayer reflective coatings such as Mo/Si, W/BC, Cr/Sc et al that are demonstrating good performance for $4\text{nm} < \lambda < 25\text{nm}$. For example for the best bulk reflectors (Os, Ir) the reflectivity changes from 20% - 25% at 50 nm down to 5 % - 8% at 35nm [1]. The practical interest to this range was stimulated by the development of 46.9 nm capillar discharge laser [2] that now is working in a repetitive mode with an average power more than 1 mW [3]. The reflective optics is a tool for manipulation of a beam of this laser. The Sc/Si multilayer coating was suggested [4] and realized as a solution to the problem[5]. The normal incidence reflectivity 45% at 46.9nm was measured with reflectometer based on capillar discharge laser[6]. Various optical elements with Sc/Si coating allow the usage of 46.9 nm laser for plasma interferometry [7], ellipsometry [8] and ablation[9]. The high resolution imaging of nonradiating objects is in progress. To increase reflectivity and heat stability W barriers are introduced between Sc and Si layers. The role of these barriers is to prevent interdiffusion and provide sharp interfaces[10]. It is clear that Sc/Si coatings can provide high reflectivity in a rather limited spectral range (which is still to be investigated). So the next goal is to extend the achieved results to the neighboring spectral intervals. The optics design basically requires the detailed knowledge of optical constants – real and imaginary parts of the refractive index n . Experimental data of this kind is very poor. This is explained by the fact that all elements especially atmospheric gases in this spectral range are characterized by extremely short penetration length of a photon. Consequently the surface are essentially contaminated and practically one never deals with a clean substrate or layer material containing in a reflection coating. So to obtain the reliable optical constants from reflectometry or ellipsometry measurements one should take care of contamination layer [11 - 13]. On the other hand from the theoretical point of view the interval under consideration lies just between the optical domain where the spectra of solids are formed by excitation of valence electrons and soft X-ray and XUV range where the excitation of core electrons are crucially important. This causes difficulties for both solid state and isolated atom approaches to *ab initio* calculation of material optical constants [4]. The methods and results of design and study of multilayer coatings containing 3d-transition metals will be presented.

References

1. E.D.Palik (Ed.), Handbook of Optical Constants of Solids, Academic Press, 1985;
2. D.W.Berreman et al, Appl. Phys.Lett., 56(22), p.2180, 1990,
3. J.J.Rocca et al, Phys. Rev. Lett., 73, pp 2192 – 2195, 1994
4. B.R.Benware et al, Phys. Rev. Lett, 81, pp.5804 – 5807, 1998
5. Yu.A. Uspenski et al, SPIE v. 3156, pp 288 – 294, 1997
6. Yu. A. Uspenski et al, NIM A448, pp 147 – 151, (2000)
7. Yu.A.Uspenski et al (to be published)
8. C.H.Moreno et al, Phys. Rev. E60, pp 911 – 917, 1999

8. B.R.Benware et al, JOSA B, pp 1 – 5, 2001
9. J.J.Rocca et al, SPIE 4065, pp 173 – 184, 2000
10. Yu. A.Uspenski, SPIE 2001 (to be m[published)
11. I.A.Artioukov et al, J. Sel. Topics on Quantum electronics, 5, pp 1495 – 1501 (1999)
12. R.M. Fechtchenko, A.V.Vinogradov, Optics lett., 25, pp 1-3, 2000
13. R.M. Fechtchenko et al, Journal of Russian Laser Research, 21, pp 62 – 68, 2000

Short Wavelength Sources for Microlithography

by

William T. Silfvast
School of Optics/CREOL
University of Central Florida
Orlando, FL 32816
407-823-6855
silfvast@creol.ucf.edu

Summary

In the past 10 years, the evolution of microlithography tools to generate smaller features on microchips has involved using shorter ultraviolet wavelength sources and larger numerical aperture transmissive optics for imaging the complex mask patterns onto the wafers. During this evolution, the imaging source went from the mercury g-line at 436 nm to the i-line at 365 nm and then to the 248 nm KrF laser. At the 248nm wavelength a laser source was necessary because the imaging optics required a very narrow linewidth (0.0004% bandwidth) at high power levels in order to obtain diffraction-limited imaging over a large ($>1\text{cm}^2$) imaging field. Presently the manufacturing tools are beginning to use the 193 nm wavelength of the ArF excimer laser. Operating at this wavelength places even more stringent requirements on the illuminating linewidth than at 248 nm.

Looking ahead, in approximately four to five years from now it is expected that an EUV stepper operating at a wavelength of 13.5nm will become available that could eventually print features as small as 30nm. Fortunately there is a very strong group of emission lines from transitions in tenth ionized xenon that radiate in the region of 13.5nm. These emission lines can be produced with significant flux from either a laser-produced plasma or a plasma discharge source. At this short wavelength, there are no transmissive optical materials available to provide imaging from the mask to the wafer. Hence reflective optics must be used for the imaging process. The multilayer reflective coatings associated with these optics allow a 3% bandwidth of the radiating source to be used, thereby removing the restriction of an extremely narrow source linewidth as was the case for the 248 nm and 193 nm tools. It is fortuitous that the scaling of radiative transition probabilities at shorter wavelengths in atoms and ions allows for a very significantly increased power emitted from an incoherent plasma source when compared to a similar source in the ultraviolet spectral region. Hence, laser sources are not required in this wavelength region to achieve the necessary flux needed for the high wafer throughputs of a microlithographic manufacturing system.

DUV and VUV Lithography Application of Excimer Laser Systems

Ivan Lalovic
Cymer, Inc., Lithography Applications Department
16750 Via Del Campo Court, San Diego, CA 92127
ilalovic@cymer.com

TALK SUMMARY:

DUV (deep ultra-violet) and VUV (vacuum ultra-violet) photolithographic projection imaging has brought several new technological and commercial challenges to the semiconductor industry. These challenges are primarily related to optical properties of the imaging materials at the exposure wavelength. Coupled with the reduction in integrated circuit (IC) design and fabrication tolerances of the critical device features, significant research, development and engineering effort has been required to achieve adequate imaging performance for volume manufacturing of sub 0.25 μ m CMOS (complementary metal-oxide-semiconductor) and other semiconductor device technologies.

Reduction of exposure wavelength has been the preferred approach for improving image resolution and enabling the scaling of semiconductor devices. However as wavelengths are reduced to the DUV, the interactions between the exposure light and optical lens materials disallow the use of broadband gas-discharge lamp sources. At DUV exposure wavelengths, the material dispersion of refractive lens materials made from fused silica (SiO₂-silicon dioxide) and calcium fluoride (CaF₂) are relatively high compared to UV illumination (365nm i-line emission of the mercury vapor lamp). High dispersion levels result in imaging deviations for light at different exposure wavelengths. Therefore, strict requirements are placed on the spectral width and shape of the propagating light. Due to superior spectral power density, the application of highly line-narrowed excimer laser sources using KrF (krypton fluoride, 248nm) and ArF (argon fluoride, 193nm) has been adopted and has proved production maturity. At the 157nm VUV exposure wavelength of an F₂ excimer, material issues are more pronounced and the choice of excimer laser technology will have decided impacts on imaging approaches for sub 100nm imaging. The spectral bandwidth requirements for lithographic excimer lasers are discussed.

The pulsed emission and energy stability of the excimer laser require additional design considerations for integration with step-and-repeat as well as scan-and-repeat exposure projection systems. Laser and illuminator designs also have to accommodate the characteristic spatial coherence, divergence, polarization and other laser beam-quality parameters in order to minimize laser impacts on image formation. Minimization of projector lens aberrations in exposure systems has also received significant attention due to effects observed on imaging. The aberration levels and observed effects on image degradation scale with increasing lens numerical aperture (NA) and decreasing image size. Therefore, various aberration measurement techniques are now widely utilized. The imaging impacts of the source wavelength offset, and therefore chromatic aberrations, have been investigated experimentally on current high-NA projection systems and through simulation, and are presented here.

In the figure below, the historical/predicted feature scaling and imaging wavelength reduction are shown. The current adoption of 193nm-wavelength illumination for 130-100nm IC node manufacturing in 2001 and the predicted integration of 157nm VUV illumination extend the regime of sub-wavelength imaging. Since image resolution is proportional to illumination

wavelength, additional advances in the photolithography process performance enable the high rate of IC device scaling. The technological challenges in achieving the lithographic feature scaling beyond the 150nm and 130nm IC nodes of today are also addressed.

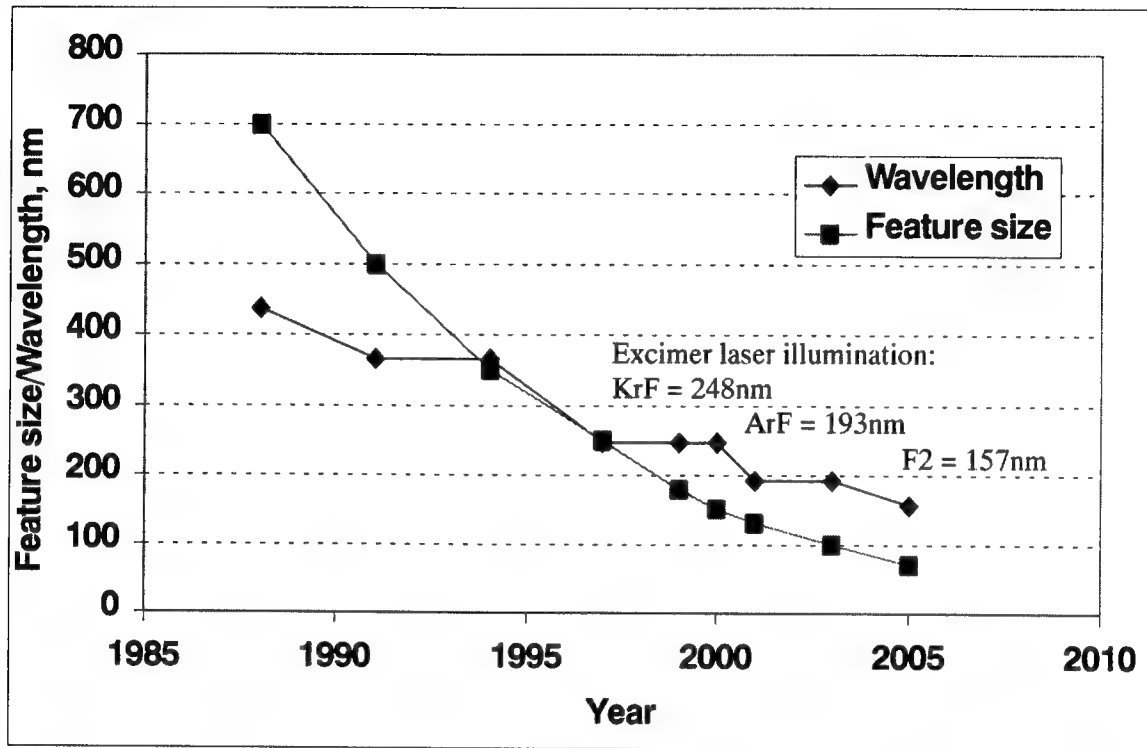


Figure: Comparison of feature (image) size and imaging illumination wavelength

Keywords: Excimer lasers, spectral bandwidth, KrF, ArF, lens aberrations, Zernike

Development on the Generation of Coherent UV Light from Nonlinear Optical Borate Crystals

Yoke Khin Yap, Tomosumi Kamimura, Masashi Yoshimura, Yusuke Mori and Takatomo Sasaki

Department of Electrical Engineering, Osaka University
2-1 Yamada-oka, Suita, Osaka 565-0871, Japan
Email: YK.Yap@osa.org

Ultraviolet (UV) radiation is viewed as a clean energy source for materials synthesis and processing. Excimer lasers are the useful source of intense UV radiation. Operation of these lasers involved high-voltage discharge of corrosive gas. A compact, maintenance-free, all-solid-state alternative is in high demand. An effective technique for producing UV light is cascaded sum-frequency generation of nonlinear optical (NLO) crystals as pumped by solid-state IR lasers ($\lambda \sim 1\mu\text{m}$). Until 1975, most NLO crystals were based on the P-O, I-O and Nb-O bonds like those in KH_2PO_4 , LiIO_3 and LiNbO_3 . Because of high resistance against laser-induced damages and good transparency of UV light, borate NLO crystals are identified as the choice for generation of high-power UV light. The first borate crystal that described for this purpose was $\text{KB}_5\text{O}_8 \cdot 4\text{H}_2\text{O}$ (KB5)¹. However, intense research on borates was initiated after the development of $\beta\text{-BaB}_2\text{O}_4$ (BBO)². A review on NLO borate crystals has been reported³.

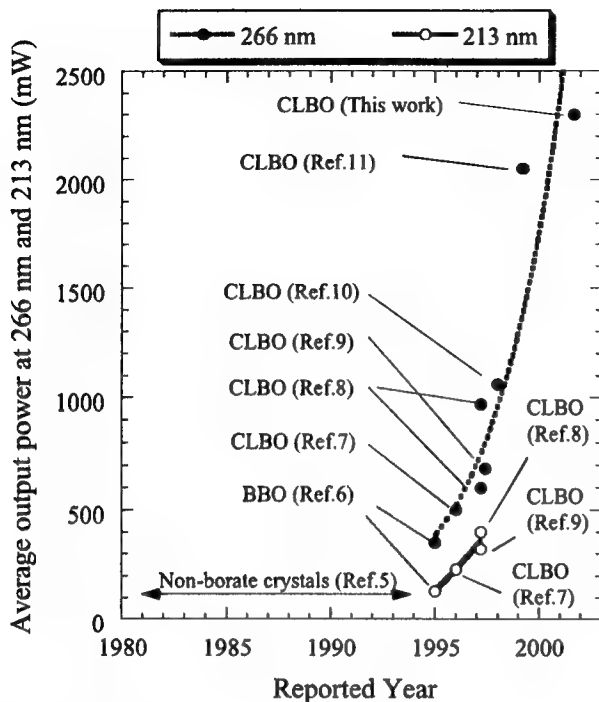
In this paper, recent progress on the generation of coherent UV light from NLO borate crystals is evaluated. Two factors are identified as the important elements for the development of such solid-state UV light source, i.e. **properties and reliability** of the NLO crystals:

I) Properties of NLO crystals

The performance of solid-state UV light source has been greatly improved after the discovery of $\text{CsLiB}_6\text{O}_{10}$ (CLBO)⁴ crystals. As shown in Fig. 1, average UV (@266nm) output power reported so far⁵⁻¹¹ was enhanced by one order of magnitude within the past six years. It is noteworthy that CLBO was demonstrated to produce deep-UV light (@193nm) by eighth harmonic generation ($\omega+7\omega$) of the Er^{3+} -doped fiber amplifier¹². The conversion efficiency from the fundamental wave was 7 %. These progresses are due to the significant nonlinearity, relatively small walk-off angle and relatively large angular, spectral and temperature acceptance bandwidths of CLBO⁷. As evidenced, the discovery of materials with desired properties can significantly enhance the progress of solid-state UV light source.

II) Reliabilities of NLO crystals

The performance of solid-state UV light source also depends on the reliability of NLO crystals. Two reliability issues are *thermal dephasing* and *laser-induced damages*. We have developed a novel technique called temperature profile compensation (TPC) to alleviate thermal dephasing¹⁰. This technique improved UV output of CLBO by 2.3-fold. Besides, we have reported that ion beam etching can enhance resistant of CLBO surface against UV laser-induced damage¹³. Recently, we have developed a new crystal growth technique to improve quality of CLBO. By this technique, CLBO with lower UV absorption and dislocation density were developed¹⁴. These crystals can have 2.5-fold higher bulk laser-induced damage threshold than fused quartz and CLBO that grown from conventional technique. These crystals were used to generate 23 W of UV light (@266 nm) with better output stability and reproducibility.



As a summary, the generation of coherent UV light by high-quality CLBO is promising. The performance of solid-state UV light source with NLO crystals can be further enhanced when thermal dephasing is alleviated and the surface resistance against laser-induced damages is enhanced. In particular, CLBO can performed long-term stability as evidenced in the past few years where UV radiation (@213 nm) from CLBO is used for pulsed-laser deposition with promising reliability and stability^{3, 15}.

Fig. 1. Progress of average UV output power from NLO crystals in the past two decades.

References:

- [1] C. F. Dewey, Jr., W. R. Cook, Jr., R. T. Hodgson and J. J. Wynne, *Appl. Phys. Lett.* 26 (1975) 714.
- [2] C. Chen, B. Wu, A. Jiang and G. You, *Sci. Sin. B7* (1984) 598.
- [3] T. Sasaki, Y. Mori, M. Yoshimura, Y. K. Yap and T. Kamimura, *Materials Science & Engineering R30/1-2* (2000) 1-54.
- [4] Y. Mori, I. Kuroda, S. Nakajima, T. Sasaki and S. Nakai, *Appl. Phys. Lett.* 67 (1995) 1818.
- [5] V. G. Dmitriev, G.G.Gurzadyan and D.N.Nikogosyan, "Handbook of Nonlinear Optical Crystals", 3rd ed., A. L. Schawlow, A.E.Siegman and T. Tamir eds., Springer (1999).
- [6] M. Oka and S. Kubota, in *CLEO 1995*, Vol. 15 of 1995 OSA Technical Digest Series (OSA, Washington D.C., 1995), p. 139.
- [7] Y. K. Yap, M. Inagaki, S. Nakajima, Y. Mori and T. Sasaki, *Opt. Lett.* 21 (1996) 1348.
- [8] Y. K. Yap, Y. Mori, S.Haramura, A.Taguchi, T. Sasaki, K. Deki, Y. Ohsako and M. Horiguchi, *OSA Trends in Optics and Photonics 10*, ASSL 1997, (OSA, Washington D.C., 1997), p. 10.
- [9] Y. K. Yap, Y. Mori, S. Haramura, A. Taguchi, K. Nishijima, T. Inoue, A. Miyamoto, H. Sakai, Y. Kagebayashi and T. Sasaki, in *CLEO 1997*, Vol. 11 of 1997 OSA Technical Digest Series (OSA, Washington D.C., 1997), p. 512.
- [10] Y. K. Yap, K. Deki, N. Kitatochi, Y. Mori, and T. Sasaki, *Opt. Lett.* 23 (1998) 1016.
- [11] T. Kojima, S. Konno, S. Fujikawa, K. Yasui, K. Yoshizawa, Y. Mori, T. Sasaki, M. Tanaka and Y. Okada, *Opt. Lett.* 25 (2000) 58.
- [12] T.Ohtsuki, H.Kitano, H.Kawai, and S.Owa, in *CLEO 2000*, OSA Technical Digest Series (OSA, Washington D.C., 2000), paper CPD9 (2000).
- [13] T. Kamimura, M. Yoshimura, K. Nakai, K. Murase, Y. Mori, T. Sasaki and K. Yoshida, in *CLEO 1999*, OSA Technical Digest Series (OSA, Washington D.C., 1999), p. 532.
- [14] T. Kamimura, R. Ono, Y. K. Yap, M. Yoshimura, Y. Mori and T. Sasaki, *Jpn. J. Appl. Phys.* 40 (2001) L111.
- [15] Y. K. Yap, S. Kida, T. Aoyama, Y. Mori and T. Sasaki, *Appl. Phys. Lett.* 73 (1998) 915.

Solid-state 263-nm laser for triggering high-voltage switches at Sandia's Z-Accelerator

A. Erlandson, C. Ebberts, J. Bartolick, W. Massey, W. Behrendt,
A. Drobshoff, J. Narduzzi, J. Caird, and S. Payne
Lawrence Livermore National Laboratory
P.O. Box 808
Livermore, CA 94551
(925-423-3709; erlandson1@llnl.gov)

Summary

We designed, built, and tested a Nd³⁺ laser that produced near diffraction-limited, 2.4-J pulses at the harmonically-converted wavelength of 263 nm. This laser is slated to be reactivated at Sandia's Z-Accelerator in Albuquerque, NM to improve triggering of the Z-Accelerator's thirty-six SF₆-filled, high-voltage switches. The switches deliver currents of several MA to electric discharges, called z-pinches, which generate intense x-rays used to to perform high-energy-density experiments.¹

The trigger laser generated pulses at 1.053 μm using an injection-seeded Nd:YLF regenerative amplifier and a 4-pass 1-cm Nd:glass rod amplifier. A phase conjugator using fluorinert was used to maintain 2-3 times diffraction-limited wavefront quality. The output from the four-pass amplifier fed three separate channels, each with a single-pass 1-cm rod amplifier and a pair of BBO crystals for frequency conversion to the fourth harmonic. With each rod amplifier producing about 3.4 J at 1053 nm, the square pulse distortion for the system was 10-20. A nearly temporally-flat output pulse was achieved over the 20-ns pulse duration, however, by using a LiNbO₃ integrated-optics amplitude modulator to shape the injected pulse to compensate for the square pulse distortion. The amplitude modulator was also used to achieve a rise time of less than 500 ps, with less than 500 ps timing jitter relative to the trigger pulse. A harmonic conversion efficiency of 25% was attained, with each channel producing ~ 850 mJ at 263 nm with 3.6 J incident radiation at 1.053 μm .

References

1. Yonas, G., "Fusion and the Z Pinch", Scientific American, August, 1998.

Ultraviolet and Blue Lasers and their Applications

Tuesday, 31 July 2001

**TuB1: Development and Applications of UV and VUV
Lasers**

Tuesday Missing Papers

TuB1.1 "TBD", D. Basting, *Lambda Physik Inc, Göttingen, GERMANY.*

TuB1.2 "TBD"

DUV lasers applied to semiconductor inspection and optical disk mastering

Shigeo Kubota, Naoya Eguchi, and Hisashi Masuda

Kubota Opto-Electronics Laboratory, Core Technology Development Center
Core Technology & Network Company, Sony Corporation
6-7-35 Kitashinagawa, Shinagawa-ku, Tokyo 141, Japan
Phone: +81-3-5448-4580, Fax: +81-3-5448-3446
e-mail: Shigeo.Kubota@jp.sony.com

ABSTRACT: We report on all-solid-state, continuous-wave, deep-UV (DUV) lasers at 266 nm and even at sub-200nm as driving force for wafer inspection and optical disk mastering.

INTRODUCTION

Recent trends in vast bit flow and huge storage media demanded by internet and entertainment requirement further push microstructure toward infinitesimal size and power. UV-DUV lasers play important roles in such industry, which manufacture, re-play, and inspect such minute structures. Among them, continuous-wave DUV lasers oscillating at 266 nm are key devices in semiconductor wafer inspection for the current 0.18 μm generation and optical disk mastering with minimum pit length 0.155 μm . We also reported a 195 nm all-solid-state, continuous wave DUV laser to be used in the next generation systems. We believe our optical approach will contribute to the simultaneous achievement of high-resolution and high-throughput processes in the cutting edge micro-fabrication.

DEEP-UV lasers

Both the DUV microscope and the DUV mastering systems employ DUV light sources, CW all-solid-state lasers at 266 nm. Figure 1 shows a photograph of the DUV laser with UV output power of 10-20 mW (Cobalt laser UW-1010) [1,2]. We resonantly frequency-double the output of a green laser (Lightwave Electronics Model 142-0532-200) to generate UV using a BBO crystal in a bow-tie ring resonant cavity. Low scattering nature of original Czochralski-grown $\beta\text{-BaB}_2\text{O}_4$ (BBO) [3], improved surface polishing, coating with low absorption and scattering, and optimizing the cavity design for high conversion with reduced damage and contamination control helped to realize high efficiency and long-term reliability of this laser. As a result, over 7000 hours of operation was achieved at single location on a BBO crystal with more than 100 mW of UV output, while input green power was 500 mW [4]. This fact means no down time throughout the year when the light source is used in 24 hour-running semiconductor mass-production plants, and thus is quite beneficial.

Recently we have reported, for the first time, an all-solid-state, continuous wave, DUV laser oscillating at 195 nm [5]. Combining the resonant 266 nm light (incident power on resonant cavity was 100mW) with Ti:Sapphire laser oscillating at 740 nm, CW power of 3 mW at 195.6 nm was generated inside a BBO crystal (Figure 2). We expect this laser will exceed the resolution limit of optical microscope attained by conventional light sources.

DEEP-UV Microscope for semiconductor inspection

Table 1 and Figure 3 show the parameters and a schematic diagram, respectively, of the deep-UV microscope to be used for defect classification on patterned Si wafer for yield enhancement [6]. The fiber connection arrangement allows flexibility in optical configuration. Speckle was reduced by a rotary diffuser. The objective lens has the numerical aperture 0.9 and focal length 2 mm. The use of the 1.4-million-pixel CCD camera specially designed for 266 nm image enhanced the advantage of the DUV microscope. The optical magnification on the CCD is either 95x or 380x by changing the imaging lens for the CCD having a different focal length. The field-of-views are 67 x 50 μm^2 or 16.6 x 12.5 μm^2 . Consequently, the maximum magnification on the 19-inch cathode-ray tube (CRT) is as high as 22,000x. Measurement without vacuum chambers allows easy and high-throughput inspection compared with SEM.

Figure 4 shows the theoretical modulation transfer function (MTF) of the DUV microscope. The deep-UV laser light focused by a high numerical aperture (NA=0.9) objective lens forms Airy radii of spots as small as $0.6\lambda/\text{NA}=0.173 \mu\text{m}$ for 266 nm illumination and 0.130 μm for 195 nm illumination, respectively. The cut-off frequencies correspond to 77 nm L&S and 55 nm L&S, which are well below the defect rules of 90nm and 65nm for current and next generation design rules of 0.18 μm and 0.13 μm , respectively. Resulted high contrast image of killer defects significantly enhance defect classification capability of the inspection tool. In particular at 266nm, even classification of defect under SiO_2 layer is possible which is transparent at this wavelength and this function can not be expected in the case of SEM.

DEEP-UV Optical disk mastering

266 nm lasers are also applied to the development of ultra-high density optical disk mastering corresponding to several times higher density than that of digital versatile disks (DVD). Chemically amplified photo resist commonly used in KrF lithography can be applied to the mastering process. The highest density demonstrated is 30 Gbytes capacity with CD disc size, of which the bit density is equal to 21Gbit/inch² (Figure 4). The jitter is well suppressed by the pit signal processing (PSP) method that controls the positions of leading and trailing edges of the signal [7].

In summary the DUV lasers are replacing conventional lamps and visible light sources in the fields of production and inspection of microstructures. We expect DUV lasers will continue to find various applications exploring new technology and business.

REFERENCES

1. M. Oka, L. Y. Liu, W. Wiechmann, N. Eguchi, and S. Kubota, IEEE J. Selected Topics in Quantum Electronics, **1**, 859 (1995).
2. Sony Precision Technology Inc. product catalog No. 610.
3. S. Kubota, M. Oka, L. Y. Liu, T. Okamoto, M. Watanabe, Y. Taguchi, H. Masuda, T. Fukui, W. Wiechmann, H. Kikuchi, and A. Godil, in PROC. SPIE **2379**, 228. (1995).
4. K. Kondo, M. Oka, H. Wada, T. Fukui, N. Umez, K. Tatsuki, and S. Kubota, Optics Letters, **23**, 195 (1998).
5. H. Masuda, A. Nogami, K. Kimura, N. Eguchi, and S. Kubota, in Advanced Solid-State Lasers, OSA Technical Digest, (Optical Society of America, Washington DC, 2001), 323.
6. N. Eguchi, M. Oka, Y. Imai, M. Saito, and S. Kubota, in PROC. SPIE **3740**, 394 (1999).
7. M. Takeda, M. Furuki, T. Ishimoto, K. Kondo, Jpn.J.Appl.Phys., **39**, 797, (2000).

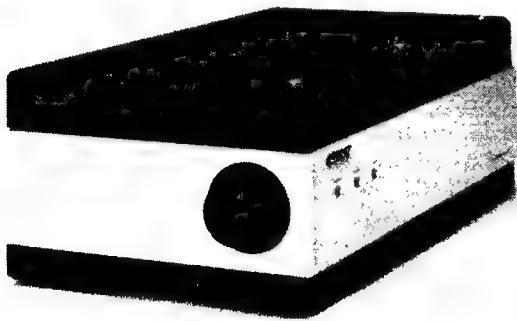


Fig. 1. CW 266 nm laser, UW-1010.

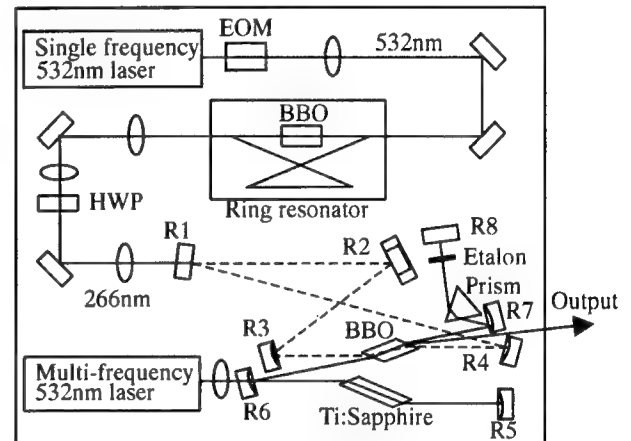


Fig. 2. Schematic of a 195 nm laser.

Wavelength	266 nm
N.A. of objective lens	0.9
Focal length of objective lens	2 mm
Optical magnification	95 x or 380 x
CCD pixel size	$4.65 \times 4.65 \mu\text{m}^2$
Number of active CCD pixels	1.4 million 1360 (H) x 1024 (V)
Field of view @ 95 x @380 x	$67 \times 50 \mu\text{m}^2$ $16.6 \times 12.5 \mu\text{m}^2$

Table 1. Specifications of 266 nm DUV microscope.

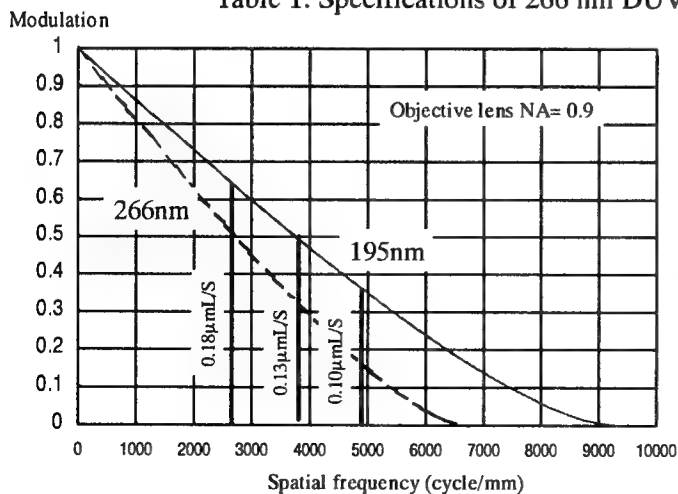


Fig. 3. Modulation transfer function.

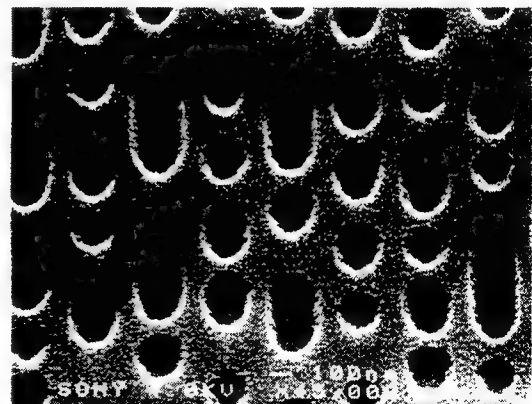


Fig. 4. 30 GB optical disk mastering using 266 nm laser. (Track pitch = $0.30 \mu\text{m}$, 3T pit length = $0.155 \mu\text{m}$).

F₂ lasers: precise shaping and trimming of photonic components

Peter R. Herman, Kevin Chen, Jianzhao Li, Midori Wei,

Department of Electrical and Computer Engineering, University of Toronto,
10 King's College Rd., Toronto, ON, M5S 3G4, Canada;

Jürgen Ihlemann, Gerd Marowsky

Laser Laboratorium Göttingen, Hans-Adolf-Krebs-Weg 1, 37077 Göttingen, Germany

Peter Oesterlin and Berthold Burghardt

MicroLas Lasersystem GMBH, Robert-Bosch-Breite 10, 37079 Göttingen, Germany

Summary

The F₂-laser Nanofabrication Facility at the University of Toronto is aimed at demonstrating the utility of applying progressively shorter wavelength lasers in micro-structuring transparent optical materials (glasses, ceramics, semiconductor materials) and in laser printing of miniature optical devices directly inside optical fibers and optical circuits.

The F₂-Laser Nanofabrication Facility consists of a Lambda Physik F₂ laser that delivers 30-mJ, 15-ns pulses at 157 nm wavelength, and 200-Hz repetition rate. The MicroLas optical delivery system can be configured for doublet imaging using CaF₂ lenses with a resolution of 5-10 micron or Schwarzschild imaging with a resolution of <1 micron. The laser beam is delivered to computer-controlled xyz stages on an optical table stabilized for submicron precision and repeatability. This unique laser processing system offers 100-fold higher fluence than current laser lithography systems that are based on excimer lasers and is the first attempt in the world to integrate 157-nm laser and optical processing to showcase photonics and lab-on-a-chip applications to industrial users.

For fused silica and related glasses, the 7.9-eV laser photons drive strong material interactions at the optical band-edge, reducing microcrack formation and improving process control over that normally attainable with longer wavelength lasers. The strong interactions also lead to small and smooth excisions, offering depth control on a scale of tens of nanometers. The 157-nm beam homogenization system and 25X Schwarzschild's lens provide a uniform (+/- 5%) on-target fluence of 3 J/cm² in a 0.25 mm x 0.25 mm field. Large area structures can be excised with lateral feature sizes as small 500 nm. The large 0.4-NA imaging lens also supports small channel excisions having steep walls. Both mask projection and direct write techniques have been employed to excise smooth surface relief structures in various grade glasses. Examples of laser fabricated phase-masks and rib waveguides will be presented.

Unlike traditional ultraviolet lasers, the 7.9-eV photons from the F₂ laser directly accesses the bandgap in germanosilicate glasses, providing a strong and direct channel for inducing large

refractive index changes in optical fibers and planar waveguides. A summary of F_2 -laser photosensitivity studies are presented together with an assessment of the prospects for shaping useful photonics structures directly inside the germanosilicate waveguides. Strong photosensitivity responses are noted especially for standard telecommunication fibers and planar optical waveguides without the need for enhancement techniques such as hydrogen loading. Because the 157-nm radiation is strongly absorbed in the germanium-doped guiding layers, non-uniform changes to the refractive index are noted under certain exposure conditions. Such conditions offer opportunities for trimming phase errors in interferometric devices and trimming waveguide birefringence. One interesting aspect of hydrogen-loaded waveguides is the ability of the 157-nm photons to 'lock-in' a permanent photosensitivity enhancement for longer wavelength sources. This enhancement is associated with Si-OH and Ge-OH defect formation. Strong (40-dB) and stable Bragg gratings were formed in such pre-treated fibers with 248-nm KrF-laser light, even for samples pre-annealed to out-diffuse the hydrogen. This F_2 -laser pretreatment enhances the ultraviolet photosensitivity by several orders of magnitude, without the aging related disadvantages of the standard hydrogen soaking. The unique opportunities for F_2 -laser photosensitivity applications in shaping and trimming photonic components will be outlined in this presentation.

The micromachining and photosensitivity results demonstrate broad applications for fabricating telecommunication devices, general optical components, and biological devices.

For more information: <http://www.ecf.utoronto.ca/~hermanp/publications.htm>

Progress in Dense Plasma Interferometry with Table-Top Soft X-Ray Laser

E. Jankowska^{a,c}, E.C. Hammarsten^a, J. Filevich^a, M.C. Marconi^b, and J.J. Rocca^a

^a Department of Electrical and Computer Engineering, Colorado State University, Fort Collins, CO 80523

^b Physics Department, Facultad de Ciencias Exactas y Naturales, Universidad de Buenos Aires, Argentina.

^c Department of Physics, Wroclaw University of Technology, Poland

Abstract: We report progress in soft x-ray interferometry of dense plasmas using a very compact 46.9 nm discharge-pumped laser. Soft x-ray interferograms of $\sim 300 \mu\text{m}$ dimension plasmas generated by $\sim 0.6 \text{ J}$ pulses from a Nd:YAG laser focused into a $< 30 \mu\text{m}$ diameter spot were recorded and analyzed. The spatial density distribution of the plasma was measured for densities up to $\sim 6.5 \times 10^{20} \text{ cm}^{-3}$.

Index terms: soft x-ray interferometry, dense plasma diagnostics, soft x-ray lasers, capillary discharge lasers.

The development of soft x-ray lasers has allowed the extension of plasma interferometry to a previously unreachable region of the plasma parameter space of high density and large plasma length [1]. The advent of compact saturated soft x-ray table-top lasers that can be fired at an increased repetition rate [2] in combination with new soft x-ray interferometers [3] now permits the application of this powerful plasma density diagnostics technique to the study of a variety of high density plasmas. We have previously used a capillary discharge pumped table-top soft x-ray laser operating at 46.9 nm in combination with an amplitude division interferometer to study the evolution of large-scale line-focus laser created plasmas [3]. This soft x-ray interferometer, that uses diffraction gratings as beam splitters, allows for significantly increased fringe visibility when compared to that obtained with the same laser source and a wavefront division interferometer based on Lloyd's mirror [4]. Interferograms of line-focus laser-created plasmas several mm in length, with densities up to $5 \times 10^{19} \text{ cm}^{-3}$, were previously reported.

In this paper we report soft x-ray interferograms that depict the evolution of a point-focus laser-created plasma. The electron density profiles constructed from the interferograms map plasma densities up to $\sim 6.5 \times 10^{20} \text{ cm}^{-3}$ in regions where the plasma is about $300 \mu\text{m}$ in diameter. The measurements correspond to Cu plasmas generated by focusing 0.62 J pulses from a Nd:YAG laser onto spots $< 30 \mu\text{m}$ in diameter ($\sim 7 \text{ TW/cm}^2$). The soft x-ray laser used in this experiment is a very compact capillary discharge-pumped Ne-like Ar amplifier that emits at a wavelength of 46.9 nm [2], corresponding to a critical density of $n_c = 5 \times 10^{23} \text{ cm}^{-3}$. The measurements were conducted using x-ray laser pulses of approximately 0.1 mJ and 1.2 ns . A description of the diffraction grating amplitude division interferometer used in the experiment was presented in a recent publication [3]. The plasma was imaged with 51.2X magnification into a gated soft x-ray sensitive detector composed of a microchannel-plate, a phosphor screen and a CCD array.

Figure 1 shows a series of interferograms corresponding to the fifth shots of the Nd:YAG laser on the same target location, a situation in which the observed plasma emanates from a $300\text{--}400 \mu\text{m}$ deep hole drilled by the previous four shots. The electron density evolution of the plasma was mapped firing the capillary discharge soft x-ray laser at different time delays with respect to the beginning of the Nd:YAG laser pulse. Abel-inversion of the fringe shift data reveals plasma electron density distributions such as that in Fig. 1, in which the electron density is plotted as a function of distance from the target. This electron density profile corresponds to an interferogram obtained 12.0 ns after the initiation of the laser pulse, the time at which the electron density is observed to reach a maximum value of $\sim 6.5 \times 10^{20} \text{ cm}^{-3}$ at a distance of $\sim 24 \mu\text{m}$ from the target plane. A pronounced density depression, caused by the interaction of the high intensity Nd:YAG laser beam with the expanding plasma is observed along the propagation axis of the laser beam. Comparison of such measurements with hydrodynamic code simulations can contribute to an improved understanding of the dynamics of high density plasmas.

This work was supported by U.S DOE grant No. DE-FG03-98DP00208. The development of the soft x-ray laser was supported by the National Science Foundation. We also gratefully acknowledge the support of the W.M. Keck Foundation. M.C. Marconi acknowledges the support of CONICET.

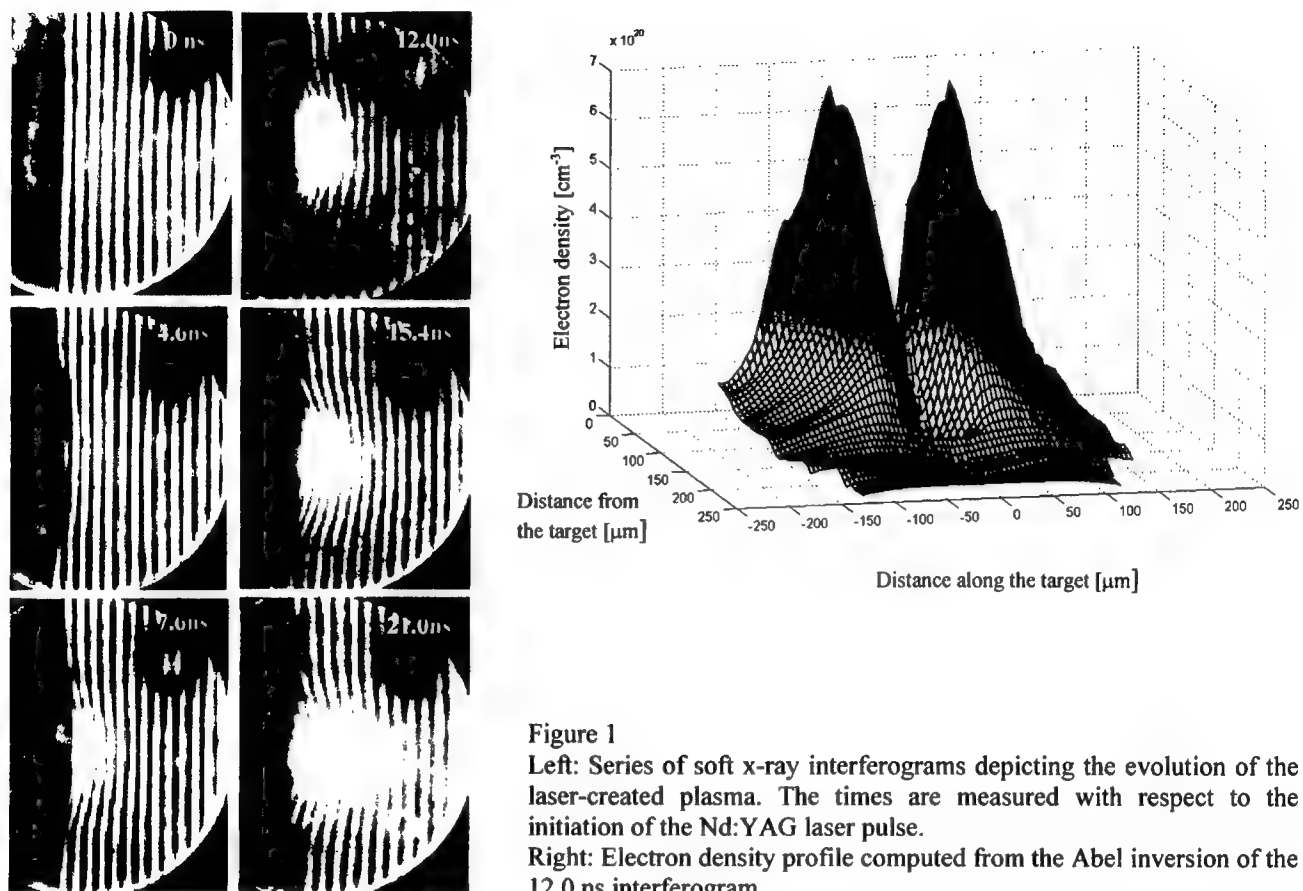


Figure 1

Left: Series of soft x-ray interferograms depicting the evolution of the laser-created plasma. The times are measured with respect to the initiation of the Nd:YAG laser pulse.

Right: Electron density profile computed from the Abel inversion of the 12.0 ns interferogram.

References.

1. L.B. Da Silva, T.W. Barbee Jr., R. Caubre, P. Celliers, D. Ciarlo, S. Libby, R.A. London, D. Matthews, S.Mrowka, J.C. Moreno, D. Ress, J.E. Trebes, A.S. Wan and F. Weber. "Electron density measurements of high density plasmas using soft x-ray laser interferometry". *Phys. Rev. Lett.* Vol.74, no20, pp 3991-3994, (1995).
2. C.D. Macchietto, B.R. Benware, and J.J. Rocca, "Generation of MilliJoule-level Soft X-Ray Laser Pulses at 4Hz Repetition Rate in a Highly Saturated Table-Top Capillary Discharge Amplifier," *Optics Lett.* Vol. 24, pp 1115-1117, (1999).
3. J. Filevich, K. Kanizay, M.C. Marconi, J.L.A. Chilla and J.J. Rocca. "Dense plasma diagnostics with an amplitude division laser interferometer based on diffraction gratings", *Optics Lett.* Vol. 25, pp 356-359, (2000).
4. J.J. Rocca, C.H. Moreno, M.C. Marconi and K. Kanizay, "Soft x-ray laser interferometry of a plasma with a table-top laser and Lloyd's mirror", *Optics Lett.* Vol. 24, pp 420-422, (1999).

Ultraviolet and Blue Lasers and their Applications

Wednesday, 1 August 2001

WB1: Visible Solid State Lasers and Amplifiers

WB2: Novel Incoherent Sources

Wednesday Missing Paper

WB2.1 "Curing with UV Lamps", J. Okamitsu and D. Harbourne, *Fusion UV Systems, Inc., Gaithersburg, MD, USA.*

Solid-state blue laser technology

Juan L. A. Chilla, A. Caprara, E. Mao, L. Spinelli, W. Seelert, J. Rosperich, A. Salokatve
Coherent Inc.
5100 Patrick Henry Dr.
Santa Clara, CA 95054

Solid-state lasers in the green are available from many companies, they are based on diode pumping and intracavity frequency doubling of Nd:YAG or Nd:Vanadate. A similar source emitting in the blue has been elusive due to the lack of a suitable gain medium. Many applications that have been developed using air-cooled argon ion lasers will benefit from the availability of a more efficient solid-state solution.

Semiconductors are in many ways ideal laser materials. They are suitable for both optical pumping and direct electrical pumping, they are able to produce high optical gain and their quantum efficiency is high. Their emission is not limited to discrete lines set by atomic levels but can instead be chosen by design. Similarly multi-layered structures with varying index of refraction can be grown with great precision.

To date, the typical implementation of semiconductor laser is what is commonly known as a "diode laser", variations of which can be found in your CD drives and carrying phone conversations and data through optical communication lines. They are electrically pumped monolithic devices, contained within a "chip" of semiconductor material with typical dimensions below the millimeter. In spite of its many applications, this particular implementation of the semiconductor laser severely limits the performance of semiconductors as laser materials.

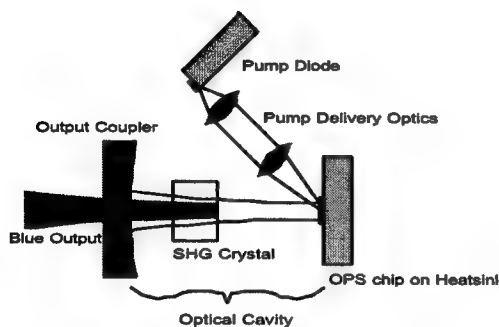


Figure 1: Frequency doubled optically pumped semiconductor laser.

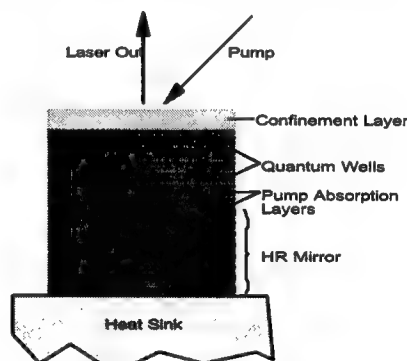


Figure 2: The OPS chip (optically pumped semiconductor).

Our approach to this problem is to use the semiconductor as we would any other solid-state laser material, pumping it optically and building it into a conventional laser cavity (Fig. 1). By using optical pumping we avoid the optical losses associated with doped materials, and we gain the ability to deliver the energy precisely where it is needed, while at the same time the fabrication process is simplified. By not restricting ourselves to a monolithic implementation we can use discrete optical components and free space propagation to obtain the desired characteristics of the output beam. The ability to access the intracavity radiation allows us to include a frequency doubling crystal and expose it to high circulating power [1].

The OPS chip (Fig. 2) consists of two sections, both semiconductor alloys grown by MBE epitaxy. The top section is the gain medium and the bottom section is a high reflecting mirror that constitutes one of the ends of the cavity. The gain at 976 nm is provided by narrow layers of InGaAs (quantum wells), the composition of the spacer layers is chosen such as to make them transparent to the laser wavelength, and strongly absorbent to the pump wavelength (around 800 nm) [2]. With this arrangement, all of the volume of the gain section is available for pump absorption, and the carriers that are generated decay rapidly to the lower energy levels available at the quantum wells, where population inversion is achieved.

The quantum wells are located at the antinodes of the standing wave pattern of the linear resonator. This periodic gain structure eliminates any possibility of spatial hole burning, making it ideal for single longitudinal mode operation. This is particularly important for intracavity frequency doubling, where nonlinear competition between modes can generate severe fluctuations of the laser output.

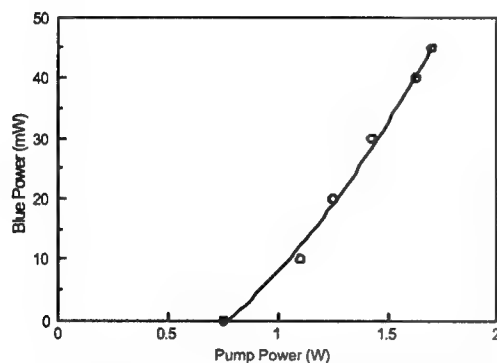


Figure 3: Pump conversion to the blue, R&D laboratory set-up.



Figure 4: Sapphire™ 488-20: solid-state blue laser.

With typical conversion efficiencies of nonlinear crystals, in order to obtain tens of milliwatts of output power in the blue it is necessary to achieve tens of watts of circulating intracavity power in the fundamental IR. An optically pumped semiconductor chip placed in a low loss cavity is able to maintain those levels with less than 2 watts of pump, easily obtained from a single broad area diode laser. Figure 3 shows results for conversion from pump radiation to blue using this technology.

After successfully demonstrating the optically pumped semiconductor laser technology (OPSL™) [1], we set out to develop a product, the result of our efforts (Fig. 4) was launched last May with the commercial name of Sapphire™ [3]. The laser, with a power specification of 20 mW, was designed for the OEM market where it is expected to replace power hungry Ar ion lasers in next generation instruments for applications such as DNA sequencing, reprographics and silicon wafer inspection.

References

1. US Patent No. 6167068, US Patent No. 5991318
2. M. Kuznetsov et al, IEEE Photonics Technology Letters, vol. 9 (1997), p. 1063.
3. http://www.coherentinc.com/cohrLasersDPSS/assets/applets/sapphire_ds.pdf

Upconversion Green Fiber Amplifier

Efrain Mejia B., Andrei Senin, J. Gary Eden

University of Illinois
Electrical and Computer Engineering Department
Optical Physics and Engineering Laboratory
607 E Healey Street
Champaign, IL 61820

Several compact green sources have been demonstrated in the past decade. The low efficiency normally associated with frequency doubling has been overcome in the commercially available 532 nm microlasers based in diode pumped Nd:YVO₄ by intra cavity frequency doubling. The fact that the 1064 nm signal is generated in a crystal ensures that the green emission has certain characteristics such as a narrow line width, linear polarization, and a stable wavelength. The availability of green laser sources having these characteristics offers the possibility for numerous applications in spectroscopy and communications. Also, green lasing has been demonstrated at around 545 nm in holmium- and erbium-doped fluorozirconate fibers¹⁻³. However, to obtain narrow linewidths and wavelength stability in these lasers, it is necessary to introduce bulk components. This complicates the design of these systems. In this work, we demonstrate an alternative that takes advantage of the high wavelength stability and single line characteristics of an atomic source, as well as the attractive characteristics of rare earth-doped fibers as *visible* amplifiers. In these experiments, small signal gains up to 12 dB were measured. Also, more than 3 mW of amplified signal was obtained when injecting 0.6 mW into the fiber.

A Ho³⁺:ZBLAN, 2500-ppm by weight, 2.4 μ m core diameter, and 0.28 NA fiber was used. Figure 1 shows the experimental apparatus. The pump signal, produced by a dye laser operating at 643.5 nm, passes through a dichroic mirror M1 and coupling lens L1. A counter-propagating probe signal is supplied by a He-Ne laser operating at 543.36 nm. The amplified signal is extracted using M1. In Figure 2, a partial energy level diagram for Ho³⁺:ZBLAN is depicted. The pump signal is absorbed by the ground state, exciting the ions to the metastable levels ⁵I₆ and ⁵I₇ through the intermediate state ⁵F₅. Then, re-absorption from these levels promotes the population to the metastable levels ⁵F₄ and ⁵S₂ via ⁵G₅ and ⁵F₃.

Figure 3 shows the pumping efficiency for a fiber 45.3 cm in length. As one can see, the 0 dB level is reached when 22 mW of pump power is launched. At this point the loss initially experienced by the probe signal is compensated for by the gain of the active medium. The net effect is that the fiber is considered transparent at this power. A gain coefficient value of 0.153 dB/mW was obtained. This value is the slope of the tangent line to the curve that intersects the origin.

In Figure 4 is plotted the measured gain as function of the launched probe signal. The circles correspond to a 43.5 cm long fiber and the crosses and squares are for a fiber 35 cm in length. The coupled pump power was 90 mW. Please note that there is a linear gain region for injected powers below -13 dBm ($50 \mu\text{W}$) that constitutes the shoulder of the saturated region. The maximum power available for the probe signal ($-2\text{dB}=600 \mu\text{W}$) was not sufficiently high to saturate the system since the gain has decreased less than 2 dB. Also, the maximum amplified signal obtained was more than 3 mW.

In conclusion, we have demonstrated amplification at 543.36 nm in a holmium-doped fluorozirconate fiber pumped at 643.5 nm. This is the first time, to our knowledge, that the characteristics of Ho^{3+} :ZBLAN fiber as an amplifier in the green has been investigated.

- [1] Allain, J.Y.; Monerie, M.; Poignant, H., "Room temperature CW tunable green upconversion holmium fibre laser," *Electron. Lett.*, Vol 26, No. 4, pp. 261 – 263, Feb. 1990.
- [2] Whitley, T.J.; Millar, C.A.; Wyatt, R.; Brierley, M.C.; Szebesta, D., 'Upconversion pumped green lasing in erbium doped fluorozirconate fibre,' *Electron. Lett.*, Vol 27, No. 20, pp. 1785 – 1786, 1991.
- [3] Funk, D.S.; Eden, J.G.; Osinski, J.S.; Lu, B., "Green, holmium-doped upconversion fibre laser pumped by red semiconductor laser," *Electron. Lett.*, Vol. 33, No. 23, pp. 1958 – 1960, 1997.

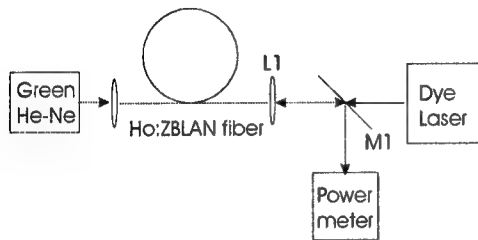


Figure 1. Experimental Apparatus.

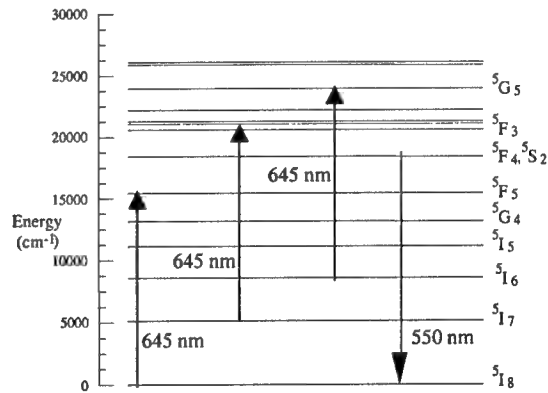


Figure 2. Energy levels for Ho^{3+} :ZBLAN

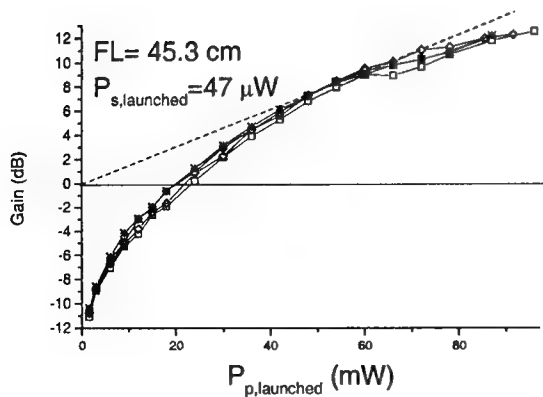


Figure 3. Pumping Efficiency.

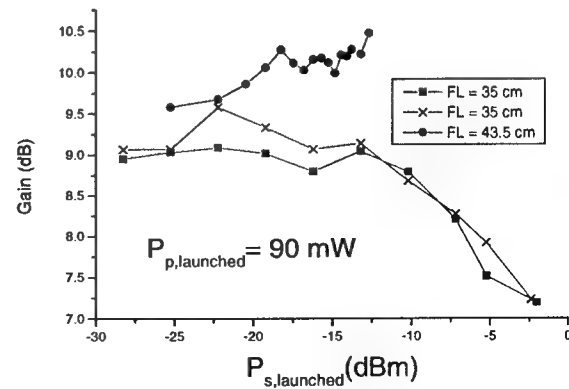


Figure 4. Measured gain for different fiber lengths (FL).

MICRODISCHARGE ARRAYS: A NEW FAMILY OF UV SOURCES

Sung-Jin Park and J. Gary Eden
Laboratory for Optical Physics and Engineering
Department of Electrical and Computer Engineering, University of Illinois
1406 W. Green St., Urbana, Illinois, 61801
Tel: 217-333-4157, Fax: 217-244-7097

We report recent progress in the fabrication of micro hollow cathode discharge arrays that can be utilized as a miniature UV generation source having the size of tens ~ hundreds of microns. Microdischarges exhibit several novel characteristics, for example, high power loading (tens ~ hundreds of kW/cc) and high operational pressure. And especially, we can easily obtain any wavelength ranges of radiation from the device just by changing discharge gases. Furthermore, since various types of device structures and device materials have been developed, a number of lighting applications are available.

Since our laboratory first demonstrated Si microdischarge devices in 1997,¹ we have developed and reported on various types of devices which were designed for several targeted applications, e.g. lighting, display, microlaser and so on.²⁻³ Recently, we have developed thin film microdischarge devices having a metal/polymer structure that is suitable for flexible device applications.³⁻⁴ These devices have a total thickness of ~30 μm , operating voltages below 90 V in neon, and operating pressures beyond one atmosphere. Most of the devices to be described employ a polyimide film as the dielectric, and metallic (Ni or Cu) foil serves as the cathode and a flexible support for the device. The polymer film, 5-10 μm in thickness, was spun onto the cathode, and the anode is a 200 nm thick Ni film or grid shaped metal screen. Cylindrical microdischarge cavities having discharge channel diameters between 20 and 150 μm were formed mechanically or with a pulsed laser, through the three layered structure. Like other polymer-based techniques, these devices offer processibility, cost effectiveness and chemical stability without any sacrifice of plasma discharge properties.

We have also successfully integrated microdischarge devices into large arrays using conventional MEM's techniques.⁵ The devices fabricated to date have square pyramidal cathodes, (50 μm)² in area at the base (Si wafer surface) and 35 μm in depth, produced by wet etching. The dielectric for the device consists of an ~8 μm thick polymer film and the multi-

layered dielectrics consist of 8 μm polymer and $\sim 1.0 \mu\text{m}$ $\text{Si}_3\text{N}_4/\text{SiO}_2$ layers. A 1500 \AA Ni film serves as the anode in this case. Two types of device arrays, ranging in size from 2×2 to 30×30 ($3.5 \text{ mm} \times 3.5 \text{ mm}$), have been fabricated. Our first tests involved arrays in which the devices have a common anode but more recent tests have been conducted with groups of 3×3 arrays on the same Si wafer but having separate power feeds. These arrays operate simultaneously at voltages as low as 210 V in 400 Torr of Ne (or Ne/Ar mixtures) and exhibit longer lifetimes than arrays having some power feed. Also, large arrays (30×30 in $4 \text{ mm} \times 4 \text{ mm}$ dimension) of Si microdischarge devices having separately addressable four 15×15 arrays operated continuously in Ne and Ne/Xe gas mixtures up to atmosphere (Fig.1). We will demonstrate deep UV generation from the arrays to excite phosphor and detailed operational characteristics and applications will be introduced.

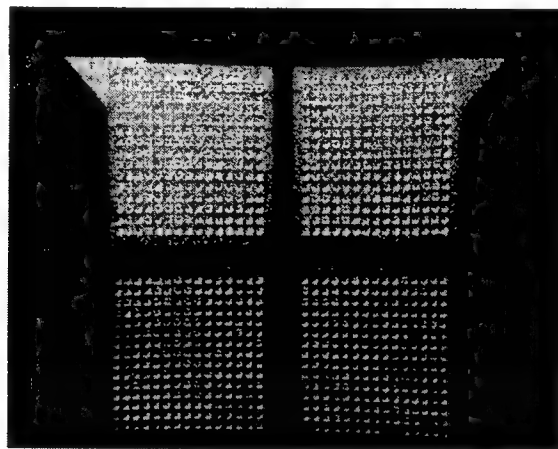


Fig. 1. Separately addressable 30×30 microdischarge arrays in Si wafer. The total area of arrays is 16 mm^2 .

REFERENCES

1. J.W. Frame, D.J. Wheeler, T.A. DeTemple, and J.G. Eden, Appl. Phys. Lett. 71(9) 1165, 1997.
2. J. W. Frame, P. C. John, T. A. DeTemple, and J. G. Eden, Appl. Phys. Lett. 72, 2634, 1998.
3. S.-J. Park, C.J. Wagner, C.M. Herring, and J.G. Eden, Appl. Phys. Lett., 77(2), 199, 2000.
4. S.-J. Park, C.J. Wagner, and J.G. Eden, IEEE Photonics Tech. Lett., 13(1), 61, 2001.
5. S.-J. Park, J. Chen, C. Liu and J.G. Eden, Appl. Phys. Lett., 78(4), 419, 2001.

AUTHOR INDEX

Artiukov, I.	MB1.1	Salokatve, A.	WB1.1
Backus, S.	MB1.2	Sasaki, T.	MB4.1
Bartels, R.	MB1.2	Seelert, W.	WB1.1
Bartolick, J.	MB4.2	Seminario, M.	MB1.1
Basting, D.	TuB1.1	Senin, A.	WB1.2
Behrendt, W.	MB4.2	Shlyaptsev, V.	MB1.1
Benware, B.	MB1.1	Silfvast, W.	MB3.1
Braley, D.	MB1.1	Spinelli, L.	WB1.1
Burghardt, B.	TuB1.4	Stagira, S.	MB2.1
Caird, J.	MB4.2	Tobey, R.	MB1.2
Caprara, A.	WB1.1	Villoresi, P.	MB2.1
Cerullo, G.	MB2.1	Vinogradov, A.	MB1.1, MB2.3
Chen, K.	TuB1.4	Wei, M.	TuB1.4
Chilla, J.	WB1.1	Yap, Y.	MB4.1
Drobshoff, A.	MB4.2	Yoshimura, M.	MB4.1
Ebbers, C.	MB4.2		
Eden, J.	WB1.2, WB2.2		
Eguchi, N.	TuB1.3		
Erlandson, A.	MB4.2		
Filevich, J.	MB1.1, TuB1.5		
Fрати, M.	MB1.1		
Gao, J.	MB2.2		
Hammarsten, E.	TuB1.5		
Hammersten, E.	MB1.1		
Harbourne, D.	WB2.1		
Herman, P.	TuB1.4		
Ihlemann, J.	TuB1.4		
Jankowska, E.	MB1.1, TuB1.5		
Kamimura, T.	MB4.1		
Kapteyn, H.	MB1.2		
Kubota, S.	TuB1.3		
Lalovic, I.	MB3.2		
Li, J.	TuB1.4		
Luther, B.	MB1.1		
Mancini, H.	MB1.1		
Mao, E.	WB1.1		
Marconi, M.	MB1.1, TuB1.5		
Marowsky, G.	TuB1.4		
Massey, W.	MB4.2		
Masuda, H.	TuB1.3		
Mejia B., E.	WB1.2		
Misoguti, L.	MB1.2		
Mori, Y.	MB4.1		
Murnane, M.	MB1.2		
Narduzzi, J.	MB4.2		
Nisoli, M.	MB2.1		
Oesterlin, P.	TuB1.4		
Okamitsu, J.	WB2.1		
Park, S.-J.	WB2.2		
Pascolini, M.	MB2.1		
Payne, S.	MB4.2		
Petersen, A.	MB4.3		
Poletto, L.	MB2.1		
Priori, E.	MB2.1		
Rocca, J.	MB1.1, TuB1.5		
Rosperich, J.	WB1.1		

**2001 IEEE/LEOS
Summer Topical Meeting**

30 July – 1 August 2001

**Ultralong Haul DWDM
Transmission and Networking**

**Copper Mountain Resort
Copper Mountain, CO**

IEEE Catalog Number: 01TH8572

ISBN: 0-7803-7100-3

ISSN: 1099-4742

The papers in this book comprise the digest of the meeting mentioned on the cover and title page. They reflect the authors' opinions and are published as presented and without change in the interest of timely dissemination. Their inclusion in this publication does not necessarily constitute endorsement by the editors, the Institute of Electrical and Electronics Engineers, Inc.

© 2001 by the Institute of Electrical and Electronics Engineers, Inc. All rights reserved.

Copyright and Reprint Permissions: Abstracting is permitted with credit to the source. Libraries are permitted to photocopy beyond the limits of U.S. copyright law, for private use of patrons those articles in this volume that carry a code at the bottom of the first page, provided the per-copy fee indicated in the code is paid through the Copyright Clearance Center, 222 Rosewood Drive, Danvers, MA 01923. For other copying, reprint, or republication permission, write to IEEE Copyrights Manager, IEEE Service Center, 445 Hoes Lane, P.O. Box 1331, Piscataway, NJ 08855-1331.

IEEE Catalog Number:	01TH8572
ISBN:	0-7803-7100-3
ISSN:	1099-4742



Ultralong Haul DWDM Transmission and Networking

Co-Chairs:

Gary Carter, *University of Maryland Baltimore County*, Baltimore, MD
Jonathan Nagel, *TerraWorx*, Shrewsbury, NJ

Technical Program Committee:

T. Carruthers, *Naval Research Lab*, Washington, DC
C. Davidson, *Tycom Laboratories*, Eatontown, NJ
V. Grigoryan, *Corvis Corporation*, Columbia, MD
A. Hasegawa, *Soliton Communications*, Kyoto, Japan

TABLE OF CONTENTS

Monday, 30 July 2001

MC1.	Advances in Ultralong Technology	
MC1.1	Ultra Long Distance Submarine DWDM Systems.....	3
MC1.2	Advances in Modeling Optical Fiber Transmission Systems	5
MC2.	PMD Mitigation	
MC2.1	Challenges of Implementing Ultra-Long Haul Networks on Embedded Fiber Systems.....	7
MC2.2	Transmission Limitations due to Polarization Mode Dispersion.....	9
MC2.3	Optical Compensation of Polarization Mode Dispersion	N/A
MC3.	Ultralong Terrestrial Systems	
MC3.1	Challenges of the Extreme Long Haul Terrestrial Transmission.....	11
MC3.2	Constraints on the Design on 2-Fiber Bi-Directional WDM Rings with Optical Multiplexer Section Protection	13
MC3.3	Raman Amplification in Ultra Long-Haul WDM Transmission Systems - A Time-Domain Perspective.....	15

Tuesday, 31 July 2001

TuC1.	Ultralong Architectures I	
TuC1.1	The Impact of Technology Advances in Optical Switching and Ultra-Long Haul Transport on Next Generation Intelligent Optical Networks.....	19
TuC1.2	Ultra-Long Haul DWDM for National Networks.....	21
TuC2.	Ultralong Architectures II	
TuC2.1	Novel Architectures for Long Haul DWDM Systems.....	23
TuC2.2	Ultra Long-Haul Terrestrial Transmission Systems	N/A
TuC2.3	Best Way to Build the All-Optical, Ultra-Long Haul Terrestrial Network.....	25
TuC3.	Dealing with Nonlinearities	
TuC3.1	Efficiency and Stability of Transmission Control of Long-Distance and High-Speed WDM Transmission using Solitons	27
TuC3.2	Carrier-Suppressed Dispersion-Managed RZ Transmissions using Novel OTDM Techniques with Phase Alternation.....	29
TuC3.3	Intra-Channel Nonlinear Effects in Dispersion Compensated DWDM Optical Networks	31
TuC4.	Ultralong with 40 Gb/s Channels	
TuC4.1	New Technologies Enabling Ultra-Long Haul DWDM.....	N/A
TuC4.2	High-Speed, High-Capacity, Long-Haul Terrestrial Networking	33
TuC4.3	Multi-Terabit/s WDM Transmissions at 40Gbit/s Channel Rate.....	35

Wednesday, 1 August 2001

WC1.	New Ultralong Technologies	
WC1.1	Advanced Fibers as Enabling Technology for ULH Networks.....	39
WC1.2	Hybrid & S-Band Raman Amplifiers	N/A
WC2.	High Capacity Ultralong Transmission	
WC2.1	Multi-Terabit Long Haul DWDM Transmission with High Spectral Efficiency.....	41
WC2.2	Strategies for Very Dense WDM ULH Terrestrial RZ Systems over All Types of Fibre.....	43
WC2.3	High Capacity Undersea WDM Transmission Systems - A Development Perspective	45

Ultralong Haul DWDM Transmission and Networking

Monday, 30 July 2001

- MC1: Advances in Ultralong Technology**
- MC2: PMD Mitigation**
- MC3: Ultralong Terrestrial Systems**

Monday Missing Paper

MC2.3 “Optical Compensation of Polarization Mode Dispersion”, K.B. Rochford, et. al., *YAFO Networks, Hanover, MD, USA*.

ULTRA LONG DISTANCE SUBMARINE DWDM SYSTEMS

Neal S. Bergano

TyCom Laboratories
250 Industrial Way West
Eatontown, NJ 07724
nbergano@tycomltd.com

Abstract: In today's internet age information flows across continents as easy as it flows across the office, thanks to undersea fiberoptic cable systems. The capacity of the next generation of undersea cables will far exceed 1Tbit/s; a level once considered exclusively the realm of laboratory experiments.

Introduction

For the past decade the transmission capacities of long-haul undersea lightwave systems have been maintaining a growth rate, which is faster than Moore's law¹ (Figure 1). This rapid growth rate has been made possible by the introduction of the Erbium-doped Fiber Amplifier (EDFA) and Wavelength Division Multiplexing (WDM) techniques. These large capacity enhancements have resulted from an increased understanding of the effects that can limit performance of WDM systems. Important strides have been made in areas of dispersion management, gain equalization, and modulation formats, which have made possible the demonstration of capacities exceeding 2 TB/s.

The Unrelenting March of Capacity

At the end of the 1980's the ultimate capacity of long-haul lightwave systems was in question. At the time it was widely known that the intrinsic capacity of optical fiber was very large; however, the capacity of transmission systems based on digital regenerators was not. This of course was due to the capacity bottleneck in the digital regenerator. The important paradigm shift came with the introduction of the EDFA.

Once the EDFA technology became available other insights and inventions enabled this rapid growth. First WDM techniques made it possible to use more and more of the available optical bandwidth in the fiber². Then, the technique of dispersion management was introduced along with new fiber types, which allowed more densely packed WDM channels³. Error correcting codes were introduced at the electronics end of the optical transmitters and receivers, which allowed for an increase in system margin⁴. Finally, new transmission formats were introduced which allowed the bit rate per channel to increase from 2.5 to 10 Gb/s⁵.

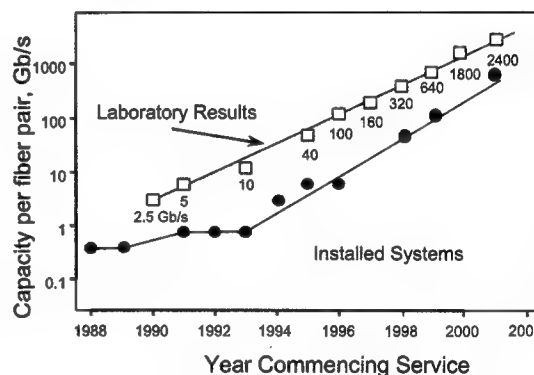


Figure 1 – Transmission capacity of laboratory experiments and installed systems vs. the year in which they were demonstrated/installed.

The transmission capacity of installed undersea cable systems has made a commensurate rise along with the increased transmission capacity of the laboratory experiments. Today, it takes 2 to 3 years from the time that the new technology is demonstrated in the laboratory until that technology is installed in the field.⁶

Looking Forward

The capacity of undersea fiber optic systems will increase by using more optical bandwidth and by using this bandwidth more efficiently. The conventional pass-band of the EDFA (C-Band) is about 40 nm wide, in the wavelength range of roughly 1526 nm to 1566 nm, corresponding to optical frequencies of 196.6 THz, to 191.6 THz. Thus, the conventional Erbium band has about 5 THz available for data transmission. The ultimate digital capacity that can be "fit" into the EDFA's C-Band will depend on how efficiently this bandwidth can be used for data transmission. This spectral efficiency expressed in (Bits/second)/Hz is defined as the system's average digital capacity divided by the average optical bandwidth of the system. The best-reported spectral efficiencies in WDM transmission range from a maximum of

1.0 bits/sec/Hz for very short (<100 km) distance, to roughly 0.5 bits/sec/Hz for transoceanic distance. Figure 2 shows the optical spectrum of 120 20 Gb/s channels after propagation over 6,200 km. In this experiment the maximum spectral density was 0.48 bits/sec/Hz.⁷

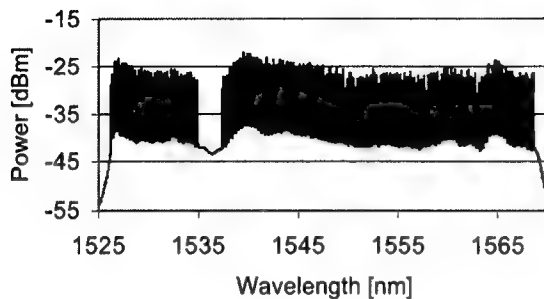


Figure 2 – Optical spectra of 120 20 Gb/s channels after traveling 6,200km.

Assuming that the spectral efficiency of installed transoceanic length systems could eventually increase to 0.5 bits/sec/Hz, gives an upper limit on the C-Band capacity of about 2.5 TB/s on a single fiber. The system's total capacity could also be improved by increasing the number of optical fibers in the cable. This becomes an engineering challenge to make the optical amplifiers more efficient in physical space; given the limited amount of space in the pressure vessels, and require less electrical power; given the practical limits of electrical power transmission in the cable.

We can continue to use this bandwidth/spectral efficiency idea to estimate the ultimate capacity of a transoceanic length system (practicality notwithstanding). The low attenuation window of typical telecommunications grade optical fibers is about 120 nm wide and extends from approximately 1500 nm to 1620 nm, corresponding to ~15 THz. Assuming the same 0.5 bits/sec/Hz spectral efficiency yields a potential capacity of about 7.5 TB/s. Erbium amplifiers can cover about 2/3 of this bandwidth by using both the C-band, and the newer "Long" wavelength band (or L-Band) in the wavelength range of about 1570 nm to 1610 nm. The leading optical amplifier candidate for the remaining short wavelength band (S-band) is stimulated Raman gain, which would be accomplished by pumping the transmission fiber at ~1430 nm. Commensurate with the required wide-band optical amplifier, is the need for wide-band transmission fibers that have a "flattened" chromatic dispersion characteristic. Such fibers have been reported recently that extend the concept of dispersion mapping by alternating both the sign and the slope of the dispersion. The resulting fiber

spans have relatively constant dispersion value over a broad-bandwidth. Ultimately, one could envision using the entire pass-band of the transmission fiber from 1300 nm to 1700 nm, corresponding to 55 THz. This would pose many challenges to fiber and system designers. For example, a very broad band optical amplifier would be needed (or combinations of amplifiers), and the added attenuation of the fiber at the shorter wavelengths would decrease the signal-to-noise ratios for WDM channels in that region.

Summary: We have come a long way from the time of the first digital regenerator undersea fiber optic cables of the 1980's which, at the time, had revolutionized international telecommunications. Optical fiber cable networks now provide the bulk of the long-haul telecommunications for voice and data on both land and across seas. Today, transoceanic cable networks are being built with multi-Terabit capacities; an achievement once thought to be the exclusive realm of "Hero" transmission experiments.

¹ Neal S. Bergano, "Undersea Fiberoptic Cable Systems: High-tech Telecommunications Tempered by a Century of Ocean Cable Experience," *Optics and Photonics News Magazine OSA*, Vol. 11, No. 3, March 2000.

² H. Taga, et al., "Over 4,500km IM-DD 2-channel WDM transmission experiments at 5Gbit/s using 138 in-line Er-doped fiber amplifiers," *OFC/IOOC'93*, postdeadline paper PD4, San Jose CA. Feb 1993.

³ F. Forghieri, R. W. Tkach, and A. R. Chraplyvy, "Fiber Nonlinearities and Their Impact on Transmission Systems," Chapter 8 in *Optical Fiber Telecommunications IIIA*, edited by Ivan P. Kaminow and Thomas L. Koch, Academic Press 1997.

⁴ J. L. Pamart, et al., "Forward error correction in a 5 Gb/s 6400 km EDFA based system," *Electron. Lett.*, Feb. 17, Vol. 30, No. 4.

⁵ Neal S. Bergano, et al., "320 Gb/s WDM Transmission (64x5 Gb/s) over 7,200 km using Large Mode Fiber Spans and Chirped Return-to-Zero Signals," *OFC'98*, paper PD12, San Jose Cal., Feb. 1998.

⁶ Neal S. Bergano and Howard Kidorf, "Global Undersea Cable Networks," *Optics and Photonics News Magazine OSA*, Vol. 12, No. 3 March 2001.

⁷ J.-X. Cai, et al., "2.4 Tb/s (120 x 20 Gb/s) Transmission over Transoceanic Distance with Optimum FEC Overhead and 48% Spectral Efficiency," *OFC'2001 PD20*, Anaheim, CA March 2001.

Advances in Modeling Optical Fiber Transmission Systems

C. R. Menyuk,* R. Holzlohner, and I. T. Lima, Jr.

University of Maryland Baltimore County

Computer Science and Electrical Engineering Department

TRC-201A, 1000 Hilltop Circle, Baltimore, MD 21250

phone: 410-455-3501, fax: 410-455-6500, E-mail: menyuk@umbc.edu

SUMMARY

In the past five years, the complexity and cost of optical fiber transmission systems has grown substantially. The greatly increased complexity of modern-day systems has led to a need for modeling methods that will allow engineers to design and optimize their systems in parallel with laboratory testbeds. A number of commercial enterprises now offer modeling tools that partially fulfill this need; however, current modeling methods are not equal to the task of accurately calculating bit error rates. Of course, there is much that current methods can do. They can be used to accurately optimize dispersion maps, modulation formats, channel spacings, and receiver bandwidths. Recently, my own group demonstrated an unprecedented agreement between theory and experiment over a distance of 24,000 km in calculating amplitude margins [1]. In this experiment, we observed voltage margins above which the error rate is greater than 10^{-6} due to marks being counted as spaces and below which the error rate is greater than 10^{-6} due to spaces being counted as marks. This achievement required us to use highly accurate models of both the receiver and gain saturation in the amplifiers.

At the same time, the holy grail of finding methods to accurately calculate bit error rates in real-world systems remains elusive. We have made important progress in this quest during the past year, and we will present those results here.

Before describing our recent progress, we note our view that this quest is not only of evident practical importance but is also a highly rewarding area of intellectual endeavor. The task of reconciling theoretical and experimental results, so that they agree to within the accuracy of both, more often than not yields unexpected insights into what is really important in the experiments. The great 19-th century mathematician, Henri Poincaré stated it best when he wrote (slightly abbreviated here), "Il est inutile de demander plus de précision (des calculs théoriques) qu'aux observations; mais on ne doit pas en demander moins." (There is no point in asking for more accuracy from theory than from the observations, but one should not ask for less.) [2].

The first advance that I will describe is the application of importance sampling to polarization problems in optical fiber transmission. In particular, we have addressed the problem of determining the outage probability of an ideal first-order compensator. In practical system design, the usual practice is to allocate some system margin for a particular

* Also at: Laboratory for Telecommunications Sciences, c/o USARL, 2800 Powder Mill Road, Bldg. 601, Rm. 110, Adelphi, MD 20783-1197

effect, *e.g.*, 2 dB of margin for polarization mode dispersion (PMD), with an assurance that the power penalty will be less than that margin with some low probability, *e.g.*, 10^{-6} . The challenge has been that it is impossible in practice to directly simulate the billions of fiber realizations that would be needed to show that the outage probability is less than 10^{-6} . Thus, workers in this field have resorted to stopgap procedures like demonstrating that the average differential group delay (DGD) is reduced as much as possible. Using importance sampling [3], we have found ways to bias the distributions of the DGD so that with 10^5 realizations or even less, we can accurately calculate the outage probability.

The second advance, which we call linearization, is based on the observation that noise beating with itself during the transmission through the optical fiber is normally quite small. One must, of course, take into account the noise beating with itself in the receiver. If noise beating with itself is small during transmission, then the noise components at the end of the transmission line will obey a multivariate Gaussian distribution [4]. We have applied this approach to our experimental dispersion managed soliton system over 24,000 km [1]. This application is a stringent test of our approach because the system is highly nonlinear. The noise components that we use are the Fourier components with phase and timing jitter removed, as is appropriate in a soliton system. The phase jitter has no effect on the received signal, but the timing jitter must be restored at the receiver. We have directly calculated the covariance matrix from Monte Carlo simulations, and we have validated the linearization assumption by computation of the timing jitter and the marginal distributions of the Fourier components. We note that this approach not only allows us to accurately calculate the probability distribution function of the receiver voltage for the marks and the spaces, but it also allows to calculate the probability contour plots for the entire eye diagram.

In conclusion, good modeling of optical fiber transmission systems has become critical to design them efficiently. Much has been accomplished in recent years, and my own group has contributed in important ways to this development. In the past year, we have applied importance sampling to calculating the outage probability of PMD compensators, and we have shown that it is possible to accurately calculate the probability distribution functions of the receiver voltage for the marks and the spaces. While much remains to be done to achieve the ultimate goal of accurately modeling bit error rates, much has been accomplished.

REFERENCES

1. R.-M. Mu, V. S. Grigoryan, C. R. Menyuk, G. M. Carter, and J. M. Jacob, "Comparison of Theory and Experiment for Dispersion-Managed Solitons in a Recirculating Fiber Loop," *IEEE J. Select. Topics Quantum Electron.*, vol. 6, pp. 248–257, 2000.
2. H. Poincaré, *Les méthodes nouvelles de la mécanique céleste—tome 1*, Gauthiers-Villars : Paris, FR, 1892, p. 1.
3. P. M. Hahn and M. C. Jeruchim, "Developments in the theory and application of importance sampling," *IEEE Trans. Commun.*, vol. 35, pp. 706–714, 1987.
4. J. C. Proakis, *Digital Communications*, McGraw-Hill : New York, NY, Chap. 2, pp. 17–79, 2001.



Challenges of Implementing Ultra-Long Haul Networks On Embedded Fiber Systems

Robert Kimball
Innovance Networks
Piscataway, NJ
rkimball@innovance.com

Abstract: *The explosion of fiber technology over the past few years has resulted in significantly longer reach networks. This paper will review some of the challenges, in terms of dispersion compensation, OSNR (optical signal to noise ratio), and fiber nonlinearities involved with implementing these technologies over legacy fiber.*

1. Introduction

The push for longer system reach in the terrestrial network is a base requirement for backbone optical networking systems¹. However, this presents significant challenges when trying to implement these networks on embedded fibers. Dispersion management, and the related problems of adequate OSNR and nonlinear penalties have significant impacts.

2. Overview of Installed Fibers

Optical fibers installed in backbone networks fall into two categories: standard fiber and NZ-DSF, which includes Lucent True Wave and Corning Leaf products. These fibers all differ slightly in terms of dispersion, dispersion slope, effective area, and loss. Table 1 summarizes the important parameters of the fibers most likely to be found in installed fiber plants.

Fiber	D Ps/nm/km	S Ps/nm ² /km	A _{eff} μm ²	α dB/km
TW-C	+2.8	0.068	50	0.205
TW-RS	+4.4	0.045	55	0.205
ELEAF	+4.2	0.085	72	0.205
SMF	+17.0	0.058	80	0.19

Table 1. Fiber Parameters

3. Dispersion Management

The fiber dispersion is generally addressed by collocating some type of dispersion compensating device at the amplifier nodes. The device may take the form of additional fiber, with generally much larger dispersion of the opposite sign, or of a grating device. The choice of technology depends on the network architecture and the applicability of broadband compensation vs. per channel compensation. Figure 1 shows the dependence of System performance on the power and the average dispersion.

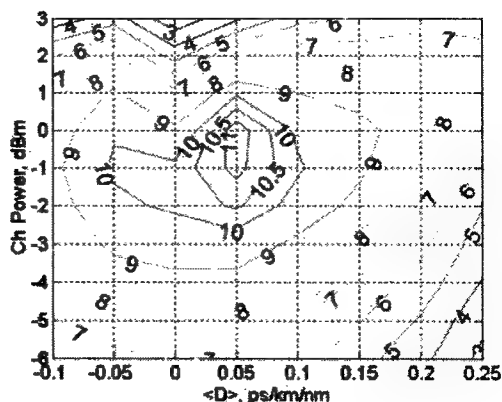


Figure 1. System Q vs. Power and Average Dispersion

Although 100% dispersion slope matching is the goal of many component vendors², these devices are generally not available. This means that per-channel dispersion compensation is needed at various places in the network. The variation of dispersion from span to span also provides significant challenges to the dispersion map designer. This variation comes from both the variation of lambda zero of the constituent fibers as well as the variation in span length. Another characteristic of the dispersion compensation devices is the fairly high insertion loss.

Optical Signal To Noise Ratio (OSNR)

The combination of accumulated ASE noise over many spans and the high gain operating regimes of the amplifiers impose severe constraints on the system OSNR. The OSNR is degraded as dispersion compensators, gain flattening filters and more advanced optical components are added to the optical path. Figure 2 shows the dependence of the overall noise figure of a line amplifier site on mid-stage loss.

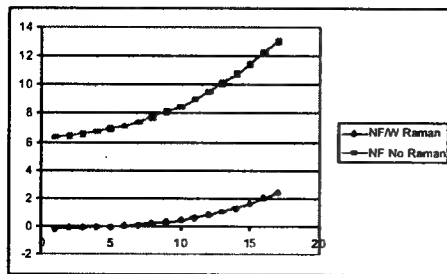


Figure 2. Noise figure vs. Mid-stage Loss

The other aspect of the OSNR that must be managed is the local deviations of the OSNR at each line amp site. The variability of the span length will not only cause large changes in the input power to the site, but also mandate large changes in the dispersion compensation device loss. The change in loss can be addressed in a number of ways, including employing a large number of amplifier codes to match the line amp design with the input power (using filters to correct for the gain tilts) or adding loss to the system to ensure constant gain throughout the system.

4. The Nonlinear Problem

The nonlinear effects of SPM, XPM, and FWM are well understood in the context of ultra long haul transmission³. The maximum intensity that can be launched into the transmission fiber is a critical parameter. This intensity is dependant on the effective area of the fiber, which varies among the fiber types. This limits the maximum available OSNR. The second place where the power is limited is in the dispersion compensator. Since dispersion compensating fibers tend to have small effective areas, the power is constrained at the input to the device. This imposes limitations on optical amplifier design.

5. 40 Gigabit Networks

At 40 Gbps the difficulty becomes much larger. The sensitivity of the dispersion map, and the tolerance of PMD and gain variations become much smaller. Forty gigabit networks will feature dynamic compensation of many of these effects. The available system reach will then be limited by the component variations of the dynamic devices.

6. Conclusion

The greatest challenge to the design of ultra long haul networks over embedded fibers is that all of the challenges related to dispersion and gain management are interdependent. Solutions that enhance one aspect, either OSNR or nonlinearity, tend to unfavourably impact the other. A balance must be met in order to maximize the performance of a given carrier's network.

¹ A. Wallace, "Ultra Long-Haul DWDM: Network Economics", OFC 2001 paper TuT1, Anaheim, CA, March 2001

² T. Veng et al., "New dispersion compensation module for compensation of dispersion and dispersion slope of non-zero dispersion fibers in the C-band" OFC 2001 paper TuH5, Anaheim, CA, March 2001.

³ F. Forghieri, et al., "Fiber Nonlinearities and Their Impact on Transmission Systems," Chapter 8 in Optical Fiber Telecommunications IIIA, edited by I. Kaminow and T. Koch, Academic Press 1997.

Invited Paper

Transmission Limitations due to Polarization Mode Dispersion

Alan E. Willner and Qian Yu

Dept. of Electrical Engineering - Systems
Univ. of Southern California, Los Angeles, CA 90089-2565
(213) 740-4664, F: (213) 740-8729, willner@milly.usc.edu

Polarization mode dispersion (PMD) [1-4] has emerged as one of the critical hurdles for next-generation high bit-rate transmission systems (≥ 10 Gb/s/channel). To first order, PMD can be represented by a differential group delay (DGD) between the two principal states of polarization. However, each of these two modes will be further split when encountering the next fiber segment, generating 4, 8, and even higher-order modes.

Older fiber may have a PMD value that is perhaps >100 times greater than present-day fiber. Even with new fiber, PMD, remains a major problem since: (i) there is still a small residual asymmetry in the fiber core, and (ii) slight PMD exists in discrete in-line components, such as isolators, couplers, filters, Erbium-doped fiber (EDF), modulators, and multiplexers. Therefore, even under the best of circumstances, PMD will still significantly limit the deployment 40-Gbit/s systems.

For a fixed PMD, DGD is a random variable that has a Maxwellian probability density function [5]. A critical aspect of PMD compensation is to account for the low-probability but high-degradation tails of this distribution. PMD is a stochastic, random process because: (i) each short discrete length of fiber will have a slightly different core asymmetry, (ii) the extent of the signal degradation caused by PMD is dependent on the state of polarization of light at a given point in the fiber link, and (iii) the state of polarization of an optical signal will wander randomly due to temperature changes and mechanical stress.

We will describe several research projects related to the challenges of PMD in high performance systems. A brief description of these topics are listed below:

1. PMD Emulator: High-PMD fiber is not commercially available, and, even if it were, it would not be able to rapidly explore a large number of different fiber conditions. Any real-fiber PMD emulator should have two key properties: (1) the DGD should be Maxwellian-distributed over an ensemble of fiber realizations at any fixed optical frequency, and (2) averaged over an ensemble of fiber realizations, the frequency autocorrelation function of the PMD emulator should resemble that in a real fiber, i.e., it should tend quadratically to zero outside a limited frequency range [5]. We have investigated a technique to accurately emulate PMD using multiple sections of PM fiber with rotatable connectors. We demonstrated that an emulator with 15 sections of PM fiber and randomly rotatable connectors generates different fiber realizations at any specific wavelength [6].

2. WDM PMD Compensation: A critical limitation in typical compensation techniques is that each wavelength-division-multiplexed (WDM) channel would require its own separate PMD compensator module. We have demonstrated simultaneous PMD compensation for four uncorrelated WDM channels using a single module that is designed to optimize the overall performance of a group of channels by reducing the impact of the DGD distribution tails. We showed that this simple compensation technique significantly reduces the probability of channel fading in a WDM system with four 10-Gb/s WDM channels and 40 ps of average DGD [7].

3. Tunable DGD Element: Typically, PMD compensators consist of a polarization controller followed by a fixed DGD section, such as a polarization-maintaining (PM) fiber [8]. The polarization controller is adjusted to optimize the system performance monitored by a feedback signal. Higher DGD values of the PM fiber can

provide good compensation of first-order PMD, but systems using this technique are susceptible to problems arising from higher-order PMD effects. For example, the compensator may locate a local minimum, rather than a true global minimum, during the continuous tracking of fiber PMD [9,10]. We showed that the variable-DGD compensator can alleviate the local-minimum problem, and provide superior performance compared to a fixed-DGD compensator by increasing the PMD tolerance limit [11].

4. Accurate Recirculating Fiber Loop: Recirculating fiber loop testbeds have been powerful tools in the research and development of medium-to-long-haul optical transmission systems [12]. In the presence of non-negligible polarization-dependent effects, specifically PMD, conventional recirculating loops are inadequate. PMD is unique because it is a stochastic process, whereas a recirculating loop exhibits some measure of deterministic behavior that artificially produces an unrealistic PMD distribution that is skewed towards higher differential group delays (DGD). We demonstrated a recirculating fiber loop testbed that is only ~100 km long and yet accurately replicates the true Maxwellian DGD distribution caused by PMD [13]. Our method used a single section of polarization-maintaining (PM) fiber and a lithium-niobate (LiNbO_3) polarization controller that is synchronized to the electronic loop controller circuitry. The tail of the power penalty distribution after 650 km transmission with an average PMD of ~22 ps is close to that expected from a Maxwellian distribution of DGD.

5. PMD-Induced RF Fading: Transmission of analog and digital subcarrier-multiplexed (SCM) signals over fiber will be severely affected by PMD [14]. The DGD between the fast and slow principal-states-of-polarization of an optical sideband in a SCM signal causes a phase difference in the corresponding received subcarrier signals, potentially leading to serious power fading of the recovered subcarrier signal due to destructive interference [15]. We investigated the statistics of PMD-induced power fading as a function of DGD for DSB-SCM and SSB-SCM signals. We found a similar susceptibility to PMD-induced power fading for both modulation formats in the absence chromatic dispersion. A significant improvement in the worst case power fading penalty (~20 dB) is achieved by using a dynamic first-order PMD compensator [16].

References

1. C.D. Poole and R.E. Wagner, *Electron. Lett.*, vol. 22, pp. 1029-1030, 1986.
2. N. Gisin, R. Passy, J.C. Bishoff, and B. Perny, *IEEE Photon. Tech. Lett.*, vol. 5, pp. 819-821, 1993.
3. J.P. Gordon and H. Kogelnik *Proceedings of the National Academy of Sciences*, vol. 97, no. 9, April 2000.
4. C.D. Poole and J. Nagel, in *Optical Fiber Telecommunications*, vol. IIIA, pp. 114-161, I.P. Kaminow and T.L. Kkoch, eds., Academic Press, 1997.
5. M. Karlsson and J. Bretel, *Optics Letters*, vol. 24., pp. 939-941, 1999.
6. R. Khosravani, I.T. Lima, P. Ebrahimi, E. Ibragimov, A.E. Willner, and C.R. Menyuk, *IEEE Photonics Technology Letters*, vol. 13, pp. 127-129, 2001.
7. R. Khosravani, S.A. Havstad, Y.W. Song, P. Ebrahimi, and A.E. Willner, *ECOC*, paper 4.2.6, Munich, Sept. 2000.
8. F. Roy, C. Francia, F. Bruyere, and D. Penninckx, *Techn. Digest, OFC/IOOC'99*, San Diego, pp. 275-277, 1999.
9. R. Noé, et. al., *IEEE/OSA J. Lightwave Technol.* 17, 1602-1616, 1999.
10. Denis Penninckx, and Stéphanie Lanne, *Proc. ECOC '2000*, Munich, Germany, vol. 3, pp. 205-206, 2000.
11. Q. Yu and A. E. Willner, *Conference on Optical Fiber Communications '01*, MO2, Anaheim, CA (OSA, D.C.).
12. N. S. Bergano, and C. R. Davidson, *IEEE/OSA J. of Light. Tech.*, vol. 13, pp. 879-888, 1995.
13. Q. Yu, S. Lee, L. Yan, Y. Xie, O.H. Adamczyk, and A.E. Willner, *Conference on Optical Fiber Communications '01*, paper WT2, Anaheim, CA (OSA, D.C.).
14. C. D. Poole and T. E. Darcie, *IEEE/OSA J. Light. Tech.*, vol. 11, pp. 1749-1759, 1993.
15. R. Hofstetter, H. Schmuck, and R. Heidemann, *IEEE Trans. Microwave Theory Tech.*, 43, pp. 2263-2269, 1995.
16. O.H. Adamczyk, A.B. Sahin, Q. Yu, S. Lee, and A.E. Willner, *Conference on Optical Fiber Communications '01*, paper MO5, Anaheim, CA, March 2001 (OSA, Washington, D.C., 2001).

Challenges of the extreme long haul terrestrial transmission

Sergey Ten
TerraWorx Inc
595 Shrewsbury Avenue
Shrewsbury, NJ 07702
sten@terraworx.com

The fast growing Internet driven data traffic concentrates among relatively few major US cities. Most of these major centers of data traffic are located at the East and West Coasts and few cities in Midwest and Texas. Optimized data centric networks must provide express transport between these major nodes and thus the cost effective extreme long haul transmission system will be required. In order to minimize the cost per bit, unnecessary O-E-O regeneration should be eliminated in the routes with up to coast-to-coast length (7500 km). Unregenerated transmission over these extreme distances is routinely achieved in undersea networks by using the state of the art advances in transmission technology such as Forward Error Correction (FEC), Chirped Return to Zero (CRZ) data format, advanced fiber and dispersion maps.^{1,2} Moreover, in undersea systems span length is tightly controlled (typically 50 km) and ambient temperature is stabilized by enormous thermal mass of the ocean. Extreme long haul distances are much more difficult to achieve in terrestrial networks where span lengths are longer (80 km average) and vary between 20 km and 140 km, fiber types can be mixed and fiber parameters are often unknown, temperature of fiber varies with outside temperature and environment in the amplifier huts may not be tightly controlled. This paper discusses these challenges in detail and shows that the combination of undersea technology with recent advances in components and subsystems can enable the extreme long haul transmission over terrestrial networks.

The challenge of longer span length can be effectively resolved by distributed Raman amplification. The recent progress in powers and prices of the 14XX nm pumps makes Raman amplification technically and economically attractive. Distributed Raman gain partially compensates fiber loss and makes terrestrial spans look like shorter undersea spans. The higher Raman gain is employed in the transmission system the better optical signal to noise ratio (OSNR) can be achieved at the receiver³. However, Raman gain is limited by double Rayleigh back scattering, which results in the multi path interference (MPI) penalty that does not appear as an OSNR degradation due to its narrow band nature. It was shown that MPI limits Raman gain to about 15 dB in terrestrial fibers³. Employing higher channel powers can also increase OSNR but fiber nonlinearities eventually degrade system performance. Nonlinear impairments are dependent on the exact dispersion map and the modulation format. CRZ used in the undersea transmission shows better tolerance to fiber nonlinearities and better linear performance than non return to zero (NRZ) format⁴ commonly employed in classical terrestrial systems. Thus, CRZ is a good format of choice for the extreme long haul systems.

Clearly, in order to design an extreme long haul system and take into account all the trade-offs described above, very accurate transmission system models should be developed and the whole design process becomes a search for a compromise between OSNR and fiber nonlinearities. We developed and validated a simulator capable of simulating Raman assisted transmission over terrestrial networks. It is based on a simulator that models transmission in undersea systems with EDFAs^{5,6}. It was validated in many experiments and results are reported elsewhere^{5,6}. Raman assisted transmission is simulated based on the model described in Ref. 7. It accurately takes into account Raman interactions between pumps, signals, and noise, as well as noise generation and its dependence on the temperature. MPI caused by double Rayleigh back scattering is also computed and added to the receiver degradations.

We validated the performance of the simulator in the recirculation loop experiment. The transmitter generated 16 WDM channels from 1542.94 nm to 1554.94 nm with 100 GHz channel spacing. The modulation format is chirped return-to-zero (CRZ) at a line rate of 12.3 Gb/s. Channels are pre-emphasized to equalize optical signal to noise ratio (OSNR) at 7500 km and the resulting spectrum exhibits a power per channel ripple of 3 dB. At the receiver, the WDM channels are demultiplexed using an optical filter before BER is measured and Q factor calculated.

We computed Q-values for the cases of -3 dBm and -1 dBm power per channel launched into the fiber. The comparison between measured and computed Q are depicted in Figures 1(a) and 1(b). The maximum deviation after 7500 km is 1.3 dB, which we attribute to polarization dependent loss. Note that with 23% FEC overhead, $Q = 8.3$ dB corresponds to error-free transmission. With -1 dBm per channel average Q is 14 dB, thus providing an average system margin of 5.7 dB to the FEC limit. Thus we prove the feasibility of 10 Gb/s extreme long haul terrestrial transmission.

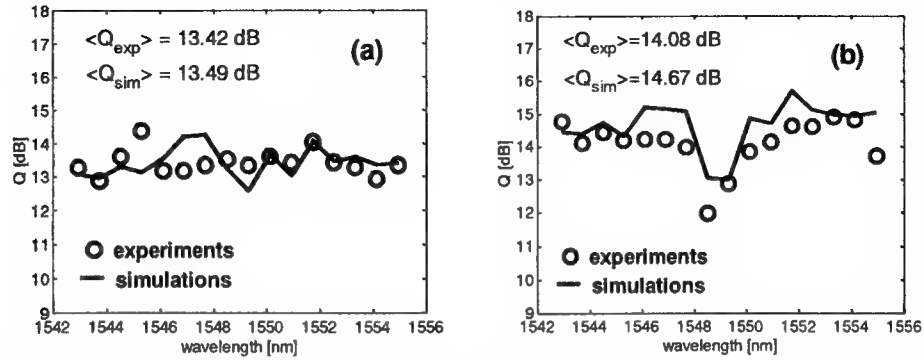


Figure 1. Measured (circles) and simulated (solid lines) values of Q after 7500 km. Power per channel (a) -3 dBm (b) -1 dBm.

At the extreme transmission distances dispersion slope of the transmission fiber results in a very large accumulated dispersion, which can be compensated on a channel-by-channel basis. Clearly, dispersion compensation modules (DCMs) with dispersion and dispersion slope compensation would facilitate dispersion management at the terminals and enable wide band extreme long haul transmission. Although, several novel technologies for the precise dispersion slope compensation are proposed, dispersion compensating fiber remains to be the most feasible and readily available solution^{8,9}. There has been a progress in the development of dispersion slope compensating fibers yet full slope compensation of widely deployed NZDS fibers is not achieved. We believe that in the next few years dispersion slope compensating DCM with full slope compensation becomes a reality and enable even wider band transmission over extreme distances. Finally, transmission fiber temperature variations result in dispersion variation¹⁰. For the 500-600 km terrestrial system these variations do not impact 10 Gb/s transmission. However, at the order of magnitude longer distance temperature induced dispersion variations impair transmission and dynamic dispersion compensation (DDC) must be invoked to reduce its impact. "Fortunately" the problem of dispersion variation is also affecting the introduction of 40 Gb/s technology and the development of DDC devices has very attractive business case for many component and subsystems companies. Currently DDC technology is maturing and becoming commercially available.

In conclusion, we are witnessing a very interesting moment when undersea transmission technology coupled with attractive business case and availability of enabling technologies can be applied in the emerging terrestrial data centric networks. We experimentally demonstrated that extreme 10 Gb/s transmission distances over 7500 km can be achieved in the terrestrial networks with sufficient margin for the real field deployment.

References:

- ¹ N.S. Bergano et.al. Optics & Photonics News, **12** (3), p. 32, 2001.
- ² J. -X. Cai et.al. OFC'01, PDP20, Anaheim, CA March 2001.
- ³ M. H. Eiselt et.al. ECOC-2000, Paper 4.4.4, Munich, Germany, September 2000.
- ⁴ B. Bakhshi et. al. OFC'01, WF-4, Anaheim, CA March 2001.
- ⁵ E.A.Golovchenko et al. OFC'99, paper ThQ3.
- ⁶ E.A.Golovchenko et al. IEEE Selected Top. in Quant. Electr., **6** (2000) p. 337.
- ⁷ H.Kidorf et al. IEEE Phot. Techn. Lett., **11** (1999) p. 530.
- ⁸ V. Srikant, OFC'01, TuH1, Anaheim, CA March 2001.
- ⁹ T. Veng et.al. OFC'01, TuH5, Anaheim, CA March 2001.
- ¹⁰ T. Kato et. al. Optics Letters, **25** (16) p.1156 (2000).

CONSTRAINTS ON THE DESIGN OF 2-FIBER BI-DIRECTIONAL WDM RINGS WITH OPTICAL MULTIPLEXER SECTION PROTECTION

João J. O. Pires

Dep. of Electrical and Computer Engineering and Instituto de Telecomunicações,
Instituto Superior Técnico, 1049-001 Lisboa, Portugal
Phone: +351 21 8418476 Fax: +351 21 8418472 E-mail: jpires@lx.it.pt

Introduction

Ring is an attractive topology to architect survivable wavelength division multiplexing (WDM) networks, because of the simple and efficient protection mechanisms that can be adopted. The protection can be obtained by switching individual wavelengths, in a so-called optical channel protection (OCHP), or by switching the entire WDM signal, in a so-called optical multiplexer section protection (OMSP) [1]. The OMSP scheme, despite being more vulnerable to faults in WDM equipment, is less expensive than the OCHP option, because it requires less switching hardware.

Bi-directional WDM ring architectures with OMSP can be implemented with 2 or 4 fibers. The 2 fiber configuration has a significant cost advantage over the 4-fiber counterpart, because requires half the number of switches, optical amplifiers and optical fibers. As a drawback, the number of wavelengths needed to implement a full-mesh connection duplicates, since half the wavelengths in each fiber are reserved for protection.

A sensible step in the design of a WDM ring is the selection of optical add-drop multiplexers (OADM) to use as network nodes. A possible strategy to construct OADMs consists on using arrayed-waveguide gratings (AWG) in a loop-back, or fold-back configuration. The fold-back configuration is more advantageous, since offers a better crosstalk performance and avoids the instabilities that can occur in rings with loop-back OADMs [2].

In this paper, we investigate the main constraints that limit the size of 2-fiber full-mesh WDM bi-directional OMSP rings using OADMs based on AWGs in a fold-back configuration.

OMSP WDM ring characterization

A 2-fibre bi-directional WDM ring uses a single fiber pair. This configuration requires that the two counterpropagating directions use two different wavelength bands. In this way, in the clockwise fiber the working traffic is mapped onto the "red" band, while in the counterclockwise fiber the working traffic is mapped onto the "blue" band. The "blue" band in the former fiber and the "red" band in the latter one are reserved for protection purposes.

Figure 1 illustrates the block diagram of an optical node of a 2-fiber bi-directional ring with OMSP. Each route within the node consists of an OADM, followed by an optical amplifier. The two 2x2 optical switches are used for protection purposes. In normal operation both the switches are in *bar state*. In the event of a failure, the switch at the edge of the node, near the faulted side, is switched to the *cross state*. With this action, the working band in one fiber is looped into the reserved band of the other fiber and proceeds in opposite direction. Note that, this node uses the band $\{\lambda_1, \lambda_2, \lambda_3\}$ for clockwise traffic and the band $\{\lambda_4, \lambda_5, \lambda_6\}$ for counterclockwise traffic. The presence of six wavelengths permits to implement a full-mesh connection in a network with 5 nodes. Actually, for a network with N nodes, the number of wavelengths required to connect every node to every other node in the ring is $N_\lambda = \lceil (N^2 - 1)/4 \rceil$, where $\lceil x \rceil$ is the smallest integer greater than or equal to x [3].

The OADMs used in the nodes are based on AWGs in a fold-back configuration. A fold-back OADM needs a larger AWG ($2M \times 2M$) than the loop-back counterpart ($M+1 \times M+1$) to support M wavelengths, but offers a better performance, as referred before. The OADMs used in the network under study should be able to support both the "red" and "blue" bands, in order to route all the capacity in the protection state. This feature implies that the 2-fiber bi-directional ring requires an OADM that must be double in size in comparison with the 4-fiber counterpart. Having, as a target, a ring with 16 nodes, the former configuration requires 64 wavelengths for a full-mesh connection, implying the use of a 128×128 AWG, while the latter one requires only a 64×64 AWG. Although, the 128×128 AWG device is currently fabricated, it will be shown in next section that the physical limitations are very serious impeding to achieve the referred target.

The network model considered in this paper consists of 60 km fiber spans, and network nodes with the configuration shown in Figure 1. A key parameter in performance analysis is the number of OADMs that a given wavelength passes without local processing (add/drop functions), denoted as N_m . For a full-mesh 2-fibre bi-directional OMSP ring with N nodes operating in the

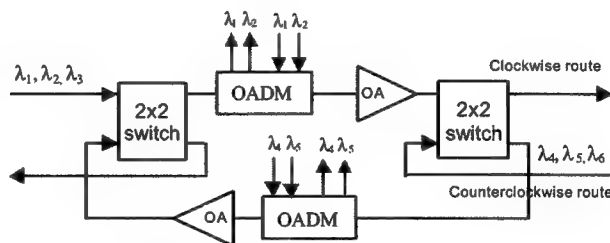


Figure 1: Configuration of a node of a 2-fiber bi-directional ring with OMSP.

normal state we have $N_m = \lceil (N-1)/2 \rceil - 1$, while for operation in the protection state it results in $N_m = (N-1) - \lceil (N-1)/2 \rceil$.

To estimate the maximum number of nodes, N , that the ring can accommodate, it is developed a transmission model that includes the effects of crosstalk from OADMs, optical amplifier noise accumulation, fiber, AWG and switch losses. In this model, it is assumed that the AWG bandwidth is wide enough, so that, the penalty due to pass-band narrowing affects is negligible, and that no significant dispersion degradation due to fiber (assumed as a large core non-zero dispersion fiber) is expected, for the distances involved. In normal state, optical amplifiers are used to compensate the overall losses (fiber, AWG and switches), and it is admitted that they have a flat gain, G_0 , and operate in a linear region, so that, the maximum output power that they can deliver is limited by the saturation power. In the protection state, the optical amplifiers at the beginning and at the end of the protection link, should have a lower gain, G_1 , to guaranty that the received power does not fluctuate significantly during the protection switching, while the other amplifiers should have a gain G_0 .

Results and conclusions

The transmission model involves the evaluation of the bit error rate (BER) of a signal at a given wavelength after propagating through N_m OADMs, for both the normal and protection states. It is assumed that the leakages from AWGs originate three types of crosstalk: interchannel crosstalk, intrachannel coherent crosstalk and intrachannel incoherent crosstalk. Using the same statistical modeling for the crosstalk as in reference 4, the BER and the system penalty can be evaluated, and hence the network size estimated. The analysis is realized considering a bit rate of 2.5 Gb/s, an AWG with an insertion loss of 10 dB and a 3-dB bandwidth of 20 GHz, an optical amplifier with a gain (G_0) of 27 dB and a noise figure of 4.8 dB, a switch with insertion losses of 1 dB and isolation less than -50 dB, and a fiber attenuation coefficient of 0.25 dB/km. In the protection state the edge amplifiers of the protection link have a gain (G_1) of 11 dB.

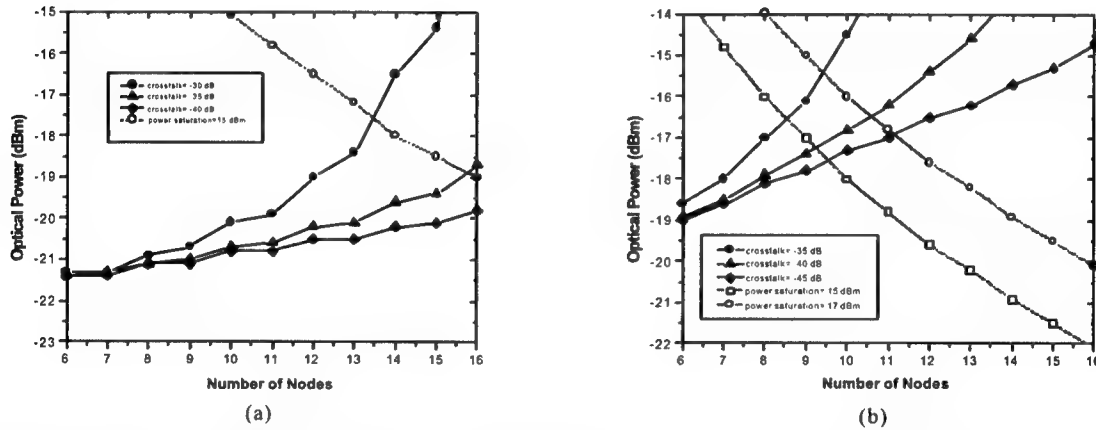


Figure 2: Optical power as a function of the number of nodes. Solid lines depict the signal input power required to achieve a BER of 10^{-12} , and dashed lines correspond to the maximum available power per wavelength for different values of the optical amplifier saturation power. (a) Corresponds to the normal state. (b) Corresponds to the protection state.

Figure 2a) shows the OADM input power required to achieve a BER of 10^{-12} in a 2-fiber bi-directional OMSP ring, operating in the normal state. This figure also indicates that a ring with 15 nodes seems to be feasible, provided that the AWG crosstalk is less than -35 dB, and the amplifier saturation power larger than 15 dBm. Figure 2b) corresponds to the same ring, but operating in the protection state. It is clearly noticeable a significant performance degradation in comparison with the normal state. Part of this degradation comes from optical SNR worsening, since the number of optical amplifiers cascaded in the protection path is larger than in the normal path. The other part is explained by the fact that the intrachannel coherent crosstalk increases as a consequence of the number of OADMs traversed without local processing (source of this crosstalk) also increases. Taking, as an example, a 10 node ring, and an AGW crosstalk of -35 dB, one observes a 2 dB additional penalty due to optical SNR degradation and a further 4.2 dB penalty coming from the intrachannel coherent crosstalk. In conclusion, the additional sources of degradation intrinsic to the protection state limits considerably the size of the ring under study, hardly permitting rings with more than 9 nodes, even if the amplifier saturation power increases to 17 dBm.

References

- [1] O. O. Gerstel et al., IEEE J. Select. Areas Commun., vol. 38, pp. 1885-1899, 2000.
- [2] D. T. van Veen et al., Proc. ECOC'99, vol. II, pp.48-49, 1999.
- [3] D. K. Hunter et al., Electron. Lett., vol. 34, pp.796-797, 1998.
- [4] J. J. O. Pires et al. Electron. Lett., vol. 35, pp. 73-75, 1999.

Raman Amplification in Ultra Long-Haul WDM Transmission Systems—A Time-Domain Perspective

Chien-Jen Chen, Minchen Ho, William S. Wong, Huan-Shang Tsai, Hak Kyu Lee, Paul Wysocki, Atul Srivastavas, and Yan Sun

Onetta, Inc., 71 Vista Montana, San Jose, CA 95134
(408) 428-2109; cjchen@onetta.com

Introduction: In ultra long-haul transmission system design, both undersea and terrestrial, the use of Raman optical amplifiers (ROAs) have become increasingly important. In distributed operation, Raman amplifiers can improve the optical signal to noise ratio (OSNR) by about 5 dB due to their low equivalent noise figure. The low noise nature of ROA can be used to increase system reach or to reduce inter- and intra-channel nonlinear impairments. Further advantages of using ROAs include flexibility in amplification band and simplicity in ROA construction. As high power pumps become available, Raman amplification becomes practical and favorable for ultra long-haul and high bit-rate systems. Considerate recent research efforts have been directed to the ROAs study of ROAs [1-3].

There are several effects limiting the usefulness of the Raman amplifiers. These effects include the transient effects [4], double Rayleigh backscattering (DRBS)/multiple path interference (MPI) [5], intensity noise induced by pump fluctuation, gain spectral dependence on signal loading and pump power, cross talk, etc. We will focus on the Raman transient effects and the double Rayleigh backscattering because they pose significant limitations on ROA application and they can be measured and modeled by a unified time-domain method.

Models: Both transient effects and double Rayleigh backscattering noise can be modeled by a set of time-dependent partial differential equations that include bidirectional pump-signal interactions through stimulated Raman scattering and Rayleigh scattering. The equations are written as follows:

$$\begin{cases} \frac{\partial}{\partial z} S^+ + \frac{1}{V_g} \frac{\partial}{\partial t} S^+ = g_R (P^+ + P^-) S^+ - \alpha_s S^+ + \gamma_s S^-, \\ -\frac{\partial}{\partial z} S^- + \frac{1}{V_g} \frac{\partial}{\partial t} S^- = g_R (P^+ + P^-) S^- - \alpha_s S^- + \gamma_s S^+, \\ \frac{\partial}{\partial z} P^+ + \frac{1}{V_g} \frac{\partial}{\partial t} P^+ = -\frac{\lambda_s}{\lambda_p} g_R (S^+ + S^-) P^+ - \alpha_p P^+ + \gamma_p P^-, \\ -\frac{\partial}{\partial z} P^- + \frac{1}{V_g} \frac{\partial}{\partial t} P^- = -\frac{\lambda_s}{\lambda_p} g_R (S^+ + S^-) P^- - \alpha_p P^- + \gamma_p P^-, \end{cases} \quad (1)$$

where z is the fiber length, t is time, λ is wavelength, S is the signal power, P is the pump power, V_g is the group velocity (which is assumed to be identical for both signal and pump), g_R is Raman gain coefficient, α is the fiber loss, and γ is the Rayleigh scattering coefficient. The subscripts s and p denote the signal and pump, while the superscripts $+$ and $-$ denote the forward and backward traveling waves, respectively.

Experiment and Simulation Results:

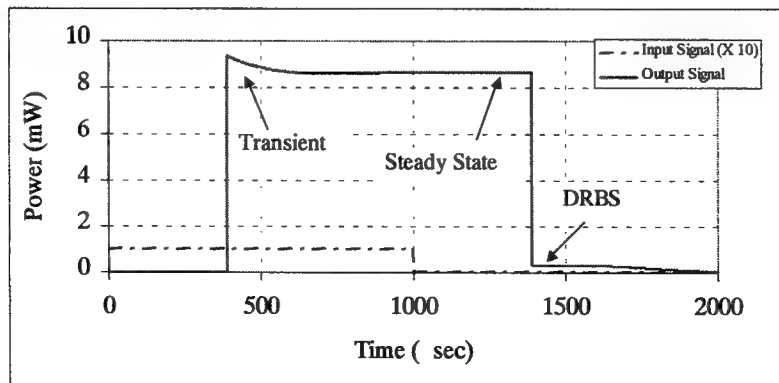


Fig. 1, A typical input and output of a Raman optical amplifier formed using 80 km TrueWave fiber. The output power transient and double Rayleigh backscattering are marked.

By using a square input pulse, we observed Raman transient effects and double scattering simultaneously. In Figure 1, we showed typical input and output powers for an 80 km TrueWave fiber. The pump wavelength was 1455 nm and the pump power was 0.8W. The signal wavelength was 1555 nm and the peak power was 0.1 mW. Fiber losses were 0.2 dB/km and 0.26 dB/km at the signal and pump wavelengths, respectively. The Rayleigh coefficients were $1.05 \times 10^{-7} \text{ m}^{-1}$ and $1.35 \times 10^{-7} \text{ m}^{-1}$ for signal and pump wavelengths, respectively. The output power transient at the leading edge of the output pulse was seen clearly [4]. When the pulse was long (greater than the fiber round trip time), the output power reached a steady state. When the input was turned off, the output signal terminated and was followed by a pedestal caused by double Rayleigh backscattering. The $\text{OSNR}_{\text{DRBS}}$ was found by calculating the relative powers of the steady state and the beginning of the pedestal.

We implemented the above-mentioned time-domain method experimentally to measure the $\text{OSNR}_{\text{DRBS}}$ for various input and pump conditions. This method yielded results that agreed very well with the results using the time-domain measurement proposed in Ref. 5. The method in Ref. 5 exhibited better sensitivity; while our method was suitable for theoretical analysis when our experiments were modeled using Eq. (1). The measured $\text{OSNR}_{\text{DRBS}}$ and ASE results were plotted along with the theoretical results in Figure 2.

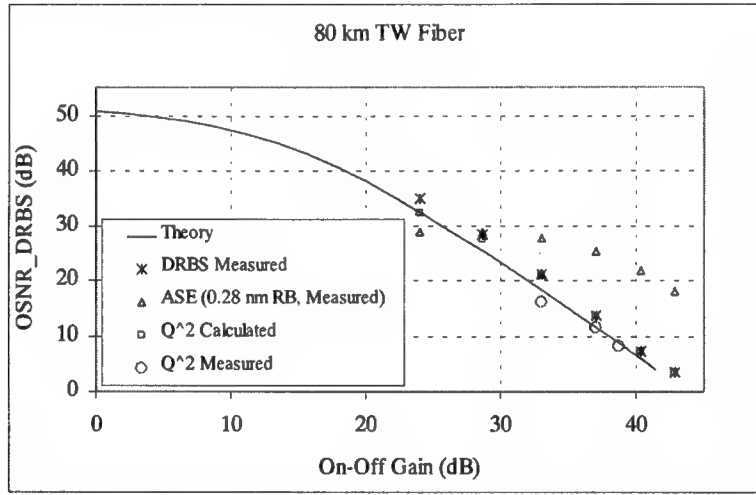


Fig. 2, Comparison of measured and theoretical DRBS results. Bit error rates were also measured and calculated.

The performance of the amplifier was evaluated by bit error rate (BER) measurement with proper dispersion compensation and signal power control. The BER is related to Q -factor [6], which may be approximated by $Q^2 = S / (N_f G h \nu B_e)$, where S is signal power, N_f is noise figure, G is gain, $h \nu$ is photon energy, and B_e is receiver electrical filter bandwidth. For ROAs, the ASE was wideband and was related to on-off gain, $G_{\text{on-off}}$, and equivalent noise figure, $N_{f,\text{equ}}$; while the DRBS noise shares the same bandwidth with signal. Due to the distributed nature of ROA, the DRBS noise had little correlation with the signal. The overall Q -factor was expressed as

$$Q^2 = \frac{S}{N_{f,\text{equ}} G_{\text{on-off}} h \nu B_e + S / \text{OSNR}_{\text{DRBS}}} \quad (2)$$

Both the measured and calculated Q -factors using Eq. (2) are plotted in Fig. 2. The agreement supports the validity of Eq. (2) and its related assumptions. The DRBS dominated the BER performance in the high gain region.

Summary: We have treated transient effect and DRBS in Raman optical amplifiers using a unified time-domain approach. Both phenomena impact performance of ultra long-haul DWDM systems using ROAs.

Reference:

- [1] Y. Emori, *et. al.*, *Electron. Lett.*, Vol. 35, No. 16, pp. 1355-1356, 1999.
- [2] M. Nissov, *et. al.*, paper TH3A.3, ECOC'97 Edinburgh, UK, 1997.
- [3] B. Zhu, *et. al.*, paper PD23, OFC'2001 Anaheim, CA.
- [4] C.-J. Chen and W. S. Wong, *Electron. Lett.*, Vol. 37, No. 6, pp. 371-373, 2001.
- [5] S.A.E. Lewis, *et. al.*, *IEEE Photon. Technol. Lett.*, Vol. 12, No. 5, pp. 528-530, 2000.
- [6] N.S.Bergano, *et. al.*, *IEEE Photon. Technol. Lett.*, Vol. 5, No. 3, pp. 304-306, 1993.

Ultralong Haul DWDM Transmission and Networking

Tuesday, 31 July 2001

- TuC1: Ultralong Architectures I
- TuC2: Ultralong Architectures II
- TuC3: Dealing with Nonlinearities
- TuC4: Ultralong with 40 Gb/s Channels

Tuesday Missing Papers

- TuC2.2 "Ultra Long-Haul Terrestrial Transmission Systems", J. Velselka and S. G. Grubb, *Corvis Corporation, Columbia, MD, USA*.
- TuC4.1 "New Technologies Enabling Ultra-Long Haul DWDM", S. El-Ahmadi and N. Robinson, *Nortel Networks, Richardson, TX, USA*.

The impact of technology advances in optical switching and long haul transport on next generation intelligent optical networks

Richard A. Jensen

Director of Advanced Technology
Sycamore Networks
150 Apollo Drive
Chelmsford, MA 01824
Richard.Jensen@sycamorenet.com

Abstract: *We discuss how advances in long haul transport and switching DWDM optical technologies are shaping next generation intelligent optical networks. Intelligent optical networking combines advances in switching and transport technologies along with network management to provide scalable, cost-effective customer solutions.*

Introduction

Advances in DWDM long haul transport and switching technologies are dramatically increasing the bandwidth capacity and distance reach of the public network. Simply providing more and more bandwidth alone is only a partial solution. Despite all the technological advances service providers find it increasingly difficult to maintain profit margins on traditional services that are not differentiated from their competition. They need to offer new, value-added services to differentiate themselves while also reducing operational expenses. Intelligent optical networking combines advances in switching and transport technologies along with software to provide scalable, cost-effective customer solutions.

Transport Technology Advances

Advances in hard-optic and electronic technologies are increasing the capacity and distance reach of the public and private networks [1-3]. Increasing the bandwidth lowers costs by reducing the amount of equipment required and reducing maintenance costs. Increasing the distance reach can dramatically lower network costs by reducing the number of expensive Optical to Electrical conversions (O/E) that is used to regenerate data signals [4].

Key Transport Technologies:

- Forward Error Correction Coding
- Raman Amplification
- New Optical Transmission Bands
- Denser Optical Channel Spacing
- Dynamic Gain Equalizers
- Dispersion and Dispersion Slope Management Techniques
- Polarization Mode Dispersion Compensation
- Reconfigurable Add/Drop Multiplexers
- New Transmission/Modulation Formats
- Wavelength Converters
- Increasing Bit Rates

Optical Switching Technology Advances

Great advances have been made in both All-Optical and O/E/O switches [5][6]. Advances in ASIC technologies have enabled O/E/O switches to provide signal grooming and other features for sizes up to 1Kx1K. Emerging all-optical technologies, for both transport switches and service switches are just coming to market and have the potential to provide bit-rate independent, reconfigurable and cost-effective network elements.

Emerging All-Optical Switch Technologies:

- 2D MEMs and 3D MEMs
- Bubble Jet
- Liquid Crystal
- Thermo-Optics
- Holograms

- Liquid Gratings
- Acousto-Optics

The Public Network Challenge

The public network challenge is how to best utilize the tremendous amount of raw data capacity that is created by new these technologies. The real issue lies in transforming that capacity into usable bandwidth that can be exploited for service delivery. The difficulty in effectively using the bandwidth originates at the physical layer of the public network and infrastructure. It is here that a new approach to network architecture is required.

Network Architecture Requirements:

- Cost Effective
- End-to-End Solution
- Scalable
- Carrier Class
- Future Proofed Against New Technologies
- Robust to Future Requirements

Intelligent Optical Networking provides an innovative and practical solution to network scaling and high-speed service delivery issues. This is done by combining switching and network management software to interconnect access, metro, and long haul transport systems. Bringing intelligence into the optical domain creates the opportunity to develop a flexible, high capacity network that will deliver an abundance of usable bandwidth and new bandwidth services.

Examples of New Bandwidth Services:

- Customer Network Management
- Optical Private Virtual Networks
- Protection as Quality-of-Service Metric
- Customized Fault Management Services
- Easier Service Provisioning and Maintenance

This powerful approach uses network management software and switching to interconnect transport systems into a seamless network fabric. It allows service providers to

combine existing legacy systems with state-of-the-art technologies and allows networks to incorporate new technologies as required. Different parts of the network can upgrade to new technologies at different rates to provide the most cost-effective solution. This future-proofs the network by allowing the access, metro and long-haul portions of the network to evolve independently.

Conclusion

Simply providing more and more capacity does not solve the bandwidth delivery problems faced by today's service providers. Intelligent Optical Networking transforms the raw capacity created by advances in technology into useable bandwidth. This enables service providers to differentiate themselves by rapid deployment of low cost flexible bandwidth services that unlock the potential of the optics in the physical layer of the network.

References

- [1] J.-X. Cai, *et al.*, "2.4 Tb/s (120x20 Gb/s) transmission over transoceanic distance using optimum FEC overhead and 48% spectral efficiency," Paper PD12, *Optical Fiber Communications Conference*, Anaheim, 2001.
- [2] S. Bigo, *et al.*, "10.2 Tbit/s (256x42.7 Gb/s PDM/WDM) transmission over 100km TeraLight Fiber with 1.28bit/s/Hz spectral efficiency," Paper PD25, *Optical Fiber Communications Conference*, Anaheim, 2001.
- [3] S. Yamamoto, *et al.*, "5 Gbit/w optical transmission terminal equipment using forward error correcting code and optical amplifier," *Electron. Lett.*, 1994, **30**, p. 254.
- [4] P. Hunt, "The search for ultra-long-haul transmission," *Lightwave*, May 22, 2001.
- [5] J. Leuthold, *et al.*, "All-Optical nonblocking terabit/s crossconnect based on low power all-optical wavelength converter and MEMS switch fabric," Paper PD16, *Optical Fiber Communications Conference*, Anaheim, 2001.
- [6] C. R. Doerr, *et al.*, "2 x 2 wavelength selective cross connect capable of switching 128 channels in sets of 8," Paper PD8, *Optical Fiber Communications Conference*, Anaheim, 2001.

Ultra-Long Haul DWDM for National Networks

Robert W. Tkach

Celion Networks

tkach@celion.com

The optical amplifiers offered the possibility of very long distance transmission almost immediately upon their availability in the early 1990s, as evidenced by their rapid adoption for regenerator free undersea systems spanning several thousand km. However, amplified systems for application in land-based networks have until very recently been focused on unregenerated lengths of several hundred km or less. There are technical reasons for this – undersea systems have generally used shorter amplifier spacing, while land-based networks have moved from approximately 40 km regenerator spacings to 80-100 km amplifier spacings. This straightforwardly leads to a reduction of about a factor of 10 in system length, for systems using the same technologies. Also, in land-based networks, the fiber plant is a given, and cannot be tailored to a specific system. In the last few years technologies have been introduced that have enabled the system length for an amplified system to be increased even at these long amplifier spacings: Forward Error Correction (FEC) chips are becoming available that offer coding gains of 10 dB; Raman amplification can effectively reduce the span loss by several dB; and improvements in modulation formats and dispersion compensation are offering increased margins.

But, beyond the technical, there are networking reasons that have limited the adoption of Ultra-Long-Haul (ULH) systems. National networks are much richer than undersea ones in their interconnection, and this leads to traffic matrices that require connections among many points, rather than very long routes carrying high capacity between two points. So previous DWDM systems were deployed with lengths of several hundred km or less, and these systems accommodated the large majority of connections without multiple hops. Indeed the standard amplifiers spacings on 80-100 km were chosen based on the notion that longer systems were not economically useful.

What has changed to alter this situation and make ULH systems economical at this time? Of course technology has improved, and reduced the cost penalty associated with long systems by allowing longer amplifier spacings. But further, the traffic matrices on national networks have begun to change under the influence of the shift to data traffic. Average connection distances have increased, and a greater concentration of traffic is seen among a smaller number of major nodes. Also, many networks have been built with shorter reach systems, and now as traffic increases, an attractive strategy is to overbuild with express routes, and use the older systems for local traffic and backhaul.

These technical, network, and business factors have combined to create an opportunity to apply ULH technology to national networks now.

NOVEL ARCHITECTURES FOR LONG HAUL DWDM SYSTEMS

Farzana I. Khatri

Sycamore Networks
4 Omni Way
Chelmsford, MA 01824
Farzana.Khatri@sycamorenet.com

Abstract: *Recent advances in DWDM technologies have significantly increased achievable capacities and distances for optical transmission systems. We discuss a recently deployed DWDM system architecture that provides important customer usability features, and gracefully scales to accommodate short, long, and ultra-long haul distances.*

Introduction

Today's service providers demand cost-effective transport solutions for optical DWDM systems in their networks [1]. In order to meet this demand, transport architectures must rapidly assimilate technology advances that increase transmission capacities, reduce the need for O-E-O regeneration, and improve system performance. Truly innovative transport architectures offer customer features such as advanced software capabilities, flexible client interfaces, and platform uniformity. These features help to further reduce service provider costs reducing deployment times, and operating expenses.

This paper reviews recent technology advances that are being deployed in the most advanced long-haul DWDM transport systems, as well as key customer usability features that further benefit service providers.

Enabling Technologies

Recent technology advances that allow us to harness the vast bandwidth of optical fiber include Raman amplification, Forward Error Correction (FEC), power and dispersion management, and L-band technologies [2]. These technologies have recently become sufficiently mature to deploy in service provider networks.

Raman amplification improves noise performance by extending optical amplification into the transmission span [3-4]. It enables transmission over ultra-long haul distances;

allows use of very long amplification spans, facilitates "hopping;" and eases future 40 Gb/s upgrades [5]. Raman amplification has been used in repeaterless undersea systems for years and has recently debuted in installed terrestrial systems due to the ever-increasing demand for bandwidth and distance.

FEC is a technique in which extra bits are electrically appended to the data stream, according to an encoding algorithm. These bits, when decoded at the receiver, allow the receiver to recognize accumulated transmission errors and correct them. As a result, FEC allows the system to operate at a very low Optical Signal to Noise Ratio (OSNR); this additional margin can be used to achieve longer transmission distances, reducing the need for O-E-O regeneration. FEC has been used for many years in undersea transmission systems [6-7]. FEC chips for telecommunications have recently become commercially available and are being used in deployed systems.

Power and dispersion management are both key enablers of long and ultra-long haul systems. DWDM channel powers must be carefully managed to avoid fiber nonlinearity which can severely degrade system performance. This not only includes pre-emphasis at the transmit side, but also power control at optical regeneration nodes. The channel powers are affected by gain ripple caused by cascaded EDFAs and passive optical components as well as by gain tilt from Raman amplification. If the channel power can be managed, longer transmission

distances can be traversed, alleviating the need for O-E-O regeneration. Careful dispersion management is another requirement for systems carrying 10 Gb/s or higher data rate traffic. If it is not properly managed, fiber slope mismatch between the installed fiber plant and the dispersion compensation fiber can cause a large dispersion variation over the different wavelength channel, degrading performance of edge channels. Dynamic gain equalization and dispersion compensation techniques are both topics of intense research [8-11].

Finally, the commercial development and availability of L- and S-band components such as EDFAs, lasers, and passive optics has the potential to double the capacity of terrestrial transport systems [3,12].

Customer Usability Features

An innovative way to reduce service-provider cost is to improve customer-usability features. Embedded software tools that allow quick and accurate provisioning and maintenance of optical networks can significantly reduce transport system operating costs and limit the possibility of human error [13]. Intelligent network management systems with automated features, such as performance monitoring and fault isolation and management, further simplify network operations and reduce cost. Flexible client interfaces (GigE, OC-48, OC-192, etc.) can reduce equipment required at central offices. Finally, a scalable and flexible architecture enables a greater range of applications for the platform, thereby reducing operations costs required for service providers to support multiple platforms.

Conclusions

Today's transport architectures must incorporate advanced DWDM technologies as well as customer usability features. These features are required to satisfy the service providers' demands for low-cost transport systems.

References

- [1] A. F. Wallace, "Ultra long haul DWDM: network economics," Paper TuT1, *Optical Fiber Communications Conference*, Anaheim, 2001.
- [2] J.L. Zyskind, *et al.*, "High capacity, ultra-long haul transmission," *National Fiber Optic Engineers Conference*, Atlanta, 2000.
- [3] A. Srivastava, *et al.*, "System margin enhancement with Raman Gain in multi-span WDM transmission," Paper FC2, *Optical Fiber Communications Conference*, San Diego, 1999.
- [4] B. Zhu *et al.*, "3.08 Tb/s (77 x 42.7 Gb/s) transmission over 1200 km of non-zero dispersion-shifted fiber with 100-km spans using C- and L-band distributed Raman amplification," Paper PD23, *Optical Fiber Communications Conference*, Anaheim, 2001.
- [5] L.E. Nelson, "Challenges of 40 Gb/s WDM transmission," Paper ThF1, *Optical Fiber Communications Conference*, Anaheim, 2001.
- [6] S. Yamamoto, *et al.*, "5 Gbit/w optical transmission terminal equipment using forward error correcting code and optical amplifier," *Electron. Lett.*, 1994, **30**, p. 254.
- [7] J. L. Pamart, *et al.*, "Forward error correction in a 5 Gb/s 6400 km EDFA based system," *Electron. Lett.*, 1994, **30**, p. 342.
- [8] C. R. Doerr, *et al.*, "Dynamic wavelength equalizer in silica using the single-filtered-arm interferometer", *IEEE Photon. Technol. Lett.*, vol. 11, pp. 581-583, 1999.
- [9] T. Huang *et al.*, "Performance of a liquid-crystal optical harmonic equalizer," *Optical Fiber Communications Conference*, Anaheim, 2001.
- [10] N.T. Quang Le, *et al.*, "New dispersion compensating module for compensation of dispersion and dispersion slope of non-zero dispersion fibres in the C-band," Paper TuH5, *Optical Fiber Communications Conference*, Anaheim, 2001.
- [11] C.K. Madsen, *et al.*, "Compact integrated tunable chromatic dispersion compensator with a 4000 ps/nm tuning range," Paper PD9, *Optical Fiber Communications Conference*, Anaheim, 2001.
- [12] A. B. Puc, *et al.*, "Long-haul DWDM NRZ transmission at 10.7 Gb/s in the S-band using cascade of lumped Raman amplifiers," Paper PD39, *Optical Fiber Communications Conference*, Anaheim, 2001.
- [13] P. Hunt, "The search for ultra-long-haul transmission," *Lightwave*, May 22, 2001.

Best way to build the all-optical, ultra-long haul terrestrial network

Linn Mollenauer
Bell Labs, Lucent Technologies
Holmdel, NJ 07733 USA

Abstract

Choice of the "all-optical" approach- transmission without the more customary electronic regeneration every 500 km or so- has recently been dictated by the economics of ultra-long-haul, Terabit-level, dense WDM. Two key technologies, viz., Dispersion-Managed Solitons and Raman amplification, enable the best performance in this all-optical mode. With them, it is possible to maintain optical transparency over vast geographical regions, such as that of the North American continent.

Summary

The conventional approach to ultra-long-haul, terrestrial transmission requires the use of expensive "OT" (optical receiver-transmitter) units (one for each channel!) at every node point, or about once every 500-600 km. Within the context of Terabit-level dense WDM, however, the sheer number of such units and the floor space they require become economically prohibitive. Fortunately, with proper design, the system can remain "all-optical", i.e., without electronic regeneration, over many (4-8) thousands of km. At the same time, it can be adaptable to an easy and purely optical "add-drop" of channels at any point along the way. The two most important ingredients of such a system are first, dispersion-managed solitons, and second, Raman amplification, especially when it is in the form of all-Raman. While either of these ingredients can provide major benefits alone, they tend to complement each other for even greater advantage.

Ultra long haul systems tend to be strongly non-linear, so it is imperative to choose the transmission mode least adversely affected by that non-linearity. Here, dispersion-managed solitons are the best: for them, self-phase modulation is beneficial (it enables them to exist!), and as with other dispersion-managed schemes, four-wave mixing can be reduced to negligible levels with proper dispersion management itself. Thus, the *only* non-linear penalty suffered by dispersion-managed solitons is from the cross-phase modulation (XPM) resulting from collisions between pulses of different channels. Here, however, the ultimate result is a nearly pure jitter in pulse arrival times, and that is easily quenched by the use of simple frequency-guiding filters and other means. By contrast, the various widely-spread-pulse modes, such as "CRZ" and "quasi-linear" transmission, tend to suffer from intra-channel four-wave mixing, which leads to the appearance of ghost pulses in normally empty bit slots, an effect that is not easy to defeat.

With other dispersion-managed modes, the solitons share the freedom to work well with many different types of transmission fiber, and with various combinations of dispersion compensating fibers that allow for nearly wavelength-independent path-average

dispersion. In contrast to the various widely-spread-pulse modes, which require large pre- and post-dispersion compensation coils precisely adjusted to each distance, with dispersion-managed solitons, the pre- and post-compensation values are relatively small and independent of distance. In close connection with this fact, with solitons, the data can be read anywhere along the path, and standard pulses can be added anywhere. This is in stark contrast to the widely spread-pulse modes, where the data is readable only at certain special points. Thus, dispersion-managed solitons are uniquely appropriate for the creation of a truly all-optical network. The consistent behavior of the solitons with distance also makes them uniquely appropriate for optical monitoring of the system.

Within the context of the 80-100 km amplifier spans that have become customary in US terrestrial transmission, the distributed amplification provided by Raman gain enables a reduction of the >8 dB noise penalty (factor by which noise at system output is increased) associated with lumped amplifiers to be reduced to <2 dB with backward Raman pumping alone, and to <1 dB when forward Raman pumping is used as well. This improvement is undoubtedly the first attraction of Raman gain, but not the only one. Perhaps the second in importance is the ease with which one can obtain nearly dead flat gain over very wide WDM bands (as much as the combined Erbium C + L bands, and without a gap); add to this the fact that the exact wavelength spread of the gain band is limited only by the available pump wavelengths. Still other factors tend to make system management easier, viz., with Raman gain, the shape of the gain band is nearly independent of signal level, in stark contrast to the strong "tilt" dependence of Erbium amplifiers. Also, it is very helpful in this regard that the net gain is always directly proportional to pump power. Finally, sophisticated gain leveling can be had from the use of wavelength/power selective Raman pumps to add gain where it is needed, rather than from the insertion of wavelength selective loss.

The relatively flat profile of signal intensity versus distance that obtains with Raman gain helps to symmetrize breathing of the dispersion-managed soliton pulses, and thus to avoid adjacent pulse interaction from pulse overlap. The flat intensity profiles also tend to reduce the XPM from soliton-soliton collisions in WDM.

In recent experiments carried out in a 500 km recirculating loop with 80 km amplifier spans, we have demonstrated "error-free" transmission ($\log \text{BER} < -9$ without the use of FEC) in Terabit-level dense WDM at 10 Gbit/s per channel (spacing 50 GHz) over distances in excess of 6500 km, even without guiding filters. With relatively weak, fixed-frequency guiding filters, we expect to increase that error free distance to well beyond 8000 km. The present spectral efficiency of 0.2 can probably be increased to about 0.3. For even greater spectral efficiencies, however, one really needs an essentially linear transmission line, a requirement that is incompatible with truly ultra long haul transmission.

Efficiency and Stability of Transmission Control of Long-Distance and High-Speed WDM Transmission Using Solitons

Masayuki Matsumoto

Department of Communications Engineering, Osaka University
2-1 Yamada-oka, Suita, Osaka 565-0871, Japan

Tel: +81-6-6879-7729, Fax: +81-6-6879-7774, Email: matumoto@comm.eng.osaka-u.ac.jp

Abstract: Control of nonlinear optical transmission by means of narrowband filters and synchronous modulators is attractive to achieve long-distance and high-speed transmission. In this paper efficiency and stability of such controls in single-channel and WDM systems are analytically and numerically studied.

Increasing demand for higher channel bitrate and higher spectral efficiency in long-distance WDM systems requires us to cope with fiber nonlinearity more seriously. Solitons, which utilize the self-phase modulation (SPM) in forming the stable pulse, are a candidate for the signal format used in high-speed (>40Gbit/s) and long-distance (>a few thousand kilometers) transmission. The nonlinear nature of the soliton, furthermore, makes it possible to stabilize its propagation by means of simple control using narrowband filters and/or modulators [1]. Very long-distance transmission with large signal-to-noise ratio maintained can be achieved by the use of sliding frequency filters or a combination of synchronous amplitude modulators and filters. However, the efficiency of the transmission control, especially that of regularizing pulse energy, becomes weaker in dispersion-managed systems where the effect of SPM is reduced due to the large dispersive pulse broadening during propagation [2]. One can recover the efficiency of the control by increasing the signal power, which works in single-channel transmission. In WDM transmission, however, the increased power leads to severe degradation of performance caused by inter-channel nonlinear effects such as cross-phase modulation (XPM). One promising way to increase the efficiency of the control in WDM dispersion-managed systems is to demultiplex and re-combine the signal periodically and to place highly nonlinear elements after the demultiplexers [3]. By this method one can stabilize the transmission channel-by-channel while the increase in inter-channel nonlinear interaction is avoided. Owing to the recovered efficiency of the control and the use of synchronous modulators, 40Gbit/s x 4ch transmission over 10,000km was achieved [4]. In this paper I analyze the efficiency and stability of the control of dispersion-managed solitons by means of narrowband filters and synchronous modulators. Highly nonlinear fibers (HNFs) are assumed as the nonlinear elements as proposed in [5],[6].

Figure 1 shows the transmission system analyzed here. Each amplifier span consists of anomalous and normal dispersion fibers with equal length and a Fabry-Perot filter. After every n ($=5$ in the following numerical simulation) spans, synchronous amplitude modulation is applied, followed by a HNF. The loss of the HNF is pre-compensated by an amplifier located before the modulator. In the case of WDM transmission, channels are demultiplexed at point A in Fig.1 and modulation and HNF are applied to each channel. The signals are then multiplexed at point B.

To quantify the effect of regularizing the pulse energy by the control, a linear stability analysis is performed [7],[8]. The maximum absolute eigenvalue of the 3×3 transfer matrix describing the evolution of small fluctuations in amplitude, width, and chirp about their stationary values is plotted as a function of the length of HNF in Fig.2(a). Stabilization of the energy is stronger for smaller γ while positive γ (in dB) means that the regularizing effect is

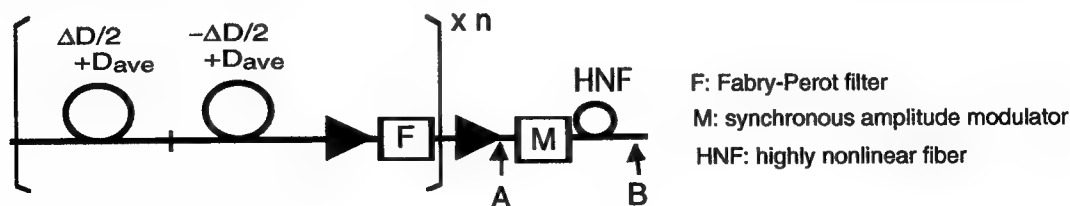


Fig.1. Unit structure of the transmission line.

Transmission fiber consists of anomalous ($\Delta D/2 + D_{ave}$) and normal ($-\Delta D/2 + D_{ave}$) dispersion fibers. Span length=50km, $n=5$, equivalent 3dB bandwidth of transmission peaks of Fabry-Perot filter=150GHz, and equivalent 3dB time width of the modulator=12ps in the numerical simulation given below.

lost. Strong stabilization of pulse energy is needed to suppress the energy jitter induced by collisions in WDM transmission and by intra-channel four-wave mixing when strong dispersion management is used.

In order to obtain stable transmission, the buildup of noise in the vacant time slots should also be suppressed. Figure 2(b) shows the growth rate of the lowest-order linear mode versus the HNF length, where we assume a Gaussian shape for the linear pulse. Figure 2(b) shows that large anomalous dispersion for the HNF is preferred for the suppression of the linear-mode growth. This is because the elimination of linear waves by the amplitude modulation is more effective for larger total dispersion of the system. The large growth rate for longer HNF lengths is due to wider spectral width of the stationary solution, which needs larger excess gain for the compensation for the filter loss. From Figs.2(a) and (b), optimum values for the dispersion D_{HNF} and length of the HNF are $\sim 2\text{ps/nm/km}$ and $7\sim 10\text{km}$, respectively.

Figure 3 shows simulated Q factor for single-channel transmission at 40Gbit/s. Large Q is obtained for HNF lengths of 7.5 and 10km with $D_{\text{HNF}}=2\text{ps/nm/km}$, which is consistent with the prediction given by Fig.2. Figure 4 shows the Q factor for 40Gbit/s x 3channel WDM transmission, where the Q factor of the central channel is plotted for different noise seeds and different pulse patterns of neighboring channels. For the channel separation of 160GHz, the error-free transmission distance is limited to about 5,000km because of the accumulation of noise in the vacant time slots induced by collisions. Further optimization of the system will be needed to increase the spectral efficiency.

In conclusion, a theoretical analysis of single-channel and WDM transmission of dispersion-managed solitons was presented. The analysis is useful for optimization of parameters of transmission control of nonlinear RZ pulses by means of filtering and synchronous modulation.

References [1] A. Hasegawa and Y. Kodama, *Solitons in Optical Communications*, Oxford, ch.8 (1995). [2] M. Matsumoto, J. Opt. Soc. Am. B **15**, 2831(1998). [3] B. Dany et al., Electron. Lett. **35**, 418 (1999). [4] O. Leclerc et al., Electron. Lett. **36**, 337 (2000). [5] A. Sahara et al., IEEE Photon. Technol. Lett. **12**, 720 (2000). [6] A. Sahara et al., J. Lightwave Technol. **18**, 1364 (2000). [7] J. Kumasako et al., J. Lightwave Technol. **18**, 1064 (2000). [7] A. Tonello et al., Opt. Lett. **25**, 1496 (2000).

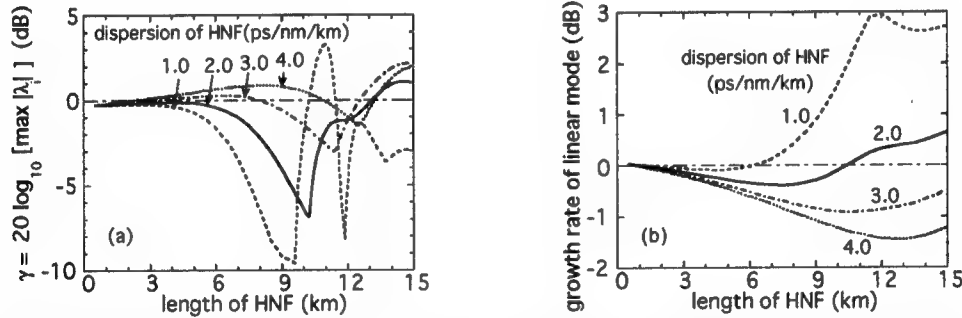


Fig.2. Efficiency and stability of soliton control. (a): growth rate per unit structure of fluctuations in amplitude of the pulse γ , (b): growth rate per unit structure of the linear mode. ΔD and D_{ave} are 8 and 0.025ps/nm/km, respectively. Loss and nonlinearity of HNF are 0.5dB/km and $n_2/A_{\text{eff}}=4.0 \times 10^{-9}$ 1/W, respectively. Pulse energy at the entrance of the transmission fiber is kept at 0.07pJ.

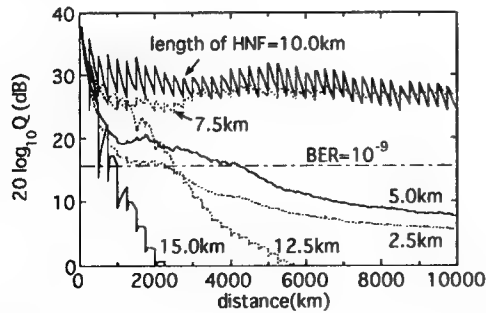


Fig.3. Q factor for single-channel transmission at 40Gbit/s.

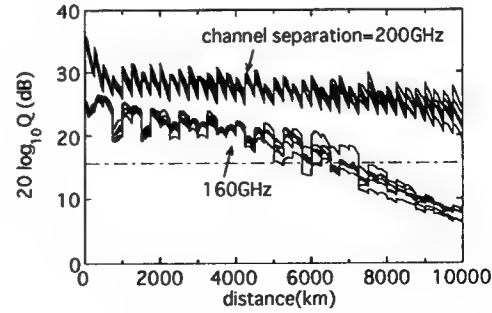


Fig.4. Q factor for 40Gbit/s x 3ch transmission. D_{HNF} and length of the HNF are 2ps/nm/km and 10km.

Carrier-suppressed Dispersion-managed RZ transmissions using novel OTDM techniques with phase alternation

H. Murai, H. T. Yamada, K. Fujii and Y. Ozeki

Oki Electric Industry Co., Ltd., 550-5, Higashiasakawa, Hachioji, Tokyo 193-8550, Japan

TEL: +81-426-6762, Fax: +81-426-6581, E-mail: murai572@oki.co.jp

Abstract: DWDM transmission characteristics of non-linear RZ pulses with duty-cycle of more than 50% and initial phase alternation are investigated both numerically and experimentally.

Introduction: The non-linear RZ coding combined with dispersion managed (DM) fiber line enables the ultra-high bit-rate transmission over the distances of several thousands km without regeneration. In the WDM regime with a fixed channel spacing, however, interchannel degradation mechanisms such as the cross phase modulation (XPM) begin to dominate, limiting the bit-rate increase per channel. The use of broader pulses alleviates the interchannel degradation if the intrachannel pulse-to-pulse interaction is controlled. An initial phase alternation technique, where the optical phase of the pulses toggles between 0 and π at the bit-rate [1][2], could be the key to overcome the problem. With the initial phase alternation, the neighboring pulses have negative optical phase correlation, leading to less pulse-to-pulse interaction and carrier-suppressed spectrum [3]. For its simpler implementation, the optical time division multiplexing (OTDM) can be utilized. In this paper, the effect of initial phase alternation with OTDM technique is experimentally evaluated with the 40 Gbit/s based DM non-linear RZ in both single-channel and DWDM transmissions.

Simulation: For the sake of simpler comparison, Figure 1 calculated the transmission distances, normalized to dispersion distance, for the single-channel phase alternation (solid line) and uniform phase modulation (broken line), assuming no ASE degradation. Parameters τ_0 and S [4] represent a duty cycle and the map strength of DM transmission line, respectively. It is clearly seen that the initial phase alternation increases the transmission distance significantly even for wider pulses of duty cycles beyond 50 %, as compared to the case of the uniform-phase modulation. As the pulse becomes broader, the transmission distance peaks at larger S . The initial phase alternation reduces the adjacent pulse overlapping because of phase cancellation, leading to less pulse-to-pulse interaction.

Transmission experiments: To examine the simulation results, the transmission experiment was conducted. Figure 2 describes the setup of re-circulating loop experiment for 40 Gbit/s WDM-DM solitons. The transmission line consisted of two amplifier spans, with short-period DM, so-called dense DM line [5]. An amplifier spacing was 45 km comprising two sets of 10 km of standard fiber (SMF, 16.5 ps/nm/km @1550 nm) and 2.5 km of dispersion compensating fiber (DCF, -64ps/nm/km @1550 nm), followed by 20 km of SMF and 5 km of DCF. The span loss was 14.5 dB. The noise figures of EDFAs were about 6 dB. The path-average dispersion was set 0.05 ps/nm/km at wavelength of 1550 nm and the average dispersion slope was 0.008 ps/nm²/km. At the transmitter, nearly Fourier transform-limited Gaussian pulses with FWHM of 14 ps (corresponding to duty cycle of 56 %) were generated by 20 GHz-sinusoidally driven EA modulator (EAM),

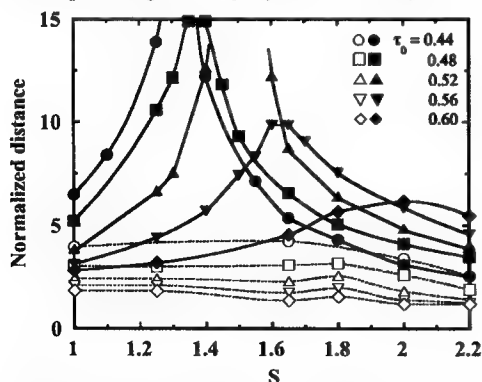


Figure 1: Calculated propagation distance (solid line; alternating phase, dashed line; uniform phase)

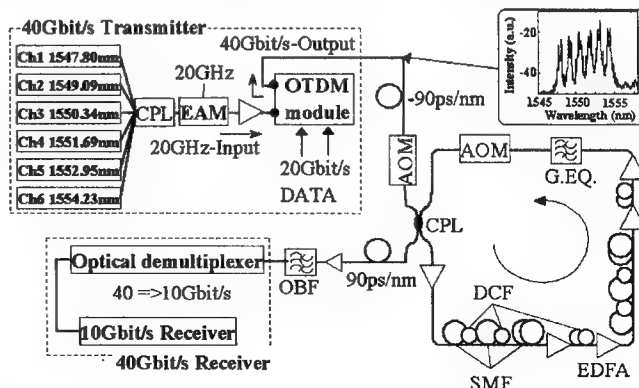


Figure 2: Experimental setup

and were encoded at 40 Gbit/s using OTDM module [6]. 40 Gbit/s data was pre-chirped, and launched into the re-circulating loop. Since the OTDM uses the optical delay of 25 ps-delay to combine two 20Gbit/s pulse streams, the optical phase difference between the interleaved 20 Gbit/s-pulse streams can be adjusted by slightly changing the wavelength of the optical pulses. In the experiment, tweaking the wavelength by ~ 0.16 nm turned out to provide π -phase difference between the adjacent pulses. Figure 3 shows measured bit error rate (BER) for 40 Gbit/s single channel transmission with and without phase alternation using this technique. Insets are measured eye-diagrams for uniform and alternating phase case. The achieved transmission distance in the case of alternating-phase soliton was 2070 km at average launched power of 4 dBm, whereas that of uniform-phase case was only 1350 km. The eye-diagram (a) was for 2700 km in the case of alternating phase and (b) for 1800 km with uniform phase case. The eye-diagram (a) does not reveal any waveform distortion due to pulse-to-pulse interaction and the transmission distance was only limited by OSNR degradation due to ASE accumulation. In the WDM experiment, the channel spacing was set to be about 150 GHz, which meets conditions that π -phase difference between adjacent pulses for all wavelength channels were realized. The average launched power for each channel was 4 dBm. Due to the slight residual dispersion slope in the DM line, the average dispersions ranged from 0.04 to 0.09 ps/nm/km among the channels, so that the launched power for channels was set to be higher for longer wavelength as shown in inset of Figure 2. Figure 4 shows measured BER of six channels WDM transmission. The worst channel was channel 5, and the achieved transmission distance was 1170 km. In this case, the limiting factor was mainly a pulse-to-pulse interaction, based on the comparison with the results of single channel transmission. The large penalty was observed in channel 2. This resulted from large deviation of the channel power from optimal level.

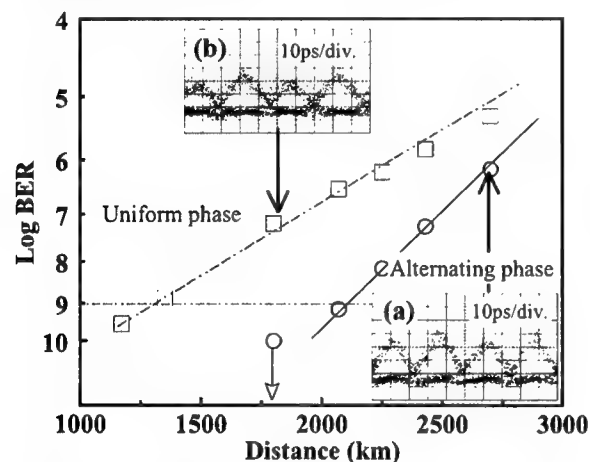


Figure 3: Measured BER for single channel transmissions.

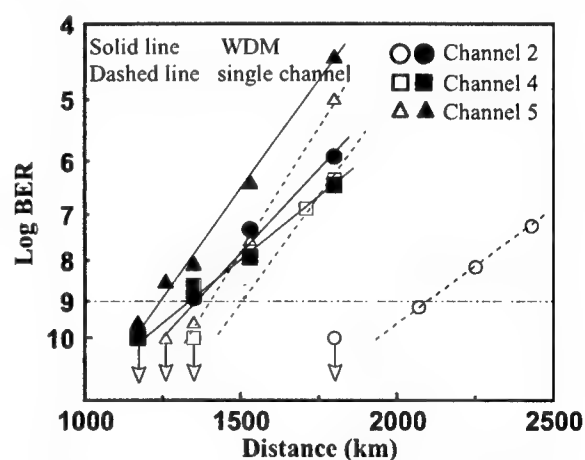


Figure 4: Measured BER for six channels WDM transmissions.

Conclusion: The transmission improvement of DM non-linear RZ with initial phase alternation was confirmed both numerically and experimentally. The simulation revealed that initial phase alternation was effective method to reduce the pulse-to-pulse interaction induced degradation for very wide pulse with duty cycle of more than 50 %. It was verified experimentally that the phase alternation enables 40 Gbit/s DM non-linear RZ transmissions beyond 2000 km, and the WDM transmission over 1100 km. The WDM transmission was limited by the pulse-to-pulse interaction due to imperfect dispersion management within the WDM channels. The phase alternating non-linear RZ transmission over properly designed DM fiber line will realize the ultra-high bit-rate long haul DWDM systems at higher spectral efficiency.

References:

- [1] A. Hasegawa and Y. Kodama, in "Solitons in optical communications", Clarendon press, Oxford, p.151, 1997.
- [2] E. A. Golovchenko et al., *Opt. Lett.*, Vol. **22**, p. 793, 1997.
- [3] Y. Miyamoto et al., OAA'99, PdP4, 1999.
- [4] N. J. Smith et al., *Opt. Lett.*, Vol. **24**, p. 1981, 1996.
- [5] T. Hirooka et al., NLGW'99, Dijon, ThA2, 1999.
- [6] H. T. Yamada et al., ECOC2000, 1.3.5, Munich, Germany, 2000.

Intra-Channel Nonlinear Effects in Dispersion Compensated DWDM Optical Networks

A. Nolasco Pinto^{1,2}, Paulo Almeida¹ and J. Ferreira da Rocha^{1,2}

¹Institute of Telecommunications, Aveiro Pole, ²University of Aveiro, Campus de Santiago, 3810-193 Aveiro, Portugal, Phone: +351 234 377918; Fax: +351 234 377901; E-Mail: anp@det.ua.pt

Nonlinear effects in optical fibers are related to anharmonic motion of silica bound electrons under the influence of the light [1]. Even though silica is intrinsically not a highly nonlinear material, the waveguide geometry that confines light to a small cross section over long fiber lengths makes the waveguide behavior marked dependent of the optical field intensity. As today's optical telecommunication systems evolve to higher bit rates and distances increasing signal power is required, to keep the necessary signal-to-noise ratio, making the fiber nonlinear behavior the main hurdle to overcome, in order to send short optical pulses at a very high repetition rates over long distances, without considerable pulse distortion or timing uncertainty. In this work we consider a generic single channel of a DWDM optical network, where losses and dispersion are fully compensated. In this scenario the only limitations to the transmission capacity of our optical channel are the noise, the channel bandwidth and the fiber nonlinear effects. The limitations imposed by channel bandwidth and noise were addressed in a remarkable work published by Claude Shannon in 1948 [2] and represent a fundamental limit. However, before being able to approach the Shannon limit we must make the signal robust against the fiber nonlinear behavior. The main topic of this work is the study of effective nonlinear compensation techniques that allow the transmission, over standard step-index fibers (G.652), of 40 and 80 Gbit/s channels over distances greater than thousands of kilometers using less than 100 GHz of optical bandwidth in DWDM networks. An interesting solution for dealing simultaneously with the chromatic dispersion and fiber nonlinearities was present by the soliton systems [3]. However, for high bit rates, which mean very short optical pulses, in system where the local chromatic dispersion and attenuation are high, like in standard step-index fibers, is not simple to maintain stable solitons with hundreds of kilometers between optical amplifiers. Yet recent works have shown that is possible to compensate completely the fiber chromatic dispersion by cascading in the optical path devices that induce a frequency dependent delay with opposite signal to the one induced by the chromatic dispersion. Nevertheless the nonlinear induced signal distortions represent a serious limitation to the total optical length that the signal can travel before being electrically regenerated. In figure 1, we considered an ideal noiseless transmission system where all linear effects are full compensated. As can be seen, the fiber nonlinear behavior impose a maximum distance of 1200 km for a 40 Gbit/s optical signal, over G.652 fibers, before the need of being electrically regenerate, considering a 10^{-9} error rate floor. From figure 1 is clear that the limitations caused by nonlinear transmission takes several forms: one is pulse distortion, other is timing and amplitude jitter and finally is also seen in figure 1 some energy in 'zeros' that was transferred from neighbor pulses. These same results were observed in laboratorial trials [4-5] and the maximum attainable distance in [5] was 720 km using a span between amplifiers of 120 km. In [8] the use of pre-chirped pulses for fiber nonlinear behavior compensation was purpose and in [6] an expression for the pre-chirp value appropriate to maintain a single pulse stable transmission both in the time and frequency domain was derived. In [7] the timing jitter was related with the nonlinear pulse to pulse interaction seen in classical soliton systems and the shadow pulses that appears at the 'zeros' was described by a special case of four-wave mixing between different spectral components in a single channel. An analytical treatment of the four-wave mixing process was presented in [8] and [9]. In this work, after making clear the relations between the fiber nonlinear behavior and the several forms of signal distortions seen in figure 1, we propose a suitable configuration scheme, for maximizing the distance that the signal can travel in the optical domain and that allow the deployment of multiple wavelength high-speed all optical networks with switching functions. In order to analyze in detail the nonlinear effects in this kind of systems we derived a mathematical description for the propagation of a strongly dispersed field in a single mode optical fiber, starting from the modified nonlinear Schrödinger equation. Assuming a solution around the linear one we obtain (1), for the propagation of two pulses U_1 and U_2 , where ΔU is the perturbation induced in the linear solution due to the fiber nonlinear behavior. The first two terms in the right side of equation (1) are the usual SPM terms, the second two are responsible for the IXPM and the last two terms are

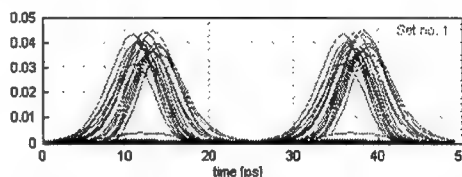


Figure 1 - Eye diagram after transmission at 40 Gbit/s over 1200 km of G.652 fiber, using optical amplifiers separated by 100 km and chirped Bragg grating devices for fully dispersion compensation.

the cause of the IFWM. It is also important to point out that in systems, where the pulses remain in its time slot during the propagation $U_1 \cdot U_2 = 0$, which means that the terms related with IXPM and IFWM vanish, but this is not the case in here, due to the strong pulse broadening induced by high local chromatic dispersion. An interesting aspect of equation (1) is that it allows determination of the induced nonlinear perturbation, considering individually each nonlinear effect. The results show, see figure 2, that the perturbation induced by SPM has a symmetrical phase and is centered with the linear pulse; its effect is a small pulse shape distortion. In contrast, the IXPM induced perturbation has a non-symmetrical phase, which induces timing jitter. As the origin of this jitter is the pulses tails superposition this gives rise to non-gaussian timing jitter, as in the soliton systems [10]. The IFWM is the result of

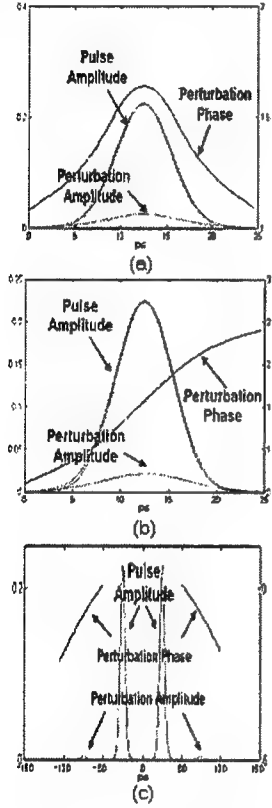


Fig. 2 - (a)- SPM; (b)- IXPM; (c)- IFWM.

the cross product between the two waves and it gives rise to a shadow pulse in the 'zeros' and amplitude fluctuations in the 'ones'. The use of chirped pulses can be an effective way of nonlinear compensation, because as soon as the chirped pulses are launched into a fiber with a high value of dispersion its energy is spread for multiple time slots and in terms of power the signal is average making its almost flat. As the problem is the transmission medium response for different levels of signal intensity this signal is extremely robust

$$\begin{aligned} \frac{\partial \Delta U}{\partial z} + i \cdot \frac{\beta_2}{2} \cdot \frac{\partial^2 \Delta U}{\partial t^2} + \frac{\alpha}{2} \Delta U = i \cdot \gamma \cdot \{ |U_1|^2 \cdot U_1 + |U_2|^2 \cdot U_2 \} \\ + i \cdot \gamma \cdot \{ 2 \cdot |U_2|^2 \cdot U_1 + 2 \cdot |U_1|^2 \cdot U_2 \} \\ + i \cdot \gamma \cdot \{ U_1 \cdot U_2^* \cdot U_1 + U_2 \cdot U_1^* \cdot U_2 \} \quad (1) \end{aligned}$$

against fiber nonlinear behavior. As we observed previously the IFWM is the more critical effect in terms of limiting the maximum attainable optical distance, however this process is quite sensitive to the phase mismatch between the involved signals and in this case the noise added to the signal by the optical amplifiers reduce its efficiency. In the scheme that we proposed the dispersion compensation devices compensate all the previously accumulated dispersion and the post-chirp value induced before the optical receiver is symmetrical to the pre-chirp induced at the optical source. Other research groups claims the advantages of leaving some residual dispersion in order to obtain a better nonlinear compensation effect. We agree with that for a point-to-point connection but that does not seem to be a suitable solution in a mesh optical network with optical switching functions where the signal can travel from different paths before reaching the receiver. In this scenario is difficult to know which is the amount of residual dispersion accumulated during the transmission that needs to be compensated at the receiver, although the value of the post-chirp is always the symmetrical of the pre-chirp value and is independent of the optical path.

Acknowledgments: This work was partially supported by Portugal Telecom Inovação (O-NODE project).

References:

- [1] - Govind P. Agrawal, Nonlinear Fiber Optics, 3rd. Edition, 2001, Academic Press.
- [2] - Claude E. Shannon, The Mathematical Theory of Communication, Bell System Technical Journal, 1948.
- [3] - A. Hasegawa and Y. Kodama, Solitons in Optical Communications, Oxford University Press, 1995.
- [4] - R. Essiambre, B. Mikkelsen and G. Raybon, Intra-Channel Cross-Phase Modulation and Four-Wave Mixing in High-Speed TDM Systems, Electronics Letters, vol. 35, no. 18, pp. 1576-1578, 1999.
- [5] - Sang-Gyu Park, A. H. Gnauck, J.M. Wiesenfeld and L. D. Garrett, 40-Gb/s Transmission Over Multiple 120-km Span of Conventional Single-Mode Fiber Using Highly Dispersed Pulses, IEEE Photonics Technology Letters, Vol. 12, No. 8, pp. 1085-1087, 2000.
- [6] - M. Zitelli, F. Matera and Marina Settembre, Single-Channel Transmission in Dispersion Management Links in Conditions of Very Strong pulse Broadening: Application to 40 Gbi/s Signal on Step-Index Fibers, Journal of Lightwave Technology, Vol. 17, No. 12, pp. 2498-2505, 1999.
- [7] - P. V. Mamyshev and N.A. Mamysheva, Pulse-Overlapped Dispersion-Managed Data Transmission and Intrachannel Four-Wave Mixing, Optics Letters, vol. 24, no. 21, pp. 1454-1456, 1999.
- [8] - Antonio Mecozzi, Carl Balslev Clausen and Mark Shtaif, Analysis of Intrachannel Nonlinear Effects in Highly Dispersed Optical Pulse Transmission, IEEE Photonics Technology Letters, vol. 12, no. 4, pp. 392-394, 2000.
- [9] - Mark J. Ablowitz and Toshihiko Hirooka, Resonant Nonlinear Intrachannel Interactions in Strongly Dispersion-Managed Transmission Systems, Optics Letters, vol. 25, no. 24, 2000.
- [10] - A. Nolasco Pinto, Govind P. Agrawal and J. Ferreira da Rocha, Effect of Soliton Interaction on Timing Jitter in Communication Systems, Journal of Lightwave Technology, vol. 16, no. 4, pp. 515-519, 1998.

High-Speed, High-Capacity, Long-Haul Terrestrial Networking

D.J. Jones, J.M. Jacob, S.R. Henion, J.G. Maloney, M.P. Kesler, M.J. LaGasse, E.R. Thoen, B. Brewington, Q. Zhang, and K.L. Hall

*PhotonEx Corporation, 200 Metro West Technology Drive, Maynard, MA, 01754
978-723-2200 tel., 978-723-2250 fax*

Today's public backbone networks have been built to support circuit-switched traffic services. Wavelength division multiplexing has significantly increased the bandwidth available in this circuit-switched architecture by allowing multiple parallel wavelength channels to propagate on the same fiber. Increased network performance also has resulted from replacing expensive electronic regeneration stations with optical amplifiers such as erbium-doped fiber amplifiers (EDFAs) and Raman amplifiers (RAs). The cost differential between optical amplifiers and electronic regenerators is so great that a new type of networking, ultra-long-haul networking, has caught on as a way to reduce equipment costs in the network. Unfortunately, many ultra-long-haul solutions sacrifice fiber capacity for longer transmission distances. That is to say, that a low capacity long distance link can be installed in a very cost competitive way, but that the cost savings for these types of links decrease as capacity increases and additional fibers have to be lit. In addition, many of these ultra-long-haul solutions have incorporated so many additional components in the transceivers and amplifiers, that they are extremely expensive when used to outfit the shorter links in the backbone.

Next-generation networking equipment will differ from what has been installed to date in two major ways. First, it will be designed to yield the cost reduction associated with ultra-long-haul networking, without sacrificing capacity on the link. Furthermore, it will be designed to scale to meet the bandwidth demands of tomorrow, which will be more dynamic than bandwidth demands of today. In this paper we will review some of the architectural and technological issues that confront high-speed, high-capacity, long-haul terrestrial networks looking forward.

High-capacity or high spectral efficiency can be achieved in a variety of ways. One is to keep the channel rate low and to put a large number of channels within a given amplifier band. Another way is to support fewer wavelength channels that run at higher rates. From a capacity standpoint, both methods may support the same bandwidth. However, there are fundamental differences that exist in these two network architecture choices. For lower rate channels, chromatic dispersion and polarization mode dispersion may not be significant impairments, but inter-channel effects such as cross-phase modulation and four-wave-mixing may be more of an issue because of the close channel spacing. Also, additional end terminal equipment is necessary to support the large number of individual wavelength channels and the network may be difficult to manage and spare. Fewer higher speed channels can support a wider variety of service interfaces with less end terminal equipment yielding a system that is relatively easy to manage and spare. The difficulty in providing this type of network is propagating the higher-speed signals over long distances. In particular, dispersion tolerances are much tighter for higher-speed channels and intra-channel nonlinearities may become an issue. However, these higher-speed channels yield another advantage in that they may be shared more efficiently in an environment where bandwidth demands are bursty as they are in data-oriented networks.

Deployed DWDM systems today typically support 2.5 Gb/s data and 10 Gb/s data channels. Systems supporting 40 Gb/s data channels will be commercially available by the end of this year. To understand how these systems will be designed, and how well they will perform, it is useful to look at the research results that have fueled their development. Recently, very high-capacity, high-speed transmission has been demonstrated by a number of groups. These experiments can be classified by the signaling scheme, return-to-zero (RZ) or non-return-to-zero (NRZ), by the fiber type, experimental or currently deployed, by the amplifier spacing, terrestrial (>65 km) or submarine (<65 km), and by the test procedure, straight-line or re-circulating loop. Grouping the results in this manner suggest some interesting trends.

Figure 1 shows some of the most recent multi-channel 40 Gb/s transmission results. This plot shows the spectral efficiency of the system versus the unregenerated distance that was demonstrated. The results are classified as described above. It is interesting to note that most demonstrations have utilized some sort of RZ signaling scheme. This choice is not surprising because RZ (filled symbols) signals are more robust to imperfect dispersion compensation and more sensitive receivers can be designed for the RZ signaling format. Note that while many of the long distance experiments have been demonstrated using submarine type (< 65 km) amplifier spacings and/or experimental fibers, distances greater than 1000 km have been achieved using terrestrial amplifier (100 km) spacings and currently deployed fiber types. The results of straight-line demonstrations using realistic amplifier spacings and fiber types are expected to be good predictors of installed fiber performance while re-circulating loop results may be difficult to extrapolate to real fiber route results because of the anomalies associated with the periodic nature of the loop.

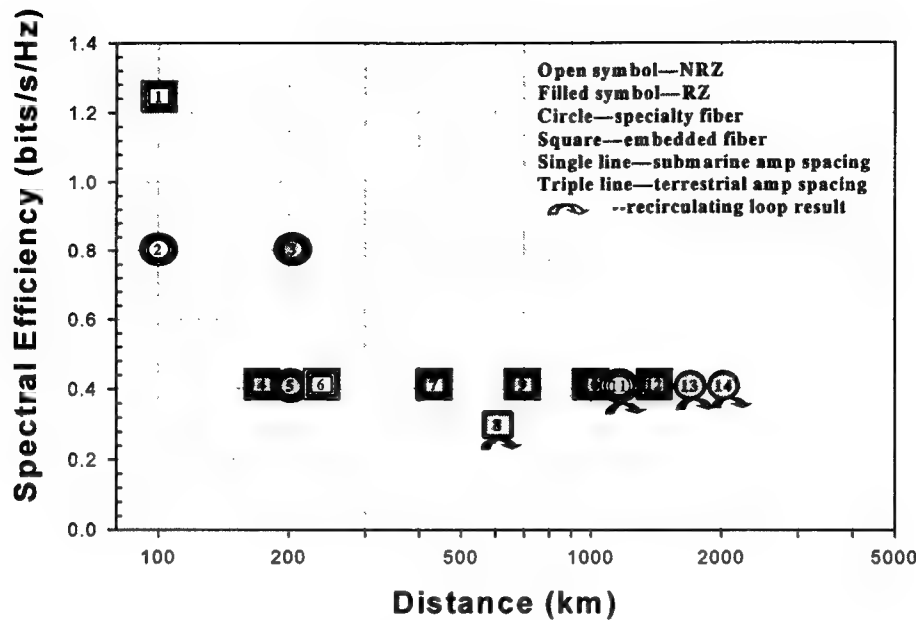


Figure 1. Recent multi-channel 40 Gb/s transmission results. The numbers within the symbol correspond to the reference at the end of the paper.

In conclusion, next generation DWDM transport equipment must be designed to take advantage of the cost savings associated with both ultra-long haul transmission and high spectral efficiency. In addition, to support bandwidth-on-demand, and other differentiated services, high-speed data channels that can be shared efficiently and provisioned flexibly will be required. High spectral efficiency systems composed of a few high rate data channels will be preferred because they can support legacy bandwidth demands with less equipment and fewer systems that are easier to manage and spare. In addition, higher channel rate systems can scale to meet the dynamic bandwidth demands of a data oriented backbone. Experimental results support the claims that long-haul 40 Gb/s DWDM transport systems can be deployed today, on existing network infrastructure.

References:

- [1] S. Bigo et al., "10.2 Tb/s transmission over 100 km TeraLight fiber with 1.28 bit/s/Hz spectral efficiency", Technical Digest of OFC 2001, PD25.
- [2] K. Fukuchi et al., "10.92 Tb/s triple-band/ultra-dense WDM optical repeated transmission experiment", Technical Digest of OFC 2001, PD24.
- [3] T. Miyakawa et al., "2.56 Tb/s unrepeated 230 km transmission with 0.8 bits/s/Hz spectral efficiency using low noise fiber Raman amplifier and 170 μm^2 - A_{eff} Fiber", Technical Digest of OFC 2001, PD26.
- [4] Y. Miyamoto et al., "Duobinary carrier-suppressed return-to-zero format and its application to 100 GHz spaced, 8 X 43 Gb/s, DWDM unrepeated transmission over 163 km", Technical Digest of OFC 2001, TuU4.
- [5] K. Shimizu et al., "Fiber-effective-area managed fiber lines with distributed Raman amplification in 1.28 Tb/s, 202-km unrepeated transmission", Technical Digest of OFC 2001, TuU2.
- [6] D. Chen et al., "3.2 Tb/s field trial over 3 X 82 km SSMF using FEC, Raman and tunable dispersion compensation", Technical Digest of OFC 2001, PD36.
- [7] R. Ohhira et al., "Novel RZ signal format with alternate chirp for suppression of nonlinear degradation in 40 Gb/s based WDM", Technical Digest of OFC 2001, WM2.
- [8] T. Otani and M. Suzuki, "40 Gb/s 25 WDM RZ signal transmission using L-band amplifiers and NZ-DSF spans", Technical Digest of OFC 2001, TuN6.
- [9] Y. Zhu et al., "16-channel 40 Gb/s carrier suppressed RZ ETDM/DWDM transmission over 720 km NDSF without polarization channel interleaving", Technical Digest of OFC 2001, ThF4.
- [10] Y. Zhu et al., "1.28 Tb/s transmission over 1000 km NDSF employing distributed Raman amplification and active gain flattening", Electron. Lett., vol. 37, no. 1, 2001.
- [11] B. Zhu et al., "3.08 Tb/s transmission over 1200 km of non-zero dispersion shifted fiber with 100 km spans using C- and L-band distributed Raman amplification", Technical Digest of OFC 2001, PD23.
- [12] E.R. Thoen et al., "Multi-Wavelength 40 Gb/s Transmission Systems for Long-Haul Applications", Technical Digest of NFOEC 2001, Session D3.
- [13] K. Suzuki et al., "1 Tb/s DWDM quasi-soliton transmission over 1500 km using dispersion managed single-mode fiber and conventional C-band EDFAs", Technical Digest of OFC 2001, TuN7.
- [14] I. Morita et al., "Benefit of Raman amplification in ultra-long-distance 40 Gb/s-based WDM transmission", Technical Digest of OFC 2001, TuF5.

Multi-terabit/s WDM transmissions at 40Gbit/s channel rate

(invited)

Sébastien Bigo and Yann Frignac

Alcatel Research and Innovation, Route de Nozay, 91460, Marcoussis, France
Ph.: +33 (0)1 69631478, fax: 0169631865, email: Sebastien.Bigo@alcatel.fr

Abstract: The advantage of alternate 50/75GHz channel spacing and vestigial side-band filtering at the receiver is discussed for multi-terabit/s WDM transmission systems at 40Gbit/s.

The recent evolution of WDM terrestrial transmission systems has been complying with two trends: increasing the total capacity to over 10Tbit/s and increasing the total distance to several thousands of kilometers. To meet the first trend, moving to higher channel rate, e.g. from 10Gbit/s to 40Gbit/s, appears as a natural step, but only if the spectral efficiency is increased. Conversely, systems with a high spectral efficiency are more sensitive to linear and non-linear cross-talk, which ultimately limits the maximum achievable error-free distance.

Out of the history of hero WDM experiments, we have selected the laboratory demonstrations with 10, 20 and 40Gbit/s channel rates complying with the basic requirements of existing terrestrial networks, i.e. incorporating fibers a single type within repeaters and relatively large repeater spacings (in excess of 65km from 1996 on). Figure 1 lists the corresponding capacity times distance products (CxD) versus time. The hero results obtained with channel rates of 80Gbit/s and above, regardless their compatibility with a terrestrial environment, are also shown. While experiments falling in this last category still lay behind, the CxDs of laboratory experiments at 10Gbit/s and 20Gbit/s rates have grown exponentially in the past years, at the same pace for both rates, doubling every 15 months, i.e. faster than the Moore's law for electronics. However, solutions based on 20Gbit/s rate are now handicapped by their incompatibility with SDH standards. Besides, the hero demonstrations at 40Gbit/s rate came out later, but rapidly caught up with that of 10 and 20Gbit/s rates, doubling their CxD every 7 month. As of now, they have outperformed the others in terms of capacity but mostly over smaller distances [1, 2]. Whether they will also ultimately exhibit significantly larger CxDs [3] than 10Gbit/s and 20Gbit/s solutions may rely on the possibilities offered by reshaping optical filters. Indeed, spectral reshaping is facilitated at 40Gbit/s by the larger channel bandwidth.

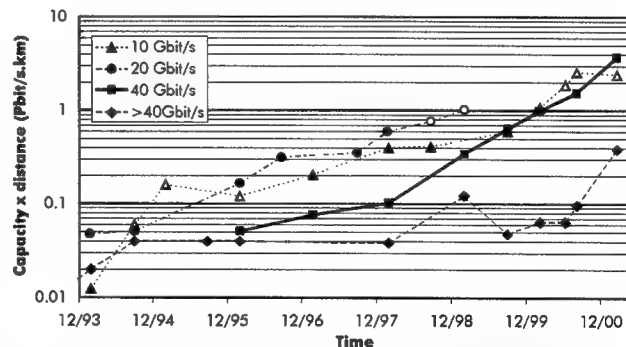


Figure 1: Evolution of terrestrial WDM lab experiments. White symbols correspond to distances larger than 1000km.

In particular, we recently proposed a new wavelength allocation scheme in combination with ultra-narrow, off-center, optical filtering at the receiver to demultiplex WDM channels at 40Gbit/s rate. Out of each channel spectrum, off-center filtering isolates one of the two side-lobes, regardless the cross-talk affecting the other side-lobe. This technique is generally referred to as vestigial side-band (VSB) filtering. With this scheme and regular NRZ format, we demonstrated the transmission of 128 channels at 40Gbit/s (5.1Tbit/s total capacity) over 3x100km of TeraLight™ fibre, to reach a record 0.64bit/s/Hz spectral efficiency [4]. Next, we theoretically investigate the tradeoffs involved in the choice of the VSB filtering technique.

In our experiment, we used a non-periodical frequency grid for our 128 WDM channels at 40Gbit/s, i.e. they are alternatively spaced by a GHz and b GHz, as schematized in the inset of Fig. 2. To achieve 5Tbit/s capacity over C and L bands (8THz total bandwidth), the condition $a+b=125$ GHz has to be met. We consider three channel spacing ratios, i.e. $(a/b)=(40\text{GHz}/85\text{GHz})$, $(62.5\text{GHz}/62.5\text{GHz})$ and the ratio used in the 5Tbit/s experiment $(50\text{GHz}/75\text{GHz})$. All the channels are assumed modulated via MZ-modulators with the characteristics of commercially available components (18GHz bandwidth). Consider a Gaussian filter with variable bandwidth from 0.2 to 0.8nm. This filter is detuned off the carrier of the channel under test, always towards the farther of the two neighboring channels [2,4]. Thus, the side-band experiencing the smallest overlap with adjacent channels is isolated while the impact of the cross-talk affecting the other side-band is minimized. In Fig. 2, we show the eye-opening Q' [5] in back-to-back. The best performance is a trade-off between crosstalk and filter bandwidth limitations. Whatever the channel spacing ratio (a/b) , a centered filter never yields the best performance. A narrow filter strongly attenuates high frequencies components of both side-bands apart the carrier, whereas a larger one does not provide sufficient cross-talk suppression [6]. Conversely, detuning the filter off the carrier enhances the higher frequencies of the favored side-band, while making very narrow filtering possible, and thereby efficient reduction of cross-talk [6]. This conclusion is evident when the channel spacing ratio (a/b) differs from unity $(62.5\text{GHz}/62.5\text{GHz})$, down to configurations where the main limitation comes from the cross-talk with the closer of the two neighboring channels (e.g. 40/85GHz).

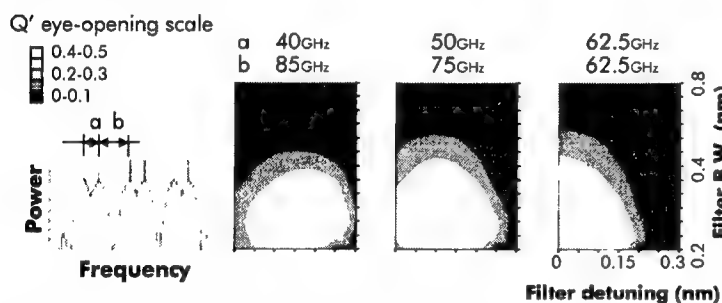


Fig. 2: Tradeoff between VSB filter characteristics and frequency allocation plan

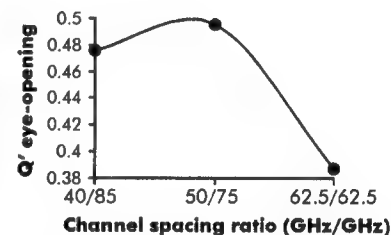


Fig. 3: Best frequency allocation plan associated assuming optimized VSB.

Fig. 3 shows the optimal Q' eye-opening factor as a function of the channel spacing ratio (a/b) , as derived from Fig. 3. The channel allocation plan of [1], i.e. $(a/b)=(50\text{GHz}/75\text{GHz})$, appears as reasonable trade-off, which, additionally, complies with the foreseen 25GHz ITU grid. In this configuration, the optimal filter bandwidth nears 30GHz, as actually used in [2,4,6]. Though the configuration $(40\text{GHz}/85\text{GHz})$ gives very similar performance as that with $(50/75\text{GHz})$, it should not be preferred, as nonlinear effects (namely four-wave mixing) resulting from the proximity of the closer neighboring channel are enhanced when propagation effects are taken into account.

In summary, we have confirmed that, to reach 5Tbit/s capacity over C+L bands with NRZ format, an asymmetric $(50\text{GHz}/75\text{GHz})$ wavelength allocation scheme provides optimal performance when associated with a detuned filter of 30GHz bandwidth.

References

- [1] K. Fukuchi, "10.92-Tbit/s (273x40-Gb/s) triple-band/ultra-dense WDM optical-repeated transmission experiment", Optical Fiber Communications (OFC'01), Anaheim, 22 March, paper PD-24
- [2] S. Bigo et al., "10.2 Tbit/s (256x42.7Gbit/s PDM/WDM) transmission over 100km TeraLight fiber with 1.28 bit/s/Hz spectral efficiency", Optical Fiber Communications (OFC'01), Anaheim, 22 March, paper PD-25
- [3] B. Zhu et al., "3.08Tb/s (77x42.7Gb/s) transmission over 1200km of non-zero dispersion-shifted fiber with 100km spans using C-band and L-band distributed Raman amplification", Optical Fiber Communications (OFC'01), Anaheim, 22 March, paper PD-25
- [4] S. Bigo et al., "5.12 Tbit/s (128x40Gbit/s WDM) transmission over 3x100km of TeraLight™ fibre", European Conference on Optical Communications, paper PD1.2, pp. 40-41, Munich, 2000.
- [5] D. Penninckx and O. Audouin, "Optical preamplified systems: defining a new eye aperture", Optical Fiber Communications, San Jose, CA, WM36, 1998.
- [6] W. Idler et al., "Vestigial side-band demultiplexing for ultra-high capacity (0.64bit/s/Hz) of 128x40Gbit/s channels", Optical Fiber Communications, Anaheim, CA, paper MM3, 2001.

Ultralong Haul DWDM Transmission and Networking

Wednesday, 31 July 2001

- WC1: New Ultralong Technologies**
- WC2: High Capacity Ultralong Transmission**

Wednesday Missing Paper

WC1.2 “Hybrid & S-Band Raman Amplifiers”, M. N. Islam, *Xtera Communications, Allen, TX, USA.*

Advanced Fibers as Enabling Technology for ULH Networks

Robert Lingle, Jr., Optical Fiber Solutions, Lucent Technologies Inc.
Bell Labs Rm 2E-39, 2000 Northeast Expy, Norcross, GA 30071; rlingle@lucent.com

In general, the lowest installed-cost-per-bit for a high capacity, long haul transmission system is obtained by managing chromatic dispersion via the deployment of advanced fibers. Now the emergence of terrestrial mesh networks has led to interest in multiplexing large quantities of data in high-speed streams and transporting it thousands of kilometers across continent between major nodes. Recent advances in the design of fiber pairs for dispersion management enable larger bandwidths for DWDM and reduced residual link dispersion for high bit rate TDM. These developments are critical for ultra long haul systems where $\sim 5\times$ longer reach targets imply the need for $\sim 5\times$ less residual link dispersion for a given bit rate. One key advance is the development of dispersion and slope-matched fiber pairs with relatively large effective areas. The resulting positive dispersion maps practically eliminate dispersion compensation as an issue for 10 and 20 Gb/s systems.

ULH systems have historically been the domain of undersea networks. Submarine transmission systems have recently operated on negative chromatic dispersion maps in which the transmission link is based on one or more non-zero dispersion shifted fibers (NZDFs) with low, negative dispersions. Compensation is then accomplished with standard single mode fiber (SSMF). The use of a negative map with SSMF to provide dispersion compensation has the advantage of completely avoiding the low A_{eff} ($\leq 20 \text{ sq. } \mu\text{m}$) and high losses (0.4 to 0.5 dB/km) associated with the highly negative dispersion compensating fibers (DCFs) commonly used in terrestrial dispersion management. Negative maps also help suppress modulation instability by virtue of operating in the normal dispersion regime.

However both the dispersion and slope of SSMF are positive while the dispersion and slope of NZDF fibers are negative and positive, respectively. It is thus impossible to compensate broadly, since the slope of the link is a distance-weighted average of the component fiber slopes. Examination of high-capacity conference papers from 1997 - 2001 (see figure) suggests that negative map schemes may have reached a "speed limit" for system capacity in the range of 7 or 8 Pb*km/s. This is a fundamental consequence of the impossibility of broadband compensation using only fibers with positive slopes. A fiber solution which offered the wide bandwidth of dispersion and slope-matched fiber pairs but avoided the area and loss penalties associated with traditional DCFs would offer new flexibility in ULH system design.

This paradigm is realized by a now-commercial generation of dispersion and slope-matched, large A_{eff} fiber pairs such as the UltraWave® SLA (super large area) and IDF (inverse dispersion fiber) set from the Lucent's Optical Fiber Solutions. The 110 sq. μm SLA fiber retains the large material dispersion of silica in the 1550 window, which results in a very low relative dispersion slope (rds) of ~ 0.003 for ease of compensation, but requires significant negative dispersion from the IDF fiber. To reduce accumulated non-linearity in a ULH system and to keep the dispersion curvature of the IDF low for best compensation, it is possible to design the negative fiber to have a moderate negative dispersion (-40 ps/nm/km) and large $A_{\text{eff}} \sim 30 \text{ sq } \mu\text{m}$ [1]. Recent experiments with these fiber sets achieve transoceanic reach at 10 and 20 Gb/s with narrow DWDM ($< 50 \text{ GHz}$) channel spacing without per-channel compensation [2].

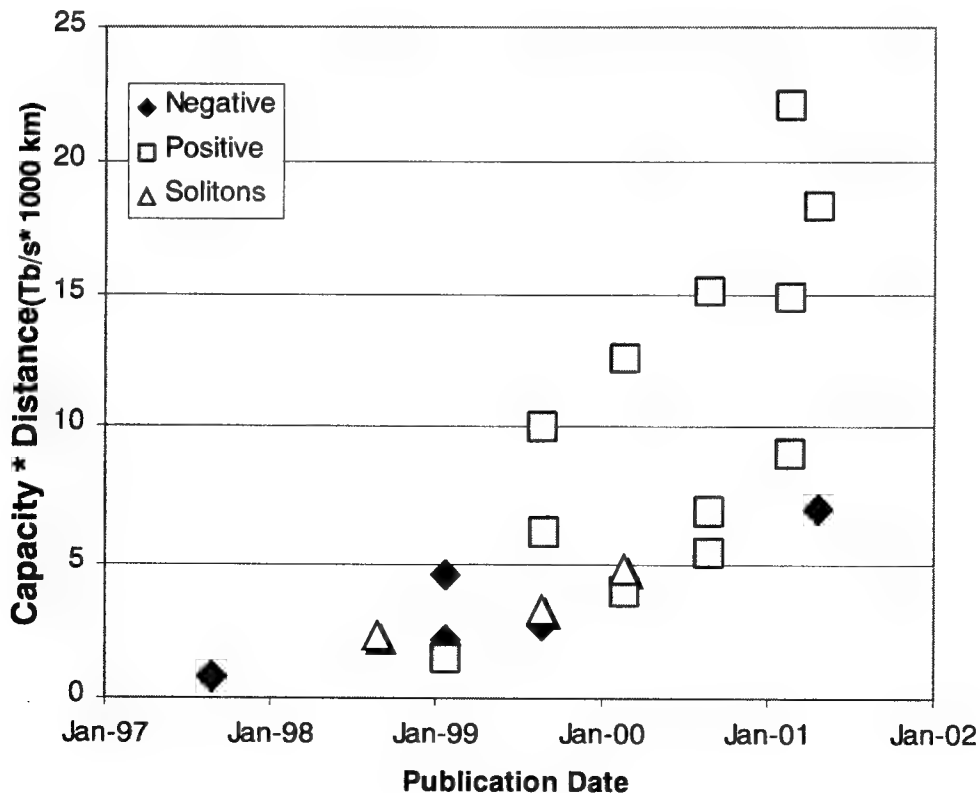
Practical issues of cabling and splicing these fibers in terrestrial applications require further development. First, submarine cables are more benign as regards microbending losses than are high fiber-count terrestrial cables. The high performance fibers in question are generally

microbend sensitive, and cabling studies are required to determine feasibility. Special splice techniques have also been developed for these fibers, and field realization of factory splicing results may require specialized equipment and training. Dispersion managed cables, as used in ocean systems, are more complex to fabricate as well as to maintain in the field.

Effective and widespread utilization of these dispersion managed spans in terrestrial ULH systems will depend on solutions to the practical issues just noted, the economic value proposition, and further systems engineering work. The practical issues are being addressed, and the need will drive solutions. Economic analyses may include issues such initial start-up costs vs. installed cost-per-bit for the fully lit system. System experiments [3] are exploring the effect of the dispersion map and what role Raman amplification will play. The moderately small effective area of the IDF fiber makes it a highly efficient distributed Raman gain medium.

Based on general considerations, we can predict that fiber research will push in the directions of larger effective areas and lower losses in both the positive and negative dispersion fibers. The Z+ silica core fiber from Sumitomo achieves a loss at 1550nm of ~ 0.170 dB/km [4]. Emphasis will likely be placed on obtaining the broadest possible compensation window. Microbending is likely to be a continual challenge. Fibers for soliton systems will also be discussed as well as the extension of traditional terrestrial dispersion maps to the case of ULH.

- [1] S.N. Knudsen *et al.*, Electron. Lett., vol. 36, p. 2067 (2000).
- [2] J.-X. Cai *et al.*, OFC'01 Paper PD20; B. Bakhshi *et al.*, OFC'01 Paper PD21.
- [3] B. Zhu *et al.*, NFOEC 2001; S.N. Knudsen *et al.*, accepted to Electron. Lett.
- [4] Kato *et al.*, Electron. Lett. Vol 35, p. 1615 (1999).



Multi-Terabit Long Haul DWDM Transmission With High Spectral Efficiency

Masatoshi Suzuki, Takehiro Tsuritani and Noboru Edagawa

KDDI R&D Laboratories, Inc.

2-1-15 Ohara, Kamifukuoka-shi, Saitama, 356-8502 Japan

TEL: +81-492-78-7835, FAX: +81-492-78-7516, E-mail: suzuki@kddilabs.jp

Introduction

Since terabit capacity per fiber has already become commercially viable even over transpacific distances using 10Gbit/s-based DWDM transmission technologies and C-band amplifiers, now the intense research efforts have been concentrated on multi-terabit transmission system development. For such applications, higher bit rates of either 20Gbit/s or 40Gbit/s will be expected so that the number of terminals can be much reduced. For multi-terabit long-haul transmission systems such as transoceanic systems, maintaining the high spectral efficiency over long distances is a crucial issue, since the impact of increasing nonlinear penalties due to narrower channel spacing will become intense as the transmission distance increases.

In this paper, technical challenges for multi-terabit long-haul DWDM transmission with high spectral efficiency are discussed.

Modulation Format

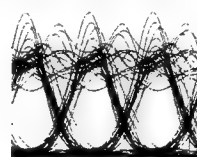
Various modulation formats to increase the spectral efficiency have been proposed. Table 1 summarizes the modulation formats[1]-[9], their spectral width and the resistance to the combination effect of self-phase modulation and accumulated dispersion.

To accommodate multi-terabit capacity within the limited bandwidth, the required spectral efficiency should be very high. Duo-binary format together with polarization division multiplexing (PDM) is a possible way to increase the spectral efficiency up to 1bit/s/Hz, but the resistance to nonlinear effects is not so large. In NRZ format, a spectral efficiency of 0.8bit/s/Hz has been achieved with PDM[10], and 1.28bit/s/Hz with vestigial sideband demultiplexing (VSB-demux) and PDM[11]. With these technologies, over 10Tbit/s transmission experiments have been demonstrated, however, transmission distance is limited to about 100km. Considering the effects of PMD and XPM, PDM technique seems difficult to apply to long haul systems.

For long distance transmission, RZ format is proved to be a suitable signal format to overcome fiber nonlinearities. Fig.2 shows the calculated waveforms after 7500km transmission for NRZ and RZ formats. Since all the pulses are isolated each other in RZ format and have the same waveform independently of the data pattern, the pattern dependence of SPM-induced waveform distortion observed in conventional NRZ format can be mitigated. To improve the nonlinear waveform distortion further, chirped RZ(CRZ) signal format

Table 1. Feature of various modulation formats

Modulation Format	Spectral width (main lobe)	Resistance to SPM-GVD	Ref.
Duo-Binary	1/2B	△	1
VSB-NRZ (w/ OBPF)	1/2B+α	○	2
Duo-Binary Carrier-Suppressed RZ	B	○	3
NRZ	B	○	-
Alternate Chirped RZ (AC-RZ) (w/ OBPF)	B+α	○	4
Band-limited OTDM RZ (w/ OBPF)	B+α	○	5
VSB-Chirped RZ (w/ OBPF)	B+α	○○	6
Carrier-Suppressed RZ/CS-RZ	2B-β	○○	7
RZ	2B	○	-
Chirped RZ/CRZ	2B+α	○○	8
DM-Soliton	>2B	○○○	9



(a) NRZ



(b) RZ

Fig.1 10Gbit/s waveform after 7500km transmission (4WDM, Large Core NZ-DSF/NZ-DSF hybrid span)

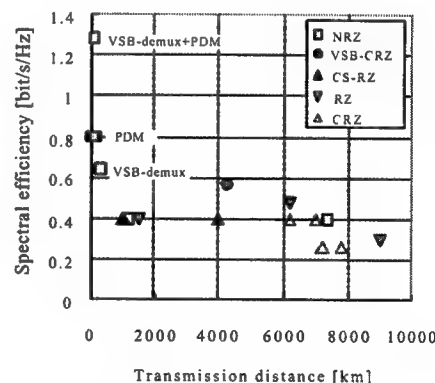


Fig.2 Spectral efficiency versus transmission distance

has been introduced[8]. Dispersion managed soliton (DM-soliton) has the largest resistance to SPM-GVD effect, but it requires the wider bandwidth[9].

To increase the spectral efficiency maintaining good transmission performance, modified RZ formats such as alternate chirp RZ (AC-RZ)[4] and carrier-suppressed RZ (CS-RZ)[7] have been proposed. Since alternate chirp between adjacent pulses requires almost zero dispersion, the tolerance of residual dispersion could be small. With narrow band optical bandpass filter (OBPF), band-limited OTDM RZ format[5] and VSB-chirped RZ format[6] have been proposed. Among them, VSB-chirped RZ seems promising since it can keep the large resistance to nonlinear effect of CRZ format without increasing

the spectral bandwidth. Excess spectral broadening to improve the transmission performance can be filtered out by the flat-top optical filter. Applicability of these modified RZ formats as well as conventional RZ and NRZ formats to long haul DWDM systems is still under investigation[12]-[15]. Fig. 2 shows the spectral efficiency versus transmission distance for various modulation formats. Note that these figures do not represent the exact comparison since the Q-factors obtained at the reported transmission distance are not the same.

VSF-Chirped RZ Transmission

Increase in spectral efficiency maintaining excellent feature of CRZ format can be expected by employing VSB-CRZ signals to avoid the spectral crosstalk between adjacent WDM channels as shown in Fig.3. A possible concern in VSB-CRZ format is the growth of the spectral sideband due to fiber nonlinearity during the transmission. Fig.4 shows the spectra before and after 4260km transmission. The extinction ratio of over 25dB between the carrier and the filtered sideband was maintained even after 4260km transmission. The tolerance of the residual dispersion of VSB-CRZ was larger than that of the conventional RZ signals because of narrower bandwidth[15].

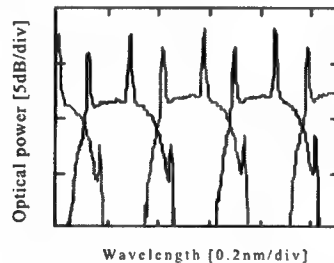
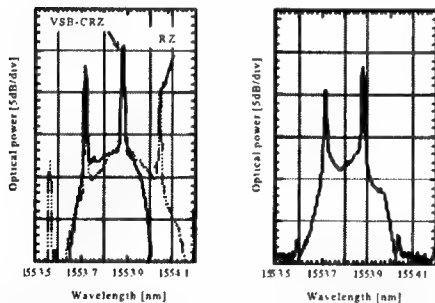


Fig.3 Spectrum of VSB chirped RZ Signals



(a) Before transmission (b) after transmission
Fig.4 VSB-Chirped RZ signal after 4260km transmission

2 Tbit/s Transmission Experiment

Feasibility of VSB-RZ long haul transmission has been demonstrated through the experiment of 35GHz-spaced-20Gbit/s 100WDM RZ transmission over 2700km using SMF-based dispersion-flattened fiber span[6]. VSB-CRZ signals were generated with narrow band OBPFs at the transmitter and spectral

efficiency of 0.6bit/s/Hz has been achieved. Fig. 5 shows Q-factor after 2700km transmission. Average Q-factor was 14.2dB. Fig.6 shows the Q-factor versus transmission distance of channel 52, which represents a typical average transmission performance of this transmission line. The Q-factor changes almost linearly with distances over 2000-4000km regime. At 4260km, Q-factor was 12.6dB. The transmission distance will be further increased by optimising the channel spacing[15].

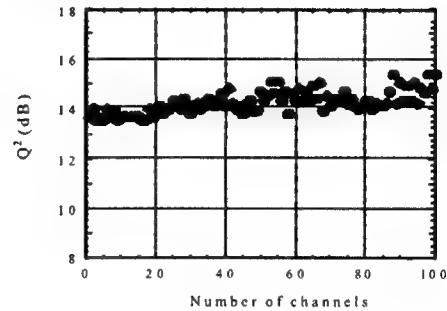


Fig.5 Q-factor after 2700km transmission

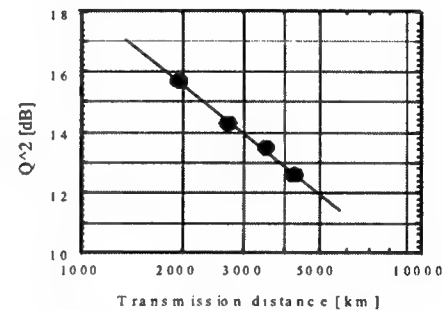


Fig.6 Q-factor versus transmission distance

Conclusion

Various modulation formats with high spectral efficiency have been proposed for multi-terabit long haul DWDM systems. VSB-chirped RZ seems a promising modulation format providing narrow spectral width and excellent robustness against nonlinear effects.

References

- /1/ Y. Yano et al., ECOC'96, PD, ThB.3.1, 1996.
- /2/ S. Bigo et al., ECOC2000, PD-1.2, 2000.
- /3/ Y. Miyamoto, et al., OFC2001, TuU4, 2001
- /4/ R. Ohira, et al., OFC2001, WM2, 2001.
- /5/ T. Miyakawa, et al., OFC2001, PD26, 2001.
- /6/ T. Tsuritani, et al., ECOC2000, PD-1.5, 2000.
- /7/ Y. Miyamoto, et al., OAA'99, PDP4, 1999.
- /8/ N. Bergano, et al., OFC'96, TuN1, 1996.
- /9/ I. Morita et al., J. Lightwave Tech., 17, pp.2506,1999
- /10/ K. Fukuchi et al., OFC01, PD-24, 2001
- /11/ S. Bigo et al., OFC01, PD-25, 2001
- /12/ G. Varcille et al, OFC01, PD22, 2001
- /13/ J.-X. Cai et al, OFC01, PD20, 2001
- /14/ B. Bakhshi et al., OFC01, PD21, 2001
- /15/ T. Tsuritani et al, OFC01, MM5, 2001

Strategies for very dense WDM ULH terrestrial RZ systems over all types of fibre

L. Billès, D. Leguen, S. Lobo, L. Bramerie, S. Del Burgo, F. Merlaud, T Georges

Corvis Algety, Lannion, France (e-mail : lbilles@corvis.com)

Abstract: Spectral efficiency will be discussed as a key issue for long reach systems. Ready to deploy, 0.4 bit/s/Hz, Nx10 Gbit/s experiments will be highlighted, as well as next generation 40 Gbit/s systems.

Introduction

High spectral efficiency and long transmission distance is required for WDM systems to cope with rapid increase of internet traffic. Moreover, capacity has to be coupled with span loss constraint of terrestrial networks, ranging between 18 and 28 dB. There is a trade-off between these three parameters. In Fig. 1, 10^{-9} uncorrected error rate distance and the spectral efficiency of laboratory transmission systems that could foresee industrial systems (with span loss greater than 18 dB) are reported.

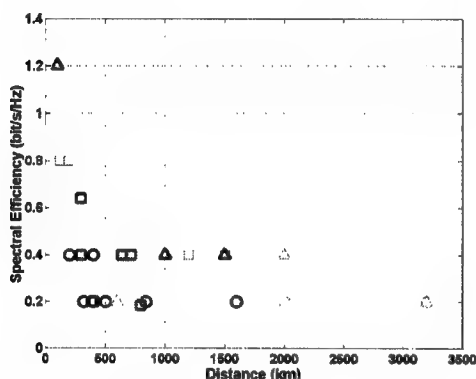


Figure 1 : Comparison of spectral efficiencies of laboratory DWDM systems (circle: 10 Gbit/s, triangle: 20 Gbit/s, square: 40 Gbit/s and light symbols: smaller span loss or corrected error rate).

0.4 bit/s/Hz was demonstrated at 10, 20 and 40 Gbit/s per channel /1-11/. It is also a realistic goal for 10 Gbit/s-based DWDM ultra-long-range terrestrial systems with large span loss. Key enabling technologies are FEC, which can provide system margins of laboratory transmission systems, Raman amplification /12/, PMD compensation, especially for 40 Gbit/s bit rate and modulation format. For short distances, when signal spectrum is clean and spectral efficiency is limited by demultiplexing capability, duobinary and polarisation multiplexing with large bit rate have proven to be the most efficient, while, for long distance transmission, non-linear robust RZ format, like dispersion managed soliton (DMS) is required. It allows a good control of temporal and spectral pulse characteristics along path, at 10 and 40 Gbit/s, which also limits intra-channel interaction. Examples are given below of compromises between reach, spectral efficiency and span loss for different fibre types using this technique, combined with alternating polarisation of adjacent channels for XPM reduction.

At 2.5 Gbit/s, thanks to Raman amplification and FEC, ULH

reach has been installed making available for the first time all-optical networking /13/.

10 Gbit/s

At 10 Gbit/s per channel, spectral efficiency can be improved allowing to increase capacity. The price to pay is to refine dispersion management (with a particular care to dispersion slope compensation) and shorter reach with lossy spans. A compromise must be found between reach, capacity and loss.

In order to illustrate this compromise, main results of dispersion-managed soliton loop experiments at Nx10.66 Gbit/s on different types of fibre are presented.

(a): SMF28 25 dB / 100 km span and 25 GHz channel-spacing:

9x10.66 Gbit/s RZ transmission was achieved with 25 GHz channel-spacing. Two different types of 2-stage amplifiers for dispersion and loss compensation have been tested: one is all-EDFA, the other one is an hybrid Raman-EDFA amplifier. Fig. 2 compares BER measurements on input fibre power against distance for the two amplification schemes. At a given distance, postchirp was fixed for all powers and optimised for best performance case.

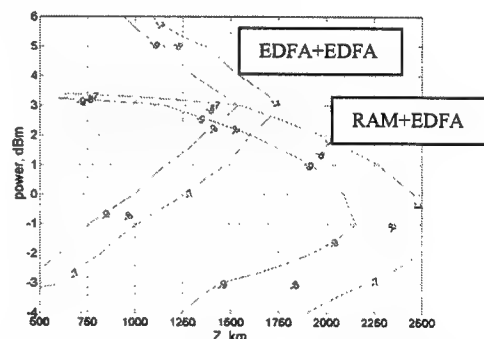


Figure 2: iso-contours for $\log_{10}(\text{BER})$ on input-fibre power per channel against distance with all-EDFA amplification (up) and hybrid Raman-EDFA amplification (down). (SMF28 25 dB/ 100 km span ; 25 GHz channel-spacing)

Non-linearities limit maximum transmission distances ($@10^{-9}$ BER) to 1500 km at +3 dBm/ch with EDFA and 2100 km at -1 dBm/ch with hybrid amplification. Noise figure improvement by about 6 dB due to Raman amplification in SMF explains differences between low power limits of both experiments. No FWM component was found after 2100 km, as expected, thanks to high local dispersion of SMF-28 fibre. As XPM is greatly reduced thanks to alternate polarisations

between adjacent channels, the main cause of non-linearity impairments is the intra-channel interaction jitter.

(b): *TWC 18 dB/ 75 km span and 25 GHz channel-spacing:*

The 10x10.66 Gbit/s RZ transmission with 25 GHz channel-spacing with alternate polarisations was demonstrated on TWC 18 dB/75 km span with Raman amplification. The TWC dispersion at 1532 nm was 2.16 ps/nm/km. The dispersion was partially compensated every 300 km. Maximum transmission distance is mainly limited to 2800 km @ 10^{-9} BER, by intra-channel interaction (Fig.3). At 1564 nm, the distance is limited to 2600 km for $D = 3.3$ ps/nm/km at -6 dBm. Here, long distance, high spectral efficiency could be maintained over this fibre thanks to span loss reduction and channel power decrease.

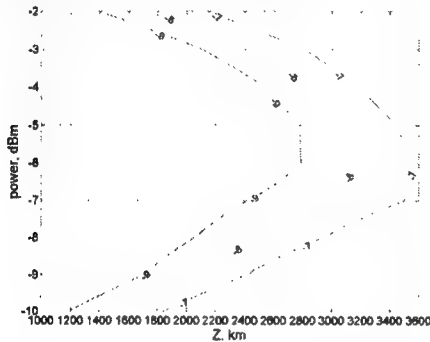


Figure 3: iso-contours for $\log_{10}(\text{BER})$ on input-fibre power per channel against distance (TWC 18 dB/ 75 km span and 25 GHz channel-spacing).

(c): *TW-RS 25 dB/ 100 km span and 50 GHz channel-spacing:*

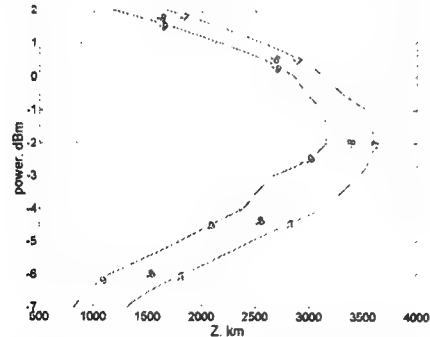


Figure 4: iso-contours for $\log_{10}(\text{BER})$ on input-fibre power per channel against distance (TW-RS 25 dB/ 100 km span and 50 GHz channel-spacing)

With high, 25 dB span loss, long distance transmission can be optimised on TW-RS, with lower spectral efficiency. The 10x10.66 Gbit/s RZ transmission with 50 GHz channel-spacing and alternate polarisations was demonstrated with Raman amplification. The maximum transmission distance is 3200 km @ 10^{-9} BER.

40 Gbit/s

(a): *DSF 21 dB/ 100 km span, single channel*

Dispersion managed soliton (DMS) transmission was tested on recirculating loop at 40 Gbit/s with alternate polarisation between successive pulses of 5 ps FWHM. The

100 km/ 21 dB span of DSF with $D = 0.63$ ps/nm/km was compensated at 90% using DCF. $Q^2 = 16.5$ dB (BER = 10^{-10}) was measured at 1800 km. Such a distance can be achieved while decreasing spectral efficiency down to 0.1 bit/s/Hz.

(b): *TW-RS 23 dB/ 100 km span and 100 GHz channel-spacing*

On the other hand, one can optimise spectral efficiency. The price to pay is a reduction in transmission reach, but trade-off can be found minimizing together TDM and WDM impairments.

10x42.6 Gbit/s DMS transmission was tested in a 6x100 km straight line experiment over 23 dB/100 km spans of TW-RS, with a 100 GHz spacing and Erbium amplification, without any in-line dispersion compensation.

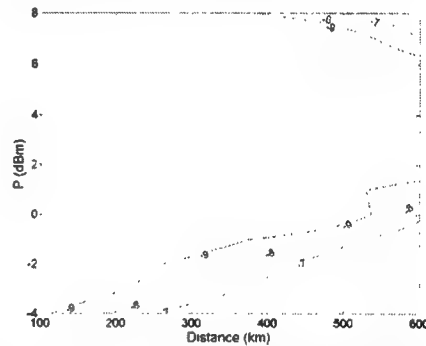


Figure 6: iso-contours for $\log_{10}(\text{BER})$ on input-fibre power per channel against distance (TW-RS 23 dB/ 100 km span and 100 GHz channel-spacing)

At 600 km, there are still comfortable margins that give a good potential for long reach using Raman amplification.

Conclusion

Following already installed WDM systems at 2.5 Gbit/s, the deployment of the next generations at 10 Gbit/s and later at 40 Gbit/s will improve spectral efficiency over most of fibre types at the price of finding a compromise between reach, span loss and capacity. The key techniques to be controlled are the DMS, Raman amplification and FEC.

References

- /1/ A. K. Srivastava, et al, OFC 2000, PD27 (2000)
- /2/ D. Le Guen et al, OFC 1999, PD4, (1999)
- /3/ Y. Zhu et al, OFC 2001, ThF4, (2001)
- /4/ T. N. Nielsen et al, OFC 2000, PD23, (2000)
- /5/ T. Ito et al, OFC 2000, PD24, (2000)
- /6/ S. Bigo, et al, ECOC2000, PD1.2, (2000)
- /7/ T. Tsuritani et al, ECOC2000, PD1.5, (2000)
- /8/ Y. Kobayashi et al, ECOC2000, PD1.7, (2000)
- /9/ T. Tanaka et al, ECOC2000, PD1.8, (2000)
- /10/ I. Morita et al, ECOC2000, vol.4, (2000), p.25
- /11/ A.R. Pratt et al, ECOC2000, vol.4, (2000), p.29
- /12/ A. Evans, OFC 2001, TuF4, (2001)
- /13/ S. Grubb et al, LEOS 2001

High Capacity Undersea WDM Transmission Systems - A Development Perspective

Michael Vaa

TyCom Laboratories, 250 Industrial Way West, Room 2D-214, Eatontown, NJ 07724, USA.

E-mail: mvaa@TyComLtd.com

Abstract: Recent progress in installed ultra-long haul undersea transmission systems and related development efforts are reviewed. Topics covered include amplifier equalization, dispersion management, and modulation formats. Practical aspects of installed systems such as initial capacity loading, system aging and design limitations due to stringent reliability requirements will also be discussed.

Introduction

Recently, numerous results on laboratory WDM transmission experiments over trans-oceanic distances with multi Tbit/s capacity have been reported [1,2]. At the same time, the ultimate capacity over a single fiber pair of transoceanic undersea WDM systems is rapidly approaching 1 Tbit/s. An important difference between lab experiments and installed systems is that the latter is typically designed for a system lifetime of 25 years. This imposes stringent reliability requirements that limit the available technology base that can be deployed and implies the need for a strong interaction between development and research to ensure manufacturability of new system concepts.

Recently installed systems

Since 1998 TyCom has installed a number of Trans-Atlantic and Trans-Pacific systems and the capacity has increased from 16 x 2.5 Gbit/s (7500 km) in 1998 to 64 x 10 Gbit/s (6500 km) in 2001. This represents a capacity increase of 1500 % over a period less than 3 years. Table 1 summarizes this development. The technology drivers for the recent capacity enhancement are increasing utilization of the EDFA C-band, effective forward error correction (FEC) coding, dispersion management and Chirped Return-to-Zero (CRZ) modulation format [3].

Bandwidth (nm)	Capacity per fiber (Gbit/s)	Distance (km)	Service date
8	16 x 2.5	7500	'98
14	16 x 10	9600	'99
21	48 x 10	6500	'00
28	64 x 10	6500	'01
28	64 x 10	8600	'02

Table 1 Installed systems

Optical amplifier technology

Realization of 28 nm bandwidth for a trans-oceanic system requires that every repeater has incorporated a gain flattening filter (GFF). The use of a GFF is made necessary because of the larger gain variations inherent

to the EDFA when the bandwidth is increased. A gain equalization filter (GEF) is applied after a number of repeaters to correct for the equalization error of the GFFs. The error depends on filter technology and the amplitude of the filter function. Fiber Bragg Grating (FBG) filter technology has been shown to be very effective in minimizing the equalization error [4]. However, depending on the quality of the FBG manufacturing process unwanted small fast variations in the filter function may arise and cause system degradation, especially when the period of the variations are comparable to the bit rate of the data signal [5]. Fig.1 shows an example of how transmission performance, measured as Q^2 (in dB), can vary when fine tuning the signal wavelength across the gain and group delay ripples caused by filter manufacturing imperfections [6]. Other candidates for equalizing filter technologies are thin film filters, long period gratings and tapered fiber filters. These technologies typically do not have fast ripples in the filter function and have potential use in undersea systems. Choice of filter technology is also determined by reliability requirements.

Another important aspect of extending the EDFA bandwidth is availability of reliable pump power. Increasing bandwidth increases the amount of power

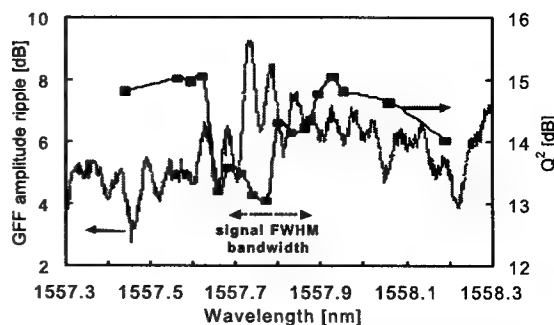


Fig. 1 Q^2 vs. wavelength tuning (squares) for a 12.3 Gbit/s CRZ signal transmitted over 6000 km in a loop experiment. The associated accumulated FBG GFF ripple is also shown.

lost in the GFF and optical power is a premium in undersea systems.

Dispersion management

To reduce the impact of fiber non-linearities in ultra-long haul systems the dispersion of the transmission line must be carefully managed. The emergence of dispersion slope compensating fibers makes it possible to reduce the accumulated dispersion to practically zero over a wide bandwidth or tailor it for optimized performance [7]. This fiber technology will be deployed in the near future. In recently installed systems, non-zero dispersion shifted fiber combined with large mode fiber constitutes the fiber spans. The spans typically have negative dispersion across the transmission spectrum, which is offset by a positive dispersion fiber span every 250 – 500 km depending on system design. The residual dispersion slope of these fiber types typically causes accumulated dispersion in the range of ± 6000 ps/nm for a trans-Atlantic system with 28 nm bandwidth. To minimize the impact of large amounts of accumulated dispersion combined with fiber non-linearities, the choice of modulation format becomes important.

Modulation format

The proper choice of modulation format depends on channel spacing, power per channel and dispersion map. For recently installed system designs, the CRZ format has proven to be superior compared to the NRZ and RZ signal formats. This is illustrated in Fig. 2 which shows system performance vs. distance for a channel with up to -6000 ps/nm accumulated dispersion (9000 km) in a 64×12.3 Gbit/s experiment for NRZ, RZ and CRZ modulation format [8]. Channel spacing is 50 GHz and 1rad bit-synchronous phase modulation for the CRZ case is applied. The CRZ format has a clear performance advantage over RZ for this system configuration; up to 2 dB for long distances, i.e. large accumulated dispersion. When

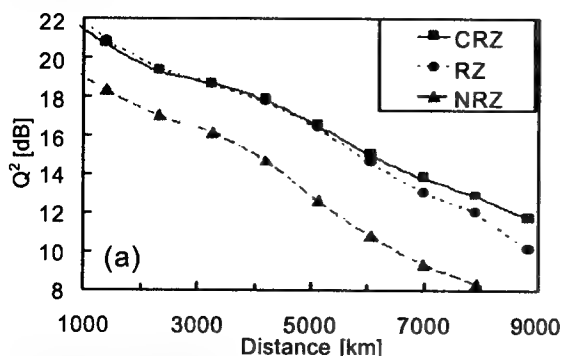


Fig. 2: Performance vs. distance for NRZ, RZ and CRZ modulation format @ 12.3 Gbit/s data rate. Channel spacing is 50 GHz.

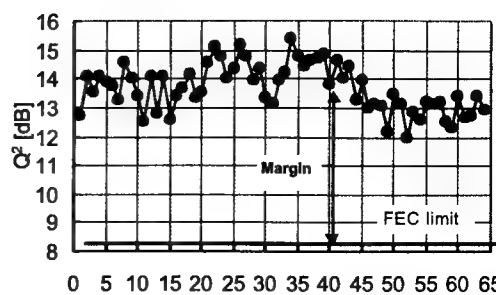


Fig. 3: System performance of a 640 Gbit/s x 7000 km loop experiment using undersea qualified technology.

reducing the channel spacing further and thereby increasing the spectral efficiency, the modulation format of choice will be determined by a trade-off between linear cross-talk and robustness against fiber non-linearities. To this end, other interesting formats currently being studied include carrier suppressed RZ, vestigial sideband RZ and alternating chirp RZ. The fact that future systems with a high channel count will operate closer to the linear regime due to small accumulated dispersion and the availability of efficient FEC codes [9] will tend to enhance the linear cross-talk aspect when deciding the preferred modulation format. Fig. 3 shows the system performance for 64 channel transmission @ 12.3 Gbit/s over 7000 km as measured in a loop experiment representative of TyCom's recently installed 28 nm Atlantic system. An average system margin of 5.2 dB was achieved [10] relative to the FEC limit, enabled by a concatenated Reed-Solomon code with 23 % overhead. The result illustrates the important contribution from recent advancements in FEC technology toward increased capacity of undersea systems.

Summary

The recent development of installed undersea cable systems has been reviewed. The capacity has increased 1500% in less than 3 years. Further bandwidth expansion in the EDFA C-band combined with strong FEC coding and technologies allowing higher spectral efficiency will drive the near term development.

References

- [1] J. X. Cai et al., PD20, OFC'01, Anaheim, 2001.
- [2] G. Varella et al., PD22, OFC'01, Anaheim 2001.
- [3] N. S. Bergano et al., PD16, OFC'97, Dallas, 1997.
- [4] B. Bakhshi et al., PD21, OFC'01, Anaheim, 2001.
- [5] K. Enns et al., IEEE Photon. Technol. Lett., 10 (1998), p. 1476.
- [6] B. Bakhshi et al., submitted for ECOC'01.
- [7] S. Wabnitz et al., ECOC'00, pp. 37-38, Munich, 2000.
- [8] B. Bakhshi et al., WF4, OFC'01, Anaheim, 2001.
- [9] C. R. Davidson et al., PD25, OFC'00, Baltimore, 2000.
- [10] M. Vaa et al., WF5, OFC'01, Anaheim, 2001.

AUTHOR INDEX

Almeida, P.	TuC3.3	Tsai, H.-S.	MC3.3
Bergano, N.	MC1.1	Tsuritani, T.	WC2.1
Bigo, S.	TuC4.3	Vaa, M.	WC2.3
Billes, L.	WC2.2	Veasey, D.	MC2.3
Bramerie, L.	WC2.2	Veselka, J.	TuC2.2
Brewington, B.	TuC4.2	Wang, T.	MC2.3
Cammarata, J.	MC2.3	Willner, A.	MC2.2
Chen, C.-J.	MC3.3	Wong, W.	MC3.3
da Rocha, J.	TuC3.3	Wysocki, P.	MC3.3
Damask, J.	MC2.3	Yamada, T.	TuC3.2
Del Burgo, S.	WC2.2	Zhang, V.	TuC4.2
Edagawa, N.	WC2.1		
El-Ahmadi, S.	TuC4.1		
Frignac, Y.	TuC4.3		
Fujii, K.	TuC3.2		
Georges, T.	WC2.2		
Gray, G.	MC2.3		
Grubb, S.	TuC2.2		
Hall, K.	TuC4.2		
Henion, S.	TuC4.2		
Ho, M.	MC3.3		
Holzloehner, R.	MC1.2		
Ibragimov, E.	MC2.3		
Islam, M.	WC1.2		
Jacob, J.	TuC4.2		
Jensen, R.	TuC1.1		
Jones, D.	TuC4.2		
Kesler, M.	TuC4.2		
Khatrri, F.	TuC2.1		
Kimball, R.	MC2.1		
LaGasse, M.	TuC4.2		
Lee, H.	MC3.3		
Leguen, D.	WC2.2		
Lima, I.	MC1.2		
Lingle, R.	WC1.1		
Lobo, S.	WC2.2		
Maloney, J.	TuC4.2		
Matsumoto, M.	TuC3.1		
Menyuk, C.	MC1.2		
Merlaud, F.	WC2.2		
Mollenauer, L.	TuC2.3		
Murai, H.	TuC3.2		
Ozeki, Y.	TuC3.2		
Pinto, A.	TuC3.3		
Pires, J.	MC3.2		
Rivera, M.	MC2.3		
Robinson, N.	TuC4.1		
Rochford, K.	MC2.3		
Simer, G.	MC2.3		
Sluz, J.	MC2.3		
Srivastavas, A.	MC3.3		
Sun, Y.	MC3.3		
Suzuki, M.	WC2.1		
Ten, S.	MC3.1		
Thoen, E.	TuC4.2		
Tkach, R.	TuC1.2		

**2001 IEEE/LEOS
Summer Topical Meeting**

30 July – 1 August 2001

WDM Components

**Copper Mountain Resort
Copper Mountain, CO**

IEEE Catalog Number: 01TH8572

ISBN: 0-7803-7100-3

ISSN: 1099-4742

The papers in this book comprise the digest of the meeting mentioned on the cover and title page. They reflect the authors' opinions and are published as presented and without change in the interest of timely dissemination. Their inclusion in this publication does not necessarily constitute endorsement by the editors, the Institute of Electrical and Electronics Engineers, Inc.

© 2001 by the Institute of Electrical and Electronics Engineers, Inc. All rights reserved.

Copyright and Reprint Permissions: Abstracting is permitted with credit to the source. Libraries are permitted to photocopy beyond the limits of U.S. copyright law, for private use of patrons those articles in this volume that carry a code at the bottom of the first page, provided the per-copy fee indicated in the code is paid through the Copyright Clearance Center, 222 Rosewood Drive, Danvers, MA 01923. For other copying, reprint, or republication permission, write to IEEE Copyrights Manager, IEEE Service Center, 445 Hoes Lane, P.O. Box 1331, Piscataway, NJ 08855-1331.

IEEE Catalog Number:	01TH8572
ISBN:	0-7803-7100-3
ISSN:	1099-4742



WDM Components

Co-Chairs:

Chris Doerr, *Bell Labs, Lucent Technologies*, Holmdel, NJ
Ed Murphy, *JDS Uniphase*, Bloomfield, CT

Technical Program Committee:

N. Boos, *Corning, S.A.*, Avon, France
B. Chang, *JDS Uniphase*, San Jose, CA
R. Espindola, *Lucent Technologies, Bell Laboratories*, Murray Hill, NJ
Y. Kim, *KAIST*, Yusong, Korea
A. Sugita, *NTT Photonics Labs*, Ibaraki, Japan

TABLE OF CONTENTS

Monday, 30 July 2001

MD1.	Introduction	
MD1.1	Photonic Network Trends and Impact on Optical Components.....	3
MD1.2	Smart Free-Space Optical Interconnects and Communication Links using Agile WDM Transmitters.....	5
MD1.3	Integrated Bragg Grating Structures	7
MD2.	Silica Waveguides	
MD2.1	Recent Advances in PLC Functional Devices.....	9
MD2.2	Wavelength Splitters for DWDM Systems	11
MD2.3	Micron-Size Bending Radii in Silica-Based Waveguides.....	13
MD3.	Joint Session between Ultralong Haul & WDM: Dynamic Dispersion & PMD Compensation	
MD3.1	Dynamically Tunable Dispersion Slope Compensation using a Virtually Imaged Phased Array (VIPA).....	15
MD3.2	Systems Applications of Advanced Fiber Grating Devices.....	N/A
MD3.3	PMD Mitigation using Diversity Detection	17
MD3.4	Concept for Individual Channel Polarization Control in a WDM Signal using an Integrated Device.....	19
MD4.	Dynamic Dispersion & Slope Compensation Methods & Devices	
MD4.1	Thin-Film based Coupled-Cavity Allpass Filters for Dynamic Dispersion-Slope Compensation	21
MD4.2	Tunable Dispersion Compensators Based on Optical Allpass Filters	23

Tuesday, 31 July 2001

TuD1.	Wavelength Add/Drop	
TuD1.1	Tunable Transparent and Cost Effective Optical Add-Drop Multiplexer based on Fiber Bragg Grating for DWDM Networks	27
TuD1.2	80-Channel Integrated Dynamic Drop Filter with Flat-Top Passband.....	29
TuD1.3	Compact Mode-Size Converters for Efficient Coupling between Fibers and Integrated Optical Waveguides	31

Wednesday, 1 August 2001

WD1.	Dynamic Gain Equalization Techniques & Devices I	
WD1.1	Dynamic Gain Equalization for Next-Generation DWDM Transport Systems	35
WD1.2	Fiber-based Acousto-Optic Gain Equalizer	N/A
WD1.3	Tapped Delay Line Dynamic Gain Flattening Filter.....	37
WD2.	Dynamic Gain Equalization Techniques & Devices II	
WD2.1	Liquid-Crystal Optical Harmonic Equalizers.....	39
WD2.2	Silica Arrayed Waveguide Dynamic Gain Equalization Filter	41
WD2.3	Optical Networking using Micromachines	43

WDM Components

Monday, 30 July 2001

- MD1: Introduction
- MD2: Silica Waveguides
- MD3: Joint Session between Ultralong Haul & WDM:
Dynamic Dispersion & PMD Compensation
- MD4: Dynamic Dispersion & Slope Compensation
Methods & Devices

Monday Missing Paper

MD3.2 "Systems Applications of Advanced Fiber Grating Devices" B. J. Eggleton, *Bell Laboratories, Lucent Technologies, Murray Hill, NJ, USA.*

Photonic Network Trends and Impact on Optical Components

by Peter Kaiser, PhD
Santec Photonics Laboratories
433 Hackensack Avenue
Hackensack, NJ 07601
Ph: 201 488 5505; Fx: 201 488 7702
pkaiser001@aol.com

Summary

The large-volume production of highly functional, integrated, standardized and low-cost optical components and subsystems is a key prerequisite for the widespread introduction of optical networking technologies in new network segments such as the Metro and Access networks. This talk describes the demand for, and the evolution of optical components from Long-Haul to Metro and Access networks, together with the unique requirements and opportunities for opto-electronic component technologies in those networks.

Due to exponentially growing Internet and data traffic, information networks are evolving from SONET/SDH-based ring networks to more cost-effective mesh network architectures with IP-over-DWDM interfaces directly. To further reduce the cost of bandwidth, there is also a trend to eliminate electronic regenerators to the maximum degree possible and to deploy large-channel-count DWDM systems with optical amplifiers (OAs) extending up to several 1000 km's ("long-reach" or "Ultra-Long-Haul" systems). Access to the 2.5, 10 and 40 Gb/s channel rates is achieved with optical add-drop multiplexers (OADMs) in combination with OAs and initially opaque (electronic), and later transparent optical crossconnects (T-OXCs) with bitrate and protocol independence for the digital optical signals. The deployment of long-reach DWDM transmission systems particularly at 40Gb/s signal rates requires the use of low-nonlinearity and low-dispersion optical fibers with dynamic chromatic and polarization-mode dispersion compensation, wideband OAs with dynamic gain equalization, high-power lasers with DWDM channel spacings of 100/50/25GHz and below, and soliton-like transmission. Reduction of the effects of fiber non-linearities can be achieved through fiber design (e.g., through large-effective core area) or through the reduction of pump power via distributed Raman amplification.

Metro Core and Access networks with DWDM are considered the next major growth area for optical networking technologies to carry the rapidly increasing traffic due to high-speed customer services. The drivers for these services are fast-growing e-business, e-commerce, educational, multimedia, video and entertainment services in addition to conventional voice and data services. Metro networks with T-OXCs and multi-service platforms will be able to carry different protocol LAN/WAN, Enterprise, Storage Area and multimedia/digital video network traffic as well as conventional

SONET/SDH services. The deployment of customer-owned dark-fiber networks (e.g., with Ethernet protocol), is already resulting in bandwidth offered at a fraction of the price of conventional high-speed services today (e.g., \$1000 per month for 100Mb/s Internet Access - Ref.: Cogent Communications). The increasing availability of asymmetric ADSL and Cable Modem services is stimulating the demand for symmetric large-bandwidth multimedia and file-transfer services and the deployment of fiber closer to the customer through the use of FTTC and FTTH by telecom operators, and fiber-fed smaller service areas by Cable network operators. While the component functionality is similar as in the long-haul network, including DWDM Multiplexers and Demultiplexers, OADMs, OXCs and OAs, the key for success of optical networking technologies in these network segments is a high level of integration of very-low-cost, highly reliable and standardized optical components that are designed for automated manufacturing and mass production. Consequently, emphasis is being placed on large-scale integration through MEMS and array technologies, long-wavelength VCSELs, tunable lasers and filters, SOAs and Erbium-doped waveguide amplifiers, integrated transceivers and transponders, hybrid integration of active and passive optical components in Photonic Integrated Circuits (PICs) and Planar Lightwave Circuits (PLCs), as well as mass-splicing, connectorization and easy fiber handling. Another important aspect is the need for low-cost operation and management of the optical network elements in the Metro and Access network environment.

In conclusion, advanced, highly functional, application-specific, integrated, and low-cost opto-electronic components comprise the enabling technologies for the ever more widespread application of optical networking technologies in next-generation optical networks, with particular emphasis on Metro and Access networks.

###

Smart free-space optical interconnects and communication links using agile WDM transmitters

Zahid Yaqoob and Nabeel A. Riza*

Photonic Information Processing Systems Laboratory, The School of Optics/CREOL, University of Central Florida
4000 Central Florida Blvd., Orlando, FL 32816-2700
Tel: 407-823-6829, Fax: 407-823-3354
yaqoob@creol.ucf.edu, riza@creol.ucf.edu

Abstract: Smart programmable free-space optical interconnects and communication links are proposed using ultrafast nanosecond scanning speeds transmitters based on the wavelength multiplexed optical scanner (W-MOS) array.

1. Introduction

The explosive growth of data traffic has urged to seek refuge in the optical domain [1-3]. Free-space optical communication promises high connectivity and dispersion free dynamic optical paths – a feature that is lacked by fiber-optic communication networks. A smart free-space optical communication network will require a mature beam steering technology with features including ultra-fast scan setting speeds, eye-safe operation, and high scan resolution for desired bit error rate (BER) at the receiver end. A new design technology called Multiplexed Optical Scanner Technology or MOST was introduced [4] for laser beam steering that promises no moving parts, low power consumption and true rapid three dimensional (3-D) beamforming to accurately control beam position, power and shape. This paper describes a practical optical network architecture for smart free-space optical interconnects and communication links using agile transmitters. These transmitters use the Wavelength Multiplexed Optical Scanner (W-MOS), a peer member of the MOST family.

2. Free-space optical interconnects and links

Fig.1 shows the proposed smart architecture for free-space optical interconnects and communication links with N optical transmitters and M optical receivers. Each transmitter has two electrical input channels; namely, the electrical data input and the λ control to the tunable laser inside the transmitter. The tunable source controls the direction of the information carrying optical beam exiting the corresponding transmitter. The distance between each transmitter is p_i ; ($i = 1, 2, \dots, N-1$) whereas the distance between each receiver is q_j ; ($j = 1, 2, \dots, M-1$) as shown in Fig. 1. Note that the size of each transmitter and receiver can be reduced to the order of a millimeter or even smaller whereas distances p_i and q_j can be independently set to a couple of microns, making it possible to use this architecture for inter-chip or inter-processor parallel data transfer. On the other end, it is also possible to place the transmitters and receivers miles from each other and use the same architecture for agile satellite communication links. W-MOS based on grating-type large surface area storage technology makes it possible to have large aperture (e.g., > 10 cm diameter) transmitters for high resolution scans. As shown in Fig. 1, each transmitter is designed to transmit in the direction of receiver R_i when each tunable laser is set to emit the wavelength λ_i . Thus by tuning a laser from λ_1 to λ_M , any of the receivers can be reached. It is also possible to simultaneously interconnect optical signals from two or more transmitters to a specific receiver by appropriately tuning the corresponding transmitter lasers.

3. Agile Transmitter using W-MOS

Fig. 2 shows a detailed schematic of the agile transmitter based on the earlier proposed W-MOS. By changing the wavelength via electronic control of the tunable laser, very high-speed beam scanning can be achieved as shown in Fig. 2(a). The potential speed of this agile transmitter is in the GigaHertz rates using the present-day state-of-the-art nanosecond tuning speed lasers [5].

* Also with Nuonics, Inc., Orlando, FL

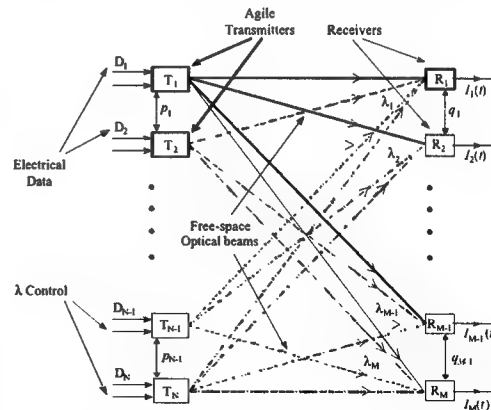


Fig. 1. Proposed smart architecture for free-space optical interconnects or communication links. T_i : i^{th} transmitter; D_i : Data from i^{th} source; p_i : Distance between transmitter i and transmitter $(i+1)$; q_i : R_i : i^{th} Receiver; q_i : Distance between receiver i and receiver $(i+1)$; $I_i(t)$: Signal at the output of i^{th} receiver; SMF: Single mode fiber.

A proof-of-concept free-space wavelength multiplexed agile transmitter using a 1-D amplitude grating (grating period $L = 1/80$ mm) as a dispersive element was setup in the laboratory using a 1560 nm fiber-coupled mechanically tuned laser with a 80 nm tunable bandwidth as shown in Fig. 2(b). Light from the fiber is collimated by a graded refractive index (GRIN) rod lens, expanded by a combination of spherical lenses S_1 and S_2 , and strikes the 1-D binary amplitude grating at normal incidence. A focussing lens of $F_3 = 125$ mm focal length is used to observe the scanning spots in 1-D. The angular scan range of the transmitter setup is limited to $\sim 0.4^\circ$ because of larger period L of the grating as suggested by the grating equation $\theta(m) = \sin^{-1}(m\lambda/L + \sin \theta_i)$, where $\theta(m)$ is the direction of the m^{th} order deflected beam when an optical beam of wavelength λ is incident at an angle θ_i . Decreasing the period L of the grating can increase the angular scan range of the transmitter. The maximum angular deflection can be increased further if the optical beam hits the grating at oblique angles. For instance, a W-MOS based transmitter using a 600 lines/mm grating (instead of 80 lines/mm) with a tunable laser having an 80 nm bandwidth centered at 1560 nm, gives a maximum scan range of $\sim 7.96^\circ$ for the 1st diffracted order and normal incidence. The angular scan increases further to $\sim 14.87^\circ$ when the laser beam is incident at 2.2° . Thus, independent control of the period of the diffraction grating, angle of incidence of the laser beam, and the bandwidth of the tunable source permits optimization of the dynamic deflection range of the W-MOS based transmitter. In addition, the chosen grating should be designed to provide maximum diffraction efficiency in the desired diffracted order.

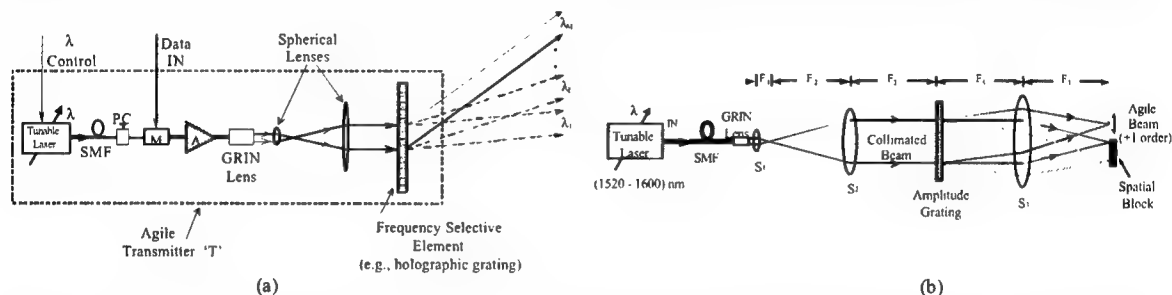


Fig. 2. (a) Schematic of an agile transmitter using W-MOS, (b) Free-space wavelength multiplexed agile transmitter laboratory setup. PC: Polarization controller; M: Optical modulator; A: Optical amplifier; F_i : Focal length of i^{th} spherical lens.

Inside the transmitter, when the beam is intensity modulated by a random information signal, the deflection becomes a stochastic function of frequency. Therefore, an intensity modulated deflected beam exiting the transmitter will display a beam spread in space. Such a spread can be estimated by the relative bandwidth $B_r = \Delta f / f$, where f is the center frequency and Δf is the bandwidth of the signal. In practical optical systems, B_r is usually a small number, which promises small beam spreads. For instance, when modulated by a 2.5 GHz signal, a W-MOS based transmitter using 600 lines/mm grating produces a beam spread varying between 0.028 mrad and 0.046 mrad, when the tunable source centered at 1560 nm is tuned over an 80 nm bandwidth. The grating equation also implies that if the deflection is large, the spread can be significant even if the relative bandwidth is small. Reducing the period L of the grating reduces the beam spread, but it also decreases the angular scan range. Thus for a given bandwidth of a tunable source, there is a trade off between the angular scan range of the transmitter and the spread of its beam.

4. Conclusion

In conclusion we have proposed a unique smart programmable free-space optical interconnects and communication links architecture using agile WDM transmitters. The scanning transmitter features ultrafast nanosecond domain scan setting speeds, wide angular scan range, and large apertures for high-resolution scans. The experimental results attest to the simplicity and functionality of our proposed novel scanning high-speed transmitter for future free-space optical interconnects and communication links at both the micro and macro scales. Extensions of this architecture to fiber and integrated optics are also possible.

5. References

- [1] N. A. Riza, "Liquid crystal electro-optical switching approaches," Invited paper at Special Symposium on Fiber-optic Crossconnects, OSA Integrated Photonic Research (IPR 2000), Quebec city, Canada, 12-15 July 2000.
- [2] D. Chiaroni, N. L. Sauze, E. Dotaro, A. Jourdan, "Circuit and packing switching in high capacity optical networks," in IEEE LEOS Summer Topical Mtgs., pp. IV35-IV36, 2000.
- [3] N. A. Riza, "Switchboard in the sky: free-space optics platform for communications and processing," in IEEE LEOS Ann. Mtgs. Digest pp. 211-212, Nov., 1998.
- [4] N. A. Riza, "MOST: Multiplexed optical scanner technology," in IEEE LEOS Ann. Mtgs. Digest pp. 828-829, Nov., 2000.
- [5] F. Delorme, G. Alibert, C. Ougier, S. Slemphes, H. Nakajima, "Sampled-grating DBR lasers with 181 wavelengths over 44 nm and optimized power variation for WDM applications," in Optical Fiber Communication (OFC '98), pp. 379-381, (1998).

Integrated Bragg Grating Structures

M. Jalal Khan, Michael Lim, Charles Joyner, Tom Murphy, H.A. Haus, H.I. Smith.

jalal@mit.edu, mikel@mit.edu, chj@lucent.com, tem@ll.mit.edu, haus@mit.edu, hismith@mit.edu

Introduction

Bragg gratings are useful components with numerous applications, including use as optical add/drop filters. Integrated gratings offer the advantages of smaller size and large-scale manufacturability over commercially available Fiber Bragg gratings. Integrated Bragg grating structures were fabricated in an InGaAsP/InP material system. This paper describes their measurement and characterization

Measurements and Characterization.

Three different classes of devices, shown in Fig 1, were measured: (1) Straight Bragg Gratings, (2) $\lambda/4$ phase-shifted Bragg Grating Resonator Cavity and (3) Coupled Bragg Resonator Cavities.

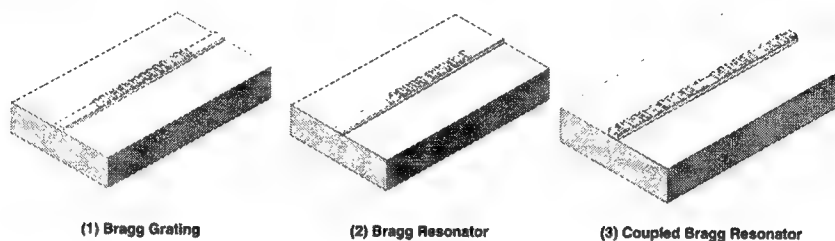


Fig 1. Classes of devices measured.

Measurement setup is shown in Fig. 2. A tunable laser source, connected to a polarization controller, was fed into a lensed fiber via a 10/90 power splitter. The splitter was used to account for any power drifts of the tunable laser source as the wavelength was scanned. The lensed fiber enabled better coupling to the smaller waveguide modes. At the output facet the light was collected using another lensed fiber and fed into a power meter. The polarization state was experimentally ascertained to remain stable over a period of many hours. Following alignment of the input and output lensed fibers numerous wavelengths scans were performed.

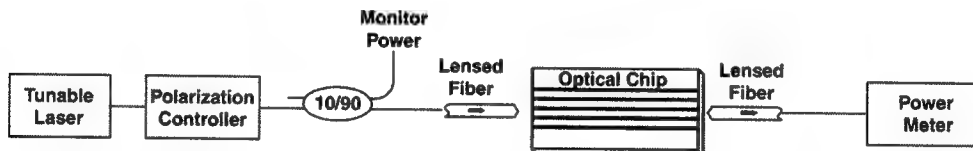


Fig 2. Measurement Setup.

Bragg Gratings

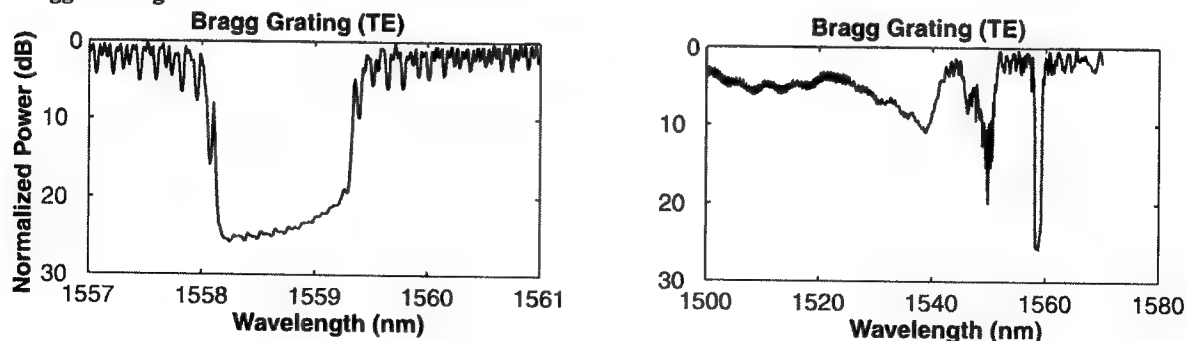


Fig 3. Bragg grating spectral response.

Fig. 3 shows two wavelength scans over a narrow and wide wavelength range performed on the same Bragg grating device using a TE polarized input. The scans reveal a clear stopband with a suppression in excess of 25 dB. The

suppression was noise-limited due to the chip layout and measurement setup. Radiation losses on the low wavelength side were observed. The decreased transmission near 1554 nm is thought to be due to phase-matched coupling by the grating between the first-order forward traveling guided mode to the second-order backward traveling guided mode. Since the waveguides were designed near cut-off we expect a second order mode to be excited at low wavelengths. The oscillations observed within the stopband and outside of it are due to Fabry-Perot modes caused by reflection from the uncoated chip facets.

Bragg Grating Resonator ($\lambda/4$ phase-shifted Grating)

Fig. 4 shows the transmission measurement on a $\lambda/4$ phase-shifted Bragg grating. As expected a resonant transmission state exactly in the center of the grating stopband is observed. The resonant transmission nearly returns to the 0 dB level, indicating an extremely low-loss resonator. The linewidth of the response was about 5 GHz which yields a measured Q in excess of 35,000. Radiation losses on the low wavelength side were also low as can be seen on the wide wavelength scan.

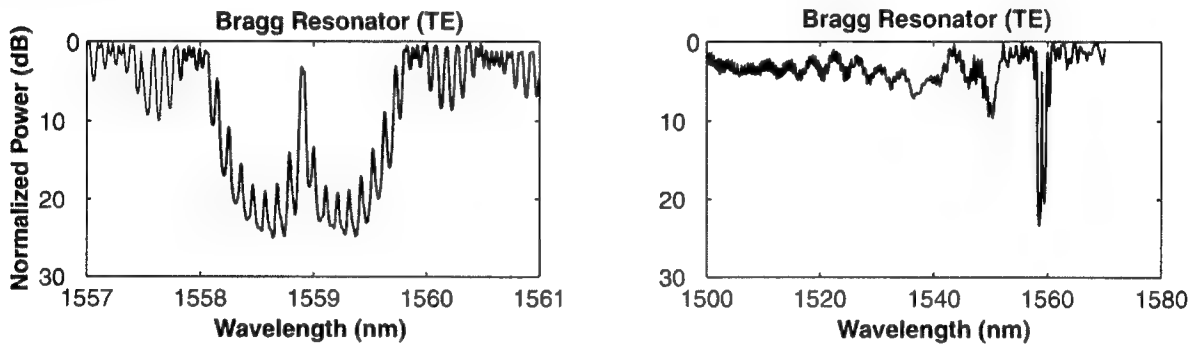


Fig 4. Bragg resonator spectral response.

Coupled Bragg Resonator Cavities.

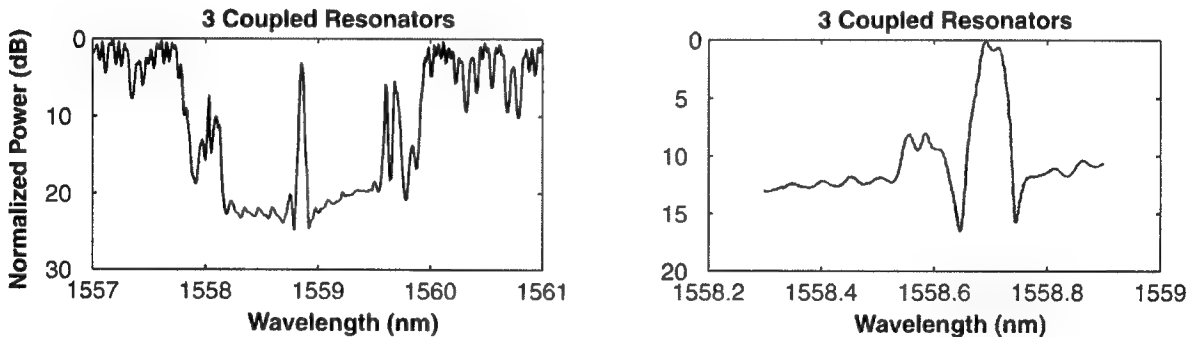


Fig 5. Three Coupled Bragg Resonators' spectral response.

Fig. 5. shows the response of 3 coupled Bragg resonators. The higher-order resonant transmission state is observed in the center of the stopband. The additional structure at the edges of the stopband and the flat-top response, with faster roll-off, is characteristic of the coupled resonators. Comparison with Coupled- Mode theory (not shown here) for all the devices showed excellent agreement.

Conclusions

Integrated Bragg grating structures with extremely low-loss and high Qs were successfully fabricated. The Bragg gratings showed a noise-limited transmission suppression within the stopband in excess of 25 dB. The measured Q of the Bragg resonators was over 35,000. Coupled Bragg resonators with flat-top responses and faster roll-offs with wavelength were demonstrated. These successfully demonstrated devices form the basic building blocks of integrated add/drop filters using Bragg gratings.

Recent Advances in PLC Functional Devices

Koichi Takiguchi

NTT Photonics Laboratories

Tokai, Naka, Ibaraki 319-1193, Japan

Phone: +81-29-287-7492, Fax: +81-29-287-7873, E-mail: taki@iba.iecl.ntt.co.jp

1. Introduction

To achieve much larger capacity in point-to-point wavelength division multiplexing (WDM) transmissions, we must increase their bit rate per wavelength as well as their channel number. Optical networks are continuing to adopt rings and packet-switched systems. These advanced optical systems require highly functional optical devices to exceed the electrical speed limit. I describe recent advances in planar lightwave circuit (PLC) [1] based functional devices, such as dispersion equalizers, large-scale arrayed-waveguide gratings (AWGs), and optical signal processing devices.

2. Dispersion Equalizers

The precise compensation of the dispersion slope of dispersion-shifted fiber (DSF) or non-zero DSF in high bit rate WDM systems is becoming increasingly important. PLC dispersion equalizer, which we have developed, has unique characteristics including compactness, dispersion variability, and the ability to provide flexible and accurate dispersion compensation [2]. Figure 1 shows the configuration of our PLC dispersion slope equalizer, which consists of an array of cascaded Mach-Zehnder interferometer equalizers with various compensation values and multiplexing AWG. We realized 8 x 40 Gb/s and 16 x 20 Gb/s equalizers, whose operational electrical bias power was greatly reduced to less than 1 W in total by employing local heating and quenching with high electrical power to thermo-optic heaters. Figure 2 shows a measured result of 8 x 40 Gb/s equalizer [3], [4].

Polarization mode dispersion (PMD) is also becoming a problem in long-haul high-speed transmission systems. We reported on the integrated-optic PMD compensator shown in Fig. 3. A deteriorated optical signal is input into an endless polarization controller and converted into TE and TM modes. The two modes are then introduced into a polarization dependent delay line for compensation and combined again [5]. Detailed operational results will be reported in the near future.

3. Large-Scale AWGs

Large-scale and high-density WDM filters are important in dense WDM systems. Figure 4 shows a 10 GHz-spaced 1010-channel WDM filter that covers both the C and L fiber bands, where ten 1x160 AWGs (AWG#k with k=1,2,...,10) with a 10 GHz spacing are connected to a primary 1x10 flat-top AWG with a 1 THz channel spacing. The phase errors of the 10 GHz AWGs were compensated for by the photoinduced refractive index change [6].

4. Optical Signal Processing Devices

Optical label recognition will be important for the coming packet-switched networks. Figure 5 shows a circuit for recognizing a 10 Gb/s and 4-bit optical pulse pattern. The pulse train is split into four replicas that are delayed and weighted by $m\Delta\tau$ and 2^{m-3} , respectively ($m=0-3$, $\Delta\tau$: pulse interval). One time slot of the multiplexed output pulses is extracted by gating. Thus the label is recognized by this digital-to-analogue (D/A) conversion in the optical region. Figure 6 shows a measured result [7].

5. Conclusion

I described recent progress on PLC functional devices. I expect these devices to play important roles in the coming advanced optical networks.

References

- [1] K. Okamoto, *IEEE Circuits & Devices Mag.*, **14**, 26, 1998.
- [2] K. Takiguchi et al., *J. Lightwave Technol.*, **16**, 1647, 1998.
- [3] K. Takiguchi et al., *ECOC2000*, Munich, **7.1.3**, 23.
- [4] K. Takiguchi et al., *submitted to Electron. Lett.*
- [5] T. Saida et al., *CPT'01*, Tokyo, Wb-4, 137.
- [6] K. Takada et al., *ECOC2000*, Munich, **PD3.8**.
- [7] T. Saida et al., *OFC'01*, Anaheim, **WY2**.

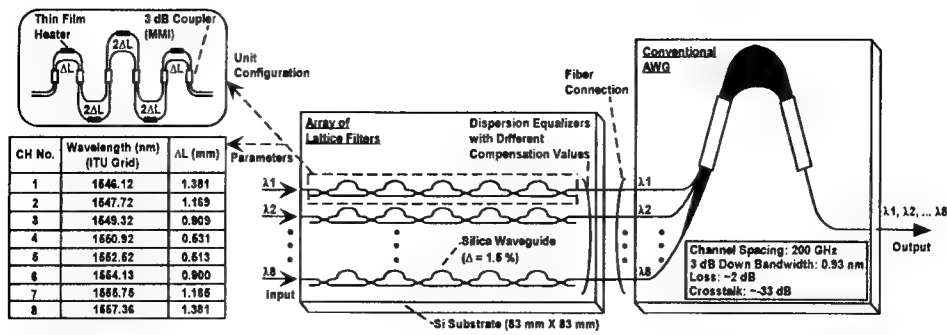


Fig. 1 Configuration of PLC Dispersion Slope Equalizer for 8 x 40 Gb/s WDM Transmission

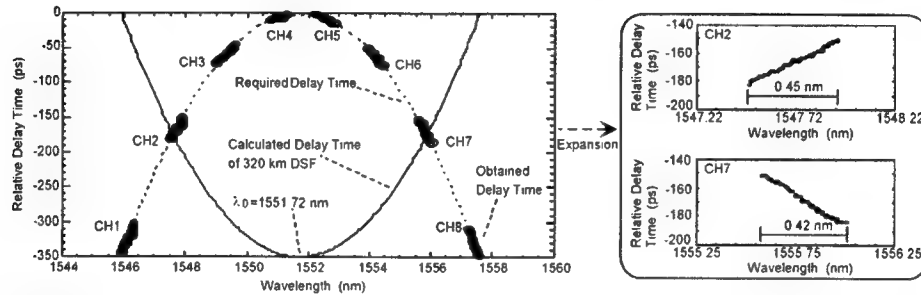


Fig. 2 Measured Relative Delay Time of 8 x 40 Gb/s WDM Dispersion Slope Equalizer

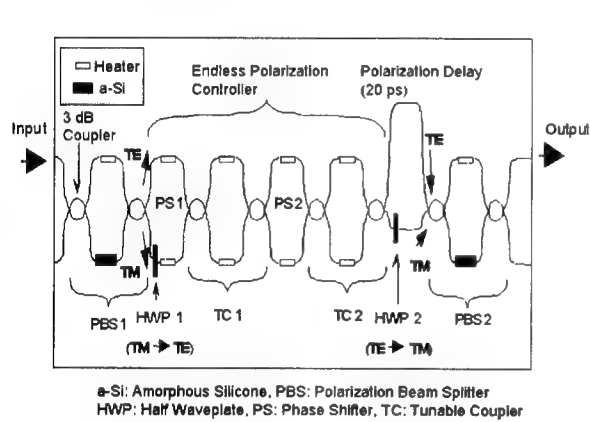


Fig. 3 Configuration of PLC PMD Compensator

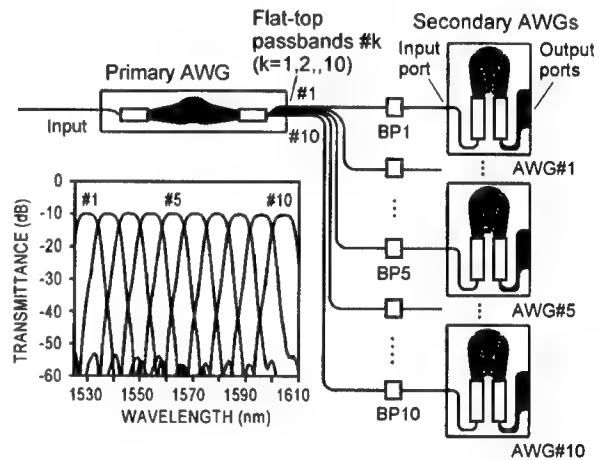


Fig. 4 Configuration of 10 GHz-Spaced 1010-Channel AWG Filter

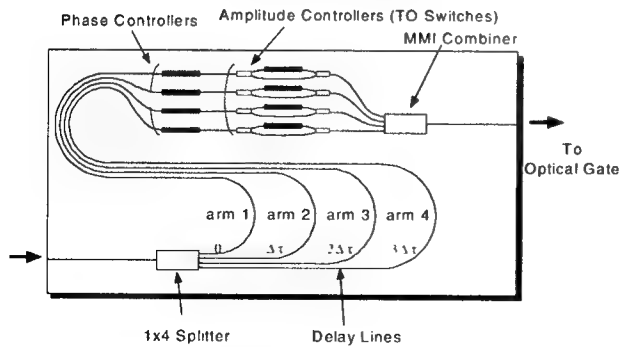


Fig. 5 Configuration of D/A Converter

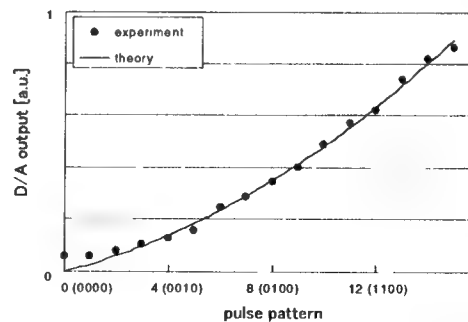


Fig. 6 Measured D/A Output vs. Input Pattern

Wavelength Splitters for DWDM Systems

T. Chiba, H. Arai, K. Ohira, H. Nonen, H. Okano and H. Uetsuka

*Optoelectronic System Laboratory, Hitachi Cable, Ltd.,
Hitaka-cho 5-1-1, Hitachi-shi, Ibaraki-ken 319-14, Japan
Tel: +81-294-25-3833, Fax: +81-294-43-7487
E-mail: chiba@lab.hitachi-cable.co.jp*

Abstract: We have demonstrated chromatic dispersion free DWDM wavelength splitters by novel configuration of monolithically integrated three identical circuits, which consist of Fourier transform-based MZIs.

1. Introduction

A density of channels in WDM systems has been higher and higher to accommodate the exploded traffic demand. Recently, a 1010 channel AWG of which the channel spacing is 10GHz has been reported[1]. On the other hand, there is a flexible system configuration to upconvert or downconvert the WDM signal by using a interleave filter, which is also called wavelength splitter / slicer / interleaver, as shown in Fig. 1. In the illustration, the 1st stage is for a band separation, the 2nd stage for up/down conversion, and, at the 3rd stage, each WDM signal is separated by AWGs. In order to make this system operate effectively, a wavelength splitter at the 2nd stage is required to have the Box-like characteristics such as the periodic response, flat-passband, low insertion loss and low crosstalk. In addition, low chromatic dispersion (CD) is indispensable for DWDM systems.

In this paper, we present wavelength splitters with a tandem configuration of Fourier transform-based MZIs. The circuit using PLC technique is fabricated with high index contrast waveguides of $\Delta 1.5\%$.

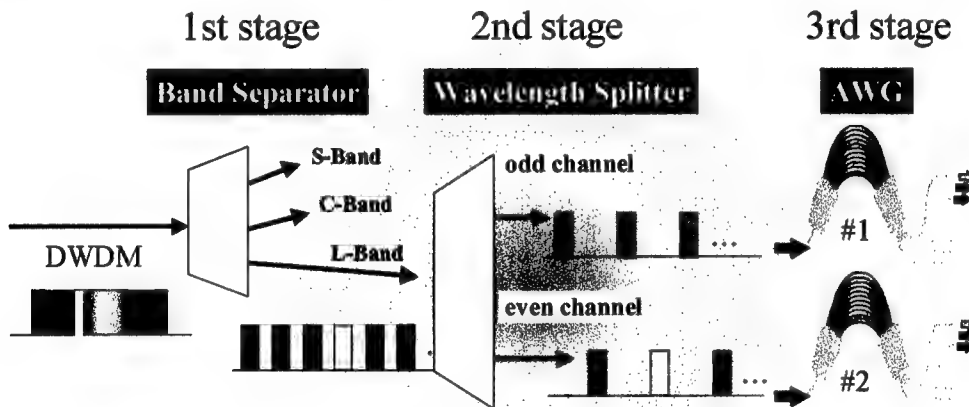


Fig.1. DWDM filter system

2. PLC configuration

Figure 2 shows our PLC-type wavelength splitter circuit configuration. The filter consists of three identical 3-stage Fourier filter circuits. Taking the phase conjugate relationship into consideration, the port #9 of Circuit 2 is connected to the port #8 of Circuit 1, and the port of #10 of Circuit 2 is connected to the port #11 of Circuit 3. In this configuration, the port combinations of #3 \leftrightarrow #2 and #3 \leftrightarrow #6 allow CD-free optical performance over the entire wavelength range of interest[2,3]. The phase conjugate relationship is maintained in the case of the port combinations of #4 \leftrightarrow #1 and #4 \leftrightarrow #5.

The configuration is useful to not only CD compensation but also smart integration of two independent circuits. In general, if two same circuits are integrated on a substrate, each circuit is arranged side by side. In the case of the wavelength splitter, each circuit can share part of its components, such as delay lines and couplers between two circuits, which are separated only by port selections. So the unique characteristic can apply very well to simultaneous MUX/DEMUX operation[4].

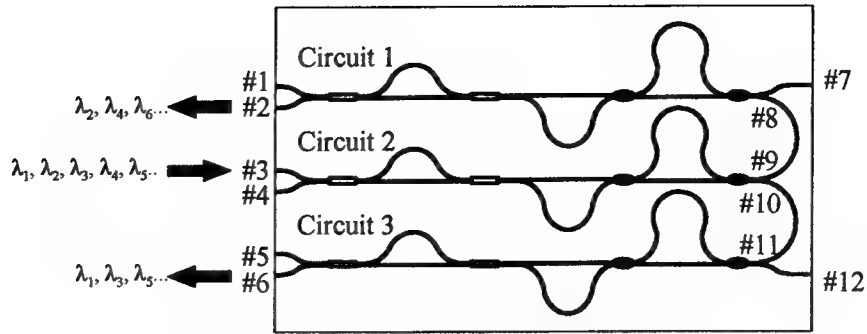


Fig. 2. Wavelength splitter with configuration of dispersion compensation

3. Fabrication and Measured Results

We fabricated a 50GHz-to-100GHz wavelength splitter based on the above design by using a high index contrast silica-on-silica PLC process. The Δ is 1.5% and the minimum curve radius is 2 mm. Consequently, the chip size was able to be shrunk $37 \times 25 \text{ mm}^2$, which is about 30% that with $\Delta 0.8\%$. We used a thermally expanded core (TEC) technique [5] to reduce the mode field miss match loss between a standard single mode fiber (SMF) and the $\Delta 1.5\%$ waveguide.

Figure 3 shows the measured spectral response of the wavelength splitter shown in Fig.2. The fabricated chip demonstrates a periodic box-like response with low crosstalk and a wide, flat pass-band. The insertion loss is less than 2 dB. Figure 4 shows the measured CD distribution on the pass band of the 3-stage tandem-type circuit for the path between #3 and #2 and for the path between #3 and #6. The CD is almost compensated.

4. Conclusion

We have demonstrated a chromatic dispersion free Fourier transform-based wavelength splitter. The device meets performance requirement necessary for actual DWDM systems. This wavelength splitter is not only applicable to MUX/DEMUX, but also valid for such applications as optical add-drop filter and bi-directional system[4,6].

5. References

- [1] K. Takada, *et al.*, "10GHz-spaced 1010-channel AWG filters achieved by tandem connection of primary and secondary AWGs", ECOC2000, PD1.1 (2000)
- [2] T. Chiba, *et al.*, "Chromatic dispersion free Fourier transform-based wavelength splitters for D-WDM", OECC 2000 Technical Digest, pp. 374-375 (2000)
- [3] H. Arai, *et al.*, "Interleave filter with box-like spectral response and low chromatic dispersion", NFOEC2000 Technical Proceedings, vol.2, pp.444-451 (2000)
- [4] T. Chiba, *et al.*, "Novel architecture of wavelength interleaving filter with Fourier transform-based MZIs", OFC 2001 Technical Digest Series, WB5 (2001)
- [5] K. Shiraishi, *et al.*, "Beam expanding fiber using thermal diffusion of the dopant", J. Lightwave Technol., vol. 8, no. 8, pp. 1151-1161 (1990)
- [6] S. Radic, *et al.*, "25GHz interleaved bidirectional transmission over non-zero dispersion shifted fiber", OFC2001 Technical Digest Series, ThF7 (2001)

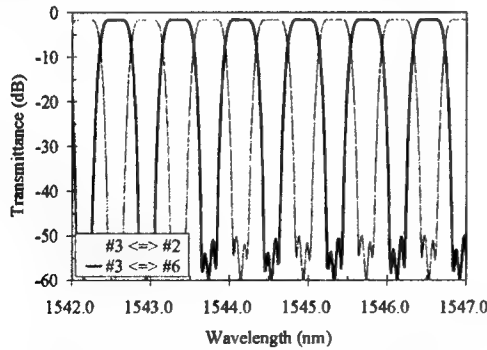


Fig. 3. Measured spectral response of fabricated 3-stage tandem type (the paths #3 to #2 and #3 to #6)

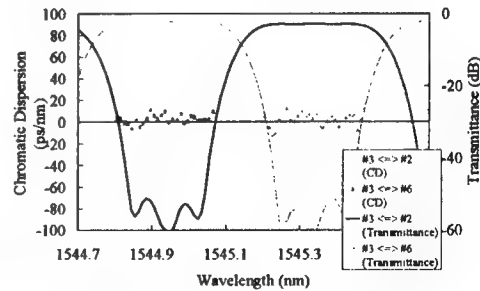


Fig. 4. Measured CD distribution and spectra (the paths #3 to #2 and #3 to #6)

Micron-size bending radii in silica-based waveguides

Kazumi Wada, Miloš Popović, Shoji Akiyama, Hermann A. Haus and Jürgen Michel

Massachusetts Institute of Technology, Cambridge, MA 02143

kwada@mit.edu, milos@mit.edu, akiyama@mit.edu, haus@mit.edu, jurgen@jurgen.mit.edu

"Silica bench" technology is well-developed and widely used in waveguide interferometric filters for channel multiplexing and de-multiplexing [1-4], and other WDM applications [4,5]. Waveguide cross-sections are relatively large so as to permit coupling to and from optical fibers with low insertion loss. There is also a relatively small loss penalty attributable to surface roughness. However, the density of integration of optical components, for example arrayed waveguide gratings (AWGs), is limited in this technology by the relatively large bending radii required to keep the radiation losses within acceptable bounds [3,4]. In addition, large components invite yield problems, so miniaturization is important.

A technology that allows small bending radii and large-angle waveguide T's would enable denser integration and smaller structures. We present here theoretical results and are currently preparing experimental evidence on a method that can increase the density of integration by orders of magnitude. A reduction in bending radius by a factor of 30-500, and of the complete bend structure dimension by 10-100 times, is predicted.

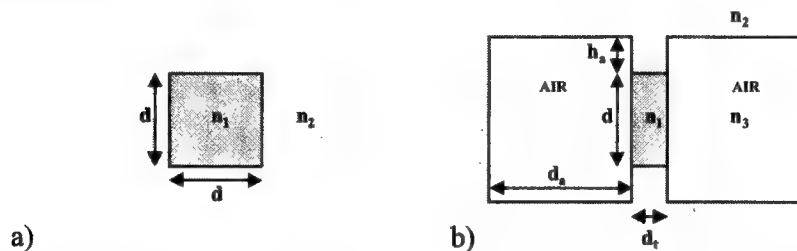


Fig. 1. Normal (a) and trench-flanked (b) waveguide cross-sections. Dimensions are d (width of low-index waveguide, and height of both), d_1 (trench waveguide width), d_2 (air trench region width), and h_1 (extent of air trench above and below the waveguide).

The method judiciously incorporates air trenches into the structure in locations where there would otherwise be unacceptably high radiation loss (such as at sharp bends). Because of this high (local) index difference, evanescent tails extending into the cladding at the bend are greatly suppressed, and the coupling of light into radiation modes is greatly reduced. On the other hand, the use of air trenches is kept to a minimum in order to preserve the advantages of low index contrast wherever possible.

The proposed air trench solution is demonstrated in designs of a waveguide bend and T-splitter. Simulations were done using the Finite Difference Time Domain (FDTD) method, primarily in two dimensions. They show that

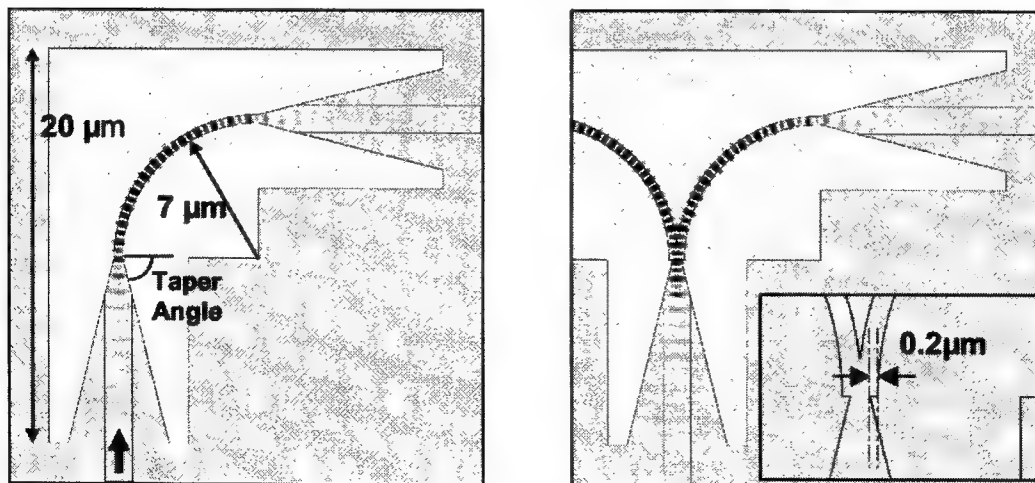


Fig. 2. Waveguide bend (left) and derived waveguide T-splitter (right). The electric field of a 50fs Gaussian pulse travelling through the bend clearly shows little radiation present in the turn. The inset on the right shows a waveguide step displacement ($0.2 \mu\text{m}$) at the input of the T-splitter.

a waveguide bend designed to have a throughput efficiency of 98% can be reduced in size by a factor of 10-100 with the use of air trenches, with the bending radius itself reduced 30-500 times.

One set of designs is shown for illustration, where we have worked with an index contrast of 2.0:1.9 (core index:cladding index). Figure 1 shows cross-sections of a normal waveguide in the low index contrast circuit (a), and a waveguide with incorporated lateral air trenches – as found in the bend region (b). The bend "component", as shown in Figure 2, includes two air trench-flanked tapers (for mode transformation) and a high index bend region. With a bend radius of $7\mu\text{m}$ and the complete structure having an edge length of $20\mu\text{m}$, we obtain 99% throughput efficiency with $<-33\text{dB}$ reflection. For comparison, a regular waveguide bend with similar (98%) throughput efficiency would require a bend radius of $230\mu\text{m}$. A T-splitter is also shown (Figure 2, right) and achieves a slightly worse throughput of 98% with $<-30\text{dB}$ reflection. Note that a step displacement of the output waveguides is required at the input (Fig. 2, right inset) to most efficiently accommodate the incoming mode.

The input and output tapers have the function to compress and uncompress the waveguide mode between the low-index contrast waveguide and the high-index contrast bend (both of which are single mode) with minimal loss. In the above simulations, a taper angle of 76° was chosen in order to minimize device size (steep taper angle) while retaining enough length in the taper to preserve quasi-single mode behaviour (shallow taper angle). For illustration, a smaller bend radius ($2\mu\text{m}$) with a steeper taper (55°) is shown in Figure 3, along with a comparison to the transmission spectrum of the bend in Figure 2. Multimode behaviour can be seen in the field plot of this bend in Fig. 3, leading to degraded performance.

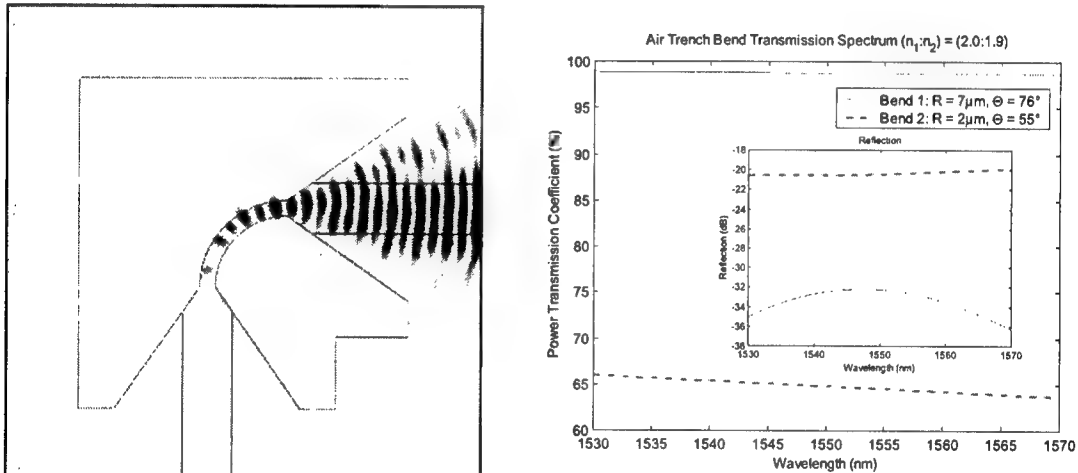


Fig. 3. Waveguide bend (left) with steep taper angle (55°) and small bend radius ($2\mu\text{m}$). Poor taper performance between the high and low index sections shows multimode behaviour at the output and hence degraded throughput efficiency. Similarly to Fig. 2, a 50fs Gaussian pulse is seen in the field plot. Transmission and reflection spectra (right) are shown for this bend and the bend in Fig. 2.

Simulations of structures similar to those in Fig. 2 in lower index contrasts (1.49:1.48) have resulted in even larger reductions of bending radius – from $6300\mu\text{m}$ for a regular bend down to $8\mu\text{m}$ with the use of an air trench. In this case the complete bend structure including tapers would have an edge length of $\sim 130\mu\text{m}$, a reduction by a factor of 50. The response for both structures above is virtually flat over the Erbium bandwidth of 1530-1570nm. By the time of the topical meeting we expect to have fabricated and tested some generic structures.

- [1] C. Dragone, "An $N \times N$ optical multiplexer using a planar arrangement of two star couplers," IEEE Photon. Technol. Lett. **3**, 812-815 (1991).
- [2] T.A. Strasser, T. Erdogan, A.E. White, V. Mizrahi and P.J. Lemaire, "Ultraviolet laser fabrication of strong, nearly polarization-independent Bragg reflectors in germanium-doped silica waveguides on silica substrates," Appl. Phys. Lett. **65**, 3308-3310 (1994).
- [3] Y.P. Li, C.H. Henry, "Silica-based optical integrated circuits," IEE Proc.-Optoelectron. **143**, no. 5, 263-280 (1996).
- [4] T. Miya, "Silica-based planar lightwave circuits: passive and thermally active devices," IEEE J. of Sel. Topics in Quan. Elec. **6**, no. 1, 38-45 (2000).
- [5] K. Takiguchi, K. Okamoto, and K. Moriwaki, "Dispersion compensation using a planar lightwave circuit optical equalizer," IEEE Photon. Technol. Lett. **6**, 561-564 (1994).

Dynamically tunable dispersion slope compensation using a virtually imaged phased array (VIPA)

S. Cao, C. Lin, G. Barbarossa, C. Yang
Avanex Corporation
Invited Paper

Abstract: A virtually imaged phased array (VIPA) can perform dynamically tunable dispersion slope compensation. The tuning mechanism is the rotation of the diffraction grating that is used to provide wavelength separation for fixed dispersion slope compensation. The range of tunability is limited by the increase in loss due to the sub-optimal incident angle on the diffraction grating upon rotation.

1. Introduction

A virtually imaged phased array (VIPA) is an optical structure that produces remarkably large angular dispersion [1]. A VIPA is produced by light focused into a tilted etalon with a 100% reflectivity coating on one side and a slightly transmissive coating on the other side. The reflections between the two mirrors construct the virtual array of phased images that make up the VIPA. Light is coupled into the etalon through an anti-reflection coated window on the 100% reflectivity side (see figure 1).

The large angular dispersion of the VIPA can be harnessed to perform dispersion compensation [2]. By using a specially designed mirror and a mirror translation mechanism, the dispersion can be tuned in real-time [3-4]. Furthermore, by including a diffraction grating between the etalon and the focusing lens, the VIPA can provide dynamically tunable dispersion compensation as well as fixed dispersion slope compensation (see figure 2) [5]. Finally, tunable dispersion and dispersion slope compensation can be simultaneously and independently tuned dynamically by rotating the diffraction grating to change its angular dispersion.

2. Tunable dispersion and fixed dispersion slope

Tunable dispersion and dispersion slope VIPA compensators both use a 3-dimensional mirror. The shape $c(y)$ of the 3-d mirror is shown in equation (1) where f is the focal length of the focusing lens, a is the distance along the focusing lens axis to the VIPA, and Θ is the tilt of the etalon [5].

$$c(y) = \frac{K}{8f^4}y^4 + \frac{K\Theta}{2f^3}y^3 + \frac{K\Theta^2 - (f-a)}{2f^3}y^2 \quad (1)$$

This mirror shape yields a constant dispersion value D across any given channel of the value shown in equation (2) where n is the index of the etalon material, c is the speed of light in vacuum, and λ is the wavelength [5].

$$D = \frac{-2n^4K}{c\lambda} \quad (2)$$

The shape of the mirror can be continuously changed along its x axis so that K is a function of x . By translating the mirror along its x axis, light from the rest of the device is incident on a different part of the mirror so the corrective chromatic dispersion changes. Similarly, by placing a diffraction grating between the etalon and focusing lens with the rules parallel to the mirror's y axis, different channels will be incident on the 3-d mirror at different values of x and therefore undergo different chromatic dispersion. If K is a linear function of x , then the device produces dispersion slope compensation.

The dispersion slope D_s is the product of the angular dispersion of the diffraction grating $d\beta/d\lambda$, the focal length of the focusing lens f , and the rate of change of dispersion along the x axis of the 3-d mirror dD/dx , see equation (3).

$$D_s = f \frac{d\beta}{d\lambda} \frac{dD}{dx} \quad (3)$$

3. Tunable dispersion slope

There are two strategies to tune the dispersion slope. The first is to operate directly through the 3-d mirror by using a MEMS actuated adaptive membrane mirror such as those used to correct wavefront

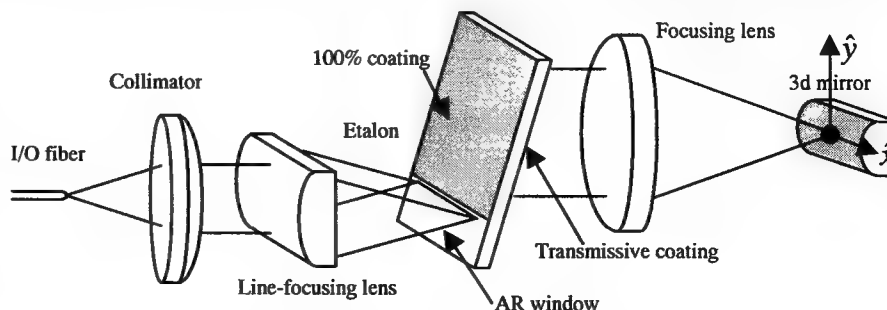


Figure 1: Schematic of a VIPA chromatic dispersion compensator.

aberrations in imaging systems. This has the advantage of essentially limitless flexibility but suffers from complicated control and practical fabrication difficulties. As the number of channels increase, the number of necessary actuators increases as well.

The second approach is to change the angular dispersion produced by the diffraction grating. One way to do this is to construct a chirped grating and tune by sliding the grating so that the average pitch varies. Unfortunately, two effects conspire to limit the feasibility of this technique. The first effect is that the diffraction loss will increase because the average pitch changes and the grating is no longer optimized for the incident angle. The second is that the chirped grating introduces wavefront distortion. This distortion will introduce even more loss. The second effect can be mitigated by limiting the severity of the grating's chirp, but this constrains the tuning range since the grating cannot be arbitrarily long.

A better way to change the angular dispersion of the diffraction grating is to simply change in the incident angle by rotating the diffraction grating. Although the insertion loss will increase because the diffraction grating is no longer in its optimal orientation, there will be no additional loss from chirp. Compared to the deformable mirror, this method is much simpler since it requires only one actuator and also has the advantage of not needing continuous power to hold position. One side effect to bear in mind is that the dispersion bias (defined as the dispersion at the center channel) will change as the diffraction grating is rotated and the dispersion slope is tuned. Fortunately, this shift can be offset by translating the 3-d mirror in tandem with the rotation of the diffraction grating. The shift in dispersion bias ΔD is shown in equation (4) where α is the incident angle and the relation between α and β is $\sin\alpha = \sin\beta + \lambda/\Lambda$ which is just the first order diffraction condition.

$$\Delta D = f \frac{d\beta}{d\alpha} \frac{dD}{dx} \Delta\alpha \quad \text{where} \quad \frac{d\beta}{d\alpha} = \frac{\cos\alpha}{\cos\beta} \quad (4)$$

The derivative of dispersion slope over incident angle $dD_s/d\alpha$ is shown equation (5) where Λ is the grating pitch.

$$\frac{dD_s}{d\alpha} = f \frac{dD}{dx} \frac{d\left(\frac{d\beta}{d\alpha}\right)}{d\alpha} \quad \text{where} \quad \frac{d\left(\frac{d\beta}{d\alpha}\right)}{d\alpha} = \frac{\sin\beta \cos\alpha}{\Lambda \cos^3\beta} \quad (5)$$

4. Insertion loss variation

As the diffraction grating is rotated, the diffraction loss changes. If this change is too large, then the practical usefulness of tunable slope is negated. Table 1 shows the characteristics for a tunable slope compensator using two different diffraction gratings designed for least loss at 1545 nm. The first grating is a surface relief transmission grating with 750 lines/mm. The second grating is a volume transmission grating with 945 lines/mm. For these measurements and calculations, $f = 5$ cm and $dD/dx = 500$ ps/nm/mm.

Table 1: Characteristics for tunable slope compensator

Grating	Optimal α	Diffraction loss	1 dB penalty range for α	ΔD_s over 1dB penalty range*
750 lines/mm	35°	1.02 dB	26° - 47°	6.3 ps/nm ²
945 lines/mm	46°	1.15 dB	36° - 58°	18.3 ps/nm ²

*This value is calculated.

5. Conclusions

Simultaneously tunable dispersion and dispersion slope compensation can be achieved by rotating the diffraction grating and translating the 3-d mirror in a VIPA dispersion and dispersion slope compensator. The slope tuning capability is three times greater for the 945 lines/mm grating than the 750 lines/mm grating. The insertion loss penalty for approximately 20° of rotation is only 1 dB for both gratings. Although the dispersion bias changes as the slope is tuned, the 3-d mirror translation can be linked to the diffraction grating rotation to compensate for this offset.

6. References

- [1] M. Shirasaki. *Optics Letters*, vol. 21, no. 5, pp 366-368, 1996.
- [2] M. Shirasaki, H. Isono, S. Cao. *Proceedings APCC/OECC 99*, pp 1367-1370, 1999.
- [3] L. D. Garrett, *et al.* OFC2000, PD7.
- [4] M. Shirasaki, *et al.* ECOC2000, Post deadline paper 2.3.
- [5] M. Shirasaki, S. Cao. OFC2001, TuS1.

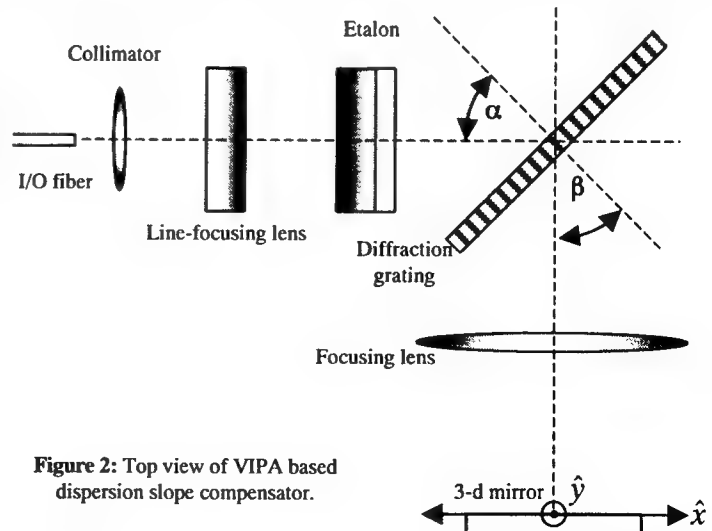


Figure 2: Top view of VIPA based dispersion slope compensator.

PMD Mitigation Using Diversity Detection

A. O. Lima (1), I. T. Lima, Jr. (1), T. Adali (1,2),
and C. R. Menyuk (1,2)

(1) Department of Computer Science and Electrical Engineering, University of
Maryland Baltimore County, 1000 Hilltop Circle, TRC205A, Baltimore, MD 21250
email: alimal@engr.umbc.edu, URL: <http://www.photonics.umbc.edu/>

(2) Laboratory for Telecommunications Sciences, c/o USARL
Bldg. 601 Rm. 131, 2800 Powder Mill Road, Adelphi, MD 20783

Introduction

In high speed optical communication systems at data rates of 10 Gbit/s and beyond, signal distortion caused by polarization mode dispersion (PMD) is a significant barrier of the transmission bit rate-distance. A considerable effort has been devoted in recent years to mitigate the effects of PMD, based on optical, electrical and opto-electrical PMD compensators (see e.g. [1]–[5]).

rate [3]. Since all high-data-rate systems use direct detection, the polarization phase information is lost during detection and diversity can provide additional advantages for PMD mitigation by more efficient use of the available information.

In this paper, we present a new diversity receiver that provides significant performance improvement compared to direct detection. By incorporating active electronics into its structure, we show further performance improvements can be achieved and the intersymbol interference (ISI) due to PMD can be further reduced.

Theory and Results

The block diagram of Fig. 1.a shows the diversity receiver that we introduce. The signal is split into three pairs of orthogonal polarization that are detected by independent photodetectors. The pairs of orthogonal polarizations improve the robustness to noise as compared to the polarization analyzing equalizer (PAE) of [5] where only one polarization was obtained in each of the three branches. The reason for the improvement in robustness is due to the fact that, with the structure in [5] part of the signal power in each branch is lost and the PAE minimizes the contribution of one of the two principal states of polarization in its operation. This results in a detected signal more sensitive to noise effects. On the other hand, our proposed configuration maintains the two orthogonal components of each branch for final detection. The proposed diversity receiver also avoids loss of information, as we obtain more complete information. The increased complexity of the receiver pays off by significant gains even without the use of an equalizer. Also, note that for the implementation with an equalizer (as shown in Fig. 1.a. and Fig. 1.b) since structure allows for parallel processing, electronic processing at high data rates such as 10 Gbit/s is still feasible.

In the first branch of the proposed diversity receiver, a linear polarization beam splitter (LPBS) is used to split the signal between vertical and horizontal polarizations. In the second branch, a quarter-wave plate ($\lambda/4$) converts the signal from circular to linear polarization before the PBS, that is rotated by 45 degrees with respect to the first PBS, to split the signal into right- and left-circular polarizations. In the third branch, the PBS splits the signal into two diagonal (45 and -45 degrees) polarizations. Discrete samples are obtained by a clock recovery (CRC) subsystem that are synchronized by an electrical delay placed before the combiner/equalizer structure. In the combiner/equalizer structure, we analyze and implement several different approaches with a combiner with and without equalization. The decision module selects the branch that has the maximum amplitude margin.

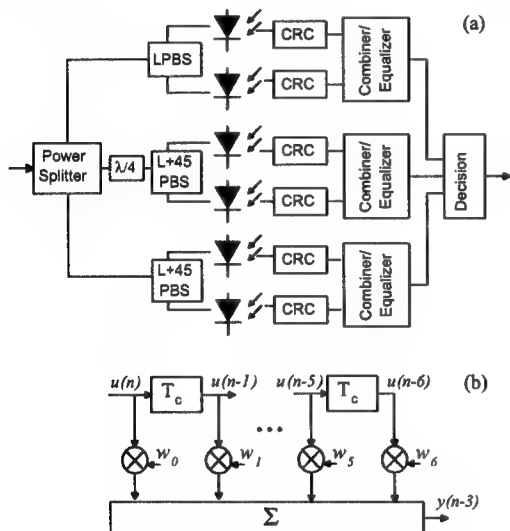


Figure 1: Electrical equalizer. (a) Diversity receiver. (b) Transversal filter.

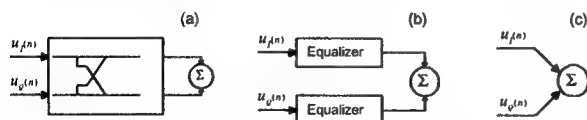


Figure 2: Combiner/equalizer structures. (a) Complex equalizer. (b) Two independent equalizers. (c) Simple combiner.

Among these PMD compensation techniques, electronic equalizers are particularly attractive in terms of compactness and versatility. In particular, successful implementation of equalization using transversal or decision feedback structures has been demonstrated at 10 Gbit/s in integrated electronics using SiGe technology [2] and recently for adaptive PMD mitigation at this

We test three different equalizer and/or combiner structures for the diversity receiver introduced. These are shown in Fig. 2. The complex equalizer can use the information within each branch most efficiently by jointly processing each signal pair. The second structure is simpler and focuses on correcting for ISI on each branch separately. The third structure is a simple combiner, utilizes only the polarization diversity to reduce the ISI.

In order to study the probability that the system penalty exceeds a certain margin, typically 2 or 3 dB, we use importance sampling applied to PMD as in [6] and [7]. This technique allows one to study outage probability due to PMD at realistic values of 10^{-6} with a relatively small number of Monte Carlo simulations. The PMD source is modeled using 80 sections of birefringent elements with the coarse step method [8], which reproduces first and higher order PMD distortions.

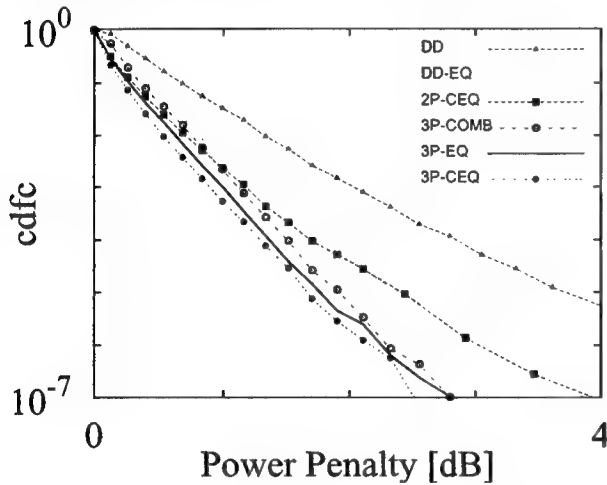


Figure 3: The cdf of the power penalty for PMD equalizers in a NRZ system with $\langle \Delta\tau \rangle = 25$ ps. The curves show results with (i) DD: direct detection without equalization; DD-EQ: direct detection with single channel equalization; (ii) 2P-CEQ: two pairs of orthogonal polarizations with complex equalizer; (iii) 3P-COMB: three pairs of orthogonal polarizations without equalization; (iv) 3P-EQ: three pairs of orthogonal polarizations with standard equalizer; (v) 3P-CEQ: three pairs of orthogonal polarizations with complex equalizer.

In this paper, we test a structure that uses independent equalizers (see Fig. 1.b) on each branch, as well as a structure that uses a complex equalizer where the main difference is in the definition of the signal and filter weights as *real* or *complex* quantities. The complex structure uses the pair of orthogonal polarizations as shown in Fig. 1.a and thus allows the design of filter coefficients (weights) by taking into account the information from both polarization signals. The equalizers used in this paper are realized as transversal filters with 7 taps with 1 bit period of tap delay using symmetric equalization, i.e., each bit is equalized using the previous three and the future three bits. In order to evaluate the optimal performance of such a scheme, we calculate the coefficients of the filter using the Wiener solution [9] given by the inverse of the input autocorrelation matrix times the cross-correlation vector of the input and the desired sequence. The filter weights are normalized in order to main-

tain the relative scaling of the signal and noise. The least mean squares (LMS) algorithm can be used to adaptively compute (or approximate) the Wiener solution as implemented in [3] for PMD mitigation.

Fig. 3 shows the complement of the cumulative distribution function (cdf) of the power penalty caused by PMD using direct and diversity detection with fixed optics. The cdf gives the probability of having a power penalty greater than a given amount. For the combiner/equalizer structure realized with complex equalizers, the configuration with two pairs of orthogonal polarizations does not provide a significant improvement in decreasing the outage probability, when compared to the equalized case with direct detection. In this case, when the fixed polarizations are not close to the principal states of polarization, there is a frequency dependence of the polarization state, causing a spread on the Poincaré sphere over the signal bandwidth. When split into orthogonal polarizations by the polarization beam splitter (PBS), the signal experiences distortion. In addition, the photodetectors extract a mixed contribution of the two principal states of polarization. For the three pairs of orthogonal polarizations, however, we can effectively cover the Poincaré sphere, and this distortion should pose less of a problem as we clearly observe in our results.

As seen in Fig. 3, significant performance gain is achieved by using the configuration with three pairs of polarizations. It provides a reduction of 2 dB on the penalty that defines an outage probability of 10^{-5} , as compared to the non-equalized case with direct detection. We also notice that the use of diversity detection without equalization provides a reduction of 1.9 dB on the penalty that defines an outage probability of 10^{-5} , as compared with direct detection without electronic equalization, and a reduction of 0.6 dB, as compared with direct detection with equalization. Hence, diversity detection can substantially reduce the penalty due to PMD. Electrical equalizers are not as efficient in diversity detection systems, as compared to direct detection, because the residual distortions caused by PMD in diversity detection do not induce as much ISI as in direct detection.

Conclusion

We introduced a new diversity receiver structure and applied importance sampling to quantify the power penalty due to PMD by numerical simulations for systems using direct and diversity detection. Our results indicate the effectiveness of diversity detection, as compared to direct detection. Hence, a diversity receiver with three fixed pairs of orthogonal polarization symmetrically distributed on the Poincaré sphere can show the true advantage of using diversity for decreasing outage probability and provide considerable improvement compared to a system based on traditional detection.

REFERENCES

- [1] R. Noé, *et al.*, *J. Lightwave Technol.* **17**, 1612–1615 (1999).
- [2] H. Bülow, *et al.*, *Technical Digest ECOC'99*, **11**, 138–139 (1999).
- [3] B. Wedding, *et al.*, *Technical Digest OFC'2001*, TuP4, 1–3 (2001).
- [4] B. W. Hakki, *et al.*, *Photon. Technol. Lett.* **9**, 121–123 (1997).
- [5] H. Bülow, *Technical Digest NOC'97*, 65–72 (1997).
- [6] G. Biondini, *et al.*, *Technical Digest OFC'2001*, ThA5, 1–3 (2001).
- [7] I. T. Lima, *et al.*, *Technical Digest OFC'2001*, Mo4, 1–3 (2001).
- [8] D. Marcuse, *et al.*, *J. Lightwave Technol.* **15**, 1735–1746 (1997).
- [9] S. Haykin, *Adaptive Filter Theory*, 3rd Ed., Prentice Hall, (1996).

Concept for individual channel polarization control in a WDM signal using an integrated device

Lothar Möller

Bell Labs, Lucent Technologies, 791Keyport-Holmdel Road, Holmdel 07733, NJ, USA, lmoeller@lucent.com

Abstract: A device that can be used for channel individual polarization controlling in WDM systems is proposed. The design concept is suitable for implementation in thermo optic material like silicon.

Introduction

In several situations in a lab or in transmission system the polarization of a signal has to be adjusted. For example if polarization sensitive components are used in a set up like high speed data modulators, polarization mode dispersion compensators, or wavelength converters, the polarization state of the signal has to be adapted to the devices. For this purpose, two features of a polarization controller were considered necessary. First the controller must be able to convert an arbitrary, time variant state of polarization into TE or TM polarization. This guarantees that the electrical field vector of the local oscillator in a coherent receiver can be optimally adjusted to the polarization of the incoming signal. A second point is that the polarization controller tracking range should be endless because the polarization state of a received signal can drift over large angle intervals, and a reset of the controller would lead to data traffic interruption.

However, there is no question that a single device, which could perform the same features individually for each WDM channel, could find applications in lab or transmission system. A "straight forward solution", consisting of an optical DeMux followed by single channel polarization controllers and an optical Mux, can have advantages in terms of insertion loss. On the other hand such a design requires for a compact realization electro-optic material like LiNbO₃, in which polarization controller can be formed. Instead of building the device as a hybrid combination, an integrated design, suitable for realization on low cost material in planar lightwave circuit (PLC) technology, is preferred due to overall cost efficiency and space reduction. Here we propose such an integrated WDM polarization controller and show how it can be formed from existing device designs, which are based on Arrayed Waveguide Grating (AWG) filters.

Design Proposal

The basic idea of the proposed concept is to emulate the polarization control function of an existing single channel polarization controller in a device, which can be built in planar waveguide technology. Once this device concept is found, an expansion from single channel operation to WDM channel operation can be made, by designing the control degrees of freedom to be wavelength selectively addressable.

As a single channel polarization controller design, we choose the proposal from Noe [1], which comprises a series of three fiber squeezers for polarization tuning. The three fiber squeezers, which are implemented in the controller, are represented in Jones calculus by the two matrices **A** and **B**

$$A(\alpha) = \begin{bmatrix} \cos \alpha & j \cdot \sin \alpha \\ j \cdot \sin \alpha & \cos \alpha \end{bmatrix}; \quad B(\beta) = \begin{bmatrix} \exp(j\beta) & 0 \\ 0 & \exp(-j\beta) \end{bmatrix} \quad (1)$$

where α and β stand for variables that describe the squeezing influence on the fiber birefringence. The polarization controller in [1] is designed in such a way that it is described by the Jones matrix product

$$T(\alpha, \beta, \gamma) = \begin{bmatrix} \cos \gamma & j \cdot \sin \gamma \\ j \cdot \sin \gamma & \cos \gamma \end{bmatrix} \begin{bmatrix} \exp(j\beta) & 0 \\ 0 & \exp(-j\beta) \end{bmatrix} \begin{bmatrix} \cos \alpha & j \cdot \sin \alpha \\ j \cdot \sin \alpha & \cos \alpha \end{bmatrix} \quad (2)$$

Due to the fact that matrices of type **B** can be more easily identified with matrices of planar waveguide devices, the matrices of type **A** will be rewritten as a product of a type **B** matrix and matrices which describe 3 dB couplers

$$A(\alpha) = \begin{bmatrix} \cos \alpha & j \cdot \sin \alpha \\ j \cdot \sin \alpha & \cos \alpha \end{bmatrix} = \begin{bmatrix} \frac{1}{\sqrt{2}} & -\frac{1}{\sqrt{2}} \\ \frac{1}{\sqrt{2}} & \frac{1}{\sqrt{2}} \end{bmatrix} \begin{bmatrix} \exp(j\alpha) & 0 \\ 0 & \exp(-j\alpha) \end{bmatrix} \begin{bmatrix} \frac{1}{\sqrt{2}} & \frac{1}{\sqrt{2}} \\ -\frac{1}{\sqrt{2}} & \frac{1}{\sqrt{2}} \end{bmatrix} \quad (3)$$

Using this expression, matrix **T** can be written as

$$T(\alpha, \beta, \gamma) = \begin{bmatrix} \frac{1}{\sqrt{2}} & -\frac{1}{\sqrt{2}} \\ \frac{1}{\sqrt{2}} & \frac{1}{\sqrt{2}} \end{bmatrix} \begin{bmatrix} \exp(j\gamma) & 0 \\ 0 & \exp(-j\gamma) \end{bmatrix} \begin{bmatrix} \frac{1}{\sqrt{2}} & \frac{1}{\sqrt{2}} \\ -\frac{1}{\sqrt{2}} & \frac{1}{\sqrt{2}} \end{bmatrix} \begin{bmatrix} \exp(j\beta) & 0 \\ 0 & \exp(-j\beta) \end{bmatrix} \begin{bmatrix} \frac{1}{\sqrt{2}} & -\frac{1}{\sqrt{2}} \\ \frac{1}{\sqrt{2}} & \frac{1}{\sqrt{2}} \end{bmatrix} \begin{bmatrix} \exp(j\alpha) & 0 \\ 0 & \exp(-j\alpha) \end{bmatrix} \begin{bmatrix} \frac{1}{\sqrt{2}} & \frac{1}{\sqrt{2}} \\ -\frac{1}{\sqrt{2}} & \frac{1}{\sqrt{2}} \end{bmatrix} \quad (4)$$

3 dB couplers possessing the matrix form used in Eq. 3 can be built by conventional couplers by adding constant phase shifts of $\pm \pi/2$ at the in- and output ports such that the desired transfer matrix is achieved. This phase shifts can be realized nearly wavelength independently by changing path length in the order of a fraction of the wavelength. With these results we are

able to construct a device based on planar waveguide technology and possessing the same overall transfer matrix as for the single channel polarization controller in [1]. A polarization beam splitter and combiner at the in- and output respectively are required for mode adaptation to the chip. After separating the incoming signal into TE and TM polarized light one of the polarizations is converted into the orthogonal one. Thus both signal parts enter the chip with the same polarization. A detailed description of this kind of mode mapping is given in [2]. This technique allows to exploit interference effects between the original TE or TM polarized lights in order to achieve mode conversion. Representing each matrix in the product (Eq. 4) by the corresponding devices and using the described mode mapping method, results in the design shown in fig. 1.



Fig. 1: Simplified overall design for a planar waveguide circuit for endless polarization control.

In order to extend this scheme to a WDM suitable polarization controller, the phase shifting has to be carried out independently for each wavelength. Therefore wavelength selectable phase shifters should substituted the phase shifters in fig. 1 which are used for polarization adjustment. Wavelength selectable phase shifters can be built using an optical DeMux, an array of parallel phase shifters, and a Mux, as shown within the dashed frame in fig. 2. Thus the complete design, possessing endless polarization control for all WDM channels and having the same transfer function for each channel depending on $\alpha(\lambda)$, $\beta(\lambda)$, $\gamma(\lambda)$ like the fiber squeezer based device described in [1] has for a single channel, is given by the overall design shown in fig. 2. Phase shifters at the input and output ports can be eliminated in slightly different designs that show the same functionality. In such a design different amounts for $\alpha(\lambda)$, $\beta(\lambda)$, $\gamma(\lambda)$ have to be adjusted. Notice parts of the design (shown within the solid frame in fig. 2) were already realized in dynamic gain equalizing filters [3]. As a control algorithm, which guarantees an endless tracking range, one can choose a similar one to that explained in detail in [1].

Designs of a single channel polarization controller containing four or more fiber squeezers are known. Additional control elements inside one polarization controller can enhance the tolerance of the design or simplify the control algorithm. The device is suitable for endless transformation of an arbitrary input polarization state into TE or TM polarization or vice versa. A device that can transform endlessly an arbitrary input state of polarization into an arbitrary output polarization state can be build by combining two of the described WDM polarization controllers. The overall set up can be simplified by removing the two polarization beam splitter and combiner and connecting their corresponding in- and output ports directly to each other. The number of DeMux and Mux compositions in the design can be reduced to five for the purpose of endlessly transformation of an arbitrary state of polarization into an arbitrary fixed output polarization state.

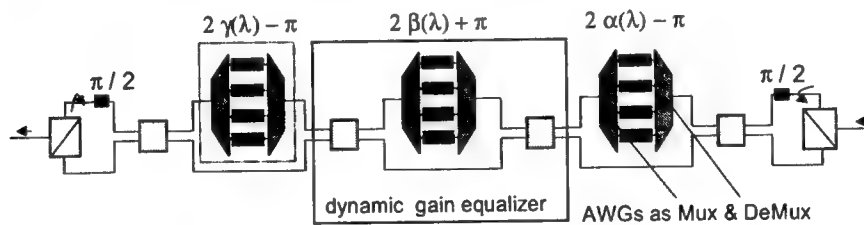


Fig. 2: Planar waveguide circuit for endless channel individual polarization controlling in a WDM signal.

Technical implementation of the design

Different kind of material systems like silicon optical bench, InP or LiNbO₃ were used in the past to build complex filter structures like AWGs. Whereas the last two candidates can be used for designing phase shifters with short response time (nsec range) silicon optical bench technology can deal with very low insertion loss. In [4] a 32 channel fiber pigtailed AWG was presented with an total insertion loss of 0.8 dB and a high background crosstalk suppression of -40 dB. From this we can estimate a minimum insertion loss of the WDM polarization controller consisting of 6 AWGs of around 5 dB (not including the significantly smaller losses caused by the polarization beam splitters). The device could be build as a hybrid combination of polarization beam splitters and the AWG chip. An overall compact design would result from the implementation of integrated polarization splitters [5] and TE/TM mode converters [6].

References

- [1] R. Noe, H. Heidrich, D. Hoffmann, "Endless Polarization Control Systems for Coherent Optics," JLT, pp. 1199-1207, 1988.
- [2] L. Moeller, H. Kogelnik, "PMD Emulator restricted to first and second order PMD Generation," ECOC'99, vol. II, pp. 64-65, 1999.
- [3] C.R. Doerr et al., "Dynamic wavelength equalizer in silica using the single-tiltered-arm interferometer," IEEE PTL, pp. 581-583, 1999.
- [4] A. Sugita et al., "Fabrication of very low insertion loss (~0.8dB) arrayed waveguide grating with vertically ...," ECOC'99, PD1-2, 1999.
- [5] M. Okuno et al., "Birefringence Control of Silica waveguides on Si and Its Application to a Polarization...", JLT, pp. 625-633, 1994.
- [6] Y. Inoue et al., "Elimination of polarization sensitivity in silica-based wavelength division multiplexer...", JLT, pp. 447-455, 1995.

Thin-film based coupled-cavity allpass filters for dynamic dispersion-slope compensation

M. Jablonski^{a,b}, Y.Tanaka^a, H.Yaguchi^a, K.Furuki^a, K.Sato^a, N.Higashi^a, and K.Kikuchi^b

(a) Oyokoden Lab Co., Ltd. 3-1-23 Niizominami, Toda-Shi, Saitama 335-0026, Japan, Phone: +81-48-445-6911, Fax: +81-48-445-6907

(b) Research Center for Advanced Science and Technology, University of Tokyo 4-6-1 Komaba, Meguro-ku, Tokyo 153-8904, Japan
Phone: +81-3-5452-5123, Fax: +81-3-5452-5125, Email: jmark@ginjo.rcast.u-tokyo.ac.jp

1. Introduction

The present and increasing need for efficient dynamic dispersion compensation devices is based on increasing bit rates of 40 Gbit/s per channel and beyond in WDM systems and bit rates exceeding 1 Tbit/s [1] in single channel systems. Higher bit rate systems feel the effects of group velocity dispersion (GVD) and dispersion-slope over much shorter distance scales requiring stricter tolerances of their dispersion maps. Such systems are in turn more sensitive to changing internal and external parameters, such as input power, path length (as in optical networks), and environmental conditions. Fine adjustments of both the GVD and higher order dispersion will be required to offset such effects, creating a need for adjustable dispersion compensation. We have demonstrated a completely thin-film based dynamic dispersion-slope compensator using two coupled two-cavity layered optical thin-film allpass dispersion equalizers (LOTADEs) in a parallel configuration suitable for a 320 Gbit/s system [2]. In comparison to other dynamic dispersion-slope compensators, such as the VIPA [3] and FBGs [4], this device offers a number of desirable attributes, such as zero polarization mode dispersion (PMD), negligible group delay ripple, and a purely quadratic group delay profile, as well as the potential for a high degree of compactness and low loss.

In this paper, single-reflection results for both a two and a four coupled-cavity thin-film allpass filter are reported. This is followed by a discussion of an improved version of the multi-reflection device written about in [2]. All filters are composed entirely of quarter wavelength layers of commonly available thin-film materials SiO_2 and Ta_2O_5 . We show adjustable dispersion-slope compensation between -7 ps^3 and -40 ps^3 over a CBW varying between 3.2 nm to 3.4 nm. The center wavelength of the filter is tunable over a 10 nm range while still maintaining almost constant dispersion-slope compensation.

2. Single-reflection TF filters

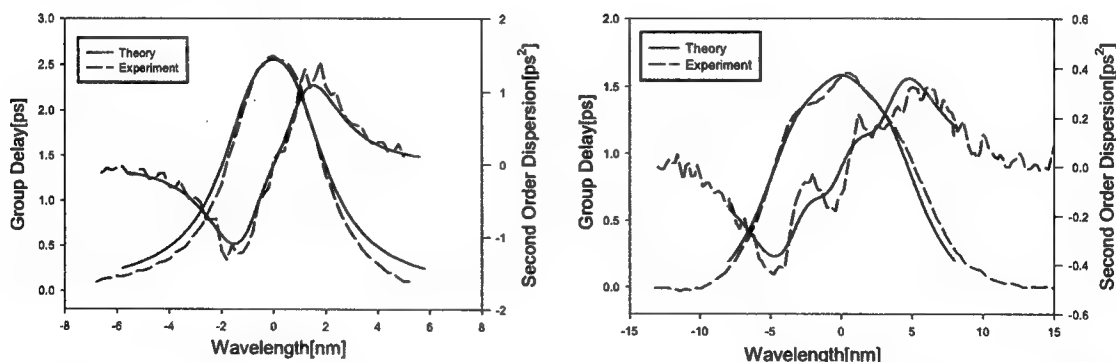


Figure 1 Dispersion characteristics of a single-reflection two-cavity (left), and four-cavity (right) LOTADE.

Single-reflection LOTADEs, while not possessing as high a FOM as multi-reflection LOTADEs, can provide reasonable TOD compensation by themselves, when used at an appropriate CBW. For example, in [5] a pair of two LOTADEs provided TOD compensation for a 1.6 ps pulse train over 60 km of DSF. However at increased CBWs, like 10 nm, the amount of TODC, on the order of 1 km of DSF fiber, is quite small.

Figure 1 shows the dispersion characteristics of two different examples of single-reflection filters. The left half shows a coupled two-cavity filter with a 3 nm CBW and a TOD value of -0.9 ps^3 . The right half shows a coupled four-cavity filter with a 10 nm CBW and a TOD value -0.1 ps^3 . It is evident from this figure that even though the

measured dispersion characteristics for the two-cavity case are closer to theory than the four-cavity case, the four-cavity experimental results still follow the theory reasonably. Both filters have a peak spectral loss between 0.1 and 0.2 dB.

3. Multiple-reflection sandwich

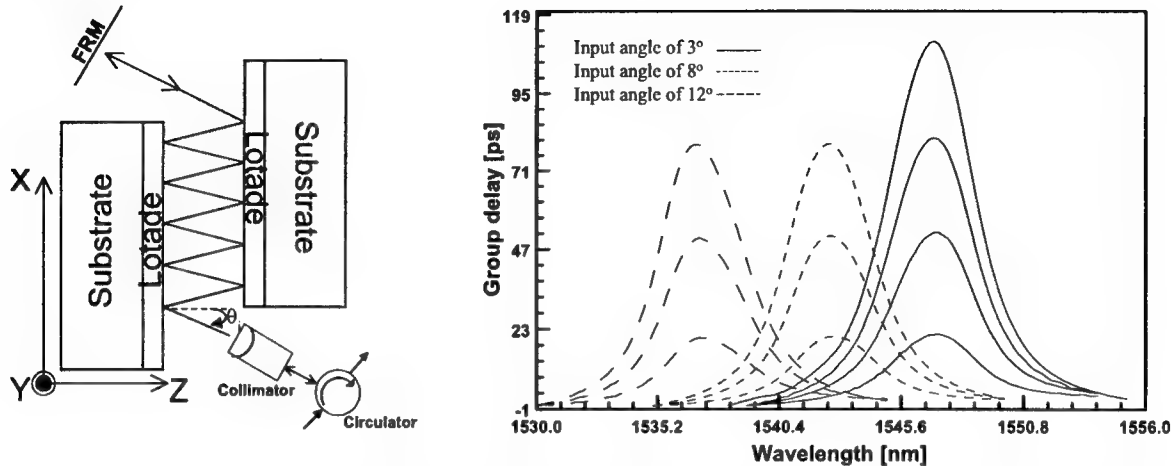


Figure 2 Multi-reflection filter structure (left), and group delay characteristics of sandwich structure (right).

By combining two of the 3 nm CBW thin-film filters in the parallel configuration shown in the left half of Fig. 2, multiple reflections are used to increase the amount of dispersion compensation without the necessity of decreasing the CBW. The filters are separated by a spacing of 3 cm and have a surface area of approximately $2 \times 3.5 \text{ cm}^2$. The center wavelength of the filter is adjusted by changing the input angle. With the use of a Faraday rotator mirror (FRM), any angle induced polarization mode dispersion (PMD) is cancelled.

The overall characteristics of the multiple-reflection filter are summarized in the right half of Fig. 2. The group delay curves for three different input angles, $\theta_i = 3, 8$, and 12 degrees, are shown, covering a change in center wavelength of 10 nm. For each input angle, the group delay curves for 8, 20, and 32 filter reflections are shown. At an input angle of 3 degrees, we show a maximum dispersion-slope value of -40 ps^3 corresponding to 44 filter reflections. The maximum range of dispersion-slope provided is from -7 ps^3 to -40 ps^3 . Good uniformity of the filter layers results in a CBW that varies by only 0.2 nm over the range of input conditions associated with the group delay curves displayed in the right half of Fig. 2.

4. Summary and conclusions

Two ways of increasing the FOM of CCAP based filters are to increase the number of cavities and to increase the number of filter applications. With this goal in mind, the single-reflection dispersion characteristics of both two and four CCAP filters were discussed and shown to agree reasonably well with theory. The two-cavity filters were then used as building blocks in a multi-reflection type device that was shown to provide adjustable dispersion-slope compensation between -7 ps^3 and -40 ps^3 within a CBW varying between 3.2 nm and 3.4 nm, with the center wavelength variable over a 10 nm bandwidth.

References

- [1] M. Nakazawa, T. Yamamoto, and K. Tamura, "1.28 Tbit/s - 70 km OTDM transmission using third- and fourth-order simultaneous dispersion compensation with a phase modulator," presented at European Conference on Optical Communications, Post-deadline paper, Munich, Sept. 3-7, 2000.
- [2] M. Jablonski et al., "Adjustable dispersion-slope compensator using entirely thin-film coupled-cavity allpass filters in a multi-reflection parallel configuration," presented at Optical Fiber Communications, TuS3, Anaheim, CA, 2001.
- [3] M. Shirasaki and S. Cao, "Compensation of chromatic dispersion and dispersion slope using a virtually imaged phased array," presented at Optical Fiber Communications, TuS1, Anaheim, CA, 2001.
- [4] S. Matsumoto et al., "Tunable dispersion equalizer with a divided thin film heater," presented at Optical Fiber Communications, TuS4, Anaheim, CA, 2001.
- [5] M. Jablonski et al., "Layered optical thin-film allpass dispersion equalizer (LOTADE): A novel device compensating for dispersion slope of optical fibers," presented at Conference on Lasers and Electro Optics, Post-deadline paper CPD16, San-Francisco, CA., 2000.

Tunable Dispersion Compensators Based on Optical Allpass Filters

C.K. Madsen

*Bell Laboratories, Lucent Technologies, 600 Mountain Ave., Murray Hill, NJ 07974
Tel: (908) 582-6095, FAX: (908) 582-4868, email: cmadsen@lucent.com*

Abstract: Planar waveguide allpass filters providing a large continuous dispersion tuning range (± 2000 ps/nm) and system performance results for 10 Gb/s NRZ signals will be discussed.

Chromatic dispersion compensation is critical for high bitrate lightwave systems. Reconfigurable optical networks introduce a need for tunable dispersion compensation since different routes may have different cumulative dispersions. In addition, tunable dispersion compensation is required for high bitrate nonlinear systems whose optimal dispersion depends on the channel power [1], which may fluctuate over time. Because of the large number of channels in dense WDM systems, periodic filters are advantageous compared to single channel devices which require a unique filter for every WDM channel. A compact planar waveguide implementation of a multichannel, fixed [2,3] and tunable [4] dispersion compensating filter has been proposed and demonstrated based on optical allpass filters. Continuous tuning was recently demonstrated for a compensator design with a fixed bandwidth utilization and small group delay ripple along with the first system performance results for 10 Gb/s NRZ signals [5]. Compensation was demonstrated across ninety periods of the filter's response, the dispersion could be tuned through zero, and a low system penalty (< 1 dB) was obtained over a large offset range (± 15 percent of the period) from the filter's center frequency.

A basic allpass filter using a ring resonator is shown in Fig. 1a. Two parameters control its group delay response: the phase, ϕ , and power coupling ratio, κ , [6]. The allpass filter architecture shown in Fig. 1b is particularly advantageous for dispersion compensating filters since complete tunability is realized with two phase shifters and the tolerances on the couplers κ composing the MZI are substantially relaxed compared to the tolerance on κ . By using a multi-stage filter where the parameters are chosen optimally for each stage, a constant dispersion (or any desired response) can be approximated over a large portion of the Free Spectral Range (FSR), thus yielding a large bandwidth utilization [3] in contrast to other periodic filters such as the lattice MZI [7] which trade off passband loss variation for dispersion [6].

The tunable dispersion compensating filters were implemented using silica-on-silicon planar waveguides defined by photolithography and reactive ion etching. A core-to-cladding index contrast of 2% and a minimum bend radius of 1 mm were used. Thin film heaters were deposited over sections of the ring and MZI to implement phase shifters. Four stages of the Fig. 1b architecture were cascaded. The roundtrip loss was 0.7 dB/ring, and the waveguide to standard singlemode fiber (SSMF) coupling loss was 0.8 dB/facet, which could be improved, for example, by coupling to high numerical aperture fiber instead. The spectral magnitude and group delay response were measured at various heater settings and input to an algorithm that determines the required heater settings for a desired dispersion given requirements on the bandwidth utilization and maximum allowable group delay ripple. Continuous dispersion tuning range is demonstrated in Fig. 1c. A passband of 16 GHz, or 60% bandwidth utilization, is maintained as well as a low group delay ripple. By conjugating the filter phases, i.e. $\phi_r \rightarrow -\phi_r$, negative dispersion is achieved.

System tests were performed using the filter to compensate a 100 km span of SSMF ($+1700$ ps/nm). A single tunable laser source was externally modulated with a 10 Gb/s NRZ signal (PRBS= $2^{31}-1$) and launched with a power of 0 dBm into the fiber. The filter was used both as a pre-compensator and post-compensator with equal results. The polarization into the filter was controlled in either case due to the waveguide birefringence, which causes polarization mode dispersion (PMD). To avoid this, a polarization diversity scheme employing a polarization beam splitter and circulator could be used. To demonstrate the large filter tuning range, a span of DCF with a total dispersion of -1700 ps/nm and a zero-length span were compensated in separate experiments as shown in Fig. 2 compared to a back-to-back measurement. The laser was then tuned across the filter. The system penalty remained below 1 dB over a tuning range equal to 30% of the FSR. Finally, the laser wavelength was tuned to the center of adjacent periods of the filter and the penalty was measured. Over a range of 17 nm (93 periods), which was limited by the optical amplifiers' gain bandwidth, the filter compensated the dispersion with a penalty of < 1 dB.

Optical, tunable allpass filters have also been realized using MEMs [8] and thin film filters [9]. A two-stage MEMs filter was demonstrated with a 100GHz FSR, ± 100 ps/nm tuning range and a 50 GHz passband width.

1. B. Eggleton, J. Rogers, P. Westbrook, T. Strasser, T. Nielsen, P. Hansen and K. Dreyer, "Electrically tunable power efficient dispersion compensating fiber Bragg gratings for dynamic operation in nonlinear lightwave systems," OFC/IOOC San Diego, CA, Feb. 23-26, 1999, PD27.
2. C. Madsen and G. Lenz, "Optical Allpass Filters for Phase Response Design with Applications for Dispersion Compensation," *IEEE Photonics Technol. Lett.*, vol. 10, no. 7, pp. 994-996, 1998.
3. C. Madsen, G. Lenz, A. Bruce, M. Capuzzo, L. Gomez, T. Nielsen, L. Adams, and I. Brener, "An allpass filter dispersion compensator using planar waveguide ring resonators," OFC/IOOC San Diego, CA, 1999, paper FE6.
4. C. Madsen, G. Lenz, A. Bruce, M. Cappuzzo, L. Gomez, and R. Scotti, "Integrated tunable allpass filters for adaptive dispersion and dispersion slope compensation," *IEEE Photon. Technol. Lett.*, vol. 11, no. 12, pp. 1623-1625, 1999.
5. C.K. Madsen, S. Chandrasekhar, E.J. Laskowski, K. Bogart, M.A. Cappuzzo, A. Paunescu, L.W. Stulz, and L.T. Gomez, "Compact Integrated Tunable Chromatic Dispersion Compensator with a 4000 ps/nm Tuning Range," Optical Fiber Communication Conference, Anaheim, CA, PD9, Mar. 19-22, 2001.
6. C. Madsen and J. Zhao, *Optical Filter Design and Analysis: A Signal Processing Approach*. New York, NY: John Wiley, 1999.
7. K. Takiguchi, K. Okamoto, and K. Moriwaki, "Planar Lightwave Circuit Dispersion Equalizer," *J. Lightwave Technol.*, vol. 14, no. 9, pp. 2003-2011, 1996.
8. C. Madsen, J.A. Walker, J.E. Ford, K.W. Goossen, T.N. Nielsen, and G. Lenz, "A tunable dispersion compensating MEMS all-pass filter," *IEEE Photon. Technol. Lett.*, V12, N6, p. 651-653, June 2000.
9. M. Jablonski, Y. Tanaka, H. Yaguchi, K. Furuki, K. Sato, N. Higashi, and K. Kikuchi, "Adjustable dispersion-slope compensator using entirely thin-film coupled-cavity allpass filters in a multi-reflection parallel configuration, Optical Fiber Communication Conference, Anaheim, CA, TuS3, Mar. 19-22, 2001.

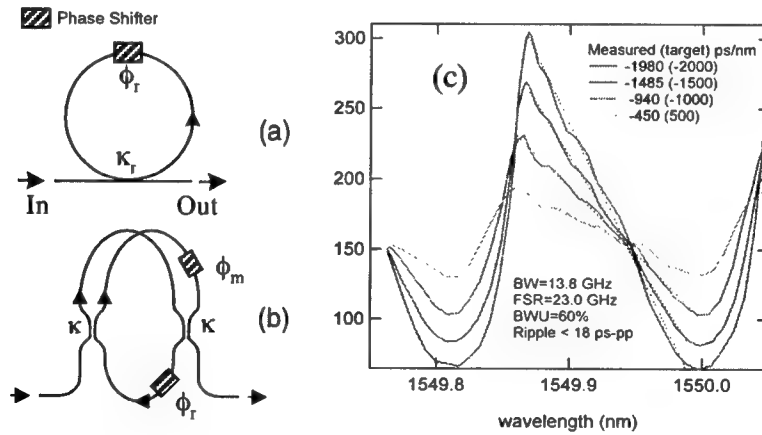


Fig. 1. Allpass filter ring resonator (a) basic and (b) fully tunable design. (c) Measured group delay demonstrating dispersion tuning from -2000 ps/nm to -500 ps/nm.

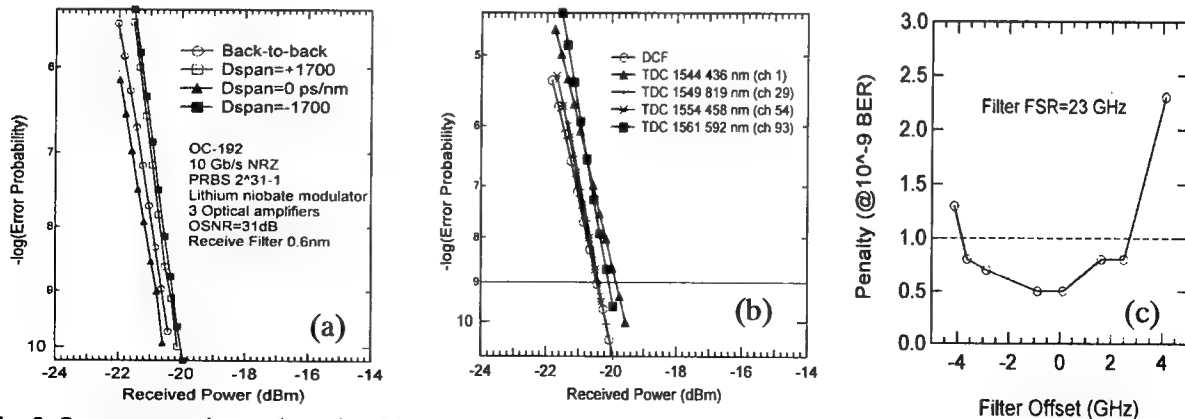


Fig. 2. System experimental results: (a) compensated span dispersions (+1700 to -1700 ps/nm), (b) intermediate and extreme channels spanning optical amplifiers' gain bandwidth, and (c) sensitivity to center frequency offset.

WDM Components

Tuesday, 31 July 2001

TuD1: Wavelength Add/Drop

Tunable Transparent and Cost Effective Optical Add-drop Multiplexer based on Fiber Bragg Grating for DWDM Networks

P. S. André, Armando Nolasco Pinto, J. L. Pinto, Teresa Almeida, M. Pousa.

Institute of Telecommunications, University of Aveiro, 3810-193 Aveiro, Portugal, E-Mail: pandre@av.it.pt

Summary:

The enormous grow in the demand of bandwidth is pushing the utilization of fiber infrastructures to their limits. To fulfill this requirement the constant technology evolution is substituting the actual single wavelength systems connected in a point-to-point topology by dense wavelength division multiplexing (DWDM) systems, creating the foundations for the Optical Transport Network (OTN). The objective is the deployment of a optical network layer with the same flexibility as the equivalent SDH, because it is more economical and allows a better performance in the bandwidth utilization. Optical add-drop multiplexers (OADM) are the simplest elements to introduce wavelength management capabilities by enabling the selective add and drop of optical channels. A wavelength tunable OADM, giving access to all the wavelengths of the WDM signals provides more flexibility to satisfy reconfiguration requirements and to enhance network protection. We proposed a tunable OADM based on fiber Bragg gratings (FBG) where the dropped channel is removed by the used of a optical circulator and the added channel is incorporated to the wavelength combo by a passive optical coupler. These OADM is transparent by design and cost effective due to the used of just one optical circulator.

The wavelength tuning capacities of the OADM are related with the FBG capacities to shift their central reflection wavelength. The significant discovery of photosensitivity in optical fibers lead to the development of a new class of in-fiber component, called the fiber Bragg grating. Basically a Bragg grating is a longitudinal periodically modulated refractive index profile in the core of an optical fiber, figure 1. Due to that modulation, it presents a reflection band centered at the Bragg wavelength λ_B . There are two main methods: to shift the Bragg grating central wavelength peak by modifying the fiber refractive index or by changing the grating period. These variations can be dynamically induced either by temperature or by mechanical stress. We present a hybrid method based on a thermal-stress thermally enhanced actuation on a FBG, to tune its central wavelength. These thermal enhanced tuning, employs a different configuration to amplify the thermal induced wavelength shift by using a positive thermal expansion material as support for the fiber Bragg grating. This hybrid tuning technique allows us to increase the tuning range and keep the thermal tuning advantages. For a typical wavelength on the region of 1550 nm the tuning coefficient is 41.1 pm/°C.

The grating used in this work was manufactured by illuminating an optical fiber exposed to a phase-mask spatially modulated UV (248 nm) writing beam originated from a KrF excimer laser. The optical fiber (standard single mode type) has been previously kept under high-pressure hydrogen atmosphere in order to enhance its photosensitivity due to hydrogen diffusion into the glass matrix. This process is reliable and gives excellent results in the reduction of the writing time of the grating.

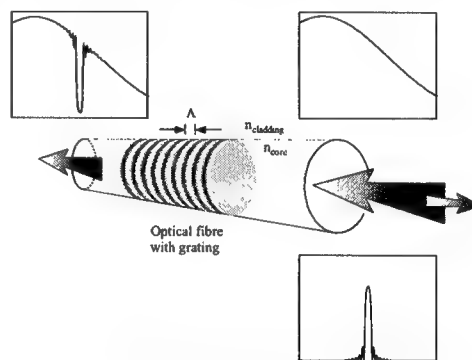


Fig. 1 – Schematic representation of a fiber Bragg grating.

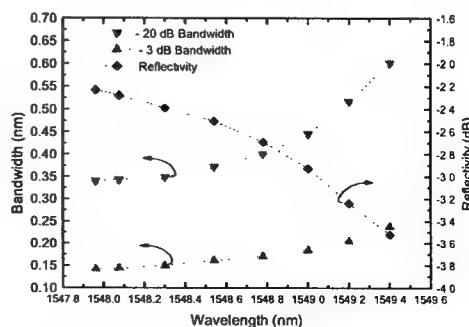


Fig. 2 – Spectral characteristics of the FBG with temperature.

The increased of temperature and stress applied on the FBG, results on a lowering of the reflectivity and an increase of the bandwidth, however these alteration on the FBG performance does not affect significantly the performance of the OADM. Figure 2 shows the variations of the reflectivity, the -3 dB and -20 dB bandwidth of the FGB with temperature. Figure 3 a) and b) presents the optical spectra of the drop channel when the temperature of the FBG was 30 and 50 C, respectively.

The tunable OADM performance and functionality was tested on a 3 channels, 50 GHz spaced, DWDM network of figure 4.

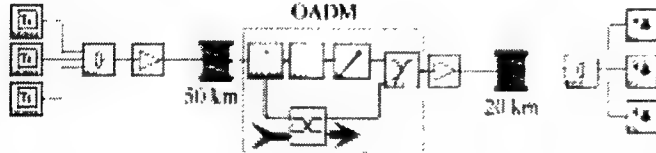


Fig. 4 – Scheme of the OADM and experimental transmission DWDM network.

Three distributed feedback lasers were externally modulated, at 2.48832 Gb/s (STM-16) with a non-return to zero $2^{15}-1$ pseudo random bit sequence. In the experimental transmission WDM link, 70 km of single mode standard fiber are used. Two Erbium doped fiber amplifiers having saturated output powers of 13 and 17 dBm and noise figures smaller than 4 dB are employed to provide the required power to compensate the link and OADM losses.

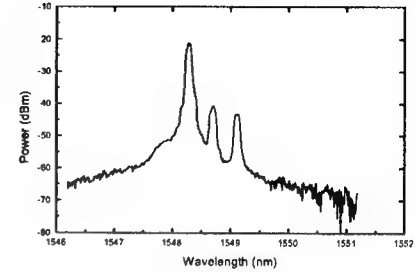
The performance of our network is assessed by the BER measurements on the central wavelength channel for a 50° C FBG temperature. Figure 5 displays the BER performance against the receiver power, for the back-to-back operation (0 km), for the drop channel on the OADM after propagation on 50 km of fiber and for the same channel just after propagation on 50 km of fiber (without be dropped at the OADM). The BER floor (measurement limit) and the 10^{-9} BER are also indicated.

The power penalty measured at a 10^{-9} BER is 0.08 dB, for the dropped channel at the OADM compared with the same channel at the OADM input after propagation on 50 km of fiber. This power penalty is due to heterodyne crosstalk induced by the leak of the signal power from the other neighbors signal components. These residual components interfere with the detection process, resulting in noise addition on the detector. The transparency of the OADM to the channel spacing and number of channels was demonstrated and the system performance degradations due to homodyne and heterodyne crosstalk induced by the FBG based OADM have been measured. The results indicate that the investigated OADM configuration is promising, due to its good spectral characteristics which results in low homodyne crosstalk, and consequently potential high cascability.

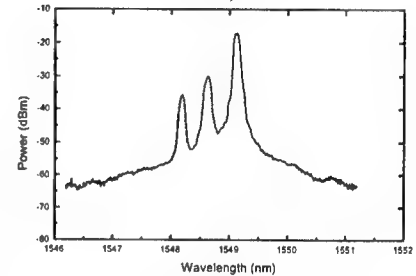
Acknowledgments: This work was supported by the DAWN PRAXIS XXI and O-NODE project.

References:

- [1] Kuninori Hattori, Masaki Fukui, Masahiko Jinno, Manabu Oguma, Kimio Oguchi, "PLC-Based Optical Add/Drop Switch with Automatic Level Control", *Journal of Lightwave Technology*, vol. 17, pp. 2562, (1999).
- [2] H. Mavoori, S. Jin, R. P. Espindola, T. A. Strasser, *Enhanced thermal and magnetic actuations for broad-range of fiber Bragg gratings - based reconfigurable add - drop devices*, *Optics Letters*, 22, pp. 714, (1999).
- [3] Alessandro Iocco, Hans Georg, Limberger, René Paul Salathé, Lorna A. Everall, Karen E. Chisholm, John A. R. Williams, Ian Bennion, *Bragg grating fast tunable filter for wavelength division multiplexing*, *Journal of Lightwave Technology*, 17, pp. 1217, (1999).



a)



b)

Fig. 3 – Optical spectra of the channel 3 dropped for 30° C and 50° C FBG temperature (top and bottom), respectively.

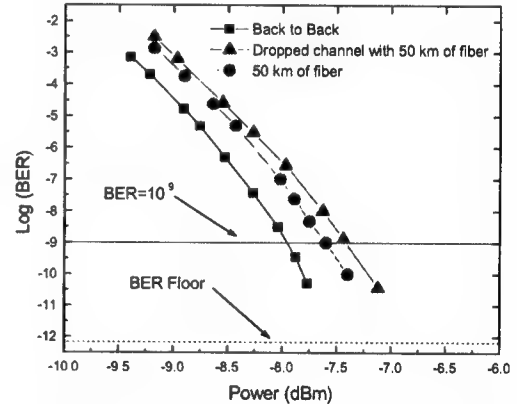


Fig. 5 – BER performance for the dropped channel.

80-Channel Integrated Dynamic Drop Filter with Flat-top Passband

P. Bernasconi*, C. Doerr, L. Stulz,
M. Cappuzzo, L. Gomez, A. Paunescu, E. Laskowski, and S. Shunk
Bell Laboratories, Lucent Technologies
791 Holmdel-Keyport Rd., Holmdel, NJ 07733 USA
(*e-mail: pgb1@lucent.com)

Introduction

The efficient management of an optical transmission system based on wavelength division multiplexing (WDM) relies on reconfigurable add/drop filters (A/D) as one of the key components. At the nodes, these devices are expected to selectively extract and/or inject a subset of channels from the optical stream without affecting the others. The fast evolution of optical systems requires A/Ds to handle a large number of channels.

We present an 80-channel drop filter based on planar waveguide silicon optical bench technology that accesses independently each channel. This approach offers design simplicity, robustness, size and cost reduction. Flat-top passbands and negligible chromatic dispersion are included features.

Device

Our device is conceived around an array waveguide grating^{1,2} (AWG) which provides the demulti- and multiplexing capabilities required by our architecture as shown schematically in Fig. 1. The 80 channels on a 50 GHz grid first pass through a circulator before entering the AWG and being spatially demultiplexed. Each one of the 80 output waveguides is followed by a switch that directs the signal either to the arm coupled to an output fiber (drop channel) or to the arm terminated with a high reflecting coating (through channel). In the latter case, the channel is reflected back into the AWG, multiplexed into the input port, and separated by the circulator from the incoming optical stream³.

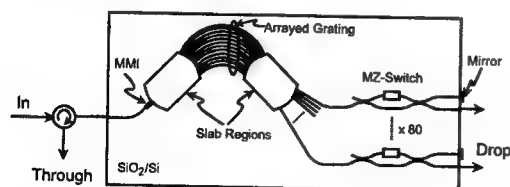


Fig.1 Scheme of the AWG-based drop filter. For details, see text

Due to the double pass through the AWG, the through channels will suffer additional losses and spectral filtering compared with the drop channels. It is thus imperative to reduce the overall insertion losses and to

flatten the transmission coefficients in the spectral range. To achieve the first goal we can use the segmentation technique⁴ between the AWG slab regions and the waveguide grating which allows a smoother transition between the refractive indices of the slab and the waveguide grating, respectively.

The flat-top passband is obtained by the proper matching of the field profiles at the input and at the output of the slab regions. At the input side, we used a single mode waveguide followed by a multi-mode interferometer (MMI) which produces a slightly double peaked intensity profile at its end⁵ through the interference between the fundamental and next two higher symmetric guided modes. The dimensions of the output waveguides are chosen so to minimize the ripple in the spectral response.

The switches are Mach-Zehnder interferometers activated thermo-optically by heating a chrome strip placed on top of one interfering arm⁶.

The dimension of the device fabricated in SiO₂ on Si with an index contrast $\Delta n/n \sim 0.8\%$ are $85 \times 45 \text{ mm}^2$.

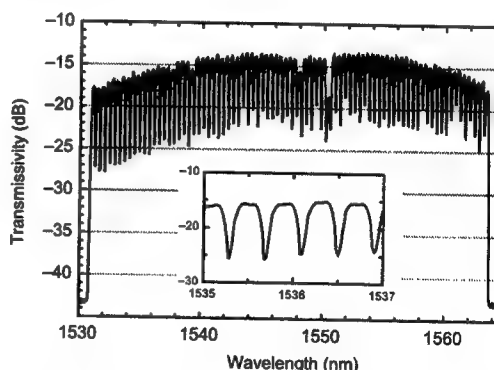


Fig. 2 Measured transmissivity from the in port to the through port for all 80 channels. No current is applied to the MZ-switches. In the inset a detail showing the flat-top passbands. Measurements include the circulator. TE polarization; resolution bandwidth = 0.1 nm.

Measurements

The measurements have been performed with light from a broadband source. In Fig. 2 we see the spectral

response at the through port without the activation of any of the MZ-switches. From the fabrication it turned out that the quiescent state of the switches is very close to the through state with few exceptions. After activation of each switch in the through state we could measure total insertion losses (circulator included) ranging from 14 dB for the central channels to 17 dB for the lateral ones. This nonuniformity can be reduced by extending the free spectral range of the grating. In the drop state the losses were 8.5, and 11 dB, respectively. Notice that in this device we did not use any segmentation technique, so we expect the losses to be further reduced in the near future. Polarization dependent losses (PDL) were constantly below 1 dB while no polarization dependent wavelength shift was observed.

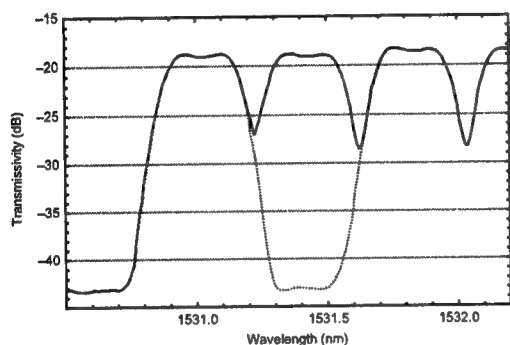


Fig. 3 Close up of the measured transmissivity from in port to through port when all the channels are in the through state (solid line) and when channel #2 is dropped (dotted line). TE polarization; resolution bandwidth = 0.05 nm.

Flat-top spectral response was achieved as shown in Figs. 2-4. The passband ripple, although polarization dependent, was always less than 0.8 dB peak-to-peak. In the through state, the filter shape was characterized by a 1, 3, and 20 dB full bandwidth of 30 ± 1 , 40 ± 1.5 , and 62 ± 3 GHz, respectively. The drop state, which does not suffer of double filtering effects, showed a little wider passbands of 31 ± 1 , 43 ± 1.5 , and 84 ± 4 GHz at the 1, 3, and 20 dB transmission points, respectively. It has to be mentioned that, although this was not affecting PDL, for TM polarization we notice a tilt of the flat portion of the passband that increased from the center to the lateral channels. This feature shall be eliminated by a proper correction in the AWG design.

The passband shapes shown in the figures guarantee a good measured adjacent channel cross-talk of less than -21 dB and less than -32 dB for nonadjacent channels in the drop state. In the through state, cross-talk is not such an important issue considering that the optical channels are first demultiplexed and then recombined travelling almost identical optical paths.

The in-to-through extinction ratio is ~23 dB and it is currently limited by the cross-talk floor at -43 dB as shown in Fig. 3. This floor is likely due to leakage through the circulator combined with reflections at fiber-wafer interface. On the other hand, as shown in Fig. 4 the in-to-drop switching extinction ratio is ~16

dB and this is currently limited by the performance of the MZ-switches.

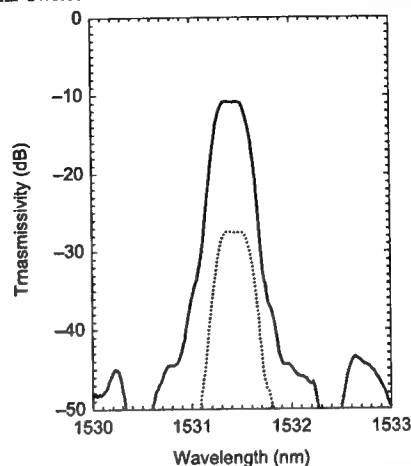


Fig. 4 Close up of the measured transmissivity from in port to drop port when all the channels are in the through state (dotted line) and when channel #2 is dropped (solid line). TE polarization; resolution bandwidth = 0.05 nm.

The actual power consumption of a single MZ-interferometer to switch between the through and the drop state is approx. 0.5 W giving a total consumption of 40 W. This does not include the temperature stabilization process to align the AWG with the wavelength grid defined by the optical channels.

Conclusion

We have presented a Si-based integrated flat-top filter which can independently drop any of the 80 channels on a 50 GHz grid. Our preliminary results show that there are still wide margins for improvement so that such devices might become extremely interesting not only under the performance point of view but also for their size and cost effectiveness.

References

- [1] M. K. Smith *et al.*, IEEE J. Select. Topics Quantum Electron., vol. 2, 236-250, 1996.
- [2] C. Dragone, IEEE Photon. Technol. Lett., vol.3, 812-815, 1991.
- [3] C.R. Doerr *et al.*, IEEE Photon. Technol. Lett., vol.11, 1437-1439, 1999.
- [4] Y.P. Li, US Patent Nr.5745618, April 28, 1998.
- [5] J.B.D. Soole *et al.*, IEEE Photon. Technol. Lett., vol.8, 1340-1342, 1996.
- [6] M. Okuno *et al.*, NTT Rev., vol. 7, 57-63, 1995

Compact mode-size converters for efficient coupling between fibers and integrated optical waveguides

Christina Manolatos and Hermann A. Haus

krist@mit.edu, haus@mit.edu

Dept. of Electrical Engineering and Computer Science

Massachusetts Institute of Technology

Cambridge MA 02139

The strong light confinement in high index-contrast structures, such as Si/SiO₂ or air, allows the design of low loss waveguide components with sizes on the order of the optical wavelength, enabling dense optical integration [1]. Because of the submicron mode-size of such waveguides, coupling light to and from optical fibers is a very challenging task. Most integrated spot-size converters are based on tapers and are a few hundreds of microns long e.g [2]. In this work we present a theoretical and numerical investigation of compact fiber-waveguide couplers that are based on lensing and high index-contrast and are only a few microns long [3]. These structures are characterized by very broadband operation which makes them suitable for WDM systems. We assume that the input mode is from a lensed single-mode fiber and can be approximated by a Gaussian. Thus a preliminary design can be obtained analytically using Gaussian beam optics and ray matrices. Finite Difference Time Domain (FDTD) simulations are performed for evaluation of the performance and optimization of the design.

An example of the basic structure used for lateral mode-size conversion is shown in the schematic of Fig.1(a) and the expected beam evolution, found analytically, is shown in Fig.1(b). The interface between the low-index and the high-index material acts as a lens and the beam spot-size reduction is achieved within less than 5.5 μ m by proper choice of the radius of curvature. Impedance matching is provided by a quarter-wave layer of index equal to the square root of the index on either side. The electric field and the wavelength response found by FDTD simulations are shown in Fig.2(a) and (b), respectively. Note that the response covers the entire wavelength range of a WDM system and that, due to reciprocity, the same coupling efficiency is obtained in both directions.

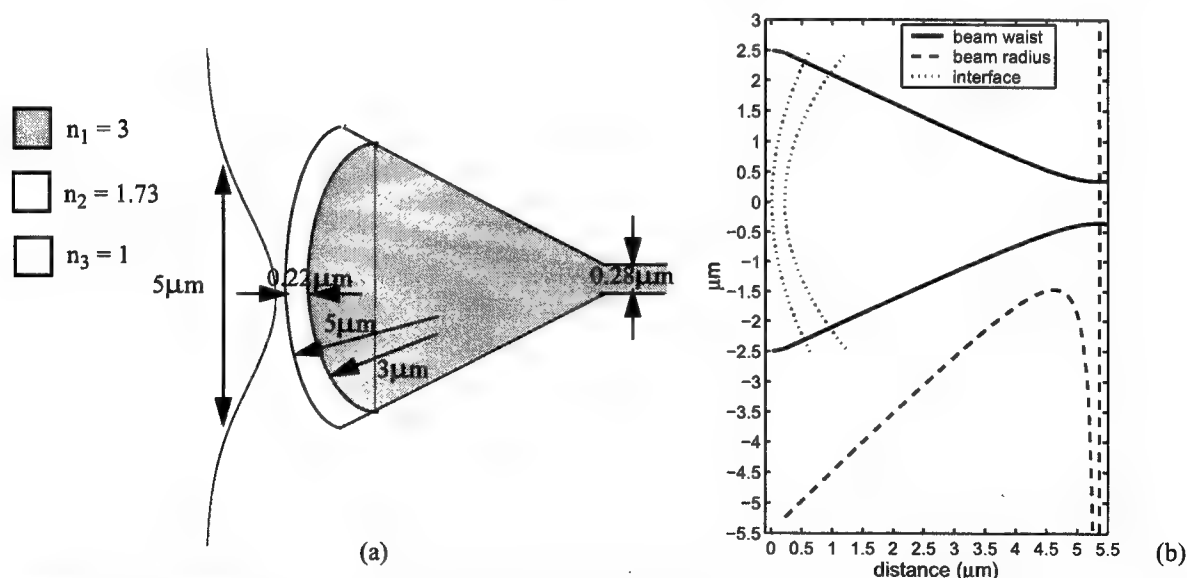


Figure 1: (a) Schematic of a planar integrated lens for lateral mode-size conversion, (b) expected beam evolution obtained by gaussian optics formalism.

In principle this design could be extended to three dimensions; however the fabrication of a structure with one or more interfaces with 3D curvature would be a very difficult task. Instead, a layered structure with graded index variation operating as a GRIN lens would be more practical. The lensing mechanisms for lateral and vertical mode conversion, can be combined as shown in the schematic of Fig. 3(a). To simplify the analysis we decompose the 3D problem into two 2D problems linked by an effective index. Figures 3(b) and (c) show the wavelength response obtained by

FDTD in the vertical and the lateral dimension, respectively, for a typical example. The total coupling efficiency is estimated as the product of the two 2D coupling efficiencies to about 80% or 1dB coupling loss. This performance is achieved in both propagation directions within a distance of $5.5\mu\text{m}$ and over a bandwidth of more than 40nm.

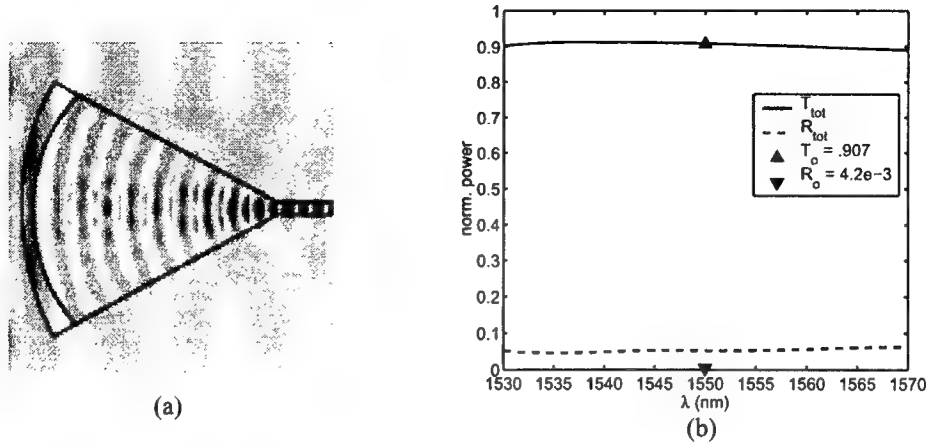


Figure 2: FDTD results (a) Electric field amplitude (b) Transmission and reflection spectra. Solid and dashed lines refer to the total transmission and reflection, respectively, and the triangles refer to coupling between the fundamental modes at 1550nm.

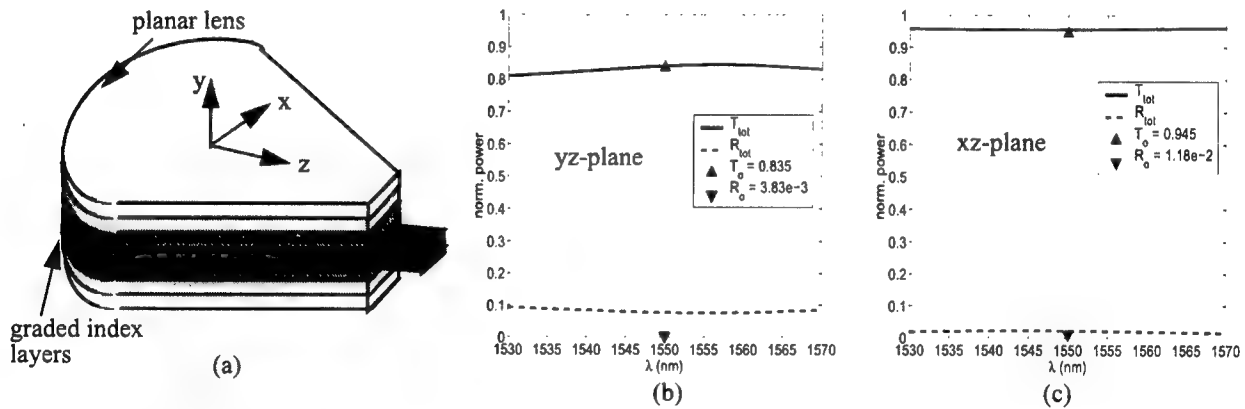


Figure 3: (a) Combination of graded index for vertical mode-conversion and planar lens for lateral mode-conversion, and wavelength response found by FDTD (b) in the yz-plane (c) in the xz-plane.

References

- [1] Y. Itaya, Y. Tohmori, H. Toba, "Spot-size converter integrated laser diodes (SS-LD's)", *IEEE J. Selected Topics Quant. Electron.*, vol. 3, no. 3, pp 968-974, June 1997.
- [2] C. Manolatou, S.G. Johnson, S. Fan, P.R. Villeneuve, H.A. Haus, J.D. Joannopoulos, "High-Density Integrated Optics", *J. Lightwave Technol.*, vol.17, no.9, pp.1682-1692, Sept. 1999.
- [3] C. Manolatou, "Passive components for dense optical integration based on high index-contrast", PhD Thesis, MIT, June 2001.

WDM Components

Wednesday, 1 August 2001

- WD1: Dynamic Gain Equalization Techniques & Devices I
- WD2: Dynamic Gain Equalization Techniques & Devices II

Wednesday Missing Paper

WD1.2 "Fiber-based Acousto-Optic Gain Equalizer" S. H. Yun, *Novera Optics, Inc., San Jose, CA, USA.*

Dynamic gain equalization for next-generation DWDM transport systems

W. J. Tomlinson
JDS Uniphase Corp.
100 Willowbrook Road, Bldg. 1
Freehold, NJ 07728-2879
Tel: 732-577-8550, x289
Email: Jack.Tomlinson@us.jdsunph.com

I. Introduction

As designs for DWDM transport systems evolve to higher and higher total system capacities, this results in increasingly stringent requirements for control of the spectral dependence of optical amplifier gains. For high-bit-rate (e.g. 40 Gb/s) systems, the channel bandwidth is sufficiently large that relatively small gain ripples and tilts can result in significant distortions of the signals. For ultra-long-haul systems, relatively small gain variations between channels can add up to unacceptable channel power differences over the total system span. With the existing fixed gain-flattening filter technologies it is very difficult to meet the basic requirements for these systems, and to account for small differences between amplifiers and aging effects, it would appear that some form of dynamic gain control will be required. In addition, dynamic gain control will be needed to compensate for changing channel loads and configurable add/drops.

II. Gain vs channel-power equalization

An important distinction, which is often overlooked, is the difference between what we will refer to as "gain equalization," and "channel-power equalization." For example, to compensate for a linear slope in the spectral gain of an amplifier, one needs a gain equalizer with a spectral loss function with a linear slope that is the negative of the gain slope. This will result in a uniform flat gain for all channels. If the amplifier gain is flat, but the powers of the input channels have a similar linear slope, using a gain equalizer with the opposite slope will equalize the output powers of the channels. However, each channel will see a gain tilt across its bandwidth, which will result in signal distortions. In such a case, one needs a channel-power equalizer, with a stair-step type of spectral response function, such that each channel can see a different gain, but a gain that is flat over its bandwidth. In this paper, we are focused on gain equalizers. Some of the technologies that are useful for gain equalizers can also be used for channel-power equalization, but with different design parameters.

III. Types of dynamic gain equalizers

Available technologies for dynamic gain equalization can be divided into three categories.

A. Dynamic tilt equalizers

A tilt equalizer has a spectral response with an adjustable linear tilt. The primary application for such equalizers is to compensate for gain tilt introduced when an amplifier, which includes a gain flattening filter appropriate for a particular set of operating conditions, is operated with a different gain or input power. In many amplifiers this is accomplished by using a simple variable optical attenuator between amplifier stages, and also adjusting pump powers. With dynamic tilt equalizers, one can achieve more accurate tilt compensation, as well as possibly reducing the require pump power, and improving noise figure. Dynamic tilt equalizers have been reported using a combination of a thick birefringent plate and a Faraday rotator,¹ and with thermo-optic waveguide Mach-Zehnder filters.²

B. Modest-resolution dynamic gain equalizers

In what we will refer to as modest-resolution equalizers, there are a few (perhaps a half dozen) attenuation resonances, with adjustable amplitudes, and usually with adjustable center wavelengths. In most cases, the elements that give rise to the resonances are connected in series, so the resulting transmission spectrum is the product of the transmission of the individual elements. Typically the cost, complexity, and insertion loss of such equalizers is a roughly linear function of the

¹ T. Naito, et al, "Active gain slope compensation in large-capacity long-haul WDM transmission system," *OSA Trends in Optics and Photonics Vol. 30, Optical Amplifiers and Their Applications*, (Optical Society of America, Washington DC 1999), pp 336-339.

² H. Nakaji et al, "Ultra-wide dynamic range Erbium doped fiber amplifiers employing variable attenuation slope compensation," in *Optical Amplifiers and Their Applications*, OSA Technical Digest (Optical Society of America, Washington DC 1999), pp 167-169.

number of resonances, which provides an incentive to make do with as few as possible. Technologies that have been demonstrated for implementing modest-resolution units include: all-fiber acoustooptic tunable filters;³ serial combinations of filters using thick birefringent plates and Faraday rotators;⁴ waveguide tapped delay-line filters;⁵ and serial combinations of waveguide Mach-Zehnder filters.⁶

C. High-resolution dynamic gain equalizers

In what we refer to as high-resolution equalizers, we have many more resonances, with adjustable amplitudes, but generally with fixed center wavelengths. In most cases this is accomplished by dispersing the spectrum across an array of variable attenuators, and then recombining the outputs from the attenuators. Thus, the filtering is done in parallel, and the cost, complexity, and insertion loss are only weakly dependent on the number of resonances. Technologies that have been demonstrated for implementing high-resolution units include: waveguide AWG-based interferometers;⁷ bulk grating based units with MEMs etalons;⁸ and bulk grating based units with liquid-crystal cells.⁹ Higher resolution versions of

these devices have been demonstrated for use as channel-power equalizers, but for gain equalizers it is important to select a resolution that is consistent with achieving a smooth, low-ripple response function, as discussed in the following section.

IV. Design parameters for high-resolution dynamic gain equalizers

In the high-resolution equalizers referenced above, the input light is spectrally dispersed across a linear array of variable attenuators or pixels. To achieve a smooth, low-ripple response function it is essential to match the spectral resolution of the unit to the pixel size. We can characterize the spectral resolution by a parameter W , which is the width (in the dispersion direction), of the beam incident on the pixel plane, for a monochromatic input signal, measured in units of the pixel pitch. Assuming that there are opaque gaps, of width gap (in units of pixel pitch), we can calculate the resulting ripple in the equalizer response for various values of W and gap , with the results shown in Fig. 1. These results show that the ripple amplitude is a rather steep function of W , and that for gap widths of a few percent of the pixel pitch, it is desirable to design equalizers for $W \sim 2$.

³ S. H. Yun et al, "Dynamic Erbium-doped fiber amplifier based on active gain flattening with fiber acoustooptic tunable filters," IEEE Photon. Technol. Lett. **11**, 1229-1231 (1999).

⁴ S. Frisken et al, "Low-loss polarization-independent dynamic gain-equalization filter," in Optical Fiber Communications Conference, OSA Technical Digest (Optical Society of America, Washington DC, 2000), Session WK, pp. 251-253.

⁵ A. Ranalli et al, "Planar tapped delay line based actively configurable gain-flattening filter," in Proceedings of ECOC 2000, Vol. 3, pp.21-22.

⁶ S. P. Parry et al, "An ultra flat Erbium doped fibre amplifier with wide dynamic range using an adaptive gain flattening filter," in *Optical Amplifiers and Their Applications*, OSA Technical Digest (Optical Society of America, Washington DC 1999), Paper OMD9; and B. J. Offrein et al, "Adaptive gain equalizer in high-index-contrast SiON technology," IEEE Photon. Technol. Lett. **12**, 504-506 (2000).

⁷ C. R. Doerr et al, "An automatic 40-wavelength channelized equalizer," IEEE Photon. Technol. Lett. **12**, 1195-1197 (2000).

⁸ J. E. Ford et al, "Broad spectrum micromechanical equalizer," in Proceedings of ECOC 1999, Vol. 1, pp 272-273.

⁹ A. Ranalli et al, "Liquid crystal-based wavelength selectable cross-connect," in Proceedings of ECOC 1999, Vol. 1, pp. 68-69.

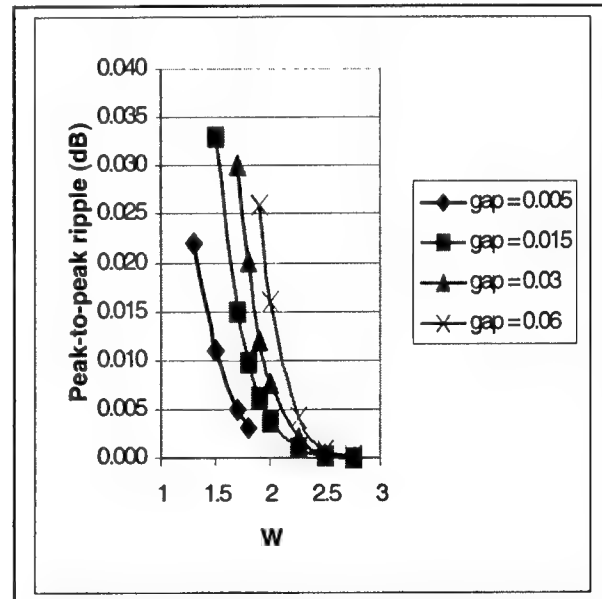


Fig. 1. Calculated ripple amplitude as a function of W and gap .

V. Conclusions

There are a variety of technologies available for dynamic gain equalization. The highest capacity systems will probably require high-resolution units, but modest-resolution units may prove in for less demanding application.

Tapped Delay Line Dynamic Gain Flattening Filter

S. Vallon, I. Cayrefourcq, P. Chevallier, N. Landru, G. Alibert, P. Laborde¹, J. Little², Al Ranalli², N. Boos.

*Corning SA, Centre Européen de Recherche de Fontainebleau
7 bis avenue de Valvins, 77210 Avon
France.*

¹*Corning Incorporated, Sullivan Park R&D Center
Science Center Drive, Corning, New York, 14831-0001,
USA.*

²*Corning Incorporated, Advanced Photonic Technologies
6300 Gateway Drive Cypress, California, 90630
USA.*

Abstract

Experimental results of an 8 tap Dynamic Gain Flattening Filter (DGFF) are presented. This device consists in a planar Silica on Silicon lightwave optical circuit including tunable couplers and delay lines. In this paper we will discuss both optical performances and the control scheme.

Introduction

The increasing demand for high transmission capacity leads to a new network generation that combines both high bit rate (40 Gbits/s) and wavelength division multiplexing (WDM) both for long and Ultra Long haul systems. At low optical powers the system performance will be degraded by noise, while non-linearities represent the upper limit to the per-channel power. Moreover, dynamic phenomena such as input power variations, temperature changes, pump power variations change the gain profile of Er-doped fiber amplifiers. In order to minimize system penalties a dynamic device is needed to compensate these changes and achieve flat gain.

Numerous devices have been developed to meet this need. Among them one can consider PLC based devices as cascaded Mach Zehnders [1] or TDL DGFF [2], AWG based per channel equalizer [3], slope compensator equalizer using variable Faraday Rotator [4].

In this paper we will focus on optical performance and the control scheme of the TDL-DGFF. This device architecture is particularly attractive due to its potential for low loss, scalability and high spectral resolution. More details can be found in reference [2].

Device

The device is a silica waveguide on silicon substrate lightwave optical circuit. It includes 14 tunable couplers based on Mach-Zehnder Interferometers and 8 adjustable time delay lines (fig. 1). Tunability is obtained through a thermo-optical effect. Tuning speed is then in the ms range.

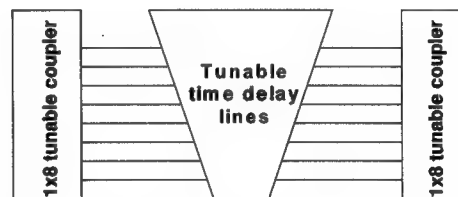


Fig.1 : 8 tap DGFF layout (waveguides & heaters levels).

The response of such device is a sum of 7 Fourier terms. The frequencies are defined by the optical path difference due to both the geometrical path difference and the index change along time delay lines induced by thermo-optical effect. The amplitudes are set through the 1x8 and 8x1 tunable coupler trees. Special care is taken in order to achieve low polarization dependence.

The DGFF module includes both the optical chip and a dedicated electronics. The latter includes the power supply for the TO phase shifters as well as embedded software for device calibration and translation of the optical parameters (amplitudes and phases) into voltages. Fig 2 shows the module.

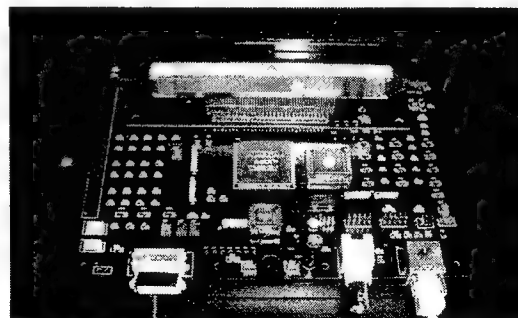


Fig. 2 : DGFF module including optical device and electronics.

Experimental set-up

The experimental set-up includes a wide band source (C+L), a DGFF module, an OSA and a computer (fig.3.).

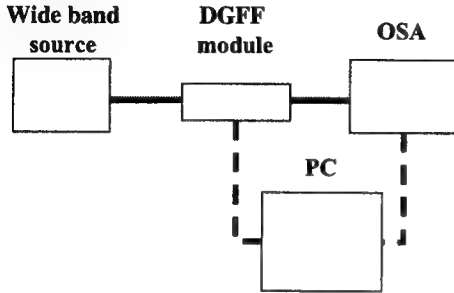


Fig.3 : Experimental set-up.

Control

The DGFF can be driven either using look-up tables or a closed-loop scheme.

In the first case, look-up tables are prepared for several operating conditions (Temperature, EDFA optical input power...). Then, by monitoring these operating conditions, the appropriate look-up table can be retrieved.

In the second case, the optical spectrum has to be monitored. Then, taking into account this input, the desired filter shape is computed as well as the phase and amplitude vector of the Fourier function. After having applied the computed state, the closed-loop control based on an error estimation and correction algorithm is launched. In average, 4 iterations are needed to converge (see Fig.4 & 5.).

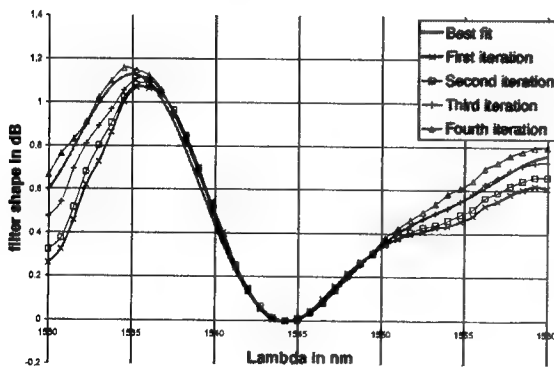


Fig.4 : Theoretical best fit and convergence of the measured spectrum (4 iterations)

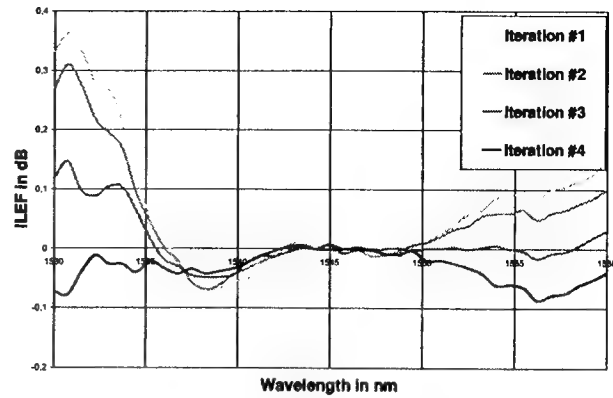


Fig.5 : ILEF convergence (4 iterations)

Optical performances

The typical optical performances of the device are the following :

Parameter	units	performance
Wavelength range	nm	C or L
Dynamic Range	dB	0-10
Slope	dB/nm	3
Max optical power	dBm	25
chip IL (fiber to fiber)	dB	3.5 mean value
Return loss	dB	45
Device response time to steady state	ms	1
Power consumption	W	< 6

Acknowledgements

We would like to acknowledge the Front End, Back End, reliability and Characterization teams from both sides of the ocean, as well as the electronics team from APT. Special thanks to Jean-Claude Presotto, Vincent Tarnier, Jay Zhang, Brad Factor and Arnaud Rigny for their special contributions and fruitful discussions.

References

- [1] G.H.B. Thompson et Al., ECOC 1999, Vol 1 pp 320-321.
- [2] A. Ranalli & Bart Fondeur., ECOC 2000, paper 7-1-2.
- [3] P.M.J.Shiffer et Al. Photon. Technol. Lett., Vol.11, n°9, pp. 1150-1152 (1999)
- [4] M. Mitamura et Al., OFC 2000, WF2, pp.87-89

Liquid-Crystal Optical Harmonic Equalizers

Jung-Chih Chiao

Chorum Technologies

1303 E. Arapaho Road, Richardson, TX, 75081, USA, 214-570-3509, jcchiao@chorumtech.com

INTRODUCTION

In wavelength-division-multiplexing (WDM) optical links, it is important to keep all lasers in a fiber at the same power levels in order to avoid signal-to-noise-ratio degradation. A major cause for dynamic power variations is the power- and wavelength-dependent gain characteristics in optical amplifiers [1]. Several dynamic amplifier-gain equalization approaches have been previously demonstrated [2-5]. In this work, we demonstrated an optical gain equalization and manipulation approach using all-optical liquid-crystal modulators and the harmonic synthesis approach. The functionality of the liquid-crystal optical harmonic equalizer (OHE) was demonstrated with dynamically gain equalization and tilting for different gain profiles by generating required transfer functions with a series of variable harmonic filters.

OPERATIONS

Figure 1 shows the configuration and a photo of a liquid-crystal harmonic gain equalizer. In this configuration, the equalizer has multiple stages of harmonic elements. Each stage includes a liquid-crystal harmonic filter to adjust the wavelength shift and a liquid-crystal attenuator to adjust the amplitude of harmonic waveform. The optical

spectrum analyzer obtains power profiles at the input/output ports of OHE and/or the output of second EDFA. The digital signal processor (DSP) compares the data with the desired gain profile, which can be accessed through the user interface, and calculate the required transfer function to flatten the power profile. The DSP then calculate the amplitude and wavelength shift for each harmonic element by expanding the required transfer function in a Fourier series. The driver circuit applies accurate biasing voltages on the liquid-crystal modulators to achieve the required harmonic shapes.

PERFORMANCE

The response times of liquid-crystal modulators to achieve required amplitude and wavelength-shifting adjustments are in the millisecond and submillisecond ranges. The required biasing voltage magnitudes for liquid-crystal cells are less than 5V. Figure 2 shows typical results of automatic equalization for different gain profiles. An amplified spontaneous emission (ASE) source is used as the input signal of EDFA in the input of OHE, without a second EDFA at the output of OHE. The flattened results were measured at the output of OHE. Fig.2 shows flatness of $\pm 0.15\text{dB}$ and $\pm 0.3\text{dB}$ in the wavelength ranges of 1528-1561nm and 1532-1562nm, respectively. Generally speaking, the flattened output profiles can be reached within less than $\pm 0.3\text{dB}$ for the required flatness levels in less than four equalization iterations. The insertion loss in the through status is around 4.5dB. The dynamic range for equalizing gain profiles is more than 10dB.

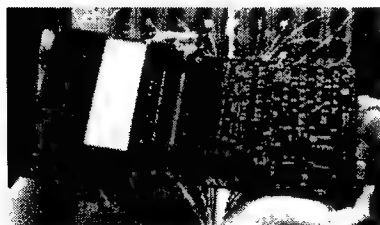
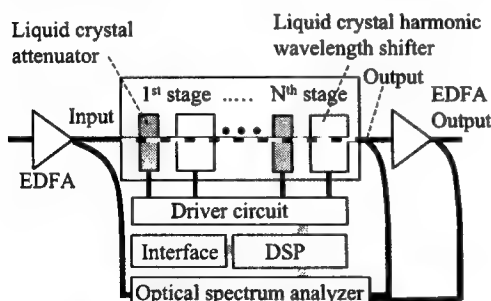


Figure 1: Configuration of a liquid-crystal optical harmonic equalizer with EDFAs and a photo of the optical harmonic equalizer.

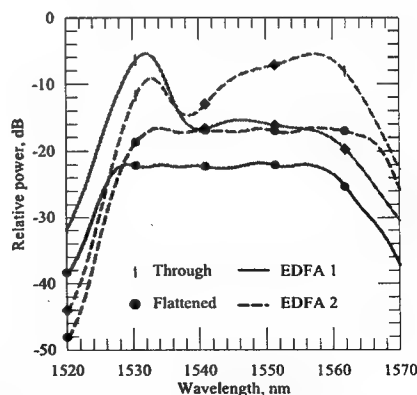


Figure 2: Equalization results and the input power profiles of EDFAs.

The OHE also has flexibility to provide any desired transfer function. For example, it allows different power levels at both ends of passband. The DSP can generate a required transfer function to achieve the desired output levels in a linear fashion. This functionality can provide a gain-tilting profile that may add more operation flexibility in networks with different types of optical amplifiers. Two tilted profiles, along with the flattened profile, are shown in Fig. 3. The flatness of gain is within $\pm 0.3\text{dB}$ and the tilting slopes are $\pm 4\text{dB}$ across 1530-1560nm. The maximum dynamic ranges for tilting slopes in this design are $\pm 10\text{dB}$ over a 30-nm range.

The measured polarization dependent losses are less than 0.15dB and 0.1dB for flattened and non-flattened (through state) profiles, respectively. The measured polarization mode dispersions are less than 0.15ps under the through, flattened and 10-dB attenuation states. The measured chromatic dispersion is less than $\pm 7\text{ps/nm}$ in the wavelength range of 1525-1565nm.

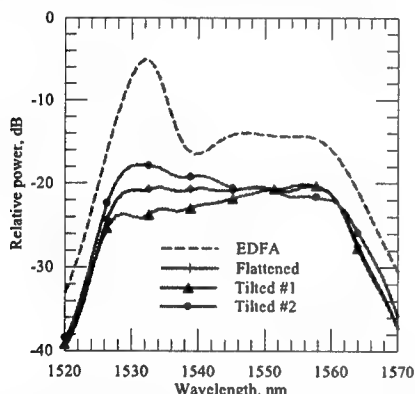


Figure 3: Flattened and tilted gains with the input power profile of EDFA.

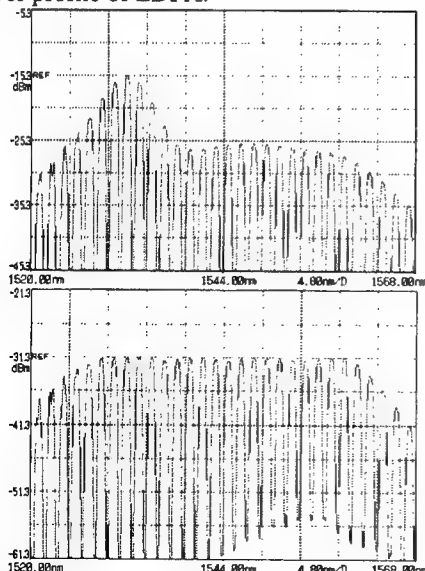


Figure 4: Flattened result for discrete-channel inputs.

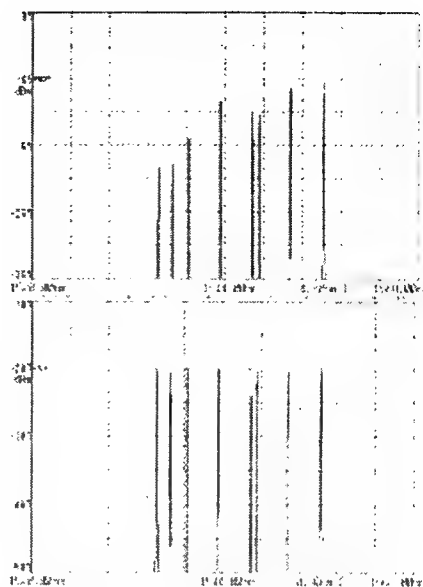


Figure 5: Flattened result for WDM-laser inputs.

Figure 4 shows the flattened result for a discrete-channel input. The discrete channels are generated using a 100-GHz interleaver filter with an ASE source as input. The flatness is within $\pm 0.3\text{dB}$ in the wavelength range of 1528-1560nm. Figure 5 shows the flattened result for multiplexed WDM lasers. The lasers have uneven channel spacings and an uneven power variation of 13dB. The flatness is within $\pm 0.3\text{dB}$.

CONCLUSIONS

Optical harmonic amplifier-gain equalizers using liquid-crystal modulators were demonstrated. Optical performances are presented. The results show great promises for dynamic, quick manipulation of gain profiles in WDM systems. The liquid-crystal optical harmonic equalizers can also be used in other wavelength ranges, such as L-band, since liquid-crystal modulators are broadband devices and the harmonic approach is wavelength independent.

REFERENCES

1. G. Keiser, "A review of WDM technology and applications," *Optical Fiber Tech.*, Vol.5, pp.3, 1999.
2. Y. Li and C. Henry, "Silica-based Optical Integrated Circuits," *IEE Proc.- Opto.*, No.5, Oct. 1996.
3. S. Parry, *et al.*, "Dynamic gain equalization of EDFAs with Fourier filters," *The Optical Amp. & App.*, 1999.
4. S. Yun, *et al.*, "Dynamic erbium-doped fiber amplifier based on active gain flattening with fiber acoustooptic tunable filters," *IEEE Photonics Tech. Ltrs*, Oct. 1999.
5. B. Offrein, *et al.*, "Adaptive gain equalizer in high-index-contrast SiON technology," *IEEE Photonics Tech. Ltrs*, Vol.12, No.5, 2000.

Silica arrayed waveguide dynamic gain equalization filter

C. R. Doerr, L. W. Stulz, M. Cappuzzo, L. Gomez, E. Laskowski, G. Bogert, and R. Pafchek**

Bell Laboratories, Lucent Technologies

791 Holmdel-Keyport Road, Holmdel, NJ 07733

732-888-7067, FAX: 732-888-7074, e-mail: crdoerr@lucent.com

*Agere Systems

9999 Hamilton Blvd, Breinigsville, PA 18031-9359

1. Introduction

One of the very first, if not the first, dynamic gain equalization filters (DGEF's) was made in silica waveguides. It consisted of a single length-imbalanced Mach-Zehnder interferometer with tunable couplers^[1]. Since then, DGEF's with more flexibility have been requested.

The arrayed-waveguide dynamic gain equalization filter (DGEF) consists of a Mach-Zehnder interferometer with a demultiplexer-multiplexer pair connected by an array of equal-length waveguide containing thermo-optic phase shifters in one arm, as shown in Fig. 1^[2]. The relative phases between the upper, "non-filtered" waveguide and the waveguides connecting the demultiplexer and multiplexer, each of which contains a band of the optical spectrum of interest, determine the transmissivity through the interferometer. To insure a smooth transmission spectrum when so desired the waveguide grating apertures are truncated such that the spectrum is not undersampled by the phase-shifter-containing waveguides. In other words, the passbands of the demultiplexer and multiplexer are wide enough to cause significant overlapping between passbands, resulting in a continuous, flat transmission spectrum when all the passbands are added together. The entire interferometer is in silica waveguides on a silicon substrate. The length of the nonfiltered arm is the equal to the lengths of the paths through the back-to-back waveguide gratings, and thus the chromatic dispersion through the device is negligible [measurements of chromatic dispersion of the arrayed-waveguide DGEF are dominated by the few-meter-long fiber leads (< 0.3 ps/nm)].

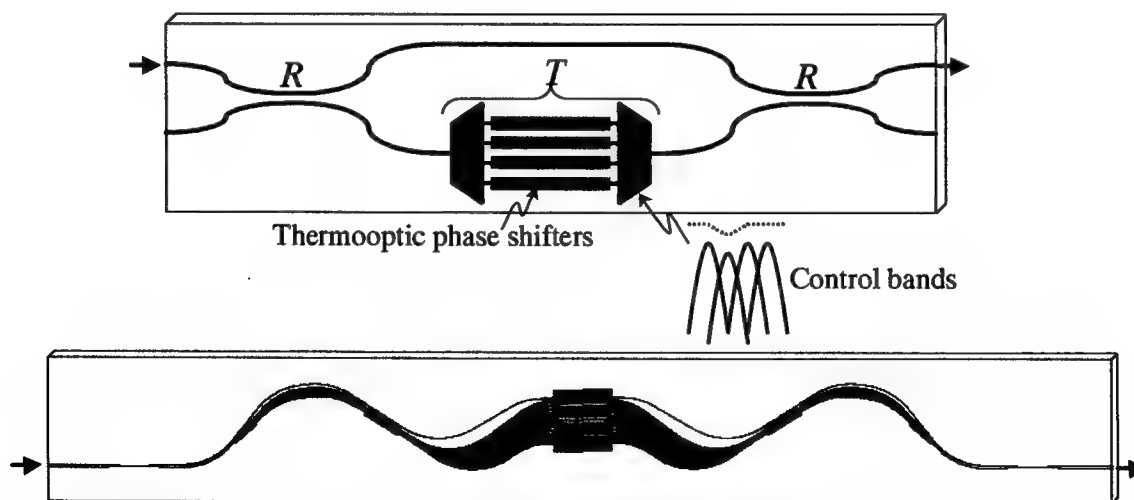


Figure 1. Schematic and waveguide layout of the silica arrayed-waveguide DGEF.

2. Achieving polarization independence

Ultra-long-haul transmission demands ultra-low polarization-dependent loss (PDL) and polarization-mode dispersion (PMD) of its components. Because of the different pattern shapes

for the filtered and non-filtered arms in the silica DGEF and because of a slight polarization dependence in the thermo-optic phase shifters, its transmission spectrum is unfortunately quite polarization dependent. One way to solve this is to use polarization diversity. Polarization diversity is employed via a circulator and polarization splitter in order to achieve polarization independent operation^[3]. Polarization diversity allows one to have only one polarization on the die. Thus the chip can be optimized for a single polarization and be manufactured with high yield. PDL < 0.3 dB and PMD < 0.03 ps (dominated by the fiber leads) under all operating conditions can be routinely obtained.

3. Achieving high spectral resolution

When a DGEF is not used in every optical amplifier, steep slopes in the gain vs. wavelength spectrum can accumulate, requiring a high-spectral resolution DGEF to flatten. The arrayed waveguide DGEF is capable of achieving a high spectral resolution, because the spectral components are controlled in a parallel fashion. An arrayed-waveguide DGEF with 44 controls spaced by 0.8-nm was demonstrated^[3].

4. Achieving low loss

The main loss in the arrayed-waveguide die is the junction between the waveguide arrays and the slab waveguides in the star couplers. This can be significantly mitigated without requiring any new mask or waveguide fabrication technology via segmentation: placing waveguides perpendicular to the waveguides in the waveguide arrays with a width that decreases with distance from the slab waveguide^[4]. Using this technology, the fiber-to-fiber loss of typical arrayed-waveguide DGEF's is now < 2.5 dB over the spectrum. The next main contributors to the loss are the circulator and polarization splitter. These can be combined into one free-space optic device, reducing loss and expense. A DGEF with both these improvements has been demonstrated, giving < 4.5 dB insertion loss and > 14 dB dynamic range across the C-band^[5].

¹ K. Inoue, T. Kominato, and H. Toba, "Tunable gain equalization using a Mach-Zehnder optical filter in multistage fiber amplifiers," *IEEE Photon. Technol. Lett.*, vol. 3, pp. 718-720, 1991.

² C. R. Doerr, M. Cappuzzo, E. Laskowski, A. Paunescu, L. Gomez, L. W. Stulz, and J. Gates, "Dynamic wavelength equalizer in silica using the single-filtered-arm interferometer," *IEEE Photon. Technol. Lett.*, vol. 11, pp. 581-583, 1999.

³ C. R. Doerr, L. W. Stulz, R. Pafchek, L. Gomez, M. Cappuzzo, A. Paunescu, E. Laskowski, L. Buhl, H. K. Kim, and S. Chandrasekhar, "An automatic 40-wavelength channelized equalizer," *IEEE Photon. Technol. Lett.*, vol. 12, pp. 1195-1197, 2000.

⁴ Y. P. Li, "Optical device having low insertion loss," U.S. Patent 5 745 618, Apr. 28, 1998.

⁵ C. R. Doerr, K. W. Chang, L. W. Stulz, R. Pafchek, Q. Guo, L. Buhl, L. Gomez, M. Cappuzzo, and G. Bogert, "Arrayed waveguide dynamic gain equalization filter with reduced insertion loss and increased dynamic range," *IEEE Photon. Technol. Lett.*, vol. 13, pp. 329-331, 2001.

Optical Networking using Micromachines

David T. Neilson

Lucent Technologies
791 Holmdel Keyport Rd
Holmdel NJ 07733
neilson@lucent.com

Lightwave communication systems use fiber-optics to transport signals between nodes, and will use optical layer networking to optimally manage signal paths under normal and disrupted network conditions. Progress in both areas is driven by the shift from voice messaging to data communications and an exponential growth in capacity demands. New micromachine devices (MEMS) are poised to significantly impact the advancement of both networking and transmission see figure 1. The deployment of MEMS based optical cross connects such as Lucent's LambdaRouter see figure 2 allow network flexibility in the optical domain and open the path to optical layer networking. Optical wavelength add-drop switches are a key component in the emerging ultra long haul (>2000km) transmission systems

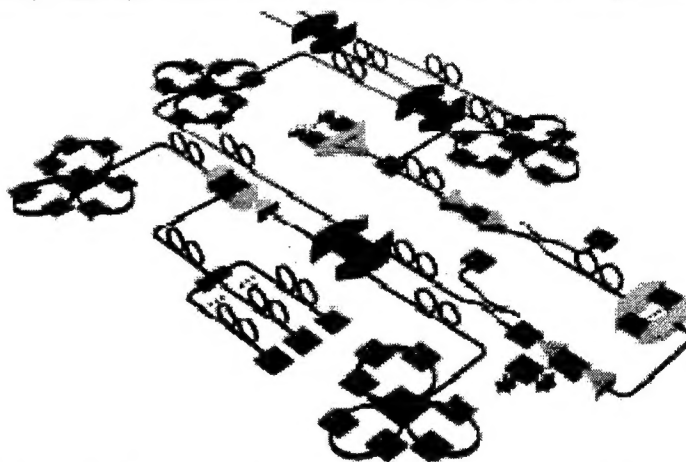


Figure 1: Optical networks showing the application space for Micromachines

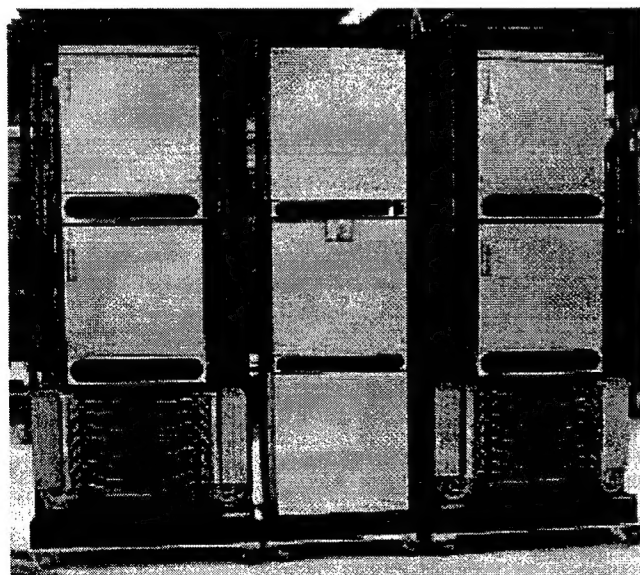


Figure 2: LambdaRouter™

and will expand the optical layer traffic management. The conversion of the optical layer from one of static links to dynamic reconfigurable network will require that the optical transmission system characteristics are reconfigurable. Demonstrations of MEMS variable attenuators, optical spectrum equalizers and dispersion compensators show the potential for robust signal transport in such networks.

MEMS components are notable for their small size, low cost, and flexible scalability. The imminent deployment of lightwave micromachines for transport and networking is expected as industry embraces the technology's maturity, capability, and economics.

AUTHOR INDEX

Adali, T.	MD3.3	Stultz, L.	TuD1.2
Akiyama, S.	MD2.3	Stulz, L.	WD2.2
Alibert, G.	WD1.3	Takiguchi, K.	MD2.1
Almeida, T.	TuD1.1	Tanaka, Y.	MD4.1
Andre, P.	TuD1.1	Tomlinson, J.	WD1.1
Arai, H.	MD2.2	Uetsuka, H.	MD2.2
Barbarossa, G.	MD3.1	Vallon, S.	WD1.3
Bernasconi, P.	TuD1.2	Wada, K.	MD2.3
Bogert, G.	WD2.2	Yaguchi, H.	MD4.1
Boos, N.	WD1.3	Yang, C.	MD3.1
Cao, S.	MD3.1	Yaqoob, Z.	MD1.2
Cappuzzo, M.	TuD1.2,WD2.2	Yun, S.	WD1.2
Cayrefourca, I.	WD1.3		
Chevallier, P.	WD1.3		
Chiao, J.-C.	WD2.1		
Chiba, T.	MD2.2		
Doerr, C.	TuD1.2,WD2.2		
Eggleton, B.	MD3.2		
Furuki, K.	MD4.1		
Gomez, L.	TuD1.2,WD2.2		
Haus, H.	MD1.3,MD2.3,TuD1.3		
Higashi, N.	MD4.1		
Jablonski, M.	MD4.1		
Joyner, C.	MD1.3		
Kaiser, P.	MD1.1		
Khan, M.	MD1.3		
Kikuchi, K.	MD4.1		
Laborde, P.	WD1.3		
Landru, N.	WD1.3		
Laskowski, E.	TuD1.2,WD2.2		
Lim, M.	MD1.3		
Lima, A.	MD3.3		
Lima, I.	MD3.3		
Lin, C.	MD3.1		
Little, J.	WD1.3		
Madsen, C.	MD4.2		
Manolatu, C.	TuD1.3		
Menyuk, C.	MD3.3		
Michel, J.	MD2.3		
Moeller, L.	MD3.4		
Murphy, T.	MD1.3		
Neilson, D.	WD2.3		
Nonen, H.	MD2.2		
Ohira, K.	MD2.2		
Okano, H.	MD2.2		
Pafchek, R.	WD2.2		
Paunescu, A.	TuD1.2		
Pinto, A.	TuD1.1		
Pinto, J.	TuD1.1		
Popovic, M.	MD2.3		
Pousa, M.	TuD1.1		
Ranalli, A.	WD1.3		
Riza, N.	MD1.2		
Sato, K.	MD4.1		
Shunk, S.	TuD1.2		
Smith, H.	MD1.3		

